Politecnico di Torino

MSc in Aerospace Engineering

Preliminary Study of a Docking System for a Lunar Pressurized Rover

Candidate: Thomas Binetti

Supervisors: Prof. Erasmo Carrera
Prof. Alfonso Pagani
Ing. Karim Abu Salem
Ing. Giuseppe Palaia

Academic Year 2024/25

Contents

II The Docking Subsystem 73

4 The Docking Subsystem 75

5 Docking Mathematical Model 91

List of Figures

List of Tables

List of Symbols

Symbol	Name	Units
β	Dundur's bimaterial constant	GPa
$\dot{\phi}_d$	Relative roll velocity (along x)	$°/s$
$\dot{\vartheta}_d$	Relative pitch velocity (along y)	$°/s$
$\dot{\psi}_d$	Relative yaw velocity (along z)	$°/s$
$\dot{x}_d$	Relative velocity along x	m/s
$\dot{y}_d$	Relative velocity along y	m/s
$\dot{z}_d$	Relative velocity along z	m/s
ℓ	Characteristic Length	m
$\ell_{II,0}$	Shock-absorber rest length	m
$\Gamma(x)$	Euler's Gamma Function	
$\hat{E}$	Second composite Modulus	GPa
κ_{ref}	Reference Contact Stiffness (C_P)	N/m^n
$\mathcal{A}$	Contact area	
$\mathcal{A}_{walkable}$	Cabin Walkable Area	m^2
$\mathcal{D}_{em}$	Equivalent Dose	mSv/y
$\mathcal{F}_c$	Contact safety factor	
$\mathcal{F}_p$	Pressurization safety factor	
$\mathcal{G}$	Dimensionless pressurization factor	
$\mathcal{M}_c$	Contact safety margin	
$\mathcal{M}_p$	Pressurization safety margin	
$\mathcal{P}_{aux,inst}$	Auxiliary Installed Power	kW
$\mathcal{P}_{com}$	COMSYS power requirement	W
$\mathcal{P}_{dock}$	Docking power requirement	W
$\mathcal{P}_{light}$	Lighting power requirement	W
$\mathcal{P}_{mob}$	Mobility power requirement	W
$\mathcal{P}_{scien}$	Scientific power requirement	W
$\mathcal{P}_{TCS}$	TCS power requirement	W

$\mathcal{P}_{tot,inst}$	Total Installed Power	kW
$\mathcal{R}_0$	Inertial Reference Frame	
$\mathcal{R}_1$	Chaser Reference Frame (Center of Docking)	
$\mathcal{R}_2$	Target Reference Frame (Center of Docking)	
μ	Reduced mass	
μ_d	Dynamic friction coefficient	
μ_s	Static friction coefficient	
ν	Poisson's Ratio	
$\omega_{d,II}$	Shock-absorber damped frequency	rad/s
$\omega_{n,II}$	Shock-absorber natural frequency	rad/s
Ω_c	Contact frequency	rad/s
ϕ_d	Relative roll angle (along x)	°
ψ_d	Relative yaw angle (along z)	°
ρ	Density	kg/m^3
$\rho_{BED,grav}$	Battery Energy Density (BED), gravimetric	kWh/kg
$\rho_{BED,vol}$	Battery Energy Density (BED), volumetric	kWh/L
$\rho_{inflatable}$	Inflatable Density	kg/m^3
ρ_h	Dimensionless double torus height	
ρ_m	Dimensionless inner torus' meridional radius	
ρ'_m	Dimensionless outer torus' meridional radius	
ρ_t	Dimensionless inner torus' toroidal radius	
ρ'_t	Dimensionless outer torus' toroidal radius	
σ_y	Yield Strength	MPa
τ_I	Contact Characteristic Time	s
$\tilde{\kappa}_{ref}$	Reference Contact Stiffness (c_p)	
$\textrm{þ}$	Relative misalignment error	
φ	r'_m/r_m ratio	
ϑ_{obst}	Obstacle inclination	°
ϑ_d	Relative pitch angle (along y)	°
ϑ^*	Torus' limit angle	°
ζ_{II}	Shock-absorber dimensionless Damping	
a	Contact area semi-major axis	m
a_d	Relative acceleration (magnitude)	m/s^2
b	Contact area semi-minor axis	m
c	Terrain Cohesion	
c_{II}	Shock-absorber Damping	$N/(m/s)$
C_{rr}	Rolling resistance coefficient	

C_g	Geometrycal coefficient	
c_I	Contact Damping (Performance Model)	$N/(m/s)$
C_P	Contact force coefficient	
c_p	Contact pressure coefficient	
D_{cabin}	Cabin Diameter	m
D_{sp}	Spring nominal radius	mm
d_{sp}	Spring wire radius	mm
DOD_f	Final Depth of Discharge	
DOD_i	Initial Depth of Discharge	
E	Young's Modulus	GPa
e	Contact area eccentricity	
E_{aux}	Auxiliary Energy	kWh
E_{batt}	Stored battery energy	kWh
$E(e)$	Elliptic Integral (II kind)	
E^*	Reduced Young's Modulus	GPa
G	Shear Modulus	GPa
$g_{\mathbb{D}}$	Moon's gravitational acceleration	m/s^2
g_0	Initial gap	m
h	Indentation Depth	
h_{cabin}	Cabin Height	m
h_{max}	Maximum indentation	m
h_t	Double torus height	
k_{φ}	Bekker's second coefficient (pressure-sinkage)	N/m^n
k_{II}	Shock-absorber Stiffness	N/m
k_c	Bekker's first coefficient (pressure-sinkage)	N/m^{n+1}
k_I	Contact Stiffness (Performance Model)	N/m^n
$K(e)$	Elliptic Integral (I kind)	
$L_{inflatable}$	Inflatable Module Length	m
L_{rigid}	Rigid Module Length	m
$m_{astronaut}$	Single astronaut mass	kg
$m_{aux,source}$	Auxiliary source mass	kg
m_{batt}	Battery mass	kg
m_{crew}	Crew mass	kg
m_{dry}	Dry mass (Cygnus)	kg
m_{empty}	Empty mass	kg
$m_{EVA,suit}$	EVA suit total mass	kg
$m_{other,source}$	Other mass in source mass	kg

m_{pl}	Payload hauling capacity	kg
m_{source}	EPS mass	kg
m_{tot}	Total Mass of the LPR	kg, ton
n	Contact exponent	
$N_{crew,em}$	Emergency crew with no range	
N_{crew}	Crew Size	
$N_{magnets}$	Total number of magnets	
n_{spring}	Spring active coils	
N_{spring}	Total number of shock-absorbers	
n_w	Number of wheels	
P	Contact force	N
P_{adm}	Contact admissible force	N
p_{LSS}	Specific LSS power requirement	$W/crew$
p_{press}	Pressurization nominal pressure	Pa
$p_{spec,grav}$	Specific Auxiliary Power	kW/kg
p_0	Contact pressure (max.)	Pa
Q	Tangential Contact force	
q_0	Tangential Contact pressure	
r_d	Relative position (magnitude)	m
r_m	Inner torus' meridional radius	m
r'_m	Outer torus' meridional radius	m
r_t	Inner torus' toroidal radius	m
r'_t	Outer torus' toroidal radius	m
R_u	Torus' first curvature radius	m
R_v	Torus' second curvature radius	m
S	Linear actuator stroke	mm
t_{EVA}	EVA time	h
$t_{m,ext}$	Extended Mission Duration	d
$t_{m,nom}$	Nominal Mission Duration	h
T_{max}	Maximum Temperature	$^\circ$
T_{min}	Minimum Temperature	$^\circ$
u_x	Displacement along x	m
u_y	Displacement along y	m
u_z	Displacement along z	m
V_{fuel}	Fuel tank volume (automotive)	
v_{nom}	Nominal Velocity	km/h
$V_{nominal}$	Power bus nominal voltage	V

$V_{tot,internal}$	Total Cabin internal Volume	m^3
v_d	Relative velocity (magnitude)	m/s
V_s	Slip Velocity	
w_{cabin}	Cabin Width	m
$x_{approach}$	Approach Distance	km
x_{obst}	Obstacle length	cm
x_d	Relative position along x	m
x_r	Mission Range	km
x'_r	Mission Range (lunar night)	km
y_d	Relative position along y	m
z_{obst}	Obstacle height	cm
z_d	Relative position along z	m

Alla mia famiglia.

Premise

This work was made in collaboration with Thales Alenia Space Italy, in Turin in the context of the Space it Up! Program and particularly in Spoke 8.

Space it Up! is a program aimed at advancing Italy's space technologies to support space exploration and utilization for the benefit of planet Earth and humankind. One of the main objectives of the program concerns the promotion of terrestrial applications derived from space technologies. The initiative focuses on strengthening activities that leverage space-based solutions to generate applications, products, or services with potential impact on emerging sectors, including international transport, planetary protection, and rural education. Particular attention is devoted to knowledge transfer and cooperation among leading national universities, research organizations, industries, and SMEs. The *Space it Up!* program identifies nine thematic areas as strategic priorities to address the challenges posed by major international players in the space sector, covering both upstream and downstream applications. These areas are organized into nine Spokes: four "Transversal Spokes" (Spokes 14), focused on enabling technologies and shared disciplines, and five "Horizontal Spokes", addressing Earth observation (Spokes 57) and space exploration (Spokes 89).

Chapter 1

Introduction

Since ancient times, humanity has gazed at the stars, driven by an enduring desire to explore and understand the cosmos. This curiosity, once limited to observation, has evolved into a focused pursuit of reaching and settling beyond our planet, with the **Moon** as the first milestone in achieving a sustained human presence in space.

The renewed interest in lunar exploration marks a significant chapter in the modern era of space exploration, aiming not only to visit the Moon again but also to establish a sustainable human presence on its surface [1]. One of the essential elements to achieve this vision is the development of a **Lunar Pressurized Rover** (LPR), a vehicle that enables astronauts to conduct extended surface operations in a safe and controlled environment. The capabilities of a pressurized rover address key challenges of lunar exploration, ranging from protection against the harsh lunar environment to the efficient transportation and support of crews over vast distances.
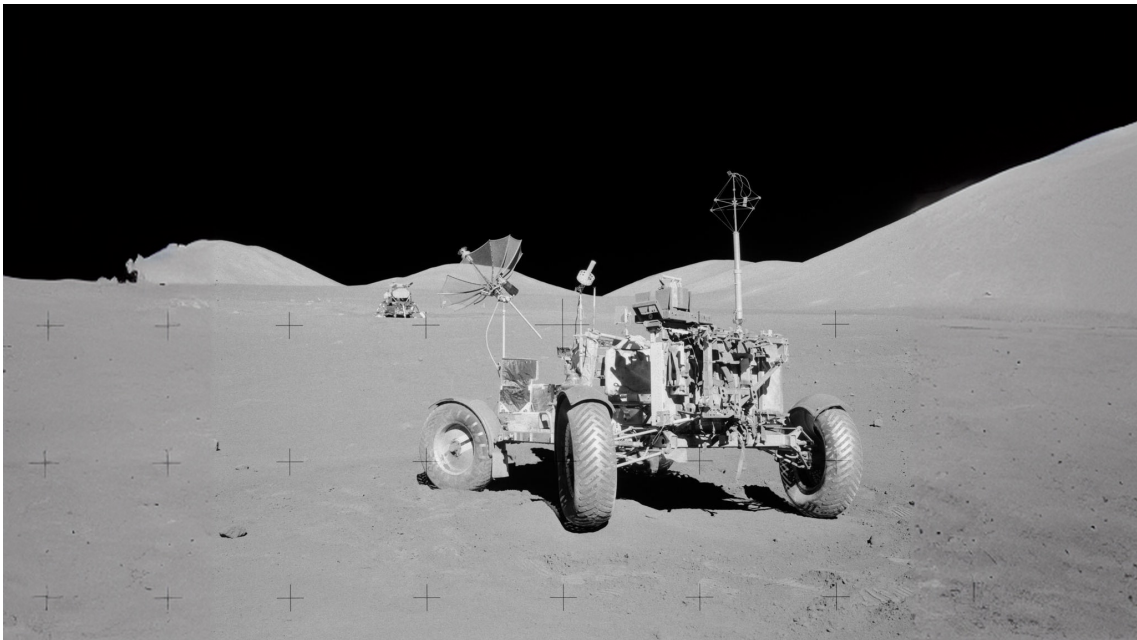
Figure 1.1: Apollo 17 Lunar Roaming Vehicle

The best example of manned vehicular activities on the surface of the Moon are the Apollo Lunar Roving Vehicles (LRVs) [2], which provided invaluable support during the Apollo missions by expanding astronauts operational range on the

Moons surface. However, these unpressurized rovers were limited in scope, allowing astronauts to conduct only short excursions due to restrictions imposed by their space suits and life-support systems. In contrast, a pressurized lunar rover would enable much **longer excursions** potentially spanning days rather than hours by providing a controlled, life-sustaining environment. Such a vehicle would be transformative in facilitating in-depth geological surveys, resource prospecting, and the preparation for potential lunar habitats.

1.1   Advantages of a Pressurized Lunar Rover

A pressurized lunar rover offers multiple **advantages** over its unpressurized competitors, in terms of:

1. astronauts' safety and comfort;

2. increased mission duration;

3. long-duration scientific exploration;

4. human settlement support on the lunar surface;

5. emergency situations.

1.1.1   Sealed vehicle benefits

Firstly, the use of a LPR enhances the **safety** and **comfort** of astronauts by providing a fully enclosed, pressurized cabin that protects them from the Moons extremely harsh environment, which consists of acute temperature fluctuations, high radiation levels, and abrasive lunar dust. The lunar surface experiences temperature changes from approximately $+120\ °C$ during the day to $-130\ °C$ at night, and these conditions, combined with limited radiation shielding on lunar surfaces, pose a considerable hazard to human health and mission success [3]. A pressurized environment not only mitigates these temperature challenges but also allows the incorporation of radiation-shielding materials that would be infeasible in a traditional suit or unpressurized vehicle.

Moreover, pressurized rovers facilitate **increased mission duration** and operational flexibility. By allowing astronauts to perform activities without space suits within the vehicle, the pressurized rover reduces the physiological burden of lengthy extravehicular activities (EVAs), where mobility is restricted by the stiffness and bulkiness of space suits. Instead, astronauts can use the rover as a **mobile habitat**, from which they can strategically plan and deploy shorter EVAs with greater frequency and lower physical strain, thereby optimizing productivity. This advantage is particularly significant when exploring regions of interest that are far from lunar landing sites or establishing more permanent lunar bases, as it expands the range and duration of scientific and logistical missions.

1.1.2   Scientific Exploration and Resource Utilization

The ability of a pressurized rover to support **long-duration** missions is also pivotal for **scientific exploration**. Lunar missions are increasingly focused on areas which

are rich in scientifically valuable resources, such as permanently shadowed regions at the lunar poles, which are believed to contain ice deposits [3]. These ice deposits could serve as a vital *in-situ* resource, providing water, oxygen, and hydrogen for human consumption, life support, and fuel production [4]. A pressurized rover allows for systematic exploration and sampling of these areas over extended periods, significantly contributing to our understanding of lunar resources and their potential for supporting future lunar bases.

1.1.3   Supporting Human Settlement on the Moon

The development of a pressurized lunar rover is integral to the larger goal of **sustainable human settlement on the Moon**. Future lunar bases will likely depend on the regular transportation of crew, materials, and resources over potentially long distances, a task that a pressurized rover is uniquely suited to accomplish. Beyond exploration, pressurized rovers can play a critical role in the logistics and maintenance of surface operations, such as:

1. the construction of habitats;

2. installation of solar panels;

3. deployment of scientific instruments.

In addition, the mobility of the rover provides a contingency plan for **emergency situations**, offering a mobile refuge for astronauts if they need to evacuate a habitat or move to a safer location. This capability enhances the safety of surface operations, making pressurized rovers a crucial component of any sustainable lunar settlement plan.

1.2   Outline

Pressurized Rovers will play an essential role in realizing the ambitious goals of modern lunar missions, acting as both mobile laboratories and habitats that bridge the gap between temporary missions and permanent lunar presence.

In the next chapters it is the aim of this work to develop a functional design of a LPR. Starting from the definition of the mission, and a list of requirements useful for the sizing and performance evaluation of a vehicle of this type, we will proceed with the evaluation of a preliminary design of the vehicle, observing the main sizing aspects that involve this class of systems. Particular attention is paid to the docking subsystem, one of the subsystems mainly used in ensuring a rigid connection, both mechanical and connective, between a moving vehicle (in this case it is represented by the rover) and a possible permanent motherbase. As for the design of the entire vehicle, starting from an in-depth research of the state of the art of the principal docking subsystem implemented in the history of space exploration, and a description of the specific requirements of the subsystem, the work continues with the subsystem sizing that touches on the main mechanical, dynamic, structural and mechatronic aspects, with the aim of establishing the mass power budgets and ensuring the correct safety of the astronauts during a mating operation for grounded vehicles. To fully evaluate the characteristics of this subsystem, an implementation

or *genetic optimization algorithm* model is developed that studies the main variables of the subsystem as well as a scaled prototype that confirms the validity of the hypothesis and simulations shown previously.

Part I

Preliminary Design

Chapter 2

Requirements

The initial step in designing a Lunar Pressurized Rover (LPR) involves the comprehensive definition of its requirements, a critical process that lays the foundation for all subsequent design phases. These requirements, which vary in scope and specificity, are influenced by both the intended performance objectives and the specific expectations of the client or mission sponsor. Clearly defining these parameters ensures that the rover will meet mission needs while adhering to technical and operational standards.

Usually, requirements are divided using the ECSS-E-ST-10-06C standards [5]. For the aim of this work, four main categories are evaluated from the proposed list. First, **performance requirements** specify the key objectives the rover must achieve, including mobility range, energy efficiency, and environmental resilience. Second, baseline parameters, often dictated by the *client needs*, establish the **design requirements**, such as the expected load capacity, endurance limits, and communication capabilities. Third, **mission requirements** depend on the mission profile and specify factors such as the type of terrain the rover will encounter, anticipated mission duration, and the frequency and length of extravehicular activities (EVAs) supported. Lastly, **regulatory and environmental constraints** ensure compliance with relevant safety, environmental, and operational standards set by space agencies and regulatory bodies, which are essential for mission authorization and international cooperation.

To build a comprehensive analysis of the LPR requirements, a state of the art study is proposed. From this, a mission profile of the mission is expressed and finally, the complete set of requirements is described.

2.1   State of the art

To identify the most critical requirements, with a particular attention to *performance requirements*, a statistical analysis is performed to facilitate a trade-off evaluation among various models. The table below provides an overview of the current state of the art in rover vehicles designed for lunar and Martian missions.

Vechicle or Author	Mission	Press.	Crew Size	L (m)	W (m)	H (m)	m_{tot} (ton)	v_{max} (km/h)	x_r (km)	$\mathcal{P}_{tot,inst}$ (kW)	Power Source	Ref.
NOMAD	Terrestrial	No	0	2.4	2.4	2.4	0.77	1.8	200	2.4	Gasoline	[2]
RATLER	Terrestrial	No	0	1							PEM fuel cells	[2]
Light Utility Rover	Lunar	No	2	4.06	2.34		0.99	1		1	Fuel cells, rechargeable Batteries	[2]
Dual Mode Lunar Roving Vehicle	Lunar	No	2	3.5	3		8	0.33			Three Radiosotope power sources	[2]
Rover First	Lunar	Yes	2	4.1	2.6		4.3	1	80		8 Shuttle type fuel cells	[2]
USRA Studies Creel	Lunar	Yes	4	7	3		6.2	18	500	6.7	Radioisotope thermoelectric generator	[2]
USRA Studies Bhardwaj	Lunar	Yes	4	11	4		7	29.4	2000	8.5	Dynamic isotope power generator	[2]
MSTS	Lunar	Yes										[2]
Hoffman, 1997	Mars	Yes	2	5				10	500	10	Dynamic isotope power system	[2]
Daylight Rover	Lunar	Yes	2				25	4	1000	10	Regenerative fuel cells	[2]
Arno, 1999	Lunar	Yes	3				6.08	20	100	6	Fuel cells	[2]
Mega Rover Thangavelu	Lunar	Yes	6	16	4.5	10	45		2000			[2]
Lunar Sortie Vehicle	Lunar	Yes	6							3.5	Radio thermal generator	[2]
Habot	Lunar	Yes	6	5			10				Photovoltaic cells	[2]
MORPHLAB	Lunar and Mars	Yes	4	4			3.7		1000	20	Dynamic isotope power system	[2]
RAMA Rover	Lunar	Yes	2	5	6	6.4	5.5		1600		Fuel cells	[6]

Table 2.1: List of the active project of rovers

2.2 Mission Definition

One of the requirement categories listed above derives from the **mission profile**. It becomes crucial to establish the mission to guide the design process effectively because, as it emerges from the state of the art analysis, this class of systems tend to vary a lot in terms of range and size. It is therefore necessary to fix a particular mission type for the LPR.

2.2.1 Remote Location

The core concept underlying the rover mission is the necessity of addressing operations conducted in *remote locations*. A **remote location** is defined as any site of activity situated at a certain distance from the primary lunar habitat, where operations are carried out to support the mission objectives. Representative examples of such remote missions include:

1. Energy Infrastructure: a **nuclear reactor**, intended to provide energy to the lunar habitat, must be located at a safe distance to minimize radiation exposure and enhance the safety of the habitat and its inhabitants. The operativity and maintenance of such a reactor require mobility to facilitate monitoring, repair, and routine inspections. A rover capable of accessing the reactor containment area would ensure the safe and efficient functioning of the energy system, while simultaneously safeguarding the well-being of the astronauts. Moreover, **nuclear waste disposal** is achieved safely if the waste is transported from the nuclear plant to disposition sites on a vehicle rather than other forms (i.e. bringing the nuclear waste manually to a disposal site, or carrying it out remotely via an unmanned vehicle).

2. Resource Extraction: **mining operations** represent another example of remote activities. While the positioning of the lunar habitat is determined by factors such as solar exposure, access to resources, and logistical considerations for module launches and landings, mining sites are optimally located in regions which are rich in extractable materials. The operation of a quarry, involving material extraction, maintenance, and monitoring, necessitates reliable transportation between the habitat and the site. A rover equipped for such tasks would enable the efficient transport of materials and the operational management of mining facilities.

3. Scientific Exploration: **scientific missions** may also necessitate remote locations to ensure the integrity of experimental results. Measurements conducted in proximity to the lunar habitat, such as temperature readings, core sampling, or surface analysis, could be compromised by anthropogenic disturbances. Conducting these experiments in an undisturbed environment is essential. Furthermore, a *pressurized rover* equipped with onboard laboratory facilities enables in-situ analysis of collected samples, eliminating the need for immediate return to the habitat. For instance, material specimens could be examined directly using microscopes and other analytical instruments housed within the rover, thereby enhancing the efficiency and goal reaching of scientific research.

In conclusion, the implementation of a versatile and reliable pressurized rover is paramount to supporting critical remote operations on the lunar surface. Pressurization not only enables extended mission duration and enhance astronaut safety but also allows for *in-situ* analysis of materials and experiments within controlled environments, ensuring the efficient and continuous functioning of energy systems, resource extraction activities, and scientific exploration missions.

2.2.2   Mission Profile

The mission profile is presented in Figure 2.1. The rover operates within a specific x_r range, encompassing two distinct approach zones $x_{approach}$: one directed towards the permanent base dubbed **motherbase** and the other towards the remote location. For simplification of purposes, it is assumed that these two segments are of equal length. During this phase of the trajectory, the rover's speed is intentionally reduced to facilitate docking and approach maneuvers. This reduction in velocity ensures precise and safe docking, either at the lunar habitat or at remote locations, particularly if the rover is pressurized and equipped with a compatible docking interface. This operational adjustment is critical to maintaining mission efficiency and ensuring seamless integration with external systems.
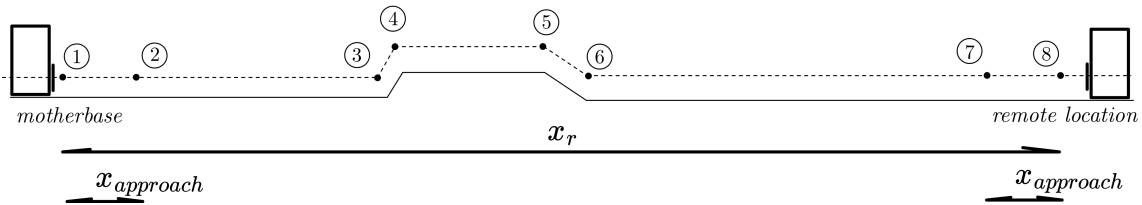
Figure 2.1: Mission Profile

It is important to note that the mission has been represented as two-dimensional. However, this simplification does not imply that the rover is restricted to linear trajectories between the base and remote locations. Steering manoeuvrers must be accounted for to navigate paths that are not perfectly aligned with the mother base.

For this type of mission, it has been chosen to restrict the **nominal mission time**, identified as $t_{m,nom}$, to a duration of less than one day. In this way, the departure and arrival towards the motherbase allow the astronauts to return to their respective bunks and sleep for the subsequent tasks in the following days. The mission can eventually be extended to an **extended mission time**, indicated as $t_{m,ext}$, to more than one day, for operations that concern extended periods of time. To ensure this type of versatility, a configuration is chosen that provides for a physical extension of the system through an inflatable module, discussed in the following chapters.

2.2.3 Reference obstacle

Another critical aspect to consider is the **reference obstacle**. The reference obstacle serves as a sizing parameter, defining the range of surface irregularities that the rover's mobility system can overcome. These obstacles include both surface elevations, such as bumps, and depressions, which reflect the inherent imperfections of the lunar terrain.
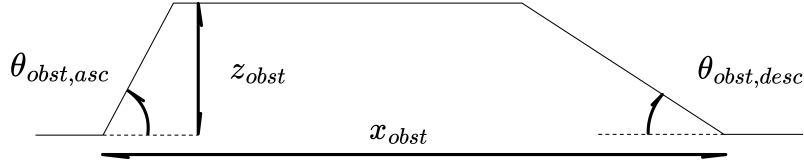
Figure 2.2: Reference Obstacle

2.2.4 Automotive considerations

From the mission definition, it becomes evident that a pressurized vehicle shares significant similarities with an automotive vehicle, particularly in terms of its structural design and functionality. However, unlike a standard car, this vehicle must also facilitate a range of operations within its interior and allow for the unrestricted movement of astronauts. Among terrestrial vehicles, the closest analogy to such a design is that of a *campervan*, which combines mobility with habitable interior spaces. To better understand the requirements, a comparative analysis is conducted by listing the primary specifications and masses of commercially available campers. This comparison serves as a reference to identify which existing rover designs, as reviewed in the state of the art, most closely align with these characteristics.

Model	m_{tot}	N_{pax}	$\mathcal{P}^{inst}_{tot}$	$\mathcal{P}^{inst}_{aux}$	V_{fuel}	x_r	v_{max}	W	L	H
Discoverer 4	3	4	100	2	0.08	700	120	2	5.5	2.6
Winnebago Solis Pocket	3.5	4	209	2	0.09	600	110	2.08	5.88	2.77
Tiffin Open Road Allegro	11.8	6	270	5	0.28	800	100	2.5	10.36	3.81
Airstream Interstate 19	4.5	4	155	2	0.09	600	110	2.02	6.4	2.8
Volkswagen California	3	4	110	2	0.08	700	120	1.9	4.9	1.99
Average	5.16	4	169	2.6	0.124	680	112	2.1	6.608	2.794
Units	*ton*		*kW*	*kW*	m^3	*km*	*km/h*	*m*	*m*	*m*

Table 2.2: Campervans specifications of vehicles currently on the market.

Moreover, a table listing nominal values for large electric cars is also considered. This statistical study is conducted to delineate average values for electric vehicles, due to the fact that **batteries** are used as the main source of power supply to the system. From the table below, it is possible to estimate the ratio between the battery and the overall mass as $m_{batt}/m_{tot} \cong 1 \div 4$.

Model	m_{tot}	N_{pax}	$\mathcal{P}_{tot}^{inst}$	$\mathcal{P}_{aux}^{inst}$	m_{batt}	x_r	v_{max}	W	L	H
Lucid Air Grand Touring	2.27	5	620	10	600	830	270	1.94	4.97	1.41
Mercedes-Benz EQS 580	2.66	5	385	10	650	770	210	1.93	5.22	1.51
Tesla Model S Plaid	2.16	5	750	10	600	637	322	1.96	4.97	1.44
BMW iX M60	2.58	5	455	10	620	450	250	1.97	4.95	1.7
Rivian R1S	3.14	7	600	10	700	515	200	2.01	5.13	1.82
Average	2.56	5	562	10	634	640	250	1.96	5.05	1.58
Units	ton		kW	kW	kg	km	km/h	m	m	m

Table 2.3: Electric car specifications of vehicles currently on the market.

2.3 Lunar environment design considerations

As stated in [7], a great deal of knowledge of the lunar environment resulted from the intensive studies and experiences of the Apollo program. The following paragraphs examine important features to the design of a vehicle for lunar operations to address the main aspects of the lunar environment and justify the selected environmental requirements.

Figure 2.3: Apollo 11 Mission image - View of moon limb, with Earth on the horizon (source: NASA).

2.3.1 Temperature

Essentially the Moon is devoid of atmosphere. Unlike the Earth, radiation to and from the lunar surface is not hindered by an atmospheric blanket. This causes severe temperature ranges and gradients. Temperature extremes on the surface range from $-233\,^{\circ}C$ within shadowed polar craters to $123\,^{\circ}C$ in the equatorial regions. Average temperatures are about $107\,^{\circ}C$ during the day and $-153\,^{\circ}C$ at night [3]. Temperature is a critical consideration for many subsystems. The thermal control

system must be able to accommodate this wide range of conditions. Furthermore, it is important to avoid thermal mismatches between bonded materials.

2.3.2 Gravity

The gravitational acceleration at the lunar equator is $g_{\leftmoon} = 1.62 \ m/s^2$, about one-sixth of the Earth's. This is critical to the design of the mobility system since weight is a primary variable in determining vehicle performance. The human factors associated with this lower gravity are also important. Apollo 12 astronauts explained that the characteristic "loping" gait seen in films was the most natural way to move; heel-to-toe "Earth" walking was more difficult and energy consuming [3]. It is therefore critical that the vehicle's inner layout accommodates the astronauts as they deal with this environment. In lunar gravity, a $0.4 \div 1.25 \ m$ vertical hop is easier than using conventional stairs. This allows steps to be much larger. Also, seats that support the knees and buttocks are often used, considering the posture people maintain.

2.3.3 Radiation

The Moon is exposed to many types of ionizing radiation that can be biologically harmful. The three dominant types are:

- the **solar wind**;

- **solar flares** associated particles (also called solar energetic particles or solar cosmic rays);

- galactic **cosmic rays**.

These forms of radiation consist mainly of protons and neutrons with some heavier nuclei. Radiation levels vary with time and usually reflect solar activity. Obviously, the vehicle must protect its occupants from these harmful types of radiation.

2.3.4 Micrometeoroids

A meteoroid is a naturally occurring solid body travelling through space, smaller than a comet or asteroid. Micrometeoroids are those meteoroids whose diameters are less than approximately one millimeter. These evaporate upon entering Earth's atmosphere but are an important consideration for lunar activities. From size and frequency distributions, it can be estimated that a micrometeoroid of about one milligram mass should be expected to strike the rover yearly, with smaller objects being more frequent and larger ones rarer. Velocities have been calculated to range from $13 \div 18 \ km/s$. It has been suggested that two to three millimetres of a tough composite material would provide effective shielding against damage by micrometeoroids in the milligram mass range. Another option is to use a buffer zone behind a less tough material. This would cause the micrometeoroid to disperse so that it cannot penetrate the hull. The rarer impacts of larger meteoroids pose a more significant hazard, especially to critical components. These components should be protected (by placing them where they cannot be struck) to ensure their safety.

2.3.5 Trafficability

Trafficability is defined as the capacity of a soil to support a vehicle and to provide sufficient traction for movement. Many elaborate walking machines were developed prior to actual landings because it was assumed that trafficability would be poor. However, from the experience of both Apollo and *Lunakod* missions, it is now known that almost any vehicle with round wheels can perform satisfactorily on the lunar surface, provided that the ground contact pressure is no greater than $7 \div 10 \; kPa$. The energy consumed by wheeled vehicles can be estimated. Important parameters include the wheel load, wheel footprint area, chord length of wheel ground contact, width of wheel ground contact, and various previously measured soil characteristics.

2.3.6 Dust

The lunar regolith has grainy characteristics very similar to silty sand. Many of the particles are sharp and glassy [3]. Accumulation and adhesion to equipment were experienced on previous missions. "Sandblasting" can occur, especially in the presence of take-offs and landings. Exposed or delicate equipment will have to be protected from the harmful effects of lunar dust. Also, dust removal equipment must be used after extra-vehicular activity.

2.4   List of Requirements

Based on the state of the art, and following the ECSS-E-ST-10-06C standards [5], a definition of the following requirements is therefore obtained. The order of presentation is selected to show the main requirements selected of the mission. If a reference is presented on the requirement, it means that the value is selected after a state of the art study of the model.

Requirements	Typology	Abbreviation
Typology	PERF	Performance
	MISS	Mission
	DES	Design
	REG	Regulatory and Environmental
Category	A	System
	B	Sub-system
	C	Component

Table 2.4: ECSS classification of requirements.

ID	Name	Symbol	Value	Un.	Ref.	Description
R-PERF-A-01	Payload mass	m_{pl}	1000	kg		The rover shall be capable to sustain m_{pl} of payload
R-PERF-A-02	Nominal crew	N_{crew}	2			The rover shall be able to support a nominal crew of N_{crew}
R-PERF-A-03	Maximum speed	v_{nom}	30	km/h		The rover shall reach a nominal speed of v during the mission
R-PERF-A-04	Primary power source	$\mathcal{P}_{tot,inst}$	≤ 10	kW		The rover shall have a primary electrical power source providing continuous power $P_{tot,inst}$
R-PERF-A-05	Secondary power source	$\mathcal{P}_{aux,inst}$	≤ 5	kW		The rover shall include secondary batteries and a photovoltaic array for managing the extended mission and peak loads, for an auxiliary power supply of $P_{aux,inst}$.
R-PERF-A-06	Lunar gravity resistance					The rover's structure shall withstand lunar gravity of $g_{moon} = 1.62\ m/s^2$
R-PERF-A-07	Lunar dust resistance					The rover shall have a dust-resistant design and employ systems to protect sensitive equipment
R-PERF-A-08	Provisions for EVA mission	t_{EVA}	10	h		The rover shall have provisions to support two EVA suits with consumables for t_{EVA} hours each per mission
R-PERF-A-09	Compatible manlock					The rover shall include a manlock for EVA access during the mission

Table 2.5: Performance requirements.

ID	Name	Symbol	Value	Un.	Ref.	Description
R-PERF-B-01	ECLSS functions					The rover shall be equipped with Environmental Control and Life Support System (ECLSS) functions, including carbon dioxide removal, humidity control, atmosphere monitoring, and temperature control
R-PERF-B-02	Inertial Guidance System					The rover shall include an inertial guidance system, orbiting lunar satellite for navigation, and obstacle avoidance capabilities
R-PERF-B-03	Docking fixture, robotic arm and storage compartments					The rover shall include docking fixtures compatible with lunar base airlocks, robotic arms for sample collection and handling, and storage compartments for tools and samples
R-PERF-B-04	Wheels	n_w	4			The rover shall include n_w independently powered wheels with double Ackermann steering and articulated frame steering.
R-PERF-C-01	Flexible Suspension					The rover shall feature adaptable suspensions to handle varying lunar terrain, optimizing stability and mobility in low-gravity environments

Table 2.6: Performance requirements (continued).

ID	Name	Symbol	Value	Un.	Ref.	Description
R-MISS-A-01	Nominal operational radius (lunar day)	x_r	150	km		The rover shall have a nominal operational radius of x_r km per mission
R-MISS-A-02	Nominal operational radius (night operations)	x_r'	100	km		The rover shall have a nominal operational radius of x_r' km for lunar night operations
R-MISS-A-03	Nominal operational time	$t_{m,nom}$	20	h		The rover shall provide an operational mission duration of up to $t_{m,nom}$
R-MISS-A-04	Extended operational time	$t_{m,ext}$	3	d		The rover shall provide an extended travel capacity for $t_{m,em}$ for a crew of N_{crew} people.
R-MISS-A-06	Emergency with no range	$N_{crew,em}$	2			The rover shall be able to support a crew of $N_{crew,em}$ in an emergency without a specific range requirement

Table 2.7: Mission Requirements.

ID	Name	Symbol	Value	Un.	Ref.	Description
R-MISS-B-01	Reference obstacles height	z_{obst}	10	cm	[3]	The rover shall be capable of climbing steps up to z_{obst} and crossing crevices of up to z_{cerv}
R-MISS-B-02	Reference obstacles inclination	ϑ_{obst}	10	°	[3]	The mobility system shall enable the rover to traverse slopes up to ϑ_{obst} on regolith terrain.
R-MISS-B-03	Reference obstacles inclination	x_{obst}	10	cm	[3]	The mobility system shall enable the rover to obstacles long up to x_{obst} on regolith terrain.

Table 2.8: Mission Requirements (continued).

ID	Name	Symbol	Value	Un.	Ref.	Description
R-DES-A-02	EVA Suits Mass	$m_{EVA,suit}$	120	kg		The rover shall incorporate a deployable ramp for EVA activities with a load capacity of $m_{EVA,suit}$
R-DES-A-03	Power Bus Voltage	$V_{nominal}$	28 ± 2	VDC	[2]	All power buses shall operate at $V_{nominal}$
R-DES-A-04	Communication System					The rover shall incorporate a communication system for direct communication with Earth and lunar EVA operations, including an omnidirectional antenna for local communication
R-DES-A-05	Launch Loads					The chassis shall withstand launch loads up to $6g$ axial and $3g$ lateral without permanent deformation

Table 2.9: Design requirements.

ID	Name	Symbol	Value	Un.	Ref.	Description
R-REG-A-01	Dose	$\mathcal{D}_{nom}$	500	mSv (per year)	[8]	The rover shall sustain a maximum dose of $\mathcal{D}_{nom}$, to ensure radiation protection onboard.
R-REG-A-02	Protection from solar and galactic radiation and micrometeoroids					The rover shall be equipped with radiation shielding to protect occupants from solar and galactic radiation, and micrometeoroids
R-REG-A-03	Thermal management					The rover shall withstand lunar temperature variations between $T_{max} = +123°C$ and $T_{min} = -233°C$

Table 2.10: Regulatory and Environmental Requirements.

ID	Name	Symbol	Value	Un.	Ref.	Description
R-REG-B-01	Insulation					The rover shall feature thermal control systems to manage internal and external temperature control
R-REG-B-02	Health Management System					The rover shall incorporate health management systems to monitor and ensure the reliability of subsystems across extended mission durations

Table 2.11: Regulatory and Environmental Requirements (continued).

Chapter 3

Preliminary Sizing

This chapter is dedicated to the definition of the main architecture of the rover. The most used configurations by conventional rovers are discussed, in order to choose the most advantageous one based on the requirements set out. The choice of a particular configuration is consequently achieved.

Thanks to the choice of the configuration, it is possible to carry out a preliminary examination of the main systems, based on the division found in [7], and continue with an estimated sizing.

This latter aspect sees an exploratory arrangement of the spaces and dimensions, in order to guarantee a perfect synergy between the chosen requirements and the habitability of the environment.

3.1 Configurations

3.1.1 Configuration types

The first step of the design process was to establish the basic configuration of the rover. The major subsystems and their relationships had to be agreed upon before in-depth work could begin. Preliminary studies showed that the pressure structure shape and mobility subsystem should be selected first because these elements have significant effects on other aspects of the design.

(a)   (b)   (c)
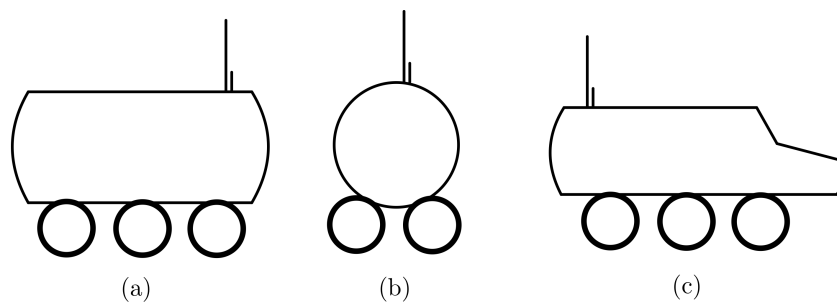
Figure 3.1: The three types of shape of the pressurized space: (a) cylindrical (b) spherical or (c) custom

Based on the configuration found in [7], [9], it is possible to categorize the configuration due to the pressure structure shape:

1. The first considered design is a slightly longer variation on the **single cylinder** often seen in literature, as a result of areonautical heritage. This design has a low center of gravity and a simple interior, providing a good pressurization distribution.

2. A second design was **spherical hull**, considered because of its optimum volume per unit mass. However, significant disadvantages included a high center of gravity and the utilization of available interior space.

3. A **custom hull**, such as the one proposed by JAXA in the *Toyota Lunar Cruiser* [9]. This design, of automotive derivation was proposed in 2022 by the collaboration of JAXA and Toyota and proposes a vehicle-like approach, rather than an habitat solution.

Another categorization revolved around the choice of the frame. Particularly, between a uniframe configuration and a multi-segmented one. The **uni-frame**, a standard one-piece frame, would be the simplest to construct and the most reliable, but it needs more ground clearance, and therefore a higher center of gravity which decreases stability. **Multiframe** designs consist of a train of multiple segments, which allow pivoting at their connections. Increased maneuverability is achieved because the vehicle can conform to terrain conditions.
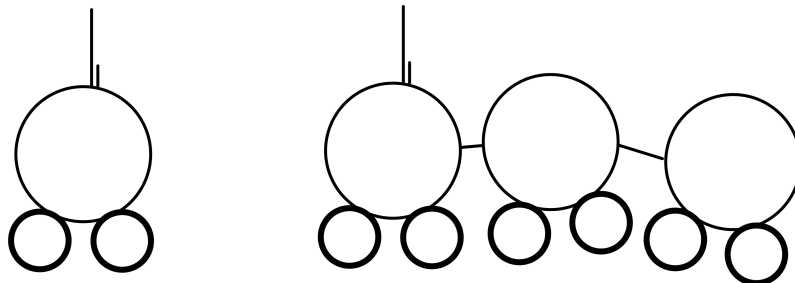
Combining those two choices, six configurations can be obtained. These are listed in the following trade-off table. The **single cylinder uni-frame** is selected due to its simplicity and similarities with the aeronautical parallel.

	Cylindrical Uniframe	Cylindrical Multi-frame	Spherical Uniframe	Spherical Multi-frame	Custom Uniframe	Custom Multi-frame
Pressurization	3	3	2	2	1	1
V/m ratio	2	2	3	3	2	2
Int. Utilization	3	3	1	1	2	2
Robustness	3	2	3	2	3	2
TOTAL	11	10	9	8	8	7

Table 3.1: Trade-off between the different configurations

In order to further expand the capabilities of the system, an **expandable** solution is developed. This configuration ensures a smaller mass while maintaining all the supply needed for the accomplish of the mission.

Figure 3.2: Expandable solution proposed: figure (1) shows the complete rigid model which is longer and heavier, figure (2) shows the expandable model in the stored configuration and figure (3) shows the expanded (deployed) configuration.
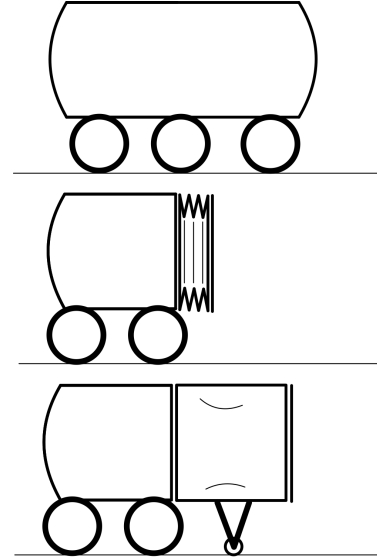
3.1.2 Modularity

Modularity in pressurized rovers refers to the ability to adapt the vehicle's design through interchangeable or reconfigurable components, enabling it to perform a variety of tasks and support diverse mission objectives. Modular designs often feature detachable payloads, reconfigurable workspaces, and adaptable interfaces for docking or connecting with other systems. Examples of modular rover concepts include the *Lunar Electric Rover* (LER) developed by NASA [10], which incorporates a modular chassis that can be reconfigured for crewed or uncrewed operations, and the European Space Agency's *HERACLES* rover [10], designed to interact with various modular cargo and scientific payloads.

The advantages of a modular rover include enhanced versatility, cost-effectiveness through component reuse, and the ability to tailor configurations to specific mission needs. Furthermore, modularity simplifies repairs and upgrades, as damaged components can be replaced without the need for extensive redesign. However, the approach is not without drawbacks. Modular systems often introduce increased mechanical and electrical complexity, which can lead to integration challenges and reduced system reliability. The need for standardized interfaces may also result in compromises in performance and added mass, both critical factors in lunar operations.
Despite its potential benefits, the low reliability associated with modular designs makes it a less suitable solution for a pressurized rover. The lunar environment, characterized by extreme temperatures, radiation, and regolith abrasion, poses significant risks to the integrity of modular interfaces. Moreover, the reliance on multiple connection points increases the likelihood of failures, particularly in high-stakes missions where redundancy is critical. As a result, non-modular, integrated designs are preferred to ensure higher operational reliability and to minimize the risks associated with extended lunar exploration.

3.2   Launch Vehicle Choice

The cargo bay dimensions and capacity (in terms of mass that can be carried to a specific orbit) of the launch vehicle affects the rover design. By completing most of the rover's construction on Earth, in-space assembly can be minimized. The following table shows the current launchers with their respective payloads for the following orbits:

1. LEO: Low Earth Orbit;

2. GTO: Geostationary transfer orbit;

3. LTO: Lunar transfer orbit;

4. MTO: Mars transfer orbit.

The availability refers to shipping costs and international agreements that have to be processed in order to launch with a specific vector, as well as the current state of development of the rocket.

A score was defined to choose a particular launcher:

$$\mathcal{S}_{launcher} = m_{pl,LTO} \cdot Av \tag{3.1}$$

where:

1. $\mathcal{S}_{launcher}$ is the launcher score.

2. $m_{pl,LTO}$ is the lunar transfer orbit transportable payload.

3. Av is the launcher availability, which is a function of the number of yearly launches of the rocket and international agreements. As the mission is intended as European, most launchers are discarded due to their lack of reachability.

	Ariane 5	Ariane 6	Falcon 9	Falcon Heavy	Yenisei	Long March 9	SLS 2	Starship Super Heavy
Nation	EU	EU	USA	USA	Russia	China	USA	USA
$m_{pl,LEO}$	20	21.7	22.8	63.8	103	140	130	150
$m_{pl,GTO}$	10.6	11.5	8.3	26.7	0	56	55	N/D
$m_{pl,LTO}$	8.9	9.7	7	22.4	0	50	46	N/D
$m_{pl,MTO}$	0	0	4	16.8	0	44	N/D	N/D
Diam.	5.4	5.4	4.6	4.6	N/D	N/D	10	9
Height	17	18	11	16.5	N/D	N/D	31	26
Availability	100%	100%	100%	100%	30%	10%	100%	0%
Score	8.9	9.7	7	22.4	0	5	46	0

Table 3.2: State of the art of the current launchers: masses are expressed in *tons* and lengths are expressed in *m*.

At the current state of the art, the first three suitable candidate launchers are:

1. SLS 2;

2. Falcon Heavy;

3. Ariane 6.

Another important aspect to take into consideration is the fairing size. A payload fairing is a structure, in the shape of a nose cone, used to protect a spacecraft payload against the impact of dynamic pressure and aerodynamic heating during launch through an atmosphere. The selection of the fairing with the smallest dimensions is conducted to adopt a conservative approach. It is reasonable to assume that larger fairings will be utilized on more powerful launch vehicles, subjecting the payload to greater mechanical stresses during the launch phase. By opting for the most restrictive fairing dimensions, it is ensured that any payload designed to fit within a smaller fairing can, with the necessary modifications, also be accommodated within larger fairings. This strategy enhances the versatility and adaptability of the payload design across various launch configurations. Therefore, among the three vectors, the **Falcon Heavy** by *SpaceX* is chosen as a candidate launcher for the mission.

3.2.1   Launcher Specifications

Falcon Heavy is a super heavy-lift launch vehicle with
partial reusability that can carry cargo into Earth orbit
and beyond. It is designed, manufactured and launched by
American aerospace company SpaceX [11].

The rocket consists of a center core on which two *Falcon 9* boosters are attached, and a second stage on top
of the center core. Falcon Heavy has the second highest
payload capacity of any currently operational launch vehicle behind NASA's *Space Launch System* (SLS), and the
fourth-highest capacity of any rocket to reach orbit, trailing
behind the SLS, *Energia* and the *Saturn V*. This section
outlines the principal characteristics of the SpaceX Falcon
Heavy launch system, focusing on payload capacities, fairing dimensions, acoustic environment, and relevant operational considerations. The data are extracted from [11].

Payload Loads

Falcon Heavy is currently the most capable operational
launch vehicle in terms of payload mass, and it supports
a wide range of orbital missions. Payload capacity varies
significantly depending on whether the mission uses an expendable or reusable configuration. The principal payload
capabilities in the fully expendable configuration are:

- Low Earth Orbit (LEO, 28.5ř): up to 63, 800 kg;

- Geostationary Transfer Orbit (GTO): up to 26, 700
  kg;

- Mars Transfer Orbit: up to 16, 800 kg.
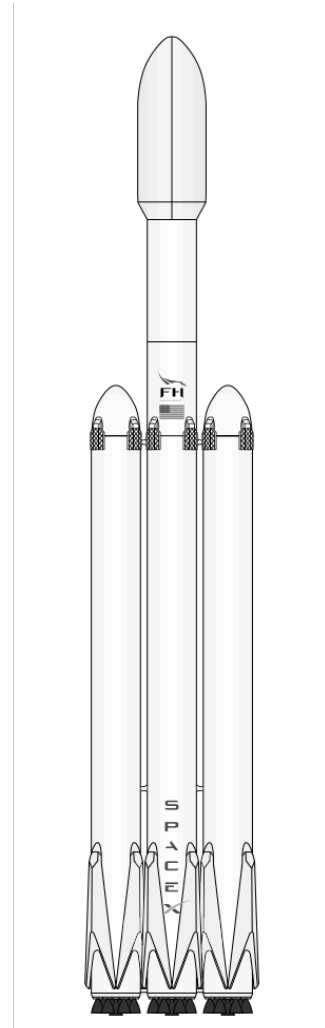
Figure 3.3: Falcon Heavy

When booster recovery is planned, payload capacity is reduced accordingly. The
high lift capability of Falcon Heavy is enabled by the combination of three Falcon
9-derived cores, each equipped with nine Merlin 1D engines, offering a total of 27
engines across the first stage.

Payload types can include single large satellites, multi-payload constellations,
and secondary payloads using deployers or ESPA-class ring interfaces. Falcon Heavy
is compatible with a wide variety of payload separation systems.

Fairing Dimensions

The Falcon Heavy utilizes a composite payload fairing which protects the payload
during atmospheric ascent. The fairing is jettisoned once the vehicle exits the densest
part of the atmosphere. Key dimensional parameters of the standard payload fairing
are:

- External Diameter: 5.2 meters (17.2 feet)

- Internal Dynamic Envelope:

    – Maximum Diameter: 4.6 meters (15.1 feet)

    – Maximum Height: 11.4 meters (36.1 feet)

- Total Fairing Height: 13.2 meters (43.5 feet)

A variety of payload adapter configurations are available, including interface diameters of 937 mm, 1194 mm, 1575 mm, and 1666 mm. The selection of adapter may constrain available dynamic envelope height.
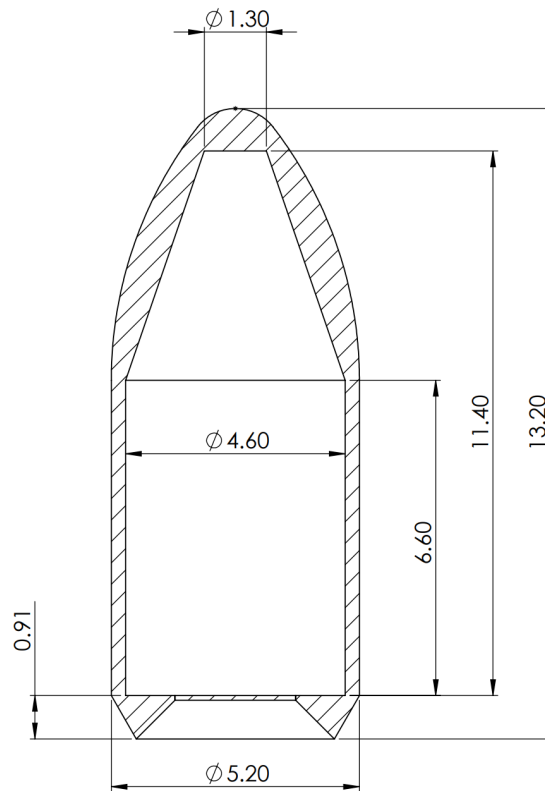
Figure 3.4: Falcon Heavy Payload Fairing Dimensions.

Ascent Loads

During ascent, payloads aboard Falcon Heavy are subjected to both axial and lateral accelerations, which must be considered in structural design and qualification. The maximum axial acceleration experienced by the payload typically occurs near the end of first stage flight or during upper stage operation, reaching up to **6 g** in nominal conditions. Lateral accelerations, which are generally lower, arise primarily from wind shear, gust loading, and steering maneuvers, with maximum expected values of approximately **2 g**. These accelerations are within the tolerances for most space-qualified hardware, but payload developers are advised to conduct dynamic analysis with mission-specific profiles provided by SpaceX during the integration process. Design requirements driven by those factors are represented in chapter 2.
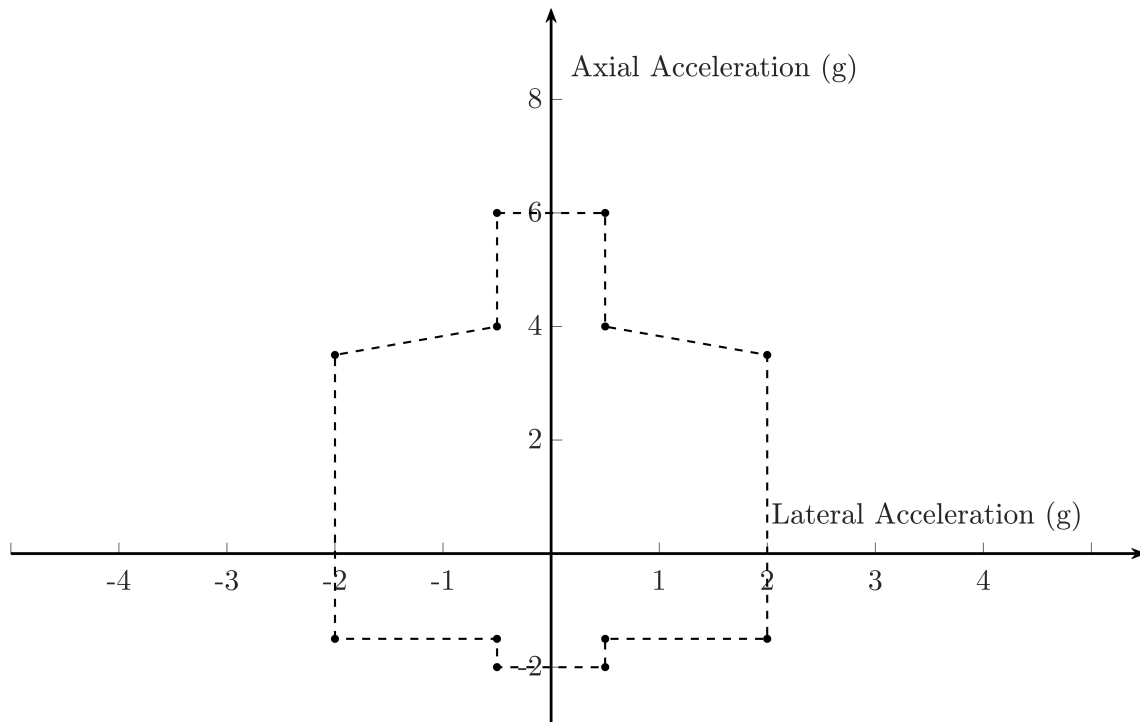
Figure 3.5: Falcon Heavy Load Limits for "standard" payloads (over 4400 lbs).

Sound Pressure Level (SPL)

The acoustic environment during launch is a critical design factor for spacecraft. Falcon Heavy provides a quantified Sound Pressure Level (SPL) profile for payload integration, assuming a 60% fairing fill factor. The table below summarizes the predicted acoustic environment at the payload interface, at the 95th percentile confidence level.
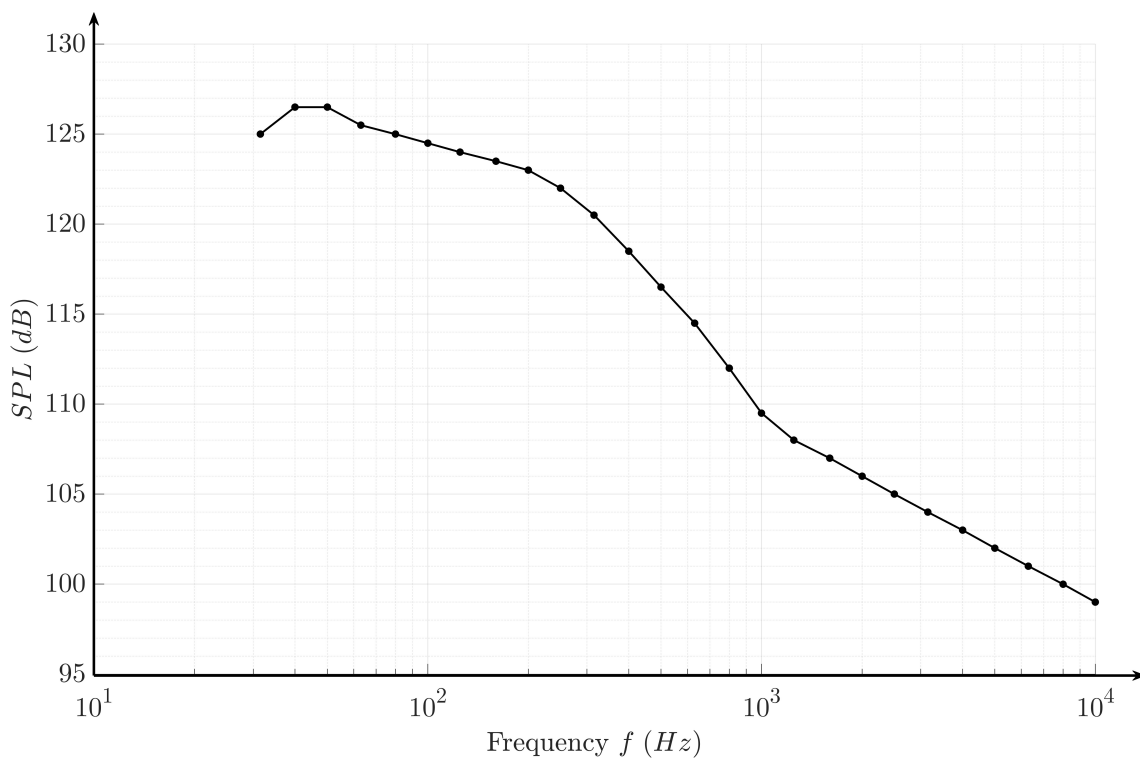
Frequency	SPL
31.5	125
40	126.5
50	126.5
63	125.5
80	125
100	124.5
125	124
160	123.5
200	123
250	122
315	120.5
400	118.5
500	116.5
630	114.5
800	112
1000	109.5
1250	108
1600	107
2000	106
2500	105
3150	104
4000	103
5000	102
6300	101
8000	100
10000	99

Table 3.3: Third-Octave Band SPL (P95, 60% Fill Factor)

These values inform payload acoustic testing and qualification procedures.

Other considerations

Several design aspects enhance Falcon Heavys operational robustness and flexibility:

1. Structural Margins: The launch vehicle is designed with a structural safety margin of 40% above maximum predicted flight loads, significantly exceeding the industry standard of 25%. This ensures high reliability under dynamic launch conditions.

2. Payload Access: Falcon Heavys fairing includes support for payload access doors. A single access port is provided as standard, located within the cylindrical portion of the fairing. Up to eight ports can be incorporated upon request, facilitating late-stage payload servicing.

3. Reusability: Falcon Heavys architecture supports partial or full reuse of its first stage boosters. Side boosters typically return for vertical landing at designated landing zones or drone ships, depending on mission profile. The center core

may also be recovered, though its recovery is typically more challenging due to higher re-entry velocity.

4. Compatibility and Integration: The vehicle supports a wide range of payload adapters and interfaces, including those from third-party vendors such as RUAG, Planetary Systems Corporation, and Airbus. Custom mechanical and electrical integration services are offered.

5. Environmental Control: An optional payload environmental control system (PECS) is available, enabling thermal and humidity control within the fairing to ensure optimal conditions for sensitive payloads during pre-launch operations.

3.2.2   Preliminary size definition

Once the launcher has been selected, the next critical step involves defining the preliminary dimensions of the pressurized rover. This process is driven by the constraints imposed by the launchers payload fairing, which determines the maximum allowable size and mass of the rover. Pressurized cylinders are nowadays a state of the art for manned space exploration missions. One example of manufacture is the **Cygnus** module commisioned by Northrop Gruman [12], whose pressurized hull is produced by Thales Alenia Space in Turin, Italy (TAS-I).
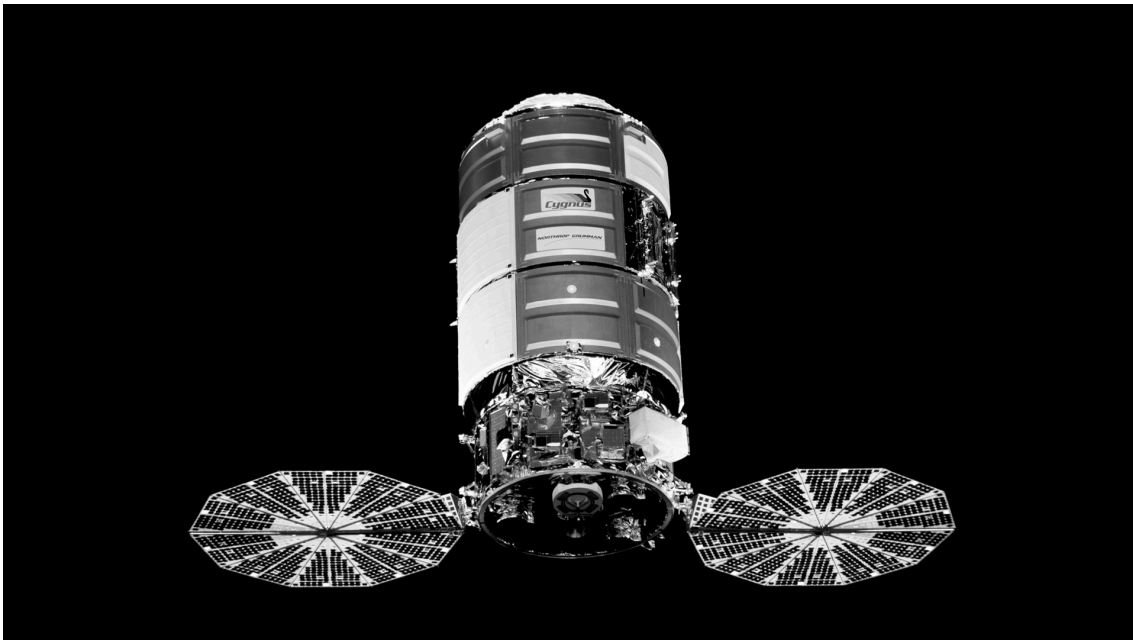
Figure 3.6: Cygnus module manufactured by Northrop Grumman.

Currently the module serves as a pressurized cargo module for the ISS. Twenty-two modules have been sent into space since 2013, and currently the model has been constructed in 4 different variants, with the latter one currently in development. The following table shows the main characteristics of the different Cygnus variants.

In August 2019, NASA decided to sole source its design for the Minimal Habitation Module (Habitation and Logistics Outpost, or HALO) of the Lunar Gateway to Northrop Grumman Innovation Systems, which offered a minimalist 6.1 m by 3 m design based directly on the Enhanced Cygnus, as well as a larger 7 m by 4.4 m design.

	Standard	Enhanced	Mission B	New (est.)	Units
D	3.07	3.07	3.07	4.4	m
L	5.14	6.39	7.89	7	m
V_{int}	18.9	27	36	38	m^3
m_{dry}	1500	1800	2000	N/D	kg

Table 3.4: Main mass and size dimension of the pressurized part of the Cygnus module

Taking into account the dimensions of the fairing, the **Standard** module was chosen in order to maximize the mass to volume ratio. The dimensions serve as a foundation for subsystem design, providing a framework within which components such as mobility, life support, and power systems must operate.

3.3 Subsystem examination

The design of a pressurized lunar rover incorporates various subsystems to address the operational, environmental, and safety challenges posed by the lunar environment. Each subsystem is critical to ensuring the functionality and reliability of the rover during extended missions. Below is a detailed list of subsystems, each with its dedicated subsection. In particular, labeling from the most critical in the design phase to the least critical:

1. Structure;

2. Mobility subsystem;

3. Electrical power subsystem (EPS);

4. Thermal control subsystem (TCS);

5. Life Support subsystem (LSS);

6. Docking subsystem;

7. Guidance, Navigation and Control (GNC) subsystem;

8. Comunications subsystem (COMSYS);

9. Scientific subsystems and external features.

3.3.1   Structure

The structural subsystem can be divided among the pressurized and the unpressurized components. The pressurized site (namely the crew cabin) consists of a rigid cylindrical shell and an expandable inflatable module. The shell design incorporates multilayer insulation to mitigate thermal cycling. These materials are chosen for their strength, thermal resistance, and micrometeoroid protection. The shell design incorporates multilayer insulation to mitigate thermal cycling. Unpressurized parts usually serve as a mechanical connection to the other subsystems (such as the mechanical connection to the powertrain or the interface with the docking subsystem).

3.3.2   Mobility subsystem

The mobility subsystem includes the wheel assembly, suspension, and steering systems. It ensures that the rover can traverse various lunar terrains, including soft soil, rocky surfaces, and craters. For example, [7] uses a double transverse wishbone design for stability, while the wheels are powered by brushless electric motors housed in protective casings. In this scenario, skid steering and Ackermann systems are also implemented for precision maneuvering.

3.3.3   Electrical power subsystem (EPS)

This subsystem is responsible for generating and distributing power throughout the LPR. Usually, when departing for the mission, the rover is fully charged. **Battery packs** are implemented for energy storage as the primary source of energy, ensuring continuous operation during periods of limited solar exposure, such as lunar night or shadowed terrain. A solar power system serves as the auxiliary energy source, utilizing high-efficiency **solar panels** to generate electricity while being far from the motherbase for the extended mission. Thermal radiators are included to dissipate heat generated by the power and energy storage systems.

3.3.4   Thermal control subsystem (TCS)

Designed to manage the extreme temperature variations on the lunar surface, this subsystem includes multilayer insulation (MLI), heat pipes, and radiators. Internal components, such as electronics and power systems, are thermally regulated to maintain functionality in temperatures ranging from $-233\,°C$ to $123\,°C$, as stated in the Environmental Requirements in chapter 2.

3.3.5   Life support subsystem (LSS)

This subsystem ensures the safety and well-being of the crew by regulating atmospheric pressure, temperature, and humidity inside the rover. It includes oxygen supply, CO_2 removal, water recovery systems, and fire suppression mechanisms. It also provides support for extravehicular activities (EVAs).

3.3.6 Docking subsystem (DS)

The docking subsystem enables the rover to interface seamlessly with the lunar habitat. A docking fixture at the rear of the rover provides direct passage between the rover and the habitat through an airlock. This system is essential for the safe transfer of crew and materials, as well as for integrating life support and power systems during extended docking periods. The docking subsystem, in particular, highlights the integration of the rover with other mission assets, reinforcing the rovers role as a versatile platform for lunar exploration.

3.3.7 Guidance, Navigation and Control (GNC)

Equipped with satellite-based guidance (like the ESA's Moonlight Mission [13]), and obstacle detection sensors, this subsystem allows for precise navigation on the lunar surface. It also provides control mechanisms for steering and docking operations.

3.3.8 Comunications

The communications subsystem facilitates real-time data, voice, and video transmission between the rover, the lunar habitat, and Earth. It includes S-band systems, omnidirectional antennas, and parabolic reflectors for long-range communication.

3.3.9 Scientific subsystems

The rover includes scientific airlocks and onboard laboratory equipment for *in-situ* analysis. These systems allow for the collection, storage, and examination of lunar samples, minimizing the need to return to the habitat for processing.

3.3.10 External features

External features include, storage bins, EVA seats, high-resolution cameras, lights, and a towing hitch. These fixtures enhance the rover's utility for various mission objectives, including transportation, sampling, and rescue operations.

3.4   Preliminary estimates

After defining the maximum allowable dimensions for the pressurized rover, as constrained by the selected launch vehicle, the next step involves establishing preliminary estimates for its mass and power consumption. These initial values serve as a baseline for the preliminary sizing of critical subsystems. This process involves integrating insights from the current state-of-the-art in automotive engineering and comparing them with existing pressurized rover designs. These estimates provide a foundation for further refinement and detailed analysis in the subsequent discussion of each subsystem.

3.4.1   Power estimate

For the preliminary power requirements for a LPR with the chosen dimension, the following systematic process can be followed:

1. Define the **mission parameters** (described in chapter 2), from which the most important ones are power requirements, as well as N_{crew}, $t_{m,nom}$, $t_{m,ext}$, operational activities and environmental conditions.

2. Identify the **power-consuming subsystems**. In the listed examination the most requiring subsystems in terms of power are:

   (a) LSS (Life Support Subsystem): For atmospheric control, CO_2 scrubbing, temperature and humidity regulation, water recovery, and fire suppression.

   (b) Thermal Control: To maintain habitable temperatures within the rover and regulate heat from internal components.

   (c) Mobility: Electric motors for driving, including uphill movement and maneuvering on uneven terrain.

   (d) Communication: For data, voice, and video transmission with the habitat or Earth.

   (e) GNC (Guidance, Navigation, and Control): For precise navigation, obstacle avoidance, and docking operations.

   (f) Scientific Subsystems: Laboratory equipment, robotic arms, and sample analysis tools.

   (g) Internal Lighting and Appliances: For visibility, food preparation, and personal hygiene.

   (h) Peak Power Loads: Such as during EVAs or docking operations.

3. Estimate a **power consumption** for each of the demanding subsystem, $\mathcal{P}_{nec}$.

4. Estimate the total installed power as $\mathcal{P}_{tot,inst} = \mathcal{P}_{nec}/\eta_{source}$, with η_{source} representing the efficiency in power transmission and distribution (losses in the powertrain as well as wirings). For conservative reasons, this value is set to $\eta_{source} = 75\%$ to take into account all the different aspects.

System	Symbol	Value	Unit	Meaning	Based on
LSS	p_{LSS}	1000	$W/crew$	Specific power for each astronaut	(ECLSS) aboard the International Space Station (ISS)
	N_{crew}	2	–	Nominal crew members	Requirement
TCS	$\mathcal{P}_{TCS}$	1000	W	Total power	(Thermal) aboard the International Space Station (ISS)
Mobility	$\mathcal{P}_{mob}$	$f(m_{tot})$		Total power	NASA's Lunar Electric Rover for continuous operation (est.)
COM	$\mathcal{P}_{com}$	500	W	Total power using S-band	Apollo missions and modern satellite comunication
Scientific	$\mathcal{P}_{scien}$	500	W	Total power	Power budgets of robotic exploration systems (like the Perseverance Rover and its onboard instruments)
Internal Lighting	$\mathcal{P}_{light}$	500	W	Total power	ISS (est.)
Docking	$\mathcal{P}_{dock}$	800	W	Total power	Apollo/Artemis missions (est.)
Total	$\mathcal{P}_{tot,inst}$	8.54	kW	Total power requirement	

Table 3.5: Power budget

The following table shows the data used for this preliminary sizing.

A preliminary estimate of the mobility system can be achieved considering the power as the product of the traction force and the nominal velocity. Assuming that the traction force T is proportional to the **rolling resistance**, $C_{rr} \cdot m_{tot} \cdot g_{\mathrm{D}}$ (C_{rr} is the called the 'rolling resistance coefficient'),

$$\mathcal{P}_{mob} = T \cdot v = C_{rr} \cdot m_{tot} \cdot g_{\mathrm{D}} \cdot v \tag{3.2}$$

it becomes clear how mass and power estimate are to be considered combined. The total process is in fact of **iterative** nature. C_{rr} values for common types of terrain are found in Table 3.6. A value of $C_{rr} = 0.020$ is used for the power estimate described in the chapter as presented in [14]. The total power required is then estimated as stated in the above table.

Terrain Type	Rolling Resistance Coefficient (C_{rr})	Notes
Asphalt (smooth)	0.010 - 0.015	Standard road conditions.
Gravel (compact)	0.020 - 0.030	Common in rural roads.
Gravel (loose)	0.030 - 0.040	Increased resistance due to loose particles.
Sand (compact)	0.030 - 0.040	Found in deserts and beaches.
Sand (loose)	0.040 - 0.100	High resistance; vehicles may struggle.
Lunar Regolith	0.010 - 0.020	Based on Apollo mission data. [14]

Table 3.6: Different types of rolling resistance for various terrains.

3.4.2   Mass estimate

The mass of the Lunar Pressurized Rover (LPR) can be subdivided in the following categories

$$m_{tot} = m_{pl} + m_{crew} + m_{source} + m_{empty} \tag{3.3}$$

in which:

1. m_{pl} is the paylaod mass, composed of all the required items needed to conclude the mission in the remote location effectively and come back to the habitat (i.e. scientific equipement, regolith samples brought by the remote mission, monitoring equiment, etc.).

2. m_{crew} is the crew mass.

3. m_{source} is the energy source mass (which comprehend both primary and auxiliary energy sources).

4. m_{empty} is the sum of all the other subsystems integrated in the LPR, apart from the EPS (estimated in the m_{source}).

3.4.3   Payload and crew mass

Both payload m_{pl} and crew m_{crew} mass are given as a requirement chapter 2. Specifically, the crew mass can be estimated as

$$m_{crew} = N_{crew} \cdot m_{astronaut}$$

in which the mass of the astronaut is given by NASA Human Integration Design Handbook (HIDH) which encompasses both the averge values for a man and for EVA suits and PLSS.

$$m_{astronaut} = 90 \ kg$$

Component	Mass	Units
Human body (average)	85	kg
IVA Clothing (e.g., flight suit, undergarments)	5	kg
Total	90	kg
EVA Suit (EMU or EMCS)	100	kg
PLSS (Portable Life Support System)	40	kg
Tools & tether systems	10	kg
Total EVA	150	kg

Table 3.7: Human body vales from NASA HIDH.

3.4.4 Source mass

The decision to address the energy source separately stems from its critical importance to the overall design. This approach ensures that the power subsystem receives focused attention, as it directly impacts the rover's operational capabilities. Notably, even if the primary energy source for the rover were to change, the mass and design of the other subsystems would remain largely unaffected. The power mass is directly connected to the power consumption. The main driver of the source mass is the battery (augmented by $k_{other,source} = 20\%$ to take into account other system components).

$$m_{source} = m_{batt} + m_{aux,source} + m_{other,source} = (1 + k_{other,source}) \cdot m_{batt} + m_{aux,source}$$

The battery mass can be estimated as

$$m_{batt} = \frac{E_{batt}}{(DOD_i - DOD_f) \cdot \rho_{BED,grav}}$$

in which:

1. E_{batt} is the stored energy battery that can be estimated as the power contribution of each subsystem multiplied by the time in which the subsystem remains fully active during the mission. The total energy stored in the rover is

$$
\begin{aligned}
E_{tot} &= \int_t P(t)dt \\
&= \sum_i P_i \Delta t_i \\
&= \sum_i P_i \left(\Delta t_{i,nom} + \Delta t_{i,em} \right) \\
&= \sum_i P_i \frac{\Delta t_{i,nom}}{t_{m,nom}} \cdot t_{m,nom} + \sum_i P_i \frac{\Delta t_{i,em}}{t_{m,em}} \cdot t_{m,em} \\
&= E_{batt} + E_{aux}
\end{aligned}
$$

The following table provides an analysis of the time fraction presented in the above equation.

In particular, assuming a constant velocity v during the entire mobility time (as a rough estimate):

$$\frac{\Delta t_{mob,nom}}{t_{m,nom}} = \frac{2 \cdot x_r / v}{t_{m,nom}} \tag{3.4}$$

This inequality comes from the assumption that the maximum mobility time corresponds to the time it takes to arrive to the remote location (the full nominal mission is conceived as A/R from the remote location). In case of emergency the mobility time t_{mob} remains the same as the same distance is prescribed for both emergency and nominal situations. Therefore:

$$\frac{\Delta t_{mob,nom}}{t_{m,em}} = \frac{\Delta t_{mob,nom}}{t_{m,nom}} \cdot \frac{t_{m,nom}}{t_{m,em}} \tag{3.5}$$

System	$\Delta t_{i,nom}/t_{m,ext}$	$\Delta t_{i,nom}/t_{m,ext}$	Based on
LSS	100%	100%	(ECLSS) aboard the International Space Station (ISS)
Thermal	100%	100%	(Thermal) aboard the International Space Station (ISS)
Mobility	$f(v, x_r)$	$\propto \Delta t_{i,nom}/t_{m,nom}$	NASA's Lunar Electric Rover for continuous operation (est.)
COM	100%	100%	Apollo missions and modern satellite comunication
Scientific	5%	1%	Power budgets of robotic exploration systems (like the Perseverance Rover and its onboard instruments)
Internal Lighting	100%	100%	ISS (est.)
Docking	5%	1%	Apollo/Artemis missions (est.)

2. DOD_f and DOD_i are respectively the initial and the final depth of discharge of the batteries. For conservative reasons DOD_f is kept as low as 20% to avoid damage, while $DOD_i = 100\%$.

3. $\rho_{BED,grav}$ is the gravimetric battery energy density, defined as the energy carried by a battery per unit mass. A normal value for those density is proposed in the following plot, evaluating energy densities of batteries used for electric vehicles (i.e. electric cars):

Battery		$\rho_{BED,grav}$	$\rho_{BED,vol}$
Lead-Acid	**Min.**	30	60
	Max.	40	80
Ni-MH	**Min.**	45	100
	Max.	80	150
Li-Ion	**Min.**	125	200
	Max.	175	400
Li-Polymer	**Min.**	175	300
	Max.	225	400
Thin Film Li-ion	**Min.**	250	400
	Max.	400	850
Units		Wh/kg	Wh/L

Table 3.8: Comparison of volumetric and gravimetric energy density used in electric vehicles (via [15]).

Thin film Li-ion batteries have been chosen for the sizing due to their high energy densities (both gravimetric and volumetric). As to the auxiliary source mass, the mass of the solar panels can be estimated by

$$m_{aux,source} = \frac{P_{aux,inst}}{p_{spec,grav}} = \frac{E_{aux}}{t_{m,ext} \cdot p_{spec,grav}}$$

with $p_{spec,grav} \cong 100 \ W/kg$ as an estimate for space graded solar panels.

Given the power consumption listed above, the total mass of the energy source can be estimated as:

$$m_{source} = 517.30 \ kg$$
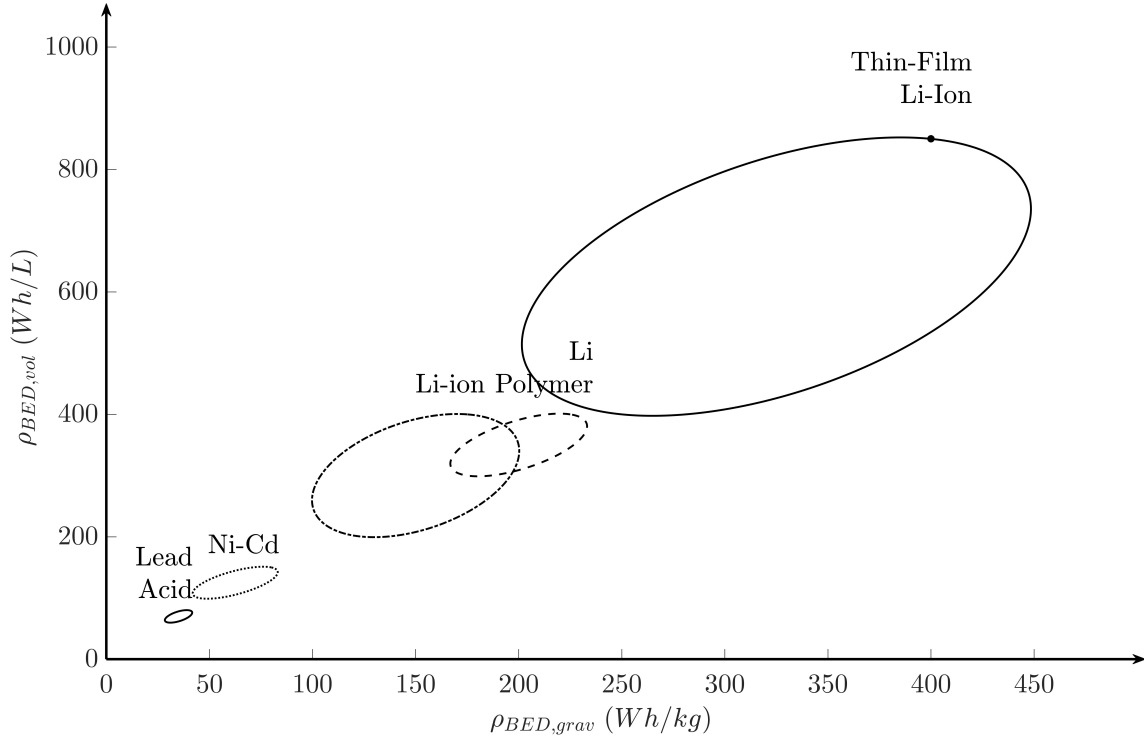
Figure 3.7: Ragone plot showing the volumetric energy and gravimetric energy of different battery types (via [15]). The marked point shows the selected values for the battery sizing.

3.4.5 Empty mass

As stated before, empty mass is defined as the sum of all the subsystems integrated in the LPR, apart from the power subsystem. Those can subdivided into:

1. **pressurized empty mass**, $m_{press,empty}$ which is composed of all the structural support needed to sustain the internal pressure. In particular:

   (a) The rigid mass is estimated as the dry-mass for the selected module used for the rigid hull structure ($m_{press,empty} = 1500\,kg$).

   (b) As for the inflatable part, the following stacking sequence is proposed to get the values for the density, estimated as the weighted sum of the layer densities with thicknesses as weights.

$$\rho_{inflatable} = \frac{\sum_i \rho_i t_i}{\sum_i t_i} \approx 700\ kg/m^3 \tag{3.6}$$

   The selected material stack sequence reflects a protection-first approach suitable for inflatable modules operating in the lunar environment. The configuration includes a Nextel ceramic outer layer, offering superior resistance to thermal loads and micrometeoroid impacts. Beneath it, a Kevlar layer serves as the primary MMOD shield, leveraging its high specific strength to arrest debris penetration. A polyurethane bladder ensures internal pressure retention, while a multi-layer insulation (MLI) package contributes to thermal stability. The overall structure exhibits an effective stacking density, balancing protection and mass efficiency.

Layer	t_i	ρ_i	$\sum_i \rho_i \cdot t_i$
Nextel	1	1500	1.5
Kevlar	2	1440	2.88
Polyurethane	0.5	1200	0.6
MLI	5	200	1
Total	8.5		5.98
Units	mm	kg/m^3	kg/m^3

Table 3.9: Inflatable module stacking sequence.

This sequence is consistent with architectures demonstrated in *NASA's TransHab* and *Bigelow's BEAM* projects, validating its applicability for long-duration surface habitats subjected to frequent thermal cycling and impact risk. Nominal values for other missions are investigated for this class of materials, while the stacking sequence is selected for its robustness and insulation with respect to the external enviornment. The inflatable mass is therefore:

$$m_{inflatable} = \rho_{inflatable} \cdot (\pi \cdot D \cdot L_{inflatable} \cdot t_{inflatable}) \qquad (3.7)$$

with:

i. $\rho_{inflatable} = 700 \ kg/m^3$ which is the inflatable density;

ii. D which is the outer diameter, the same as the rigid strucutre ($D = 3.07 \ m$);

iii. $L_{inflatable}$ which is the inflatable module extended length. This parameter is chosen in order to accomodate all appliances for the extended mission.

iv. $t_{inflatable}$ the proposed inflatable module thickness.

2. **unpressurized empty mass**, $m_{unpress,empty}$ that spans all other subsystems:

(a) Mobility; the proper sizing will be discussed in the following chapters but a rough estimate would be to consider it as a fraction of the total mass:

$$m_{mobility} = k_{mobility} \cdot m_{tot}$$

with $k_{mobility} = 3.4212\%$ given the mobility-to-mass ratio presented in [16] (Total mass: 7015 kg, Mobility mass: 240 kg).

(b) Life Support (LSS); [7] offers a preliminary estimation of the LSS loads. The total mass load can be divided in the table above. Hence, by defining a $i-$load density $\rho_{LSS,i}$, the total load can be estimated as

$$m_{LSS} = \sum_i^{N_{loads}} \rho_{LSS,i} \cdot N_{crew} \cdot t_{mission} = \left(\sum_i^{N_{loads}} \rho_{LSS,i} \right) \cdot N_{crew} \cdot t_{mission}$$

Life Support System Loads	Value	Units
Metabolic O2	0.83	kg/man day
Metabolic CO2	1	kg/man day
Potable H2O	1.86	kg/man day
Metabolic H2O	0.35	kg/man day
Handwash H2O	1.81	kg/man day
Shower H2O	3.63	kg/man day
Perspiration and Respiration H2O	1.82	kg/man day
Urinal Flush H2O	0.49	kg/man day
Urine H2O	1.5	kg/man day
Food Sofids	0.73	kg/man day
Food H2O	0.45	kg/man day
Food Packaging	0.45	kg/man day
Fecal Solids	0.03	kg/man day
Charcoal required	0.06	kg/man day
Trash	0.82	kg/man day

Table 3.10: LSS System Loads (ref. [7]).

(c) Thermal Control, GNC, Comunications, Docking and Scientific subsystems and external features. The following table shows addressable values for the other subsystems

Appliance	Function	Approx. Mass (kg)	Dimensions (m, $L \times W \times H$)
Galley Unit	Food preparation and storage	70	$1.0 \times 0.5 \times 0.5$
Thermal Control Unit	Radiator loops, heat exchange	200	$1.2 \times 0.8 \times 0.5$
GNC Subsystem	Internal positioning and control systems	100	$0.8 \times 0.6 \times 0.4$
Water Recovery System	Reclaims water from humidity/urine	300	$1.2 \times 0.6 \times 0.8$
Refrigerator / Freezer Unit	Medical or food cold storage	70	$0.6 \times 0.6 \times 0.8$
Laptop Workstation	Command, monitoring, research	10	$0.5 \times 0.3 \times 0.1$
Lighting Assembly	Illumination for habitat	10	$0.4 \times 0.2 \times 0.1$
Medical Kit	Emergency care and health monitoring	30	$0.6 \times 0.4 \times 0.2$
Stowage Locker	General storage of tools, clothes, etc.	50	$0.5 \times 0.5 \times 0.5$
Fire Suppression System	Safety appliance	10	$0.4 \times 0.2 \times 0.1$
TOTAL	$m_{other,empty}$	850	

Table 3.11: Other Subsystem Mass estimate based on the ISS.

The following plot shows the empty mass subdivision presented in the LPR.

Empty mass subdivision
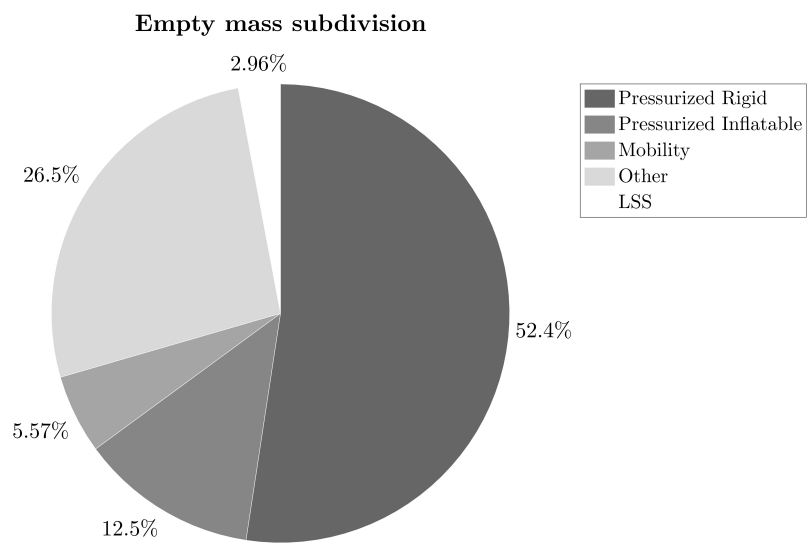
Figure 3.8: Empty mass subdivision piechart: a great portion of the empty mass is dedicated to the pressurized structure.

3.4.6 Conclusion

The preliminary estimation of mass and power requirements is an inherently iterative process, as both parameters are intrinsically linked. An increase in mass directly impacts power consumption, while power availability constrains the possible mass of energy storage and supporting systems. This iterative approach ensures that the final design achieves an optimal balance between performance, efficiency, and mission constraints.

Battery Volume Convergence Plot

$Final : 0.186\ m^3$

$V_{batt}\ (m^3)$

Iterations
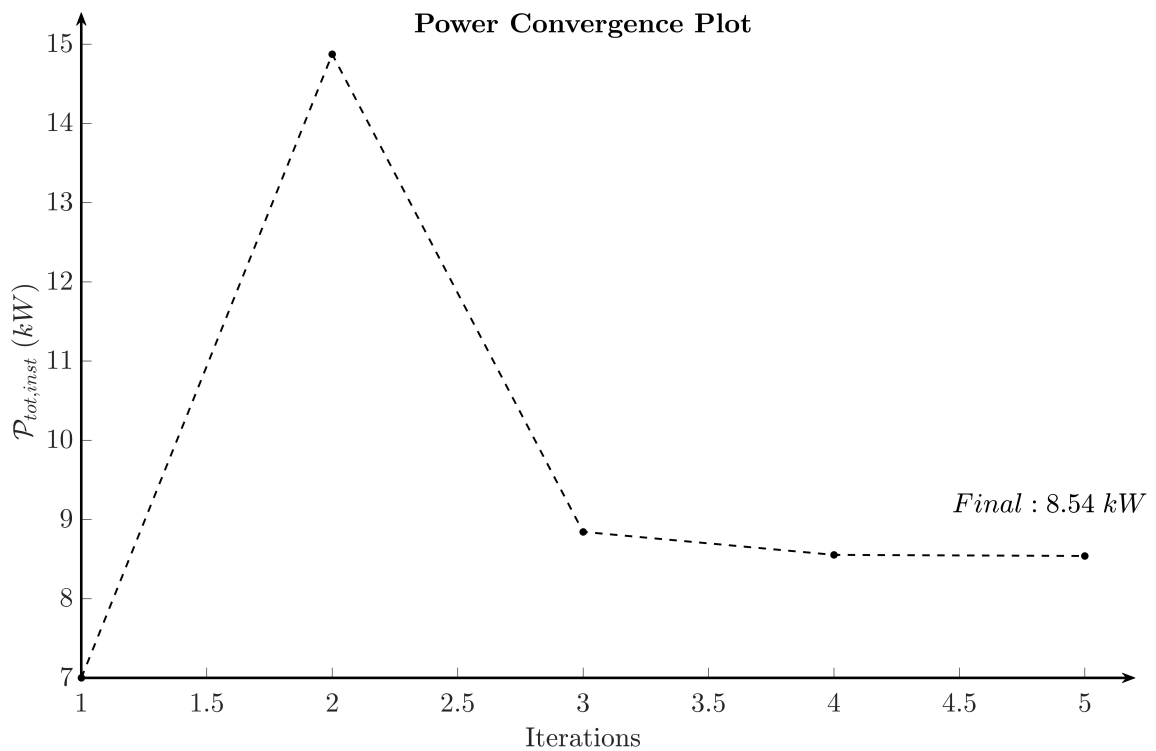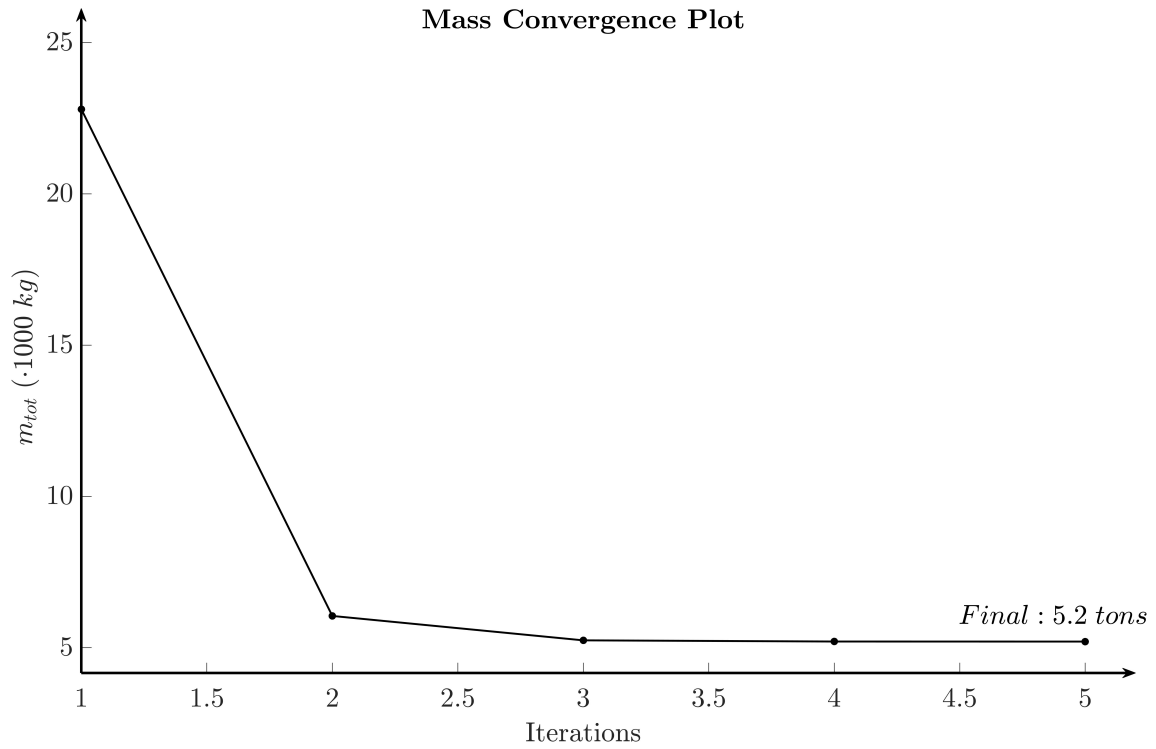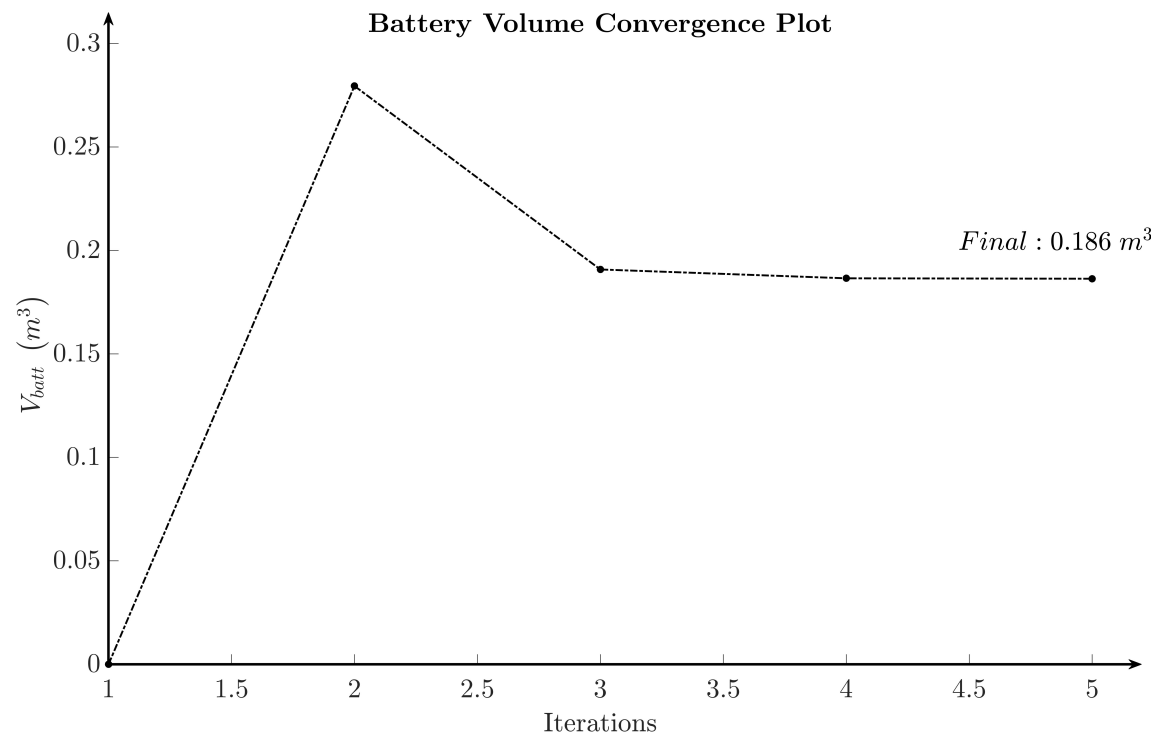
The current plots show the mass and power convergence plots obtained from the iterative process. In summary, the following table provides an estimate of the total mass of the rover.

Total mass subdivision
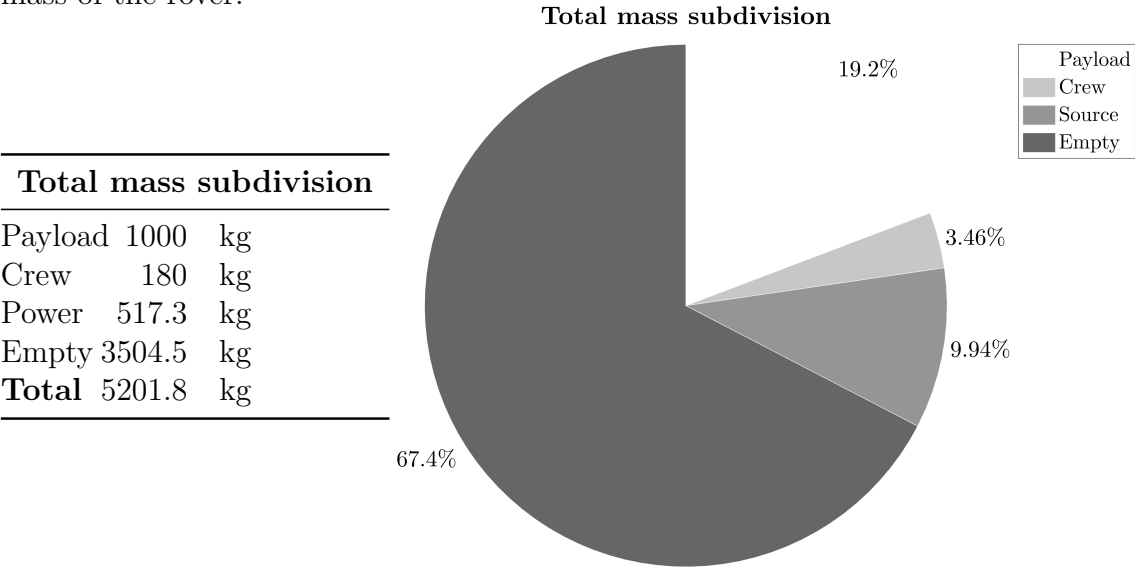
Total mass subdivision		
Payload	1000	kg
Crew	180	kg
Power	517.3	kg
Empty	3504.5	kg
Total	5201.8	kg

19.2%

3.46%

9.94%

67.4%

Payload
Crew
Source
Empty

3.4.7 Parametric Study

A parametric study was conducted to investigate the variation in total mass and power of the systems. The following plots show:

1. the m_{tot} variation with respect to the mission range x_r, for different values of rolling gravimetric battery energy density. Those two parameters affect the the source mass, hence the overall mass of the system.

2. the m_{tot} variation with respect to the extended mission time and the auxiliary power supply. Both parameters are indicative of the extended mission duration. Higher $p_{spec,grav} = (P/m)_{aux}$ is indicative of performing materials for the overall sustaining structure of the solar panels (lighter materials). The change is however not much effective, as this mass is merely a portion of the m_{source}.
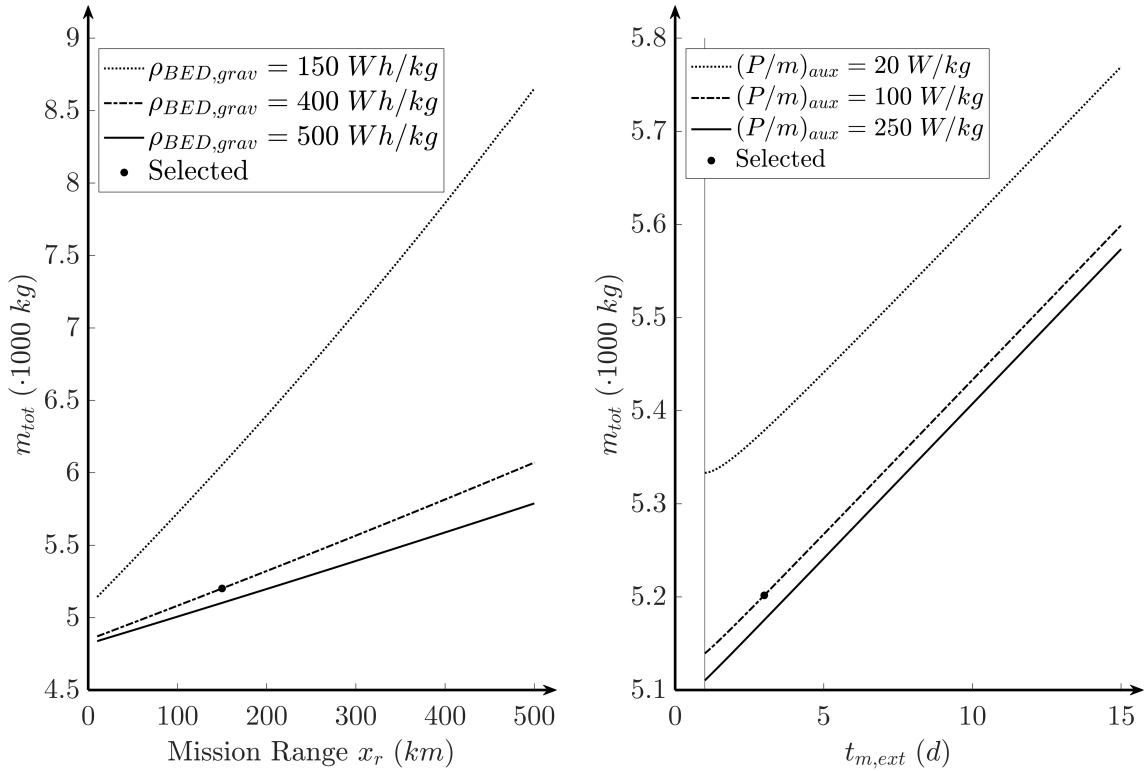
3. The $\mathcal{P}_{tot,inst}$ variation with respect to nominal speed, for different values of rolling resistance coefficient. Those two parameters affect the LPR power request, the source mass, hence the overall mass of the system. The choice of the velocity is attributed to performance request (listed in requirements), while C_{rr} (the wheel rolling resistance) is different given the mission lunar geographical point of application that may affect the overall power request.

4. The $\mathcal{P}_{tot,inst}$ variation with respect to the nominal mission time and and the number of crew members. Both parameters affect the total mass of the rover, and hence, require a larger power supply. The solution proposes an impacting aspect of the N_{crew} members given that a larger crew needs more space to live and stay in the nominal mission. In this example, the larger pressurized mass corresponds to the dry mass presented in Table 3.4.

$$N_{crew} \propto m_{press}$$

the m_{tot} variation with respect to the extended mission time, for different values of the specific auxiliary power (the solar panel power divided by their mass). It is clear that by augmenting this parameter, the Technological Readiness Level of the mission decreases, assessing possible solutions for future analysis.
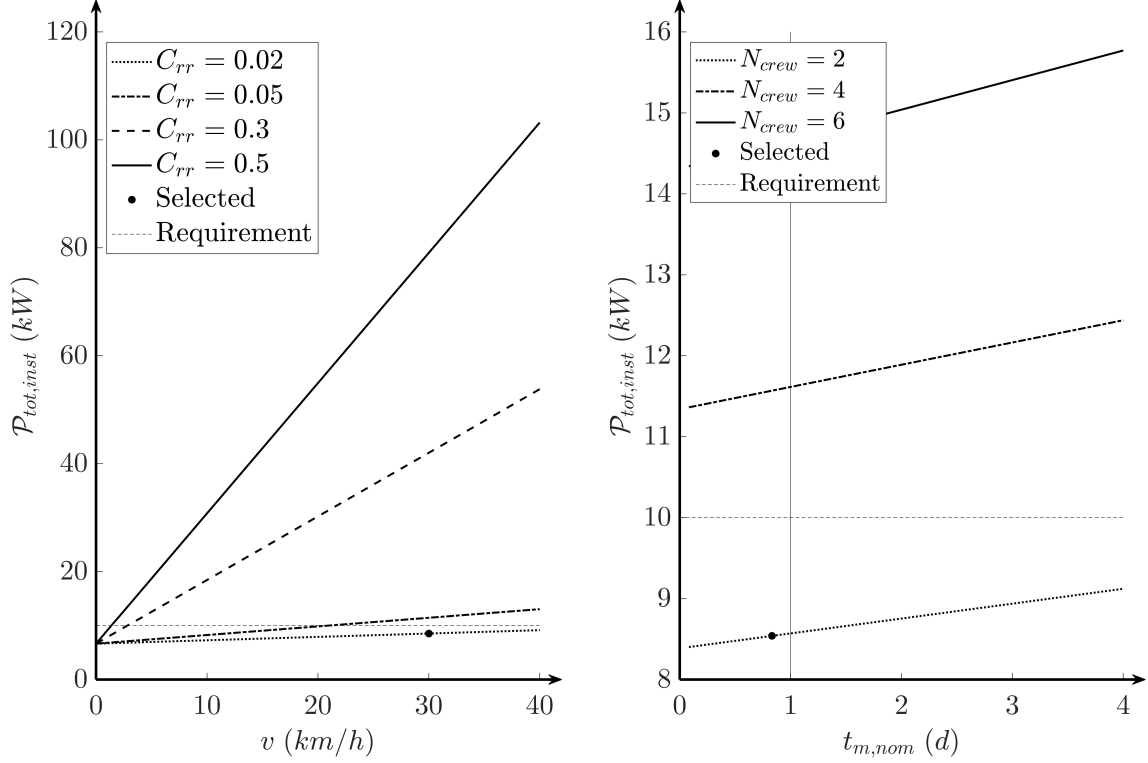
5. The total internal volume $V_{tot,internal}$ as a function of the inflatable length, for different values of inflatable thickness. Inflatable length directly affects the overall volume linearly (given Equation 3.7), while a thicker inflatable structure derives from additional environmental shielding. Both parameters however, show the important leap in size with respect to the rigid volume, estimated by Table 3.4.

6. Finally, the total walkable area $\mathcal{A}_{walkable}$ of the internal cabin, for different diameters and lengths (see Figure 3.9). For the diameters, the two candidate sizes are the proposed ones in Table 3.4, while length of the inflatable module is varied according to reasonable boundaries. The linearity of the trend is expected given that the walkable area is the product between the cabin width w_{cabin} and the cabin total length (both for the rigid and the inflatable module).

$$\mathcal{A}_{walkable} = w_{cabin} \cdot (L_{rigid} + L_{inflatable}) = D \cdot \sqrt{1 - \left(\frac{h_{cabin}}{D_{cabin}}\right)^2} \cdot (L_{rigid} + L_{inflatable})$$

(3.8)

with $h_{cabin} = 2\ m$ as the cabin height. This value is selected in order to permit astronauts to stand inside the module, while ensuring a space on top and on the bottom of the cabin for subsystem storage and stowing.
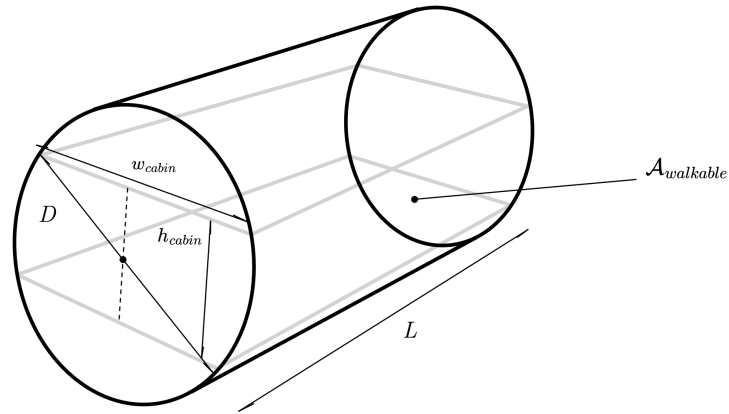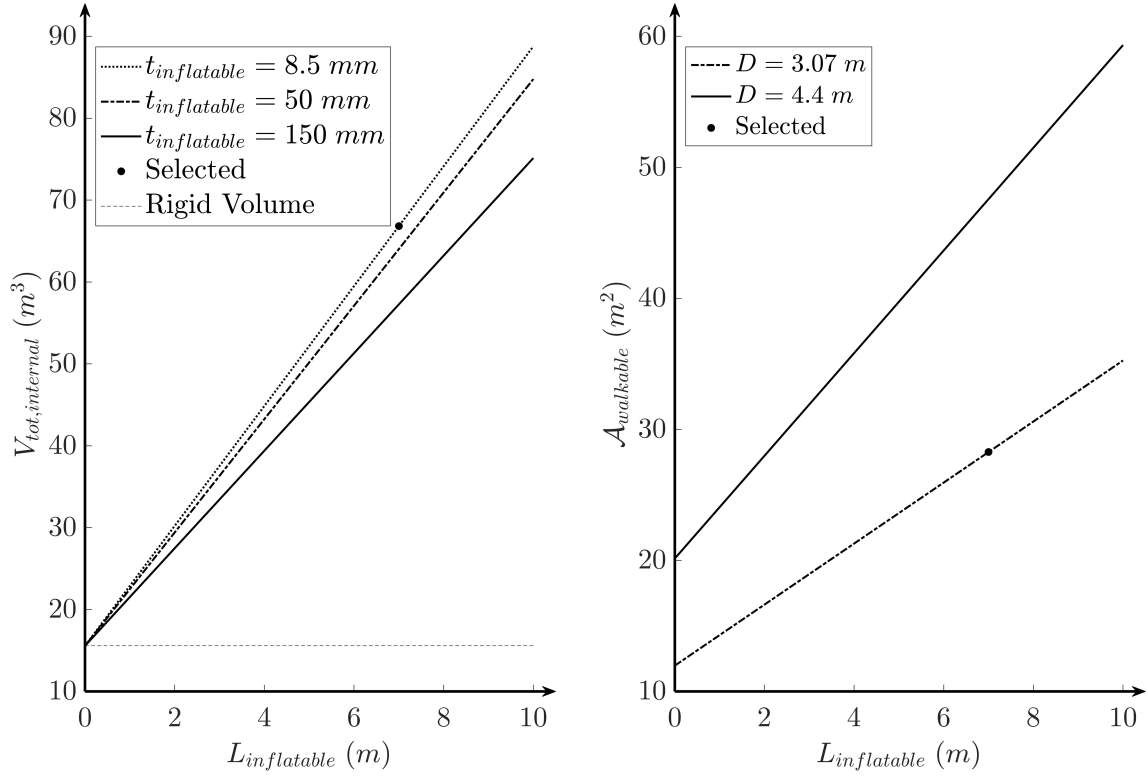
Figure 3.9: Walkable area of the LPR.

3.5   Final provisions

3.5.1   Interior Design

The interior design of a pressurized lunar rover plays a vital role in ensuring the safety, comfort, and operational efficiency of the crew during prolonged surface missions. The layout must integrate critical systems such as life support, navigation, and scientific workspaces while optimizing the use of the limited interior volume. Special attention is given to ergonomics, ensuring that astronauts can perform tasks, rest, and move within the rover without unnecessary constraints.

The design must accommodate modular and adaptable configurations to support diverse mission objectives. This section presents the process of defining the interior design, focusing on the balance between functional requirements, spatial limitations, and the needs of the crew to create a practical and habitable environment. The following depictions show the internal disposition of both the stored and the expanded configurations.
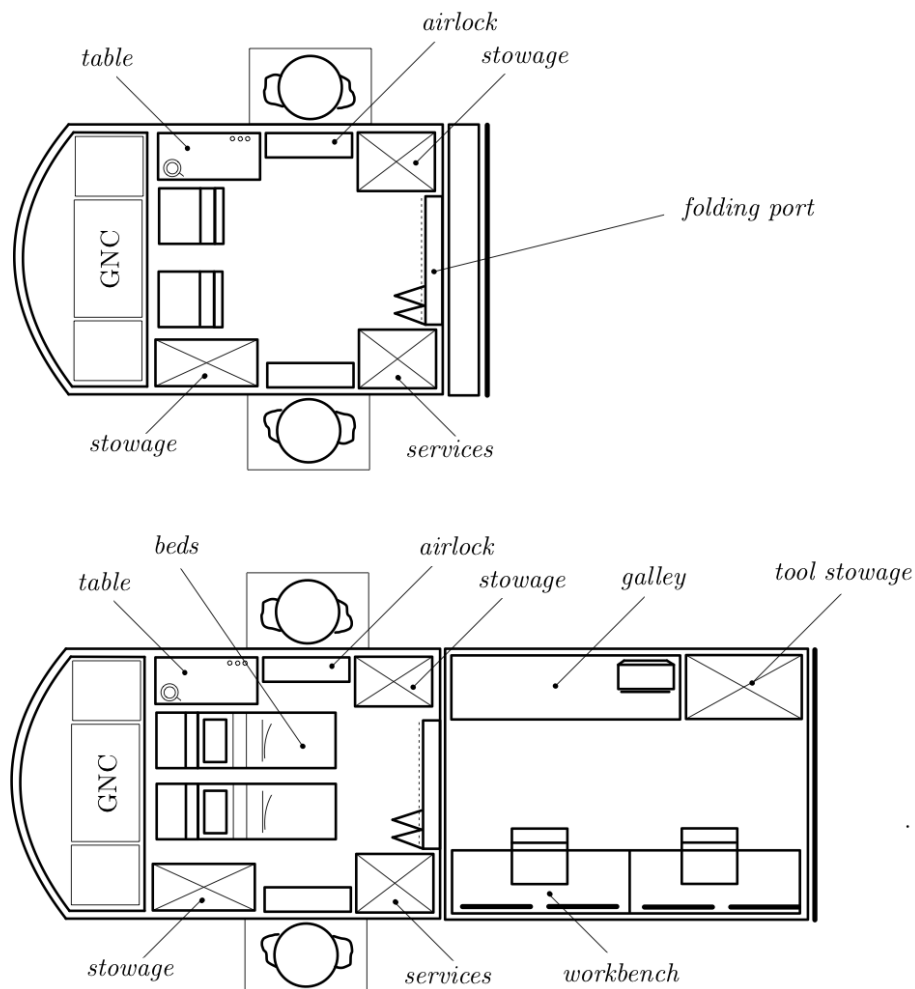
Figure 3.10: Interior design of the stored and the expanded configurations.

3.5.2 Name choice

In conclusion, a name was selected for the project. The Pressurized Rover presented in this work will be referred as **PROTEUS: Pressurized Rover for Operations, Transport, and Exploration of Unknown Surfaces**.

Proteus is an early prophetic sea god or god of rivers and oceanic bodies of water in Greek mythology, one of several deities whom Homer calls the "Old Man of the Sea" (via [17]). The name Proteus itself is derived from the Greek word protos, meaning first. This etymology suggests that he was one of the earliest sea gods, predating even Poseidon in some accounts. The romantic aspect of the name lies in the fact that, just as centuries ago sailors tried to navigate the seas and currents of the Mediterranean, so today astronauts aim to explore the unknown Seas of the Moon (*Lunar Maria*).

Figure 3.11: *Proteus, A Greek Sea God Who Possessed* is a drawing by Mary Evans Picture Library. The inscription reads: "Proteus, a thread of Ocean and Tethys. Egypt hears Proteus, with ambiguous words, telling the mystical story of the fire."

Part II

The Docking Subsystem

Chapter 4

The Docking Subsystem

The next main aspect of the proposed work is to design docking subsystem for grounded vehicle applications. The main concepts concerning mating operations will be introduced in the subsequent chapter. Several mechanisms will be described so as to create a solid technical reference. This reference will be used throughout this work to outline the similarities and differences between the proposed mechanisms and the implemented and theorized existent solutions. It will also be used to describe the identified advantages and disadvantages.

4.1   Mating operations

A **mating operation** is a maneuver designed to join two spacecrafts. This connection can be temporary, or partially permanent such as for space station modules [18]. These operations allow to transfer cargo and crew between spacecraft as well as to perform in-situ (or on-orbit) servicing missions. In general, the spacecrafts involved in a mating operation are called *chaser* and *target*:

1. The **chaser** assumes an active role;

2. The **target** maintains its relative kinematic state.

There are two types of mating operations: docking and berthing [18]. On the one hand, in a **docking** operation (Figure 4.1), the GNC of the chaser controls the relative state with the target so as to ensure suitable contact conditions (relative misalignments, relative velocities, etc). In this case, the capture location coincides with the structural connection.
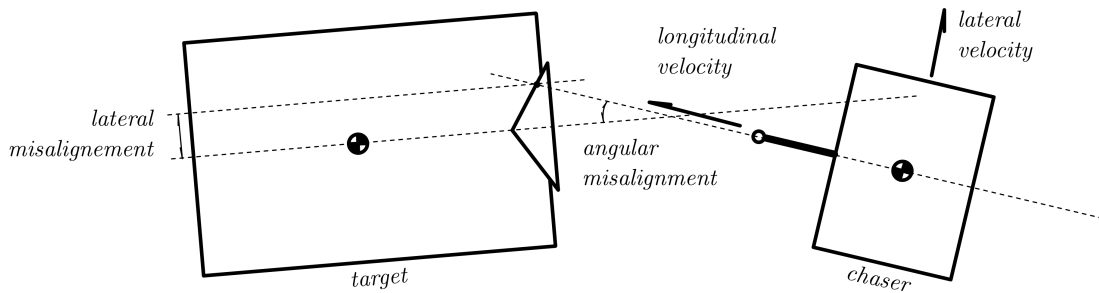
Figure 4.1: Docking Scheme

On the other hand, during a **berthing** operation (Figure 4.2), the GNC of the chaser ensures a suitable relative state between the spacecrafts. This relative state is characterized by a relative pose and zero nominal relative linear and angular velocities. Subsequently, a manipulator fitted to either the chaser or the target clamps the other vehicle. Finally, the manipulator approaches the matching attachment interfaces mounted on the satellites.
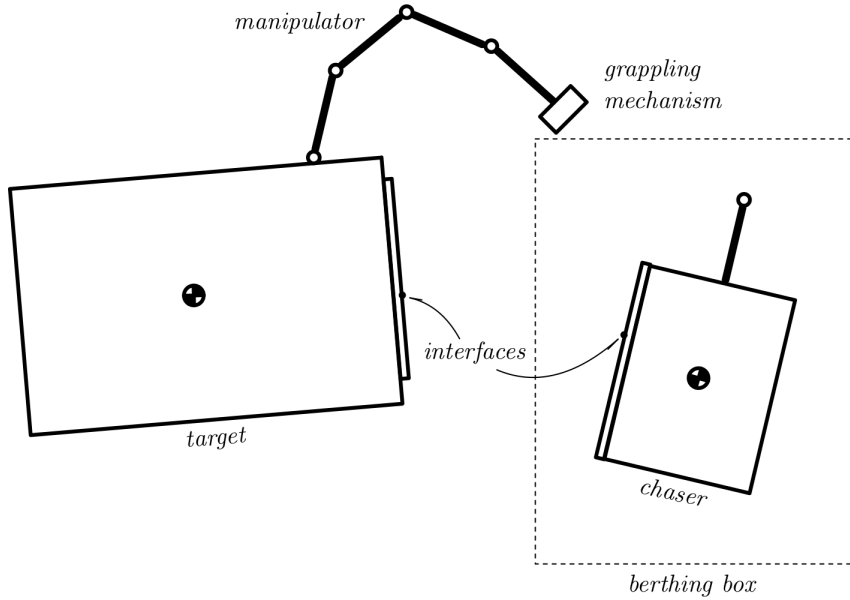
Figure 4.2: Berthing Scheme

4.2   Classification

The architecture of a docking system may be either *central* or *peripheral*. All the early Soviet and American space programs used central architectures for their docking mechanisms.

A **central docking mechanism** is composed of a male part mounted on the chaser and a female part fitted to the target. The male part is a *probe* (also called rod or pin). The female part is a *drogue* (conical frustum) that guides the probe toward its apex. Once the probe reaches the apex, a first capture device performs ***soft docking***. The retraction of the probe combined with guiding geometries eliminate the relative motion and align the interfaces. Finally, a set of hooks or bolts, or a combination of both achieves what is known as ***hard docking***.

The main advantage of a central architecture is its relative simple design. This simplicity facilitates the analysis and development of this kind of mechanisms. However, this architecture presents a main drawback: after docking the probe and the reception cone obstruct the transfer tunnel needed to exchange crew and cargo. This problem was pointed out during the first meeting between the Americans and the Soviets for the Apollo-Soyuz Test Project (ASTP) in 1970 [19]. In this meeting, the American probe, considering the inconveniences caused by the presence of the Apollo probe assembly after docking, proposed as design criterion the elimination of any docking gear that might have blocked the passageway between the spacecraft.

As a result, during this project, the first peripheral docking mechanism was designed and tested in space.

In a **peripheral docking system**, all the docking gear is accommodated in the periphery of the mechanism. This feature leaves the center of the mechanism free. However, a peripheral docking system is far more complex to design and study than a central mechanism.

4.2.1   History of the Docking Subsystems

The first docking maneuver ever performed took place on March 16th, 1966, during the Gemini VIII mission [20]. After this first success, two central mechanisms with more advanced features were tested. On this regard, The Soyuz docking mechanism designed by the Soviets was tested for the first time on October 30th, 1967 [21]. This test was the first autonomous unmanned space docking. Moreover, the first mating of the American Apollo docking Mechanism took place on March 7th, 1969 [22]. The collaboration between the two superpowers led to the test of the first peripheral docking system; the Apollo-Soyuz docking mechanism, on July 17th, 1975 [23]. The former mechanism was further developed becoming the Androgynous Peripheral Attachment System (APAS). It was intended to serve the Buran spacecraft in the late 1980s. Subsequently, another update was implemented to the APAS for the Shuttle-Mir missions. The first docking between these spacecrafts took place in 1995 [24]. In 2007, the Orbital Express Capture System (OECS) successfully mated the spacecraft Astro and NEXTSat in the DARPASs Orbital Express Mission.

With the rapid development of the Chinese activities in space, the China Manned Space Agency (CMSA) has produced several space systems. One of this is the APAS-2010 which is a new version of the APAS introduced before. Subsequently, NASA developed a new kind of peripheral docking mechanism based on active electric actuators that set an international standard for all the spacecrafts in orbit, the International Docking System Standard (IDSS). This docking system is an evolution from the APAS, whose latest version was defined in 2022.

Figure 4.3 shows a timeline containing the countries involved in the development of a particular docking mechanism and the year in which each mechanism was tested.
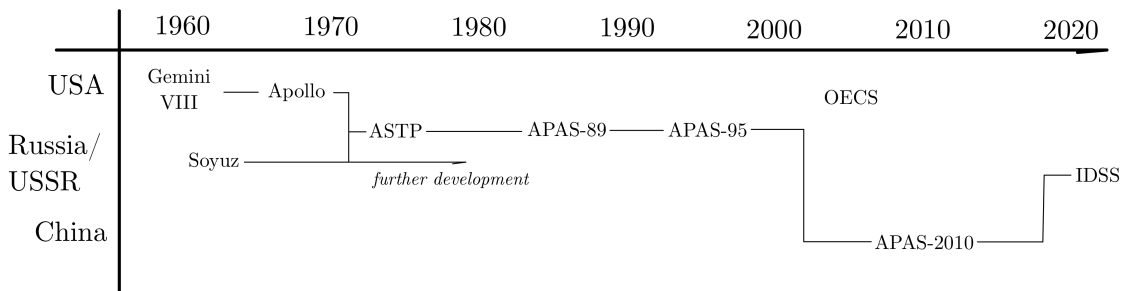
Figure 4.3: Evolution of the Docking Systems

4.3   Docking Architectures

4.3.1   Gemini docking system

This docking mechanism was a rigid male cone (probe) part of the Gemini spacecraft combined with a cup interface (drogue). The drogue was linked to the target spacecraft by seven shock absorbers clustered in three locations to dampen the relative longitudinal and lateral velocities. The longitudinal shock absorbers were equipped with an orifice damper and a spring in parallel for reusability. Regarding the lateral ones, they were not equipped with springs. The instroke orifices of the dampers were larger than the outstroke ones to minimize the rebound. The probe was equipped with an alignment feature called the indexing bar. This indexing bar had as its counterpart a V-shaped matching guide in the female cone. For this reason, there was a single possible coupling configuration between the satellites. The capture was accomplished by three latches on the Agena. Finally, the Agena was also equipped with a motorized unit to pull inward the cone latched to the chaser.
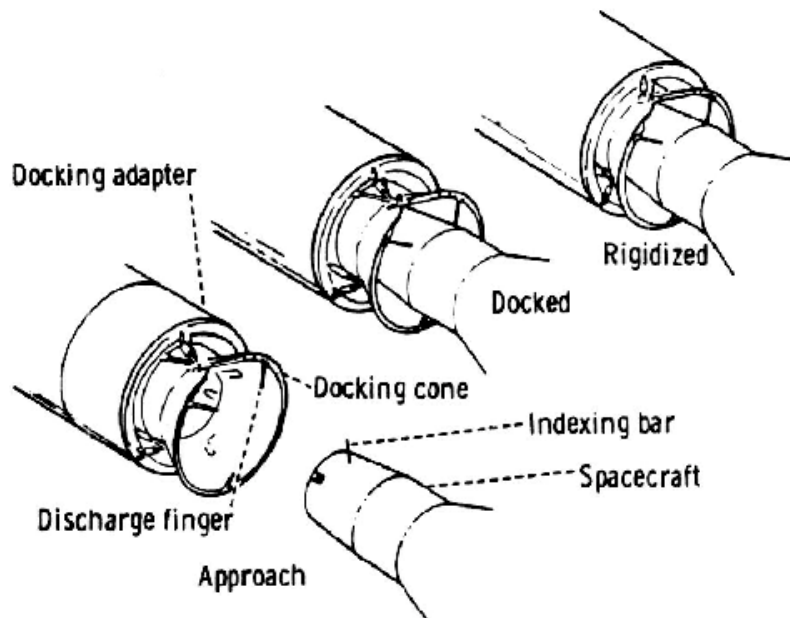
Figure 4.4: Gemini VIII docking system scheme

4.3.2   Soyuz docking system

The development of this central mechanism started in the 60s and is still in used today. The system is again based on a probe and a drogue mechanism. The original probe of the mechanism was equipped with a small ball screw and a large ball screw. The longitudinal shock attenuation was achieved by using the small screw. The forced retraction of this element caused the compression of a coil and Belleville spring as well as the rotation of an Electro-Mechanical Brake (EMB). The EMB was composed of a hollow rotor made of aluminum rotating between two magnets. The lateral impact was attenuated by the probe deflection (bending).

    In this case, capture was accomplished by combining two latches on the probe head with the female socket. A catch-up transducer on the head of the probe

verified the operation. The subsequent retraction of the probe was performed by an electric drive acting on the large ball screw. During retraction, the pitch and yaw angular misalignments were eliminated by a linkage assembly. Moreover, the roll misalignment was zeroed by the interaction of narrowing guides in the socket with the latches hinged to the probe head.
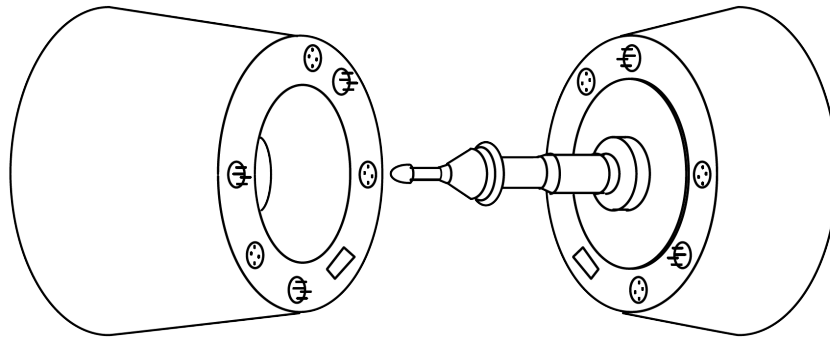
Figure 4.5: Soyuz docking system scheme

The original mechanism did not allow the crew to transit from one satellite to the other. For this reason, the design of the system was reviewed and updated Figure 4.5. To accommodate the transfer tunnel, both the probe and the drogue became part of the hatches of the spacecraft. This modification led to a more compact docking mechanism. The length of the probe was decreased and therefore its bending was not sufficient to dampen the lateral impact. Thus, it was spherically suspended and connected to one end to two lateral attenuation systems. Another major change was the incorporation of a friction brake to dissipate the longitudinal relative velocity.

During the forced retraction of the probe, the rotation of the electromechanical brake dissipates part of the energy up to a certain stroke. After this, when the probe enters the socket, a self-regulating friction brake dissipates a great part of the energy. This system is currently being used for the docking operations between the ISS and the Soyuz, Progress, and ATV spacecraft.
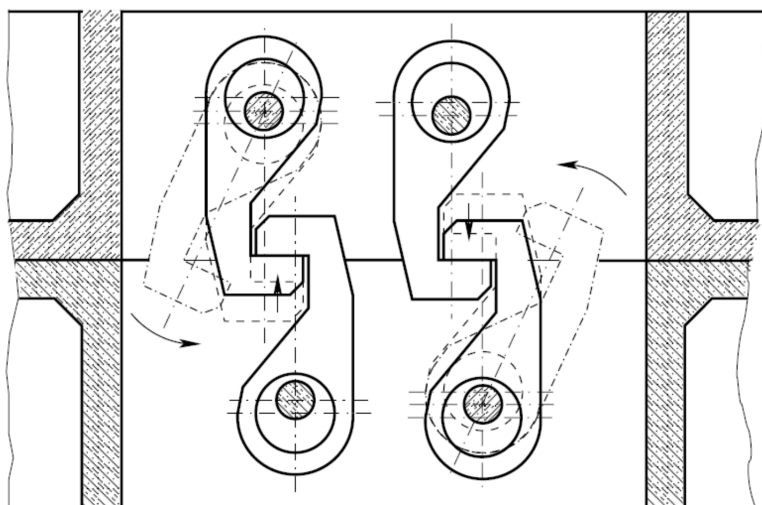
Figure 4.6: Structural latches (hook type)

4.3.3   Apollo docking system

This system was used during the lunar-landing missions to connect and disconnect the Apollo Command and Service Module (CSM) with the Lunar Module (LM). This system was characterized by a probe and drogue architecture Figure 4.7. The probe was composed of a central piston, three beams for centering, and three piston pitch bungees that served as air/oil shock attenuators.

During the docking maneuver, the initial coupling was accomplished by three spring-loaded latches hinged to the probe head. These latches engage the socket placed on the vertex of the female cone. The release of the latches was performed by DC motors located in the central piston.

The shock attenuation and vehicle centering were accomplished as follows. The centering beam was hinged to both the piston and a link Figure 4.8. In turn, the link was hinged to a collar concentric with the piston. The shock attenuator was hinged to both the beam and the collar. This linkage was duplicated radially around the probe at three places 120° apart. When impact occurred, the compression of the central piston produced a compression in the shock attenuator by the simple lever formed by the beam and the link. With the compression, the linkages expanded providing centering.

The shock attenuators were based on air/oil dampers. Inside each damper, the fluid flow through orifices produced the damping effect. The attenuators were sealed by metal bellows. A mixture of argon and helium filled the bellows and the compensator piston cavity to create an air spring.

Dry nitrogen was used during the automatic retraction of the probe. A delta of pressure was generated inside the central piston creating the force needed for the closure.
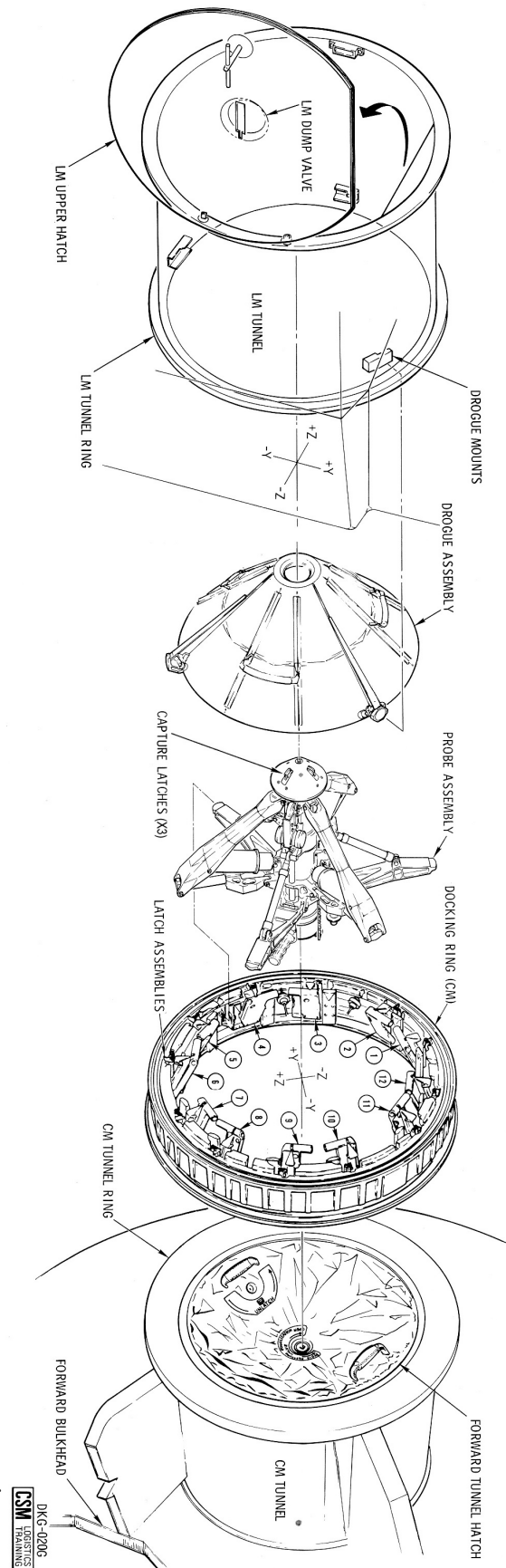
Figure 4.7: The Apollo docking system

The system was activated by energizing an explosive initiator that pierced a pressure vessel containing the dry nitrogen. The nature of this system allowed for only two prime and two backup retractions.
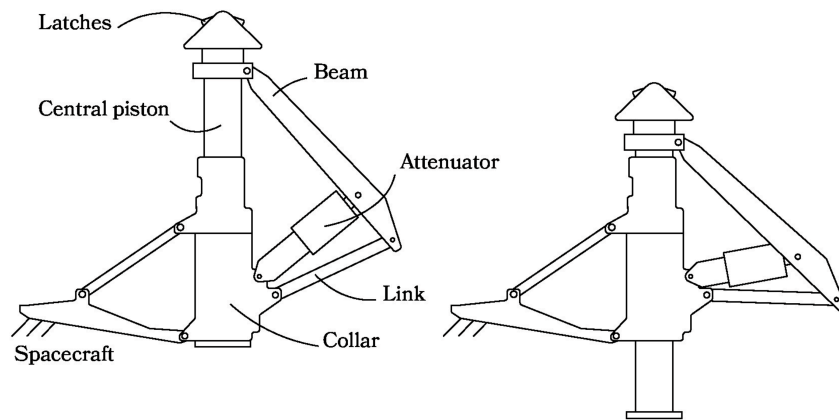
Figure 4.8: Schematic view of the Apollo docking system in fully deployed (left) and retracted (right) configurations

Finally, twelve individually actuated hooks created the final structural connection between the satellites.

During the Apollo missions, the probe assembly was removed and stored to allow the crew transfer from one vehicle to the other Figure 4.9. Moreover, also the drogue assembly was removed and stored. As stated before, this issue was discussed during the first ASTP meeting in 1970 leading to the design of the first peripheral system.
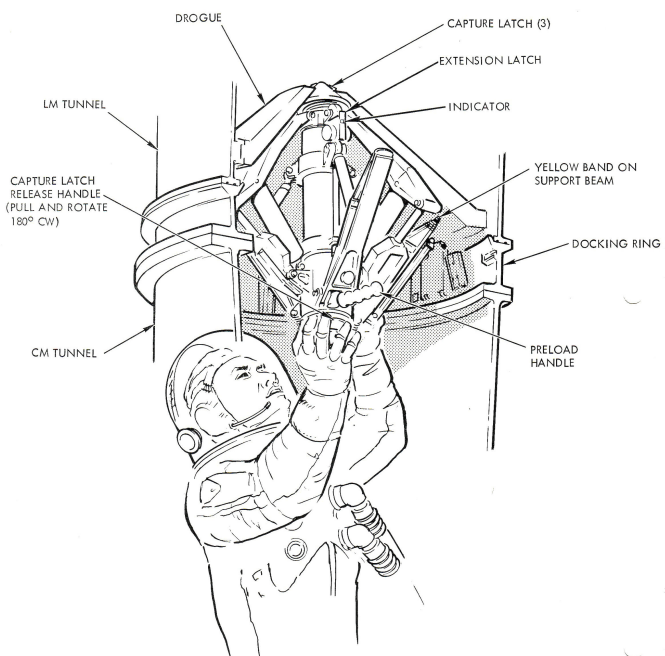
Figure 4.9: Sketch of an astronaut removing the probe assembly after docking. This image was used during the first meeting of the ASTP by the Americans to state why a central docking mechanism should be avoided

4.3.4   ASTP docking system

The Apollo-Soyuz Docking Mechanism (ASTP) was the first peripheral docking system. Besides being peripheral, it was also androgynous. In an **androgynous system**, either half of the mechanism may assume an active or passive configuration. This feature increases the safety as if one of the halves fails to deploy the other may be activated. During the ASTP design phase, several technical meetings were held to define the interfaces of the halves of the mechanism, the attenuation system, the structural connection system, etc. The idea proposed by the Americans in 1970 of creating the peripheral system was well received as in November 1971 they discovered that the Soviet engineer, Vladimir Syromyatnikov, was already working on a solution of this kind.
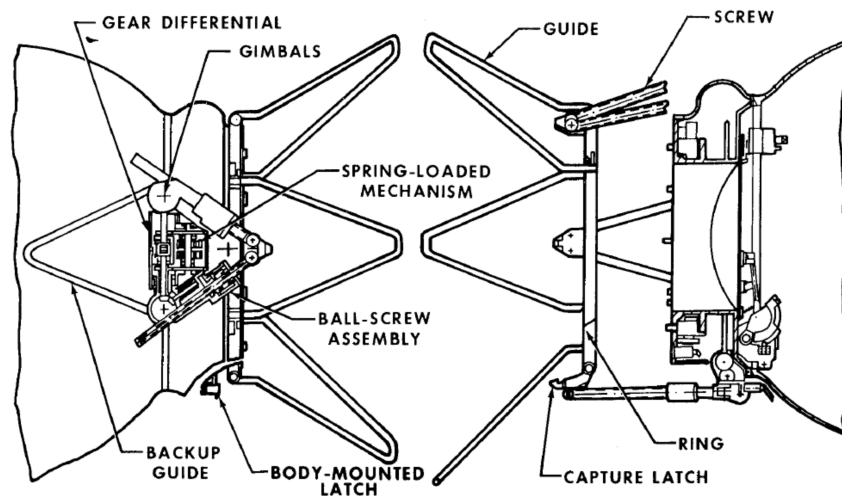
Figure 4.10: Concept of the androgynous mechanism created by Syromyatnikov

After this November meeting the general layout of the system was defined [18]: The design concept includes a ring equipped with guides and capture latches that were located on movable rods which serve as attenuators and retracting actuators, and a docking ring on which are located peripheral mating capture latches with a docking seal. Moreover, the partners decided to use the capture spring-loaded latches designed by the Americans and the structural latches used on both the Soyuz and the Salyut. However, each country decided to use their own attenuation technology: the Americans kept the hydraulic damper as in the Apollo lunar missions while the soviets prefer their more sophisticated electromechanical brake.

Figure 4.11 shows a technical drawing of the flight model. In particular, the moving ring of the mechanism was connected to the spacecraft by six ball screws gimbaled to both ends in a 6UPU passive configuration. During impact between the mechanism halves, the forced retraction of each ball screw rotated an EMB. Finally, the synchronized deployment and retraction of the whole ring was accomplished by a single electric motor combined with differential transmissions.

Figure 4.12 shows a technical drawing of the American half. In this figure, the fine alignment features are visible: the alignment socket and pin which had a counterpart on the Soviet half.
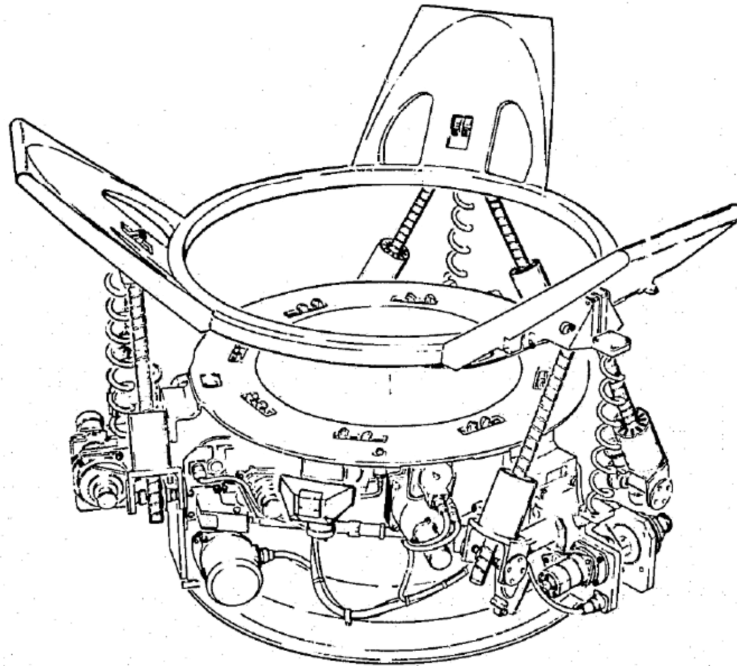
Figure 4.11: Technical drawing of the flight model of the Soviet half
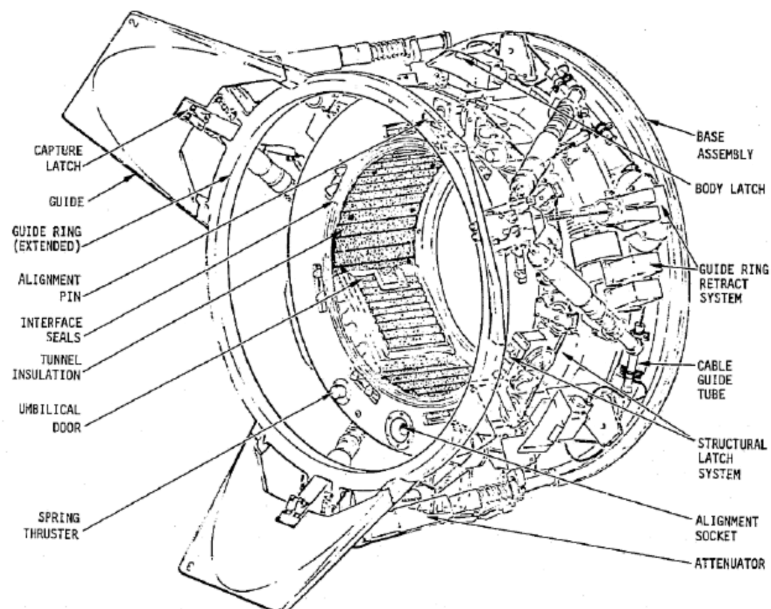
Figure 4.12: Technical drawing of the flight model of the American half

4.3.5   Androgynous Peripheral Attachment System (APAS)

The ASTP docking system evolved into the APAS-89. It was initially developed for
the reusable orbital spacecraft Buran [18]. This system adopted the EMB technology
for attenuation and spring-loaded mechanical latches for soft docking. The petals
used for the coarse guiding were changed from an outwards configuration to an
inwards one Figure 4.13. A subsequent version of this mechanism was used during
the Shuttle-Mir and Shuttle-ISS missions (APAS-95). The CMRA have developed a
variant of this system know as APAS-2010. This system evolved into the IDSS and
it is now commonly used for ISS docking of pressurized spacecrafts [25].
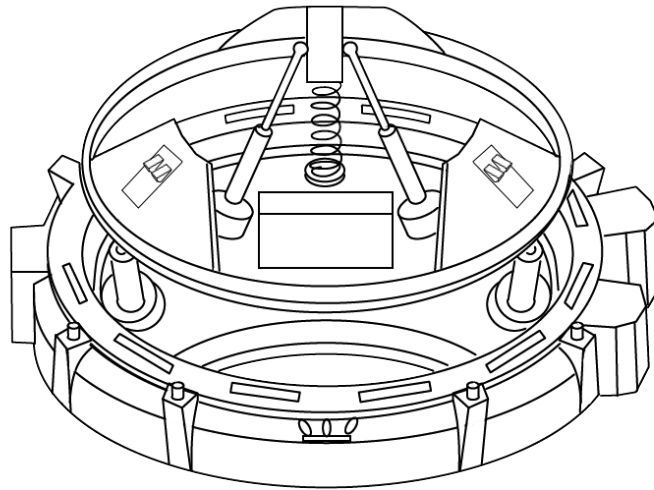
Figure 4.13: APAS docking system scheme. It is clear that the model was used as
a baseline for the IDSS used commonly today.

4.3.6   Orbital Express Capture system (OECS)

The OECS was used during the DARPAs Orbital Express mission. During this
mission, the satellites Astro and NEXTSat performed several maneuvers showing
the feasibility of autonomous mating for on-orbit servicing of unmanned vehicles.
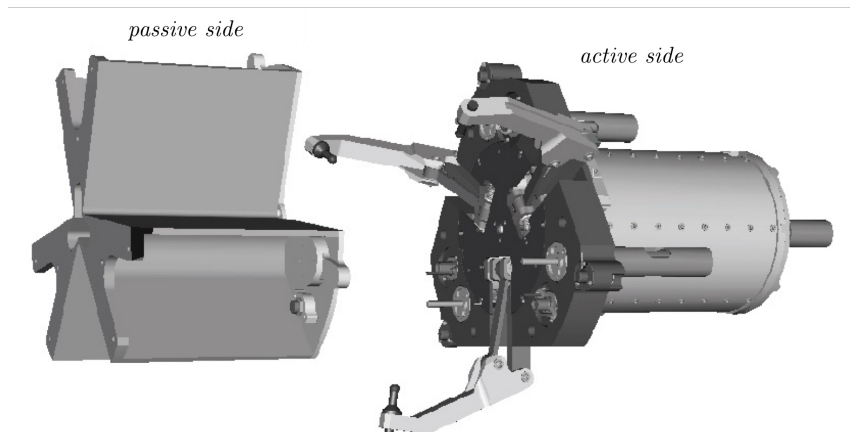
Figure 4.14: OECS Scheme

The capture system consists of a passive and an active side. The active side is equipped with three grappling fingers with a common actuator. The passive side consists of three wedges between which the fingers may be received. This half of the mechanism is equipped with laser sensors to verify the presence of the fingers. The docking sequence may be seen in Figure 4.15. In the first phase (1), the fingers are deployed while the passive side performs a station keeping maneuver. Subsequently, the motor is activated and the fingers are closed toward the target by means of a ball screw. The bodies are aligned by the interaction of the fingers with the passive guides (2). After this (3), the linkage tips bring the bodies together as they engage a shelf feature on the passive side. Push-off rods dampen the impact between the mechanism halves. These rods are equipped with a spring and a Coulomb damper. Finally, the passive side is fully constrained by a set of cavities combined with cones (4). The stiffness of the connection is increased by applying a preload with the motor. Once the desired preload is reached, a brake maintains it.
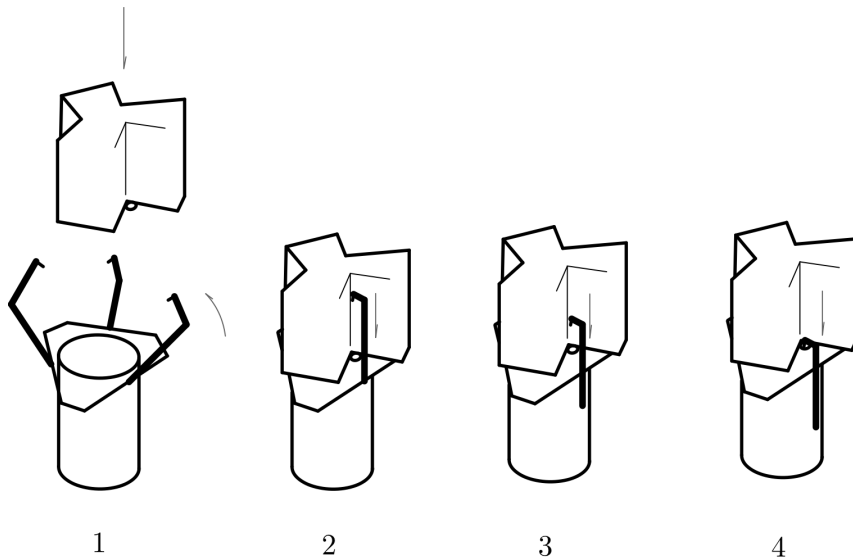
Figure 4.15: OECS Mechanism Description.

4.3.7 Other docking mechanisms

There are some docking mechanisms that, although in an early stage of development, are worth mentioning. An example of said systems is the ARCADE docking mechanism [18]. This mechanism is composed of two mating parts. The first part is a passive spring-damper probe equipped with a soft iron tip. The second part is a conic drogue. The drogue is equipped with an electromagnet to capture the tip of the probe, a miniature linear actuator to approach the interfaces after soft docking, and three locking solenoids for hard docking. Thus, all the active features of the mechanism are mounted on the female side. The following figure shows both the female and male parts of the ARCADE docking mechanism.

Another interesting example is the semi-androgynous mechanism described in [18]. This mechanism was designed for small satellites. It consists of two interfaces equipped with eight petals able to open and close by means of a disk cam mechanism.
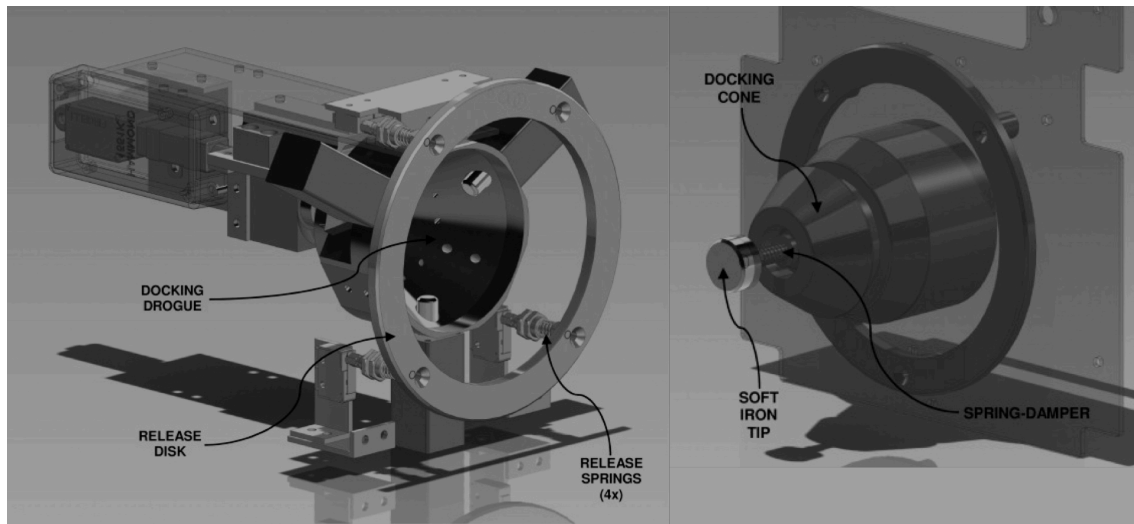
Figure 4.16: ARCADE docking mechanism

Before docking, one of the interfaces changes its shape to a drogue configuration while the other deploys the petals. When the passive interface is within the reach of the active one, the petals are closed around the probe securing the mechanical connection between the parts.

4.4   Mechanisms concepts

Many of the proposed docking subsystem shared similarities and differences among their design choices. In this section, the mechanism concepts considered as possible candidates for the docking system will be disclosed. These concepts were defined with the scope of suggesting alternative designs amongst which making a motivated choice of the preferred one.

4.4.1   Peripheral fixed design

The docking system employed during the Gemini VIII mission featured a peripheral design, wherein the male and female components are defined by two truncated cones (*frustums*). Upon achieving proximity, the spacecraft initiate final approach sequences, utilizing onboard thrusters to fine-tune their trajectory. The truncated cone design of the docking interfaces guided the spacecraft into proper alignment, allowing for a smooth and secure connection.

Once contact was established, the docking system's latching mechanisms engaged, creating a rigid link between the vehicles. This secure connection enabled the combined spacecraft to operate as a single unit, facilitating the transfer of control and data systems as necessary.

1. *approach and deplyement*   2. *alignment*   3. *soft docking*   4. *hard docking*
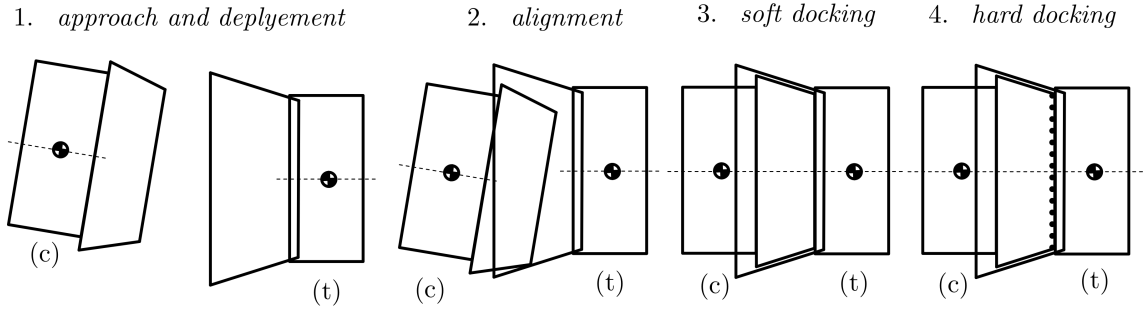
Figure 4.17: Peripheral fixed design

4.4.2 Probe and Drogue (Soyuz-like)

Another mechanism concept is the *probe and drogue* used by the Soyuz module. TAS-I developed a central docking mechanism during the STEPS project [18].
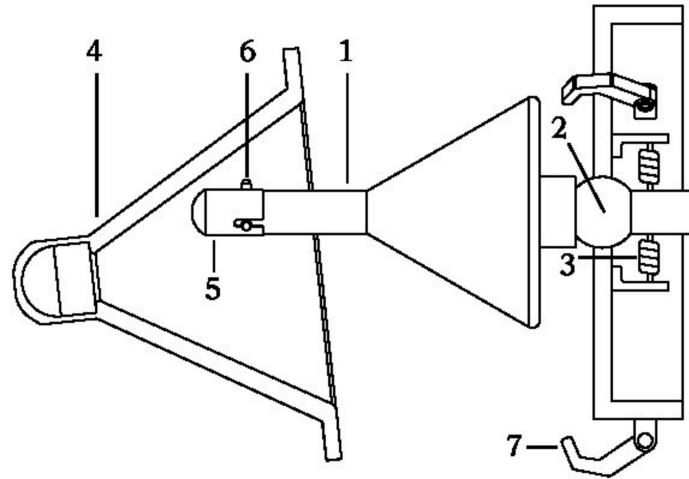
Figure 4.18: STEPS' probe and drogue docking

This system is equipped with a retractable central probe (1). This part is launched fully retracted and is actuated up to its maximum length in the deployment phase. The probe is mounted on a spherical joint (2) that allow it to rotate about all the axes. These rotations are passively controlled by four preloaded traction springs (3). A drogue (4) located on the passive side guides the probe (alignment phase) toward a socket located at its vertex. The probe is equipped with a cap (5) that translates relatively controlled by a preloaded spring. This element is necessary to reduce the contact forces with the drogue upon impact.

The four docking phases of the probe and drogue docking concept are depicted in the previous figure. In particular, during the second phase, post contact thrust of the chaser toward the target may be necessary to guarantee the contact of the probe with the reception cone and the sliding movement toward the soft docking configuration.

1. *approach and deplyement*   2. *alignment*   3. *soft docking*   4. *hard docking*

Figure 4.19: Probe and drogue manuever

4.4.3   Stewart Platform (IDSS-like)

The IDSS (or the APAS) uses a Stewart-Gough platform and a drogue as passive half. The following figure shows the complete maneuver.

1. *approach and deplyement*   2. *alignment*   3. *soft docking*   4. *hard docking*

Figure 4.20: Stewart platform manuever (IDSS-like).

In the approach and deployment phase, the GNC of the spacecraft reduces the distance between chaser (*c*) and target (*t*). Simultaneously, the platform is positioned in the middle of its workspace. During the alignment phase, the poses of the male and female docking interfaces are matched using only the control system of the docking mechanism. On the one hand, the platform with position control is equipped with an optical system to identify the relative pose between the chaser and the target. Using this information, the position set to the actuators of the platform is generated exploiting the inverse kinematics of the manipulator. On the other hand, the platform with impedance control aligns the interfaces using guiding geometries placed on both sides combined with force sensors. As soon as the contact between the male and female interfaces starts, the force sensors measure the exchanged wrench and the control algorithm works to create suitable force reference values to the actuators of the moving part. These force references are created by means of a stiffness strategy combined with the direct kinematics of the platform. The result is the alignment of the moving part with the female reception cone. For both the position and impedance control architectures, the alignement phase in Figure 4.20 shows that the interfaces of the mechanism are aligned regardless the relative pose between the spacecraft. In the soft docking phase, a capture system guarantees a first mechanical connection. Subsequently, both mechanisms start working with a position control logic so as to approach the spacecraft up to their final pose while limiting the maximum exchanged forces. Finally, hard docking is achieved using fastening devices.
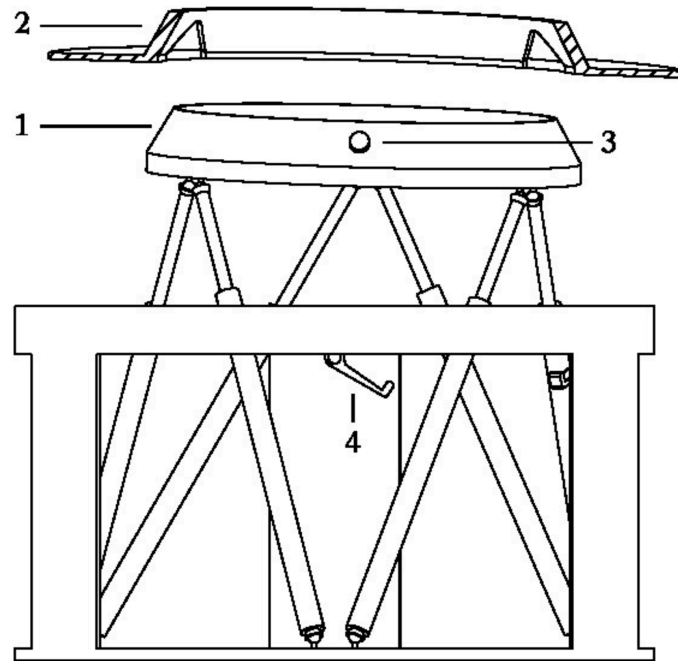
Figure 4.21: Stewart-Gough platform

Figure 4.21 show the mechanism concept. The platforms are composed of six prismatic actuators linked to both a moving ring and a support fixed to the chaser spacecraft. The moving ring is a frustum (1) designed to fit inside the reception cone mounted on the target (2). Regarding the manipulator with position control (figure 4.2), the dimensions of the female reception cone are very similar to the ones of the moving ring. In this case, the position errors between the parts are eliminated using the optical feedback. In contrast, the unit with impedance control is equipped with a larger reception cone to recover the position errors at the beginning of the maneuver. In the alignment phase, spring-loaded pins (3) guide the male part exploiting conical grooves inside the female part. These conical grooves act as coarse alignment guides to recover rolling angular misalignments about the axes of the cones. The soft docking is completed when the pins enter suitable sockets in the vertex of the conical grooves (not shown). The hard docking is achieved using three actuated hooks (4) combined with suitable seats.

4.4.4   Non-conventional designs

The image shows the basic concept of the articulated arms system, similar to the one used in the OECS mission.

In the figure, (1) represents the adapter ring of the target spacecraft.. The three arms (2) are initially stowed in the chaser. During the first phase of the docking procedure, the arms are simultaneously and symmetrically deployed using a main central actuator (3). This actuator is connected to each arm through a suitable transmission not depicted in detail in figure 4.9. Each linkage is equipped with a gripper (4) linked to the arm by a spherical joint that allows its rotations in the alignment phase.
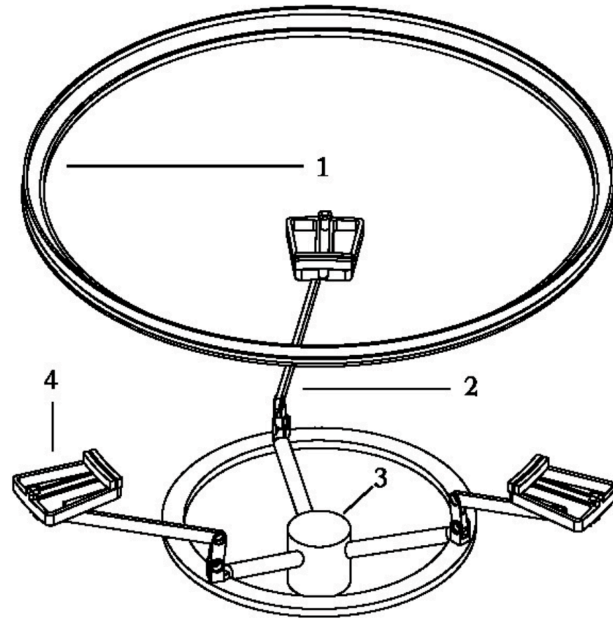
Figure 4.22: Articulated arms design (deployed).

In this phase, the contact between each gripper and the ring aligns the former as it may rotate about the spherical joint. Once a first gripper comes into contact with the ring, it is closed by an actuator to accomplish a first partial soft docking. Subsequently, due to the motion of the chaser toward the target, a relative rotation of the two spacecraft takes place about the spherical joint of the clamped gripper. This approach allows the other grippers to clasp the ring in sequence to conclude the soft docking phase. Subsequently, the main central actuator retracts simultaneously and stows the set of arms into the chaser, bringing the target in the final position relative to the chaser.
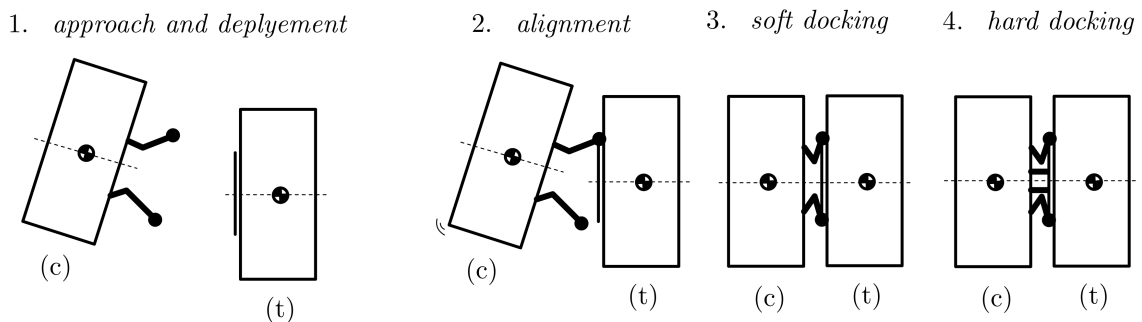
Figure 4.23: Articulated arm manuever

Chapter 5

Docking Mathematical Model

The development of an accurate mathematical model is a fundamental step in the analysis and design of the docking subsystem. Such a model enables the prediction of system behavior under various operational conditions, facilitating performance evaluation and optimization. This chapter presents the mathematical formulation governing the docking process, encompassing the dynamic and kinematic relationships that describe the interaction between docking interfaces. Starting from the kinematics, and the definition of a *center of docking* (analogous to other mechanical theories such as elasticity and aerodynamics), the model proceeds with the introduction of the dynamics of the system. Particular attention is given to the forces and torques, as well as the constraints imposed by mechanical requirements. The proposed model serves as a basis for subsequent simulations and validations.

5.1 Kinematics

5.1.1 Center of Docking

To define (and compare) efficiently the various docking solutions, this work proposes an innovative kinematic model. Let two bodies (i.e. *chaser* and *target*) have their own distinct motion. The properties of those bodies are defined in an inertial reference frame $\mathcal{R}_0$. Each body has its own **center of docking**, a local frame $\mathcal{R}_1$ and $\mathcal{R}_2$ whose origins are described by $\boldsymbol{r}_1$ and $\boldsymbol{r}_2$ in $\mathcal{R}_0$ such that there exists a condition where

$$\mathcal{R}_1 \equiv \mathcal{R}_2 \tag{5.1}$$

This condition is called the *aligned* condition. If such a condition is perpetrated for a sufficient amount of time, the two bodies are said to be *docked*. The set of individual maneuvers necessary to **achieve** and **maintain** the aligned condition is called **docking**.

An alternative, more practical, definition is the following. Consider the relative position $\boldsymbol{r}_d = \boldsymbol{r}_2 - \boldsymbol{r}_1$ whose components in $\mathcal{R}_0$ are denoted by (x_d, y_d, z_d). And consider the relative misalignment between $\mathcal{R}_1$ and $\mathcal{R}_2$, for instance the Roll-Pitch-Yaw angles $(\phi_d, \vartheta_d, \psi_d)$ formed between the frame $\mathcal{R}_2$ and the transposed frame $\mathcal{R}_1'$ in the origin of $\mathcal{R}_2$ (same position, but different angular position). This 6 degrees of freedom completely define the relative state between the two frames. If there exists such a condition where Equation 5.1 is performed, one has

$$\begin{cases} x_d = 0 \\ y_d = 0 \\ z_d = 0 \end{cases} \qquad \begin{cases} \phi_d = 0 \\ \vartheta_d = 0 \\ \psi_d = 0 \end{cases} \qquad (5.2)$$

This condition is called the *aligned* condition. The following figure represents the described situation.
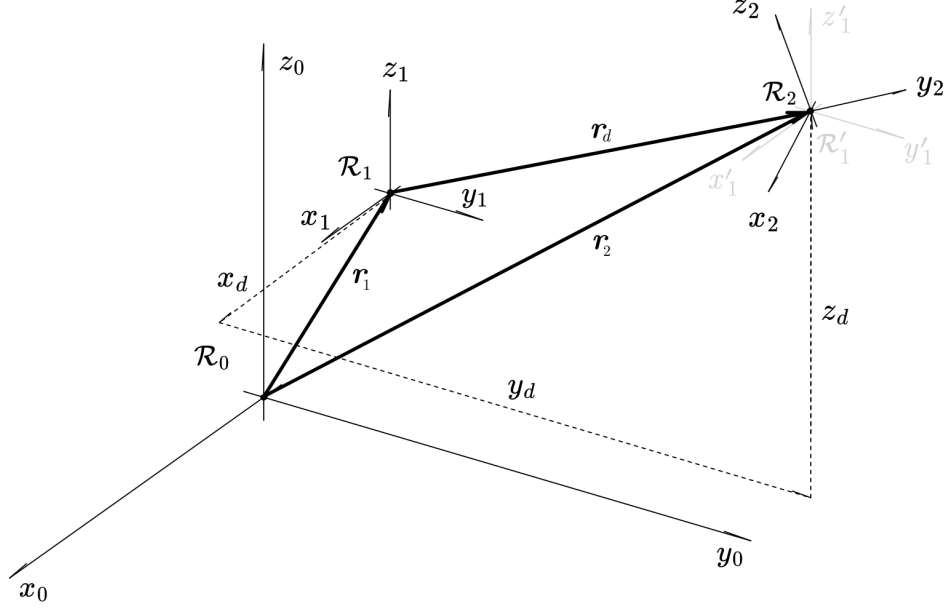
Figure 5.1: The reference frames described in the center of docking definition.

By defining more rigorously those conditions, it is possible to retroactively compare the previous docking mechanisms and design to compare the various solutions. One important aspect to address is the fact that this definition does not require a "matter point" (i.e. a point defined by a physical constraint, like a surface, a pointed tip or a marker) to be fulfilled. For instance:

1. considering a *probe and drogue* system, a good choice for the center of docking would be on the tip of the probe and of the drogue; this is a "matter point" that could be chosen for investigating the properties of the system;

2. considering, instead, a *peripheral* system (like the IDSS), a good choice for the center of docking would be in the center of the peripheral circle; no "matter point" is prescribed here, but the considerations still remain the same.

Another practical usage of such a tool is the fact that, usually, docking subsystem requirements are given in the local frame of the center of gravity (subsequently

referred as G) of the system (both for chaser and target). This procedure, however, assumes that all the docking components act rigidly with respect to G. This argument could not be true if the docking system is considered as flexible. For instance, if the docking mechanics is completely decoupled with respect to G, or if the components are made from a flexible material.

If not explicitly established $\mathcal{R}_1$ refers to target and $\mathcal{R}_2$ refers to chaser (i.e. the LPR).

5.1.2 Classical kinematics parameters

The relative dynamics of the chaser $\mathcal{R}_2$ with respect to the target $\mathcal{R}_1$ define a trajectory

$$
\gamma : \begin{cases}
x_d = x_d(t) \\
y_d = y_d(t) \\
z_d = y_d(t) \\
\phi_d = \phi_d(t) \\
\vartheta_d = \vartheta_d(t) \\
\psi_d = \psi_d(t)
\end{cases}
$$

whose tangent vector represents the relative **translational velocity** and its derivative the **translational acceleration**

$$
\boldsymbol{v}_d = \frac{d\boldsymbol{r}_d}{dt} = \frac{d\boldsymbol{r}_2}{dt} - \frac{d\boldsymbol{r}_1}{dt} = \boldsymbol{v}_2 - \boldsymbol{v}_1 \tag{5.3}
$$

$$
\boldsymbol{a}_d = \frac{d\boldsymbol{v}_d}{dt} = \frac{d\boldsymbol{v}_2}{dt} - \frac{d\boldsymbol{v}_1}{dt} = \boldsymbol{a}_2 - \boldsymbol{a}_1 \tag{5.4}
$$

The components of the **angular velocity** pseudovector were first calculated by Leonhard Euler using his Euler angles and the use of an intermediate frame.

1. One $x-$axis rotation of the reference frame $\mathcal{R}_1'$ $\hat{\boldsymbol{e}}_{x,1'}$.

2. One $y-$axis rotation in the reference frame $\mathcal{R}_1''$ $\hat{\boldsymbol{e}}_{y,1''}$.

3. One $z-$axis rotation in the reference frame $\mathcal{R}_2$ $\hat{\boldsymbol{e}}_{z,2}$.

Euler proved that the projections of the angular velocity pseudovector on each of these three axes is the derivative of its associated angle (which is equivalent to decomposing the instantaneous rotation into three instantaneous Euler rotations). Therefore

$$
\boldsymbol{\omega}_d = \dot{\phi}_d \hat{\boldsymbol{e}}_{x,1'} + \dot{\vartheta}_d \hat{\boldsymbol{e}}_{y,1''} + \dot{\psi}_d \hat{\boldsymbol{e}}_{z,2}
$$

This basis is not orthonormal and it is difficult to use, but now the velocity vector can be changed to the fixed frame or to the moving frame with just a change of bases. Such rotation takes the nomenclature $1 - 2 - 3$ given the respective axis

rotation on the three reference frame. For example in $\mathcal{R}_1'$, or alternatively, in $\mathcal{R}_1$ since those reference frames are aligned but rigidly transposed

$$\begin{pmatrix} \omega_{d,x} \\ \omega_{d,y} \\ \omega_{d,z} \end{pmatrix} = \begin{pmatrix} 1 & 0 & -\sin\vartheta_d \\ 0 & \cos\phi_d & \cos\vartheta_d\sin\phi_d \\ 0 & -\sin\phi_d & \cos\vartheta_d\cos\phi_d \end{pmatrix} \begin{pmatrix} \dot{\phi}_d \\ \dot{\vartheta}_d \\ \dot{\psi}_d \end{pmatrix} \tag{5.5}$$

and vice-versa,

$$\begin{pmatrix} \dot{\phi}_d \\ \dot{\vartheta}_d \\ \dot{\psi}_d \end{pmatrix} = \begin{pmatrix} 1 & \sin\phi_d\tan\vartheta_d & \cos\phi_d\tan\vartheta_d \\ 0 & \cos\phi_d & \sin\vartheta_d \\ 0 & \sin\phi_d/\cos\vartheta_d & \cos\phi_d/\cos\vartheta_d \end{pmatrix} \begin{pmatrix} \omega_{d,x} \\ \omega_{d,y} \\ \omega_{d,z} \end{pmatrix} \tag{5.6}$$

For small angles is it possible to see that the transformation matrix becomes identical. And such:

$$\begin{pmatrix} \dot{\phi}_d \\ \dot{\vartheta}_d \\ \dot{\psi}_d \end{pmatrix} \cong \begin{pmatrix} \omega_{d,x} \\ \omega_{d,y} \\ \omega_{d,z} \end{pmatrix}$$
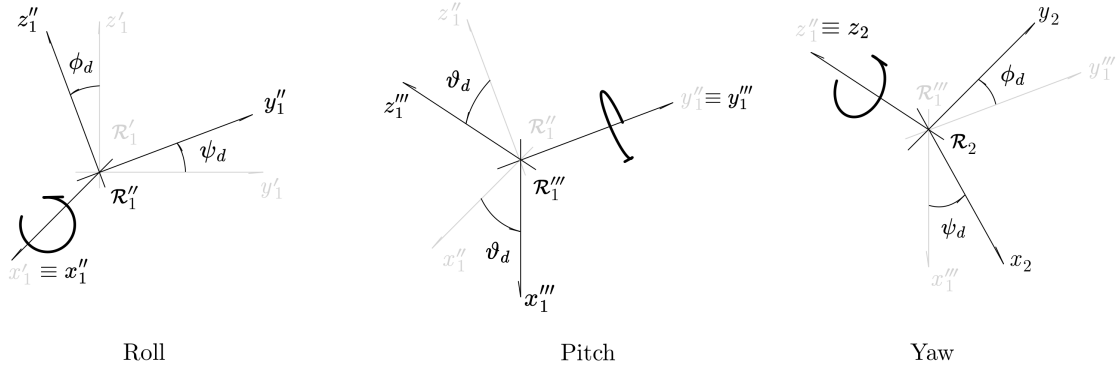
Figure 5.2: Roll-Pitch-Yaw angle representation.

5.1.3　Misalignments

The definition of the center of docking heavily relies on the concept of *misalignments*, both expressed in terms of positional misalignments (x_d, y_d, z_d) and angular misalignments $(\phi_d, \vartheta_d, \psi_d)$. The following table denotes the meanings of those misalignment errors. For a land vehicle (like a LPR) the following basic considerations should be addressed:

1. the presence of a **terrain** inserts a physical barrier that could not be trespassed; unlike a docking maneuver in space, this adds an additional parameter that needs to be taken into consideration;

2. the presence of **gravity** also affects the fact that some symmetries presented in micro-gravitational environment cannot be restored (for instance, the complete axial symmetry of the chaser and target is lost, because a vehicle cannot dock upside down, since gravity imposes an "up" and "down" direction).

Table 5.1 shows the effects of those misalignments for a ground vehicle docking system. The two vehicles are spaced in this representation to show the various misalignments.

Type	Representation	Misalignment type	Solution
TRANSLATION		Translation x	Approach / Distancing $\leftrightarrow$ (coupled with wheels)
		Translation y	Passive/Active solution required
		Translation z	Presence of a ground surface
ROTATION		Rotation x	Presence of a ground surface
		Rotation y	Presence of gravity
		Rotation z	Passive/Active solution required

Table 5.1: Misalignment representation of the various degrees of freedom of a docking subsystem.

5.1.4   Decoupling

The misalignments considerations bring the attention to an important aspect of a docking system designed for land vehicles. If the following hypothesis hold true:

1. the system is considered rigid;

2. the terrain in which the vehicle operates is smooth enough.

The mechanics of the system could be **decoupled** in a longitudinal motion (in the $yz-$plane of the frame $\mathcal{R}_1, \mathcal{R}_2$ respectively) and a latero-directional motion (in the $xy-$axis of the frame $\mathcal{R}_1, \mathcal{R}_2$ respectively).
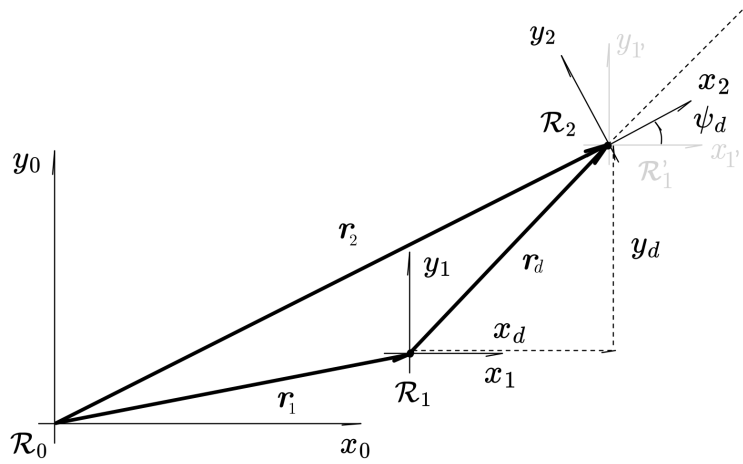
Figure 5.3: Bidimensional center of docking representation.

The two proposed hypothesis for the decoupling need to be verified. Real materials are not infinitely rigid, and some are very flexible (like tyres). Lunar terrain, mainly composed of regolith is both soft and extremely irregular. Therefore, this decoupling process is considered as a first approximation that needs to be later extended to the general case, including those physical effects.

In this context, the relative state of the two systems can be described by 3 parameters, (x_d, y_d, ψ_d). The trajectory simply becomes

$$\gamma : \begin{cases} x_d = x_d(t) \\ y_d = y_d(t) \\ \psi_d = \psi_d(t) \end{cases}$$

with an angular velocity that reduces to

$$\boldsymbol{\omega}_d = \dot{\psi}_d \hat{\boldsymbol{e}}_{z,1}$$
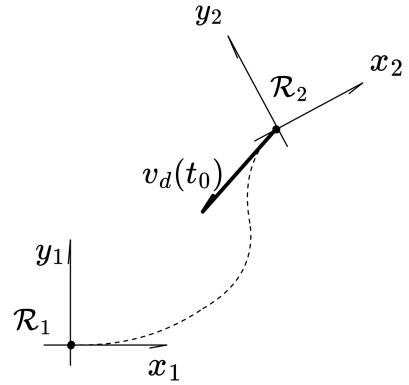
5.1.5 Analogy with center of mass and pressure

The concept of the center of docking introduced in this work presents a strong analogy with the **center of pressure** in aerodynamics and the **center of mass** in mechanics. In aerodynamics, the center of pressure represents the point where the resultant aerodynamic force acts, effectively summarizing the distributed pressure forces into a single equivalent force. Similarly, in mechanics, the center of mass is the unique point where the total mass of a system can be considered to be concentrated for the purpose of analyzing translational motion. Extending this reasoning to docking mechanics, the center of docking represents the critical reference point through which the docking kinematics of two bodies can be described. Each body, whether chaser or target, possesses its own center of docking, defined in an inertial reference frame. The alignment of these centers, expressed mathematically as Equation 5.1, Equation 5.2, parallels the equilibrium conditions seen in both aerodynamics and mechanics - wherein forces or mass distributions are effectively condensed into a single representative location. Just as the center of pressure determines the aerodynamic stability of a vehicle and the center of mass dictates its inertial response, the center of docking governs the stability and success of the docking process. If the alignment condition is maintained over time, docking is achieved, much like how equilibrium conditions in aerodynamics and mechanics ensure stability in their respective domains. This analogy highlights the unifying principle of a singular, effective point that encapsulates the complex interactions within a system and facilitates both theoretical understanding and practical implementation in docking maneuvers.

5.2   Dynamics

Once the respective references are defined, the dynamics of the complete system is investigated. The kinematical considerations address the complete understanding of the vehicle dynamics and how it relates to the docking one.

5.2.1   Rigid Vehicle Dynamics

Like traditional docking systems, the mechanics of the vehicles are intrinsically linked with the docking mechanism. Examples of this can be found during docking maneuvers in spacecrafts [25] as well as in other vehicles (i.e. submarines or military aircrafts). Understanding the general mechanics of the vehicle is essential to provide an idea on how both the LPR and the docking subsystem would respond to external disturbances.
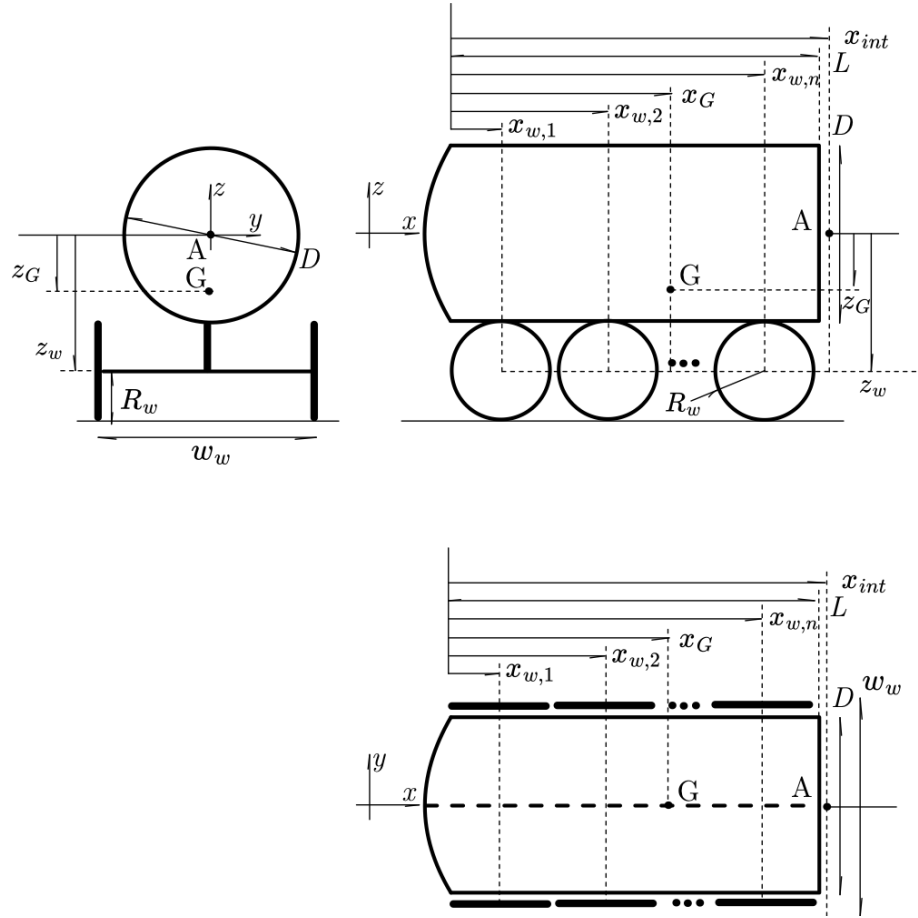
Figure 5.4: Reference frame used for the dynamics of the rigid vehicle.

Through this work, various assumptions will be made about the model that is going to be implemented. If no additional information is listed, the following hypothesis should be considered:

1. the rover is a ***rigid body*** of constant mass, where all the forces and torques can be located in the center of mass G.

$$m_{tot}\, \boldsymbol{a}_G = \sum_k \boldsymbol{F}_k = \boldsymbol{F} \qquad \frac{d\boldsymbol{H}_G}{dt} = \sum_k \boldsymbol{M}_{G,k} = \boldsymbol{M}_G$$

where m_{tot} is the total mass, $\boldsymbol{a}_G$ is the acceleration, $\boldsymbol{F}$ is the total force and $\boldsymbol{H}_G, \boldsymbol{M}_G$ are the angular momentum and the total torque (with respect to G).

2. The considered actions (forces and torques) are considered as point-acting.

Both of those assumptions will be discarded once the model is better refined. Usually, the dynamics of the vehicles will be presented in the center of mass reference frame $\mathcal{R}_G \neq \mathcal{R}_2$ as shown in the picture.

Rectilinear motion

Assuming that the terrain is rectilinear, the rover follows the current state of motion
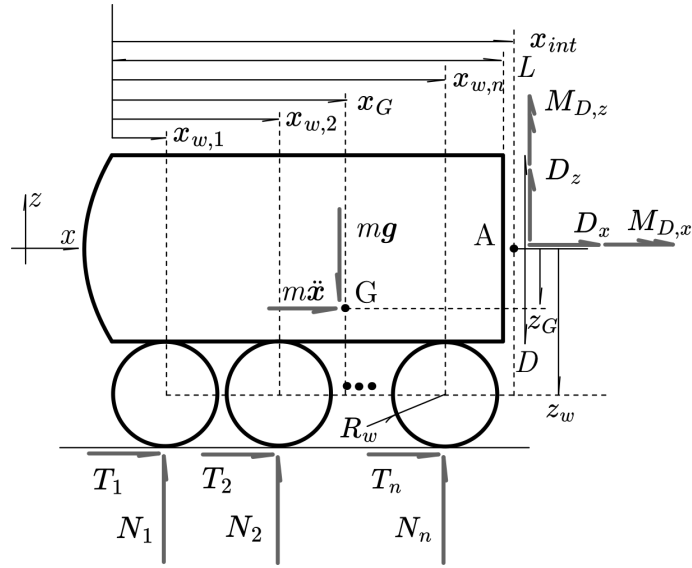
Figure 5.5: Rectilinear motion free body diagram.

$$
\begin{cases}
\rightarrow x : -\sum_{k=1}^{n_w/2} \left(T_k^{(r)} + T_k^{(\ell)} \right) + m\ddot{x} + D_x = 0 \\
\rightarrow y : D_y = 0 \\
\rightarrow z : \sum_{k=1}^{n_w/2} \left(N_k^{(r)} + N_k^{(\ell)} \right) - mg + D_z = 0 \\
\circlearrowleft x : M_{D,x} = 0 \\
\circlearrowleft y : \sum_{k=1}^{n_w/2} \left(N_k^{(r)} + N_k^{(\ell)} \right) \cdot (x_G - x_{w,k}) + \\
\qquad + \sum_{k=1}^{n_w/2} \left(T_k^{(r)} + T_k^{(\ell)} \right) \cdot (z_w + R_w) + D_z \cdot (x_G - x_{int}) + M_{D,y} = 0 \\
\circlearrowleft z : D_y \cdot (x_G - x_{int}) + M_{D,z} = 0
\end{cases}
\tag{5.7}
$$

where $D_i, M_{D,i}$ are the docking actions (forces and torques) exchanged with the docking system in the point of interface between the docking subsystem and the rest of the vehicle, $N_k^{(j)}$ are the terrain normal forces (k : wheel number, j: subscript

for (ℓ) and (r), left and right respectively), mg is the weight, $m\ddot{x}$ is the inertial force along the direction of motion, and $T_k^{(j)}$ are the traction forces (left and right), whose equation are given by the internal equilibrium of the wheel

$$\circlearrowleft \text{wheel} : T_k^j \cdot R_w - C_k^j = 0$$

Given acting torques as inputs and initial conditions, the complete rover's trajectory can be completely resolved. Even in this simple case an interesting observation comes from the interaction of the tire with the soil. Such dynamics will be explored in the following chapter.

Longitudinal inclined motion

If the terrain is not planar, the dynamics of the rover can be expressed as follows.

Figure 5.6: Longitudinal inclined motion.

$$\begin{cases} \rightarrow x : -\sum_{k=1}^{n_w/2} \left(T_k^{(r)} + T_k^{(\ell)} \right) + m\ddot{x} + D_x + mg\sin\zeta_{inc} = 0 \\ \rightarrow y : D_y = 0 \\ \rightarrow z : \sum_{k=1}^{n_w/2} \left(N_k^{(r)} + N_k^{(\ell)} \right) - mg\cos\zeta_{inc} + D_z = 0 \\ \circlearrowleft x : M_{D,x} = 0 \\ \circlearrowleft y : \sum_{k=1}^{n_w/2} \left(N_k^{(r)} + N_k^{(\ell)} \right) \cdot (x_G - x_{w,k}) + \\ \qquad + \sum_{k=1}^{n_w/2} \left(T_k^{(r)} + T_k^{(\ell)} \right) \cdot (z_w + R_w) + D_z \cdot (x_G - x_{int}) + M_{D,y} = 0 \\ \circlearrowleft z : D_y \cdot (x_G - x_{int}) + M_{D,z} = 0 \end{cases} \tag{5.8}$$

given ζ_{inc} the longitudinal inclination angle of the plane. As before, a crucial observation should be made about the number of wheels imposed n_w. For a four-wheeled vehicle (like a car) even if the terrain is not sufficiently smooth, all the wheels should lay on ground, because an ideal ground plane can be inserted (assuming the tires are stiff enough) passing between the assumed point of contact of the wheels. With more than 4 wheels this argument is not true (two points identify uniquely a line, not three). Hence the dynamics is a bit more complex if one has to consider which couple of wheels is the drive wheel and which isn't.
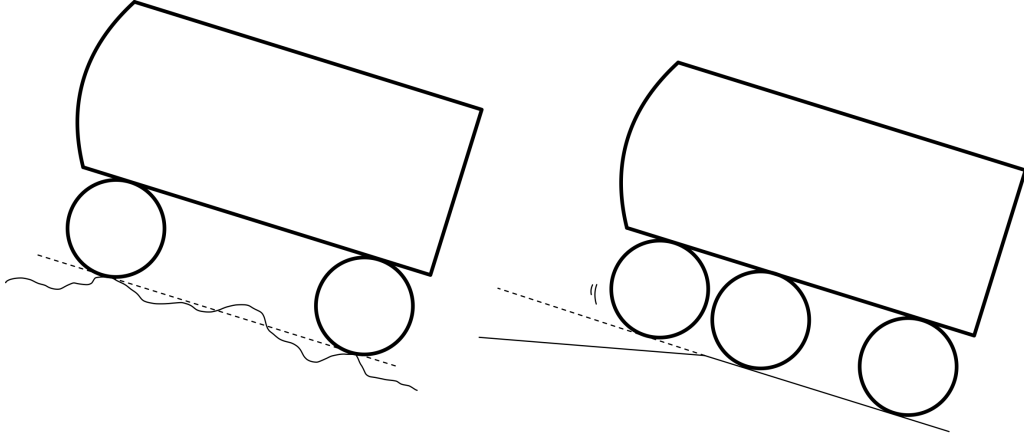
Figure 5.7: Terrain adhesion difference between a four wheeled design (left) and a six (or more) wheeled design (right).

Lateral inclined motion

The lateral inclined motion problem yields the following.
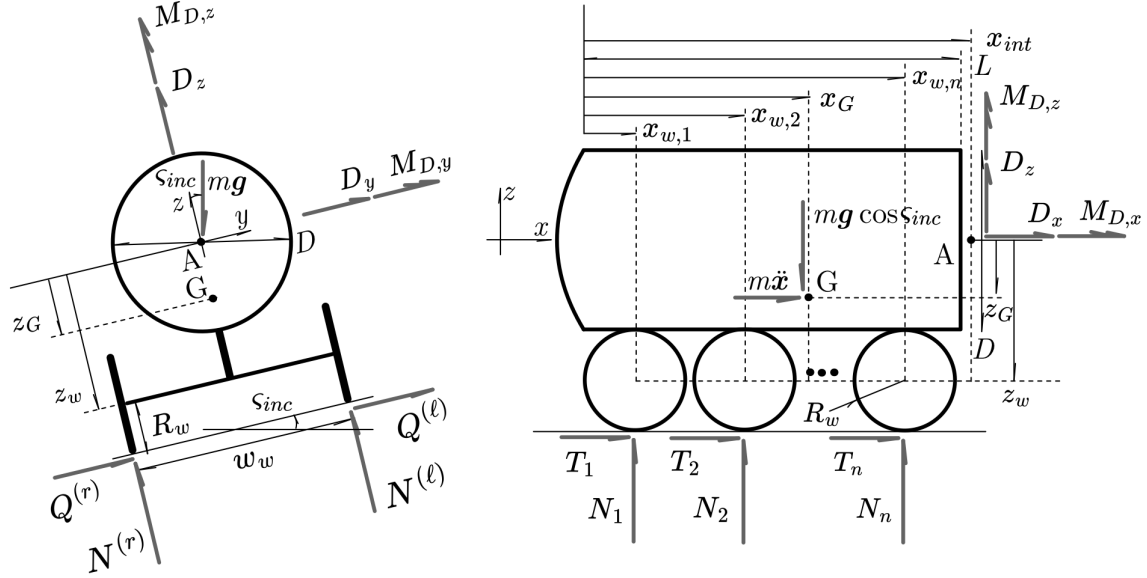
Figure 5.8: Lateral inclined motion

$$
\begin{cases}
\rightarrow x : -\sum_{k=1}^{n_w/2} \left(T_k^{(r)} + T_k^{(\ell)} \right) + m\ddot{x} + D_x = 0 \\[2mm]
\rightarrow y : \sum_{k=1}^{n_w/2} \left(Q_k^{(r)} + Q_k^{(\ell)} \right) - mg\sin\varsigma_{inc} + D_y = 0 \\[2mm]
\rightarrow z : \sum_{k=1}^{n_w/2} \left(N_k^{(r)} + N_k^{(\ell)} \right) - mg\cos\varsigma_{inc} + D_z = 0 \\[2mm]
\circlearrowleft x : \sum_{k=1}^{n_w/2} \left(Q_k^{(r)} + Q_k^{(\ell)} \right) \cdot (z_w + R_w) + M_{D,x} = 0 \\[2mm]
\circlearrowleft y : \sum_{k=1}^{n_w/2} \left(N_k^{(r)} + N_k^{(\ell)} \right) \cdot (x_G - x_{w,k}) + \\[2mm]
\qquad + \sum_{k=1}^{n_w/2} \left(T_k^{(r)} + T_k^{(\ell)} \right) \cdot (z_w + R_w) + D_z \cdot (x_G - x_{int}) + M_{D,y} = 0 \\[2mm]
\circlearrowleft z : -\sum_{k=1}^{n_w/2} \left(Q_k^{(r)} + Q_k^{(\ell)} \right) \cdot (x_G - x_{w,k}) + D_y \cdot (x_G - x_{int}) + M_{D,z} = 0
\end{cases}
\tag{5.9}
$$

given ς_{inc} the lateral inclination angle of the plane and Q_k^j the lateral friction interactions. In this case, the new friction actions prevent the vehicle from slipping. Alternatively, the inertia of the rover marks the maximum lateral inclination angle a vehicle can hold without losing adhesion on the ground.

General inclined motion

The general inclination case is the following, which addresses all observations listed above.

$$
\begin{cases}
\rightarrow x : -\sum_{k=1}^{n_w/2} \left(T_k^{(r)} + T_k^{(\ell)} \right) + m\ddot{x} + mg \cos\varsigma_{inc} \sin\zeta_{inc} + D_x = 0 \\[2ex]
\rightarrow y : \sum_{k=1}^{n_w/2} \left(Q_k^{(r)} + Q_k^{(\ell)} \right) - mg \sin\varsigma_{inc} + D_y = 0 \\[2ex]
\rightarrow z : \sum_{k=1}^{n_w/2} \left(N_k^{(r)} + N_k^{(\ell)} \right) - mg \cos\varsigma_{inc} \cos\zeta_{inc} + D_z = 0 \\[2ex]
\circlearrowleft x : \sum_{k=1}^{n_w/2} \left(Q_k^{(r)} + Q_k^{(\ell)} \right) \cdot (z_w + R_w) + M_{D,x} = 0 \\[2ex]
\circlearrowleft y : \sum_{k=1}^{n_w/2} \left(N_k^{(r)} + N_k^{(\ell)} \right) \cdot (x_G - x_{w,k}) + \\[2ex]
\qquad + \sum_{k=1}^{n_w/2} \left(T_k^{(r)} + T_k^{(\ell)} \right) \cdot (z_w + R_w) + D_z \cdot (x_G - x_{int}) + M_{D,y} = 0 \\[2ex]
\circlearrowleft z : -\sum_{k=1}^{n_w/2} \left(Q_k^{(r)} + Q_k^{(\ell)} \right) \cdot (x_G - x_{w,k}) + D_y \cdot (x_G - x_{int}) + M_{D,z} = 0
\end{cases}
\tag{5.10}
$$

Turning

Turning is the maneuver needed to accomplish a certain curve during trajectory. This maneuver strictly depends on the steering mechanism inserted. Given [26], the Ackermann steering mechanism was chosen as a suitable steering mechanism for the problem.
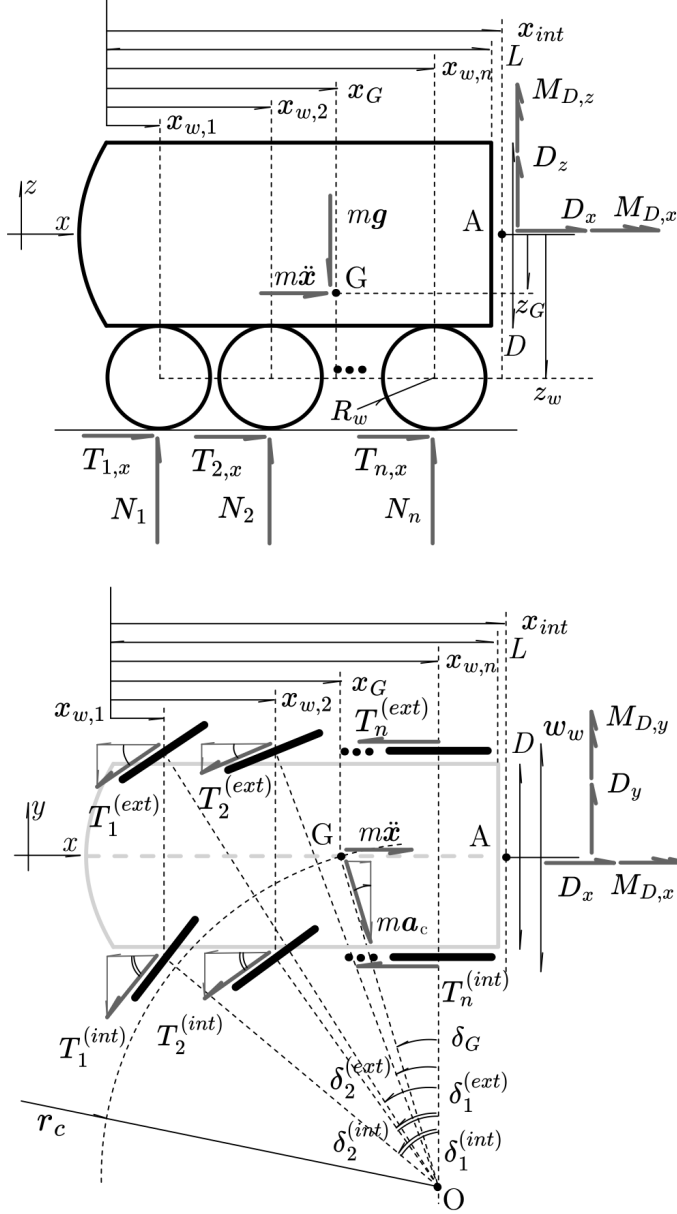
The Ackermann angles follow the following kinematical equations:

$$\begin{cases} \tan \delta_k^{(int)} = \dfrac{x_{w,3} - x_{w,k}}{r_c - w_w/2} \\ \tan \delta_k^{(ext)} = \dfrac{x_{w,3} - x_{w,k}}{r_c + w_w/2} \end{cases}$$

given r_c the turning radius of curvature with respect to the turning center O and w_w the spacing between the wheels. The imposition of those turning angles determines:

1. a decomposition of traction forces:

$$\begin{cases} T_{k,x}^j = T_k^j \cos \delta_k^j \\ T_{k,y}^j = T_k^j \sin \delta_k^j \end{cases}$$

2. a **centripetal force** that points to O:

$$a_c = \frac{v_x^2}{r_c}$$

Figure 5.9: Ackermann Steering Mechanism.

The centripetal force can be itself decomposed along the x and y axis given the following

$$\begin{cases} \tan \delta_G = \dfrac{x_{w,3} - x_G}{r_c} \\ a_{c,x} = a_c sin\delta_G \\ a_{c,y} = -a_c cos\delta_G \end{cases}$$

The equations therefore yield the following

$$
\begin{cases}
\rightarrow x : -\sum_{k=1}^{n_w/2} \left(T_{k,x}^{(int)} + T_{k,x}^{(ext)} \right) + m\ddot{x} + D_x + ma_c \sin \delta_G = 0 \\[2mm]
\rightarrow y : -\sum_{k=1}^{n_w/2} \left(T_{k,y}^{(int)} + T_{k,y}^{(ext)} \right) + D_y - ma_c \cos \delta_G = 0 \\[2mm]
\rightarrow z : \sum_{k=1}^{n_w/2} \left(N_k^{(int)} + N_k^{(ext)} \right) - mg + D_z = 0 \\[2mm]
\circlearrowleft x : M_{D,x} = 0 \\[2mm]
\circlearrowleft y : \sum_{k=1}^{n_w/2} \left(N_k^{(int)} + N_k^{(ext)} \right) \cdot (x_G - x_{w,k}) + \\[2mm]
\quad + \sum_{k=1}^{n_w/2} \left(T_k^{(int)} + T_k^{(ext)} \right) \cdot (z_w + R_w) + D_z \cdot (x_G - x_{int}) + M_{D,y} = 0 \\[2mm]
\circlearrowleft z : -\sum_{k=1}^{n_w/2} \left(T_k^{(int)} \cdot \frac{r_c - w_w/2}{\cos \delta_k^{(int)}} + T_k^{(ext)} \cdot \frac{r_c + w_w/2}{\cos \delta_k^{(ext)}} \right) + \\[2mm]
\quad + m\ddot{x}r_c + D_y \cdot (x_3 - x_{int}) + M_{D,z} = 0
\end{cases}
\tag{5.11}
$$

where the last equation was performed around O instead of G.

5.2.2 Target dynamics

Target dynamics depend on the interaction of the target with the chaser (i.e. the vehicle) and the surrounding environments. Traditional space docking systems conceive a docking maneuver in which the target is moving. In this case, the performed assumption is that the target remains solidly fixed with terrain.

If $\mathcal{R}_0$ is chosen to be congruent with the terrain (a fair assumption that the ground is inertial, given the scales) and $\mathcal{R}_1$ is the target center of docking frame, it is possible to find a particular **rigid** and **inertial** transformation between the two frames, such that the quantities expressed in $\mathcal{R}_0$ can be also expressed in $\mathcal{R}_1$. In other terms, if the target is considered linked with the terrain, both $\mathcal{R}_0$ and $\mathcal{R}_1$ can be treated interchangeably. Given this assumption, the initial condition on the target is that:

$$
\boldsymbol{r}_1(t_0) = \boldsymbol{r}_{1,0} \quad \boldsymbol{v}_1(t_0) = 0 \quad \boldsymbol{a}_1(t_0) = 0
$$

Those quantities can vary depending on the momentum transferred from the chaser to the target during docking and act as momentary shocks. Once the docking procedure is finished, it is requested that those quantities come back to the initial condition (i.e. the target has not started moving).

$$
\boldsymbol{r}_1(t_f) = \boldsymbol{r}_{1,0} \quad \boldsymbol{v}_1(t_f) = 0 \quad \boldsymbol{a}_1(t_f) = 0
$$

Therefore, the final condition of the docking requires

$$
\boldsymbol{r}_d(t_f) = 0 \quad \boldsymbol{v}_d(t_f) = 0 \quad \boldsymbol{a}_d(t_f) = 0
$$

5.3 Inital conditions specifications

A key specification that needs to be discussed in this process is the one regarding the initial condition of the docking subsystem. The following is a collection of initial condition specifications borrowed from the previous docking architectures based on [18], [25].

Category	Name	Symbol	STRONG Mission (STEPS)	OECS	IBDM	IDSS	Un.
Translational misalignment	Lateral y	$y_d(t_0)$	± 0.05	± 0.058	± 0.05	± 0.01	m
	Lateral z	$z_d(t_0)$	± 0.05	± 0.058	± 0.05	± 0.01	m
Relative translational velocity	Long. x	$\dot{x}_d(t_0)$	± 0.03	< 0.03	$\pm 0.05 \div 0.1$	$\pm 0.05 \div 0.1$	m/s
	Lateral y	$\dot{y}_d(t_0)$	± 0.01	$-$	± 0.01	± 0.04	m/s
	Lateral z	$\dot{z}_d(t_0)$	± 0.01	$-$	± 0.01	± 0.04	m/s
Angular misalignment	Long. x	$\phi_d(t_0)$	± 3	± 5	± 5	± 4	$^\circ$
	Lateral y	$\vartheta_d(t_0)$	± 3	± 5	± 5	$\pm 4^1$	$^\circ$
	Lateral z	$\phi_d(t_0)$	± 3	± 5	± 5	$\pm 4^1$	$^\circ$
Relative angular velocity	Long. x	$\dot{\psi}_d(t_0)$	± 0.1	$-$	± 0.5	± 0.2	$^\circ/s$
	Lateral y	$\dot{\vartheta}_d(t_0)$	± 0.1	$-$	± 0.15	$\pm 0.2^1$	$^\circ/s$
	Lateral z	$\dot{\phi}_d(t_0)$	± 0.1	$-$	± 0.15	$\pm 0.2^1$	$^\circ/s$

Table 5.2: Technical specifications regarding relative misalignments and velocities between the spacecrafts used to design the listed missions.

Based on this specifications, the following table is proposed for the PROTEUS mission, aligning with the current state of pressurized manned docking mechanisms.

Category	Name	Symbol	PROTEUS	Un.
Translational misalignment	Lateral y	$y_d(t_0)$	± 0.01	m
	Lateral z	$z_d(t_0)$	± 0.01	m
Relative translational velocity	Longitudinal x	$\dot{x}_d(t_0)$	$\pm 0.05 \div 0.1$	m/s
	Lateral y	$\dot{y}_d(t_0)$	± 0.04	m/s
	Lateral z	$\dot{z}_d(t_0)$	± 0.04	m/s
Angular misalignment	Longitudinal x	$\phi_d(t_0)$	± 5	$^\circ$
	Lateral y	$\vartheta_d(t_0)$	$\pm 5^1$	$^\circ$
	Lateral z	$\psi_d(t_0)$	$\pm 5^1$	$^\circ$
Relative angular velocity	Longitudinal x	$\dot{\phi}_d(t_0)$	± 0.02	$^\circ/s$
	Lateral y	$\dot{\vartheta}_d(t_0)$	$\pm 0.2^1$	$^\circ/s$
	Lateral z	$\dot{\psi}_d(t_0)$	$\pm 0.2^1$	$^\circ/s$

Table 5.3: Technical specifications regarding relative misalignments and velocities between the spacecrafts used to design the PROTEUS mission.

The following table is used to define the misalignment requirements in chapter 7. Particular attention is dedicated to the longitudinal angular velocity (roll velocity)

---

[1]Vector sum of y and z misalignments.

which is smaller compared to the space counterparts given the presence of terrain. As proposed in Table 5.1, even for rough terrains, the "roll" state of the LPR is not a problem.

Chapter 6

Contact mechanics

Contact mechanics examines the behavior of surfaces in contact under various loads, focusing on forces, stresses, and deformations. In lunar exploration, it is crucial for optimizing both the docking system in the alignment phase and rover mobility, traction, and durability on challenging terrains. This chapter outlines the key principles of contact mechanics and their applications to homogeneous continuums, to wheel-soil interaction and load distribution in mechanical systems. The sources for the following chapter are [27], [28], [29], [30].

6.1 Kinematics of contact

Consider the non-conformal contact problem shown in the figure, where two bodies identified by subscripts 1 and 2, respectively, make initial contact at the point O. So far, no forces have been applied and the contact is restricted to a single point.
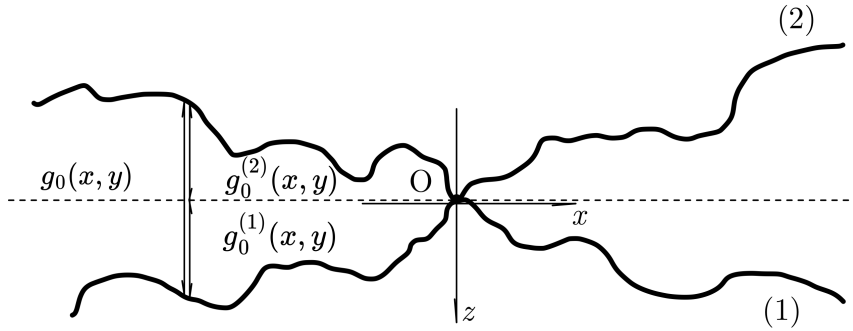
Figure 6.1: Initial gap between the bodies.

If the profiles of the bodies are smooth, it is possible to identify a common tangent plane at the point of contact and a common normal. Points in the tangent plane will be defined by Cartesian coordinates (x, y) and choose the $z-$axis to point into body 1 as shown. The undeformed profiles of the bodies can then be defined by the functions $g_0^{(1)}(x, y)$ and $g_0^{(2)}(x, y)$. In many cases, it is possible to find that the contact problem depends on the geometry of the two bodies only through the composite initial gap function

$$g_0(x, y) = g_0^{(1)}(x, y) + g_0^{(2)}(x, y) \tag{6.1}$$

which is the gap between the bodies in the undeformed configuration illustrated, measured perpendicular to the tangent plane. It is also possible to define a simpler equivalent contact problem in which a body with a profile defined by makes contact with a **plane surface**.
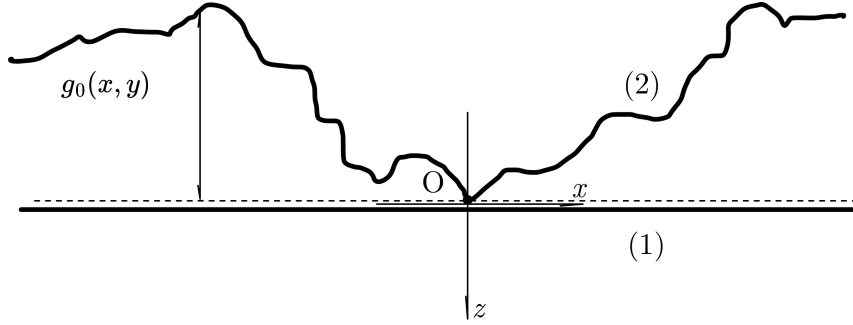
Figure 6.2: Re-definition of the problem as the contact between a plane (body (1)) and a surface $g_0(x, y)$ (body (2)).

6.1.1   Enstablishment of the contact region

Suppose now to push the two bodies together by a normal force P. If they were rigid, this would imply a concentrated reaction force between the bodies at O hence an infinite contact pressure (force per unit area). The bodies will therefore inevitably deform slightly, establishing a finite contact region $\mathcal{A}$, shown in figure.
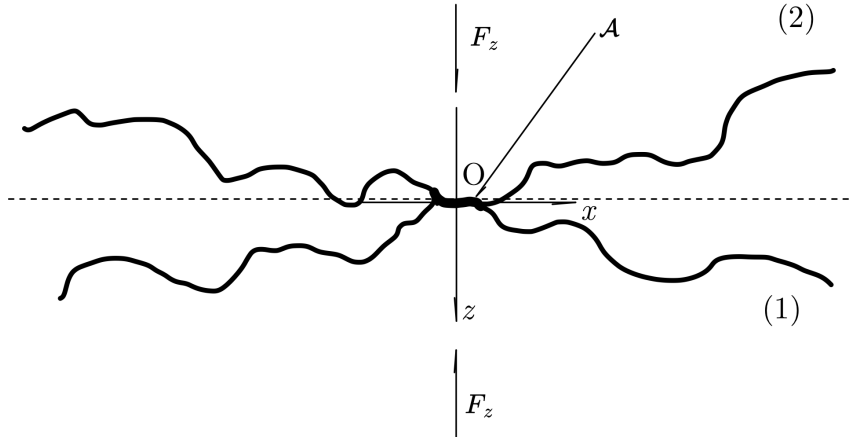
Figure 6.3: Contact region $\mathcal{A}$

In order to formulate the contact problem, one shall consider approaching this condition by two steps. In the first step, move the upper body downwardsi.e. along the common normalby some rigid-body displacement h. This will simply reduce the initial gap g_0 everywhere by h. One then superposes the deformation of the bodies, which is characterized through the surface displacements $u_z^{(1)}(x, y)$, $u_z^{(2)}(x, y)$. A vertically downward displacement of the lower body 1 will tend to increase the gap, whereas a downward displacement body 2 will decrease it. The final gap $g(x, y)$ is given by the expression

$$g(x, y) = g_0(x, y) - h + u_z^{(1)}(x, y) - u_z^{(2)}(x, y)$$
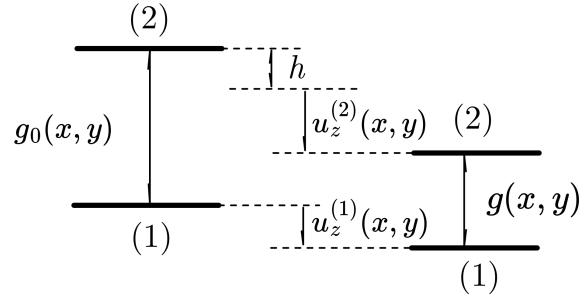
Figure 6.4: Description of the various terms forming the gap $g(x, y)$

6.1.2 Definition of contact

It is assumed that the bodies are not allowed to interpenetrate each other, so the gap cannot be negative. In fact, the *contact region* $\mathcal{A}$ is defined as the region in which the final gap is null. The rest of the interface is then the *separation region* $\tilde{\mathcal{A}}$ in which $g(x, y) > 0$. For simplicity, suppose that the contact is frictionless so that there is a purely normal pressure $p(x, y)$ transmitted between the bodies. With these definitions, one can establish a formal statement of the frictionless contact problem through the conditions

$$
\begin{cases} g(x, y) = 0 & \text{on} \quad \mathcal{A} \\ p(x, y) > 0 & \text{on} \quad \mathcal{A} \end{cases}
\qquad
\begin{cases} g(x, y) > 0 & \text{on} \quad \tilde{\mathcal{A}} \\ p(x, y) = 0 & \text{on} \quad \tilde{\mathcal{A}} \end{cases}
$$

Notice that everywhere $g(x, y) \cdot p(x, y) = 0$ for all (x, y) on the surface of the bodies.

6.2 Three-Dimensional frictionless elastic problems

To complete the formulation of the problem, it is necessary to relate the contact pressure to the displacements. The following assumptions are made:

1. the strains are everywhere small;

2. the superposition principle can be applied;

3. An Eulerian kinematics holds i.e. the deformations can be referred to the original undeformed configuration.

It has already been remarked that the contact area is generally small and hence that the strains due to contact forces are concentrated in a small region. It follows that the exact geometry of the bodies a long way away from the contact region is relatively unimportant, since these regions experience at most a rigid-body motion. It is therefore possible to simplify the problem considerably by assuming that the body extends to infinity. In most cases, it is also possible to simplify the elasticity problem by assuming that the deformations due to a given traction distribution are the same as those that would be produced in an equivalent body with a *plane surface*.

6.2.1   Normal Loading of the Half-Space

If an isotropic half-space $z > 0$ is loaded on normal tractions so that

$$\sigma_{xz}(x, y, 0) = \sigma_{zx}(x, y, 0) = 0$$

for all x, y, the elastic stress field can conveniently be expressed in terms of a single potential function φ satisfying

$$\nabla^2 \varphi = 0$$

(solution proposed by [28], Sect. 5.7). In particular, the normal traction and the normal displacement at the surface $z = 0$ are given by

$$\sigma_{zz}(\rho, \vartheta, 0) = -\frac{\partial^2 \varphi}{\partial z^2} \quad u_z(\rho, \vartheta, 0) = -\frac{1 - \nu}{G} \frac{\partial \varphi}{\partial z}$$

The fundamental problem for the frictionless half-space is that in which the only loading comprises a concentrated normal force $F_z = P$ acting at a point which one can take as the origin.
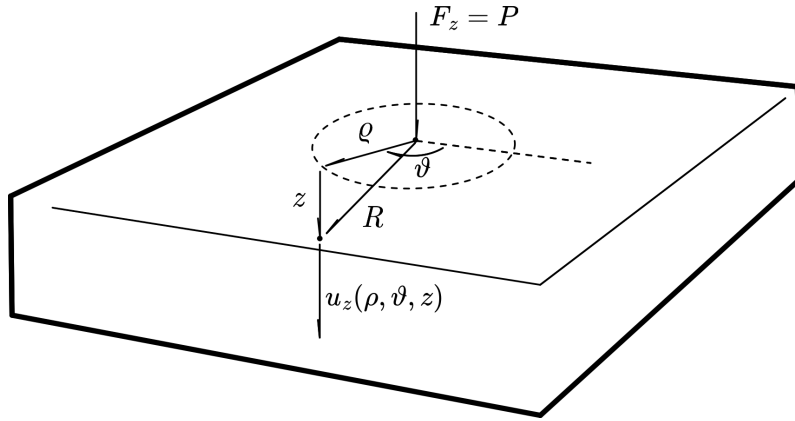
Figure 6.5: Point force in half space elastic medium.

If the material is isotropic, the stress and displacement fields will be axisymmetric and hence functions of ρ and z only. In particular, the normal surface displacement $u_z(\rho, \vartheta, 0)$ as a function of the distance ρ from the point of application of the force. The complete stress and displacement field for this problem can be obtained by substituting the harmonic function [27]:

$$\varphi = -\frac{P}{2\pi} \log (R + z)$$

where $R = \sqrt{\rho^2 + z^2}$. This yields, inside the medium

$$\sigma_{zz}(\rho, \vartheta, z) = z \frac{\partial^3 \varphi}{\partial z^3} - \frac{\partial^2 \varphi}{\partial z^2} = -\frac{3Pz^3}{2\pi R^5}$$

To verify that this corresponds to a concentrated normal force, one considers the equilibrium of the layer $z \in (0, h)$. The radial tractions $\sigma_{z\rho}(\rho, \vartheta, h)$ on the bottom surface $z = h$ are axisymmetric and hence self-equilibrating, but the normal tractions sum to a resultant force in the z-direction equal to

$$2\pi \int_0^{+\infty} \sigma_{zz}(\rho, \vartheta, h) r \, dr = \int_0^{+\infty} \frac{3Ph^3}{2\pi \sqrt{(r^2 + h^2)^{5/2}}} r \, dr = -P$$

which is independent of h. Thus, to maintain equilibrium of the layer, there must be a concentrated force P in the $z-$direction at the origin, as shown. Using the definition of displacement

$$u_z(r, \theta, 0) = \frac{P(1 - \nu)}{2\pi G r}$$

6.2.2 The composite elastic modulus

The kinematic contact conditions involve only **relative displacement**

$$u_z(x, y) = u_z^{(1)}(x, y) + u_z^{(2)}(x, y)$$

Except where otherwise stated, one shall assume in this work that the materials are isotropic, in which case

$$u_z(x, y) = \frac{P}{\pi E^* r}$$

where

$$\frac{1}{E^*} = \frac{1 - \nu_1}{2G_1} + \frac{1 - \nu_2}{2G_2} = \frac{1 - \nu_1^2}{E_1} + \frac{1 - \nu_2^2}{E_2}$$

This is the only point at which the modulus of the materials enters into the calculation, and hence the separate properties only influence the contact problem through their contribution to E^*. In particular, for any given frictionless contact problem, one can always define an equivalent problem in which one of the two bodies is taken to be rigid (e.g. $E_2 \to +\infty$), in which case E^* is the plane strain modulus of the remaining fictitious deformable material, and $u_z(x, y)$ is its normal surface displacement. One shall generally make use of this simplification wherever possible.

6.2.3 Integral equation

Since the elastic problem is linear, additional solutions can be obtained by superposition. The displacement field is therefore

$$u_z(x, y) = \frac{1}{\pi E^*} \int_{\mathcal{A}} p(\xi, \eta) \frac{d\xi d\eta}{r(\xi, \eta)}$$

where $r(\xi, \eta) = \sqrt{(x - \xi)^2 + (y - \eta)^2}$. Using this definition in the contact area, where

$$u_z(x, y) = h - g_0(x, y) \quad \text{on} \quad \mathcal{A}$$

$$\frac{1}{\pi E^*} \int_{\mathcal{A}} p(\xi, \eta) \frac{d\xi d\eta}{r(\xi, \eta)} = h - g_0(x, u) \quad \text{on} \quad \mathcal{A}$$

in many contact problems, the contact force

$$P = \int_{\mathcal{A}} p(x, y)\, dxdy$$

is prescribed and the rigid body h is unknown. In fact, there is one extra unknown and one extra equation. Evaluation of the integral is complicated by the presence of the square root term representing the distance $r(\xi, \eta)$. A more convenient integral form can be obtained by choosing the field point $A(x, y)$ as the origin of a system of polar coordinates (r, θ).

$$u_z(x, y) = \frac{1}{\pi E^*} \int_0^\pi \int_{S_1(\theta)}^{S_2(\theta)} p(r, \theta) dr d\theta$$

where the points S_1, S_2 define the intersections between a line through P and of inclination θ and S_1, S_2 the boundary of the contact area.
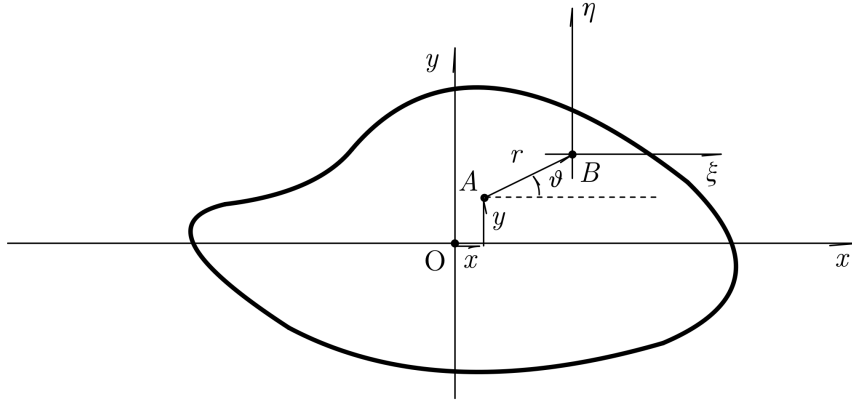
Figure 6.6: Field point integration.

6.2.4   Indentation by a Flat Elliptical Punch

The integration is particularly straightforward if the contact area is defined by an ellipse

$$\mathcal{A} = \left\{ (x, y) : \frac{x^2}{a^2} + \frac{y^2}{b^2} < 1 \right\}$$

and the pressure is of the form

$$p(x, y) = p_0 \left(1 - \frac{x^2}{a^2} - \frac{y^2}{b^2} \right)^{-1/2}$$

corresponding to a total force of

$$P = \int_{-a}^{a} \int_{-b\sqrt{1-x^2/a}}^{+b\sqrt{1-x^2/a}} p(x, y) dxdy = 2\pi p_0 ab$$

If the points $P = (x, y)$ and $Q = (\xi, \eta)$, then

$$\begin{cases} \xi = x + r cos\theta \\ \eta = y + r sin\theta \end{cases}$$
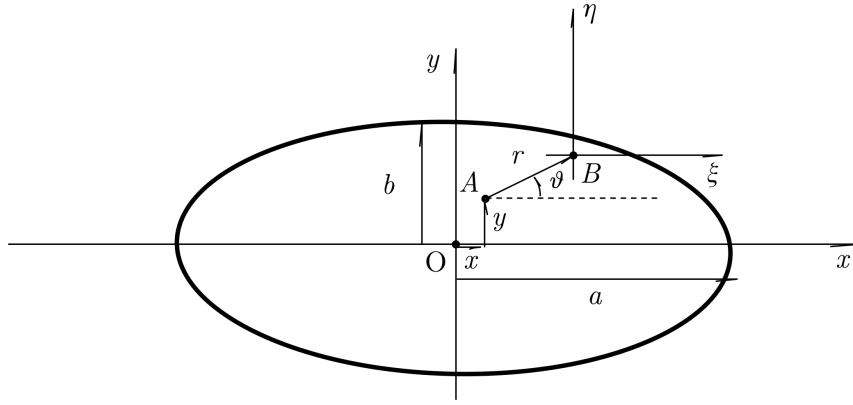
Figure 6.7: Elliptical contact area.

and

$$1 - \frac{\xi^2}{a^2} - \frac{\eta^2}{b^2} = C_0 - C_1(\theta)r - C_2(\theta)r^2$$

where

$$C_0 = 1 - \frac{x^2}{a^2} - \frac{y^2}{b^2}$$

$$C_1(\theta) = 2\left(\frac{x\cos\theta}{a^2} + \frac{y\sin\theta}{b^2}\right)$$

$$C_2(\theta) = \frac{\cos^2\theta}{a^2} + \frac{\sin^2\theta}{b^2} = \frac{1 - e^2\cos^2\theta}{b^2}$$

where e is the eccentricity of the ellipse

$$e = \sqrt{1 - \left(\frac{b}{a}\right)^2}$$

using this notation (demonstration in [27]), one obtains

$$u_z(x, y) = \frac{P}{E^*\pi a}K(e)$$

where $K(e)$ is the **complete elliptic integral of the first kind**

$$K(e) = \int_0^{\pi/2} \frac{d\theta}{\sqrt{1 - e^2\cos^2\theta}}$$

It should be noted that this expression is independent of x, y and hence of the position of the field point P, provided only that it lies within the ellipse. It follows that the contact pressure distribution under a flat rigid punch of elliptical planform is

$$p(x, y) = \frac{P}{2\pi ab}\left(1 - \frac{x^2}{a^2} - \frac{y^2}{b^2}\right)^{-1/2}$$

and the indentation depth (the punch has $g_0(x, y) = 0$)

$$h = u_z(x, y) = \frac{PK(e)}{\pi E^*a}$$

6.3   Hertzian Contact

If the contacting bodies are smooth, the gap function $g_0(x, y)$ can be expanded as a power series in x and y, for points sufficiently near to the origin. Furthermore, since the coordinate system satisfies the conditions

$$g_0(0,0) = \frac{\partial g_0}{\partial x}(0,0) = \frac{\partial g_0}{\partial y}(0,0) = 0$$

(the surface is smooth and tangent in $(0,0)$), the first non-zero terms in this series are the quadratic terms

$$g_0(x, y) = Ax^2 + By^2 + Cxy \tag{6.2}$$

with

$$\frac{\partial^2 g_0}{\partial x^2} = 2A \qquad \frac{\partial^2 g_0}{\partial y^2} = 2B \qquad \frac{\partial^2 g_0}{\partial x \partial y} = C$$

The elastic contact problem for a gap function defined above was first solved by Hertz (1882) and the resulting stress and displacement fields are generally referred to as **Hertzian contact**. The equation of contact yields

$$u_z(x, y) = h - g_0(x, y) = h - Ax^2 - By^2 - Cxy$$

6.3.1   Geometrical considerations

The coefficients of the above equation are given by

$$\frac{\partial^2 g_0}{\partial x^2} = 2A \qquad \frac{\partial^2 g_0}{\partial y^2} = 2B \qquad \frac{\partial^2 g_0}{\partial x \partial y} = C$$

Those functions define a two-dimensional *curvature tensor*. For any of the two surfaces $g_0^{(1)}, g_0^{(2)}$, in fact, it is possible to find a suitable **principal reference frame** $\left(x_1^{(k)}, x_2^{(k)}\right)$ [27], such as

$$g_0^{(k)}\left(x_1^{(k)}, x_2^{(k)}\right) = \frac{\left(x_1^{(k)}\right)^2}{2R_{x,1}^{(k)}} + \frac{\left(x_2^{(k)}\right)^2}{2R_{x,2}^{(k)}} \tag{6.3}$$

where the subscript (k) represent the two bodies respectively. This means that, in general, the two principal axis $\left(x_1^{(k)}, x_2^{(k)}\right)$ are not aligned between the two bodies. Defining α as the angle between first two axis

$$\alpha \; : \; \angle\left\{x_1^{(1)}, x_1^{(2)}\right\}$$

It is possible to define a coordintate system (x, y) in which the Equation 6.2 can be defined such so $C = 0$ and A, B are given by [27]:

$$\begin{cases} B + A = \dfrac{1}{2}\left(\dfrac{1}{R_{x,1}^{(1)}} + \dfrac{1}{R_{x,2}^{(1)}} + \dfrac{1}{R_{x,1}^{(2)}} + \dfrac{1}{R_{x,2}^{(2)}} \right) \\[3mm] |B - A| = \dfrac{1}{2}\left[\left(\dfrac{1}{R_{x,1}^{(1)}} - \dfrac{1}{R_{x,2}^{(1)}} \right)^2 + \left(\dfrac{1}{R_{x,1}^{(2)}} - \dfrac{1}{R_{x,2}^{(2)}} \right)^2 + \right. \\[3mm] \qquad \left. +2\left(\dfrac{1}{R_{x,1}^{(1)}} - \dfrac{1}{R_{x,2}^{(1)}} \right)\left(\dfrac{1}{R_{x,1}^{(2)}} - \dfrac{1}{R_{x,2}^{(2)}} \right)\cos(2\alpha) \right]^{1/2} \end{cases} \tag{6.4}$$

Adopting the same convention used in [27], and setting

$$B > A \qquad \frac{B}{A} > 1$$

it is possible to drop the absolute value in the above equation. In particular, this requires that the $x-$ and $y-$axes be interchanged in the cylindrical contact problem.

$$\begin{cases} B + A = \dfrac{1}{2}\left(\dfrac{1}{R_{x,1}^{(1)}} + \dfrac{1}{R_{x,2}^{(1)}} + \dfrac{1}{R_{x,1}^{(2)}} + \dfrac{1}{R_{x,2}^{(2)}} \right) \\[3mm] B - A = \dfrac{1}{2}\left[\left(\dfrac{1}{R_{x,1}^{(1)}} - \dfrac{1}{R_{x,2}^{(1)}} \right)^2 + \left(\dfrac{1}{R_{x,1}^{(2)}} - \dfrac{1}{R_{x,2}^{(2)}} \right)^2 + \right. \\[3mm] \qquad \left. +2\left(\dfrac{1}{R_{x,1}^{(1)}} - \dfrac{1}{R_{x,2}^{(1)}} \right)\left(\dfrac{1}{R_{x,1}^{(2)}} - \dfrac{1}{R_{x,2}^{(2)}} \right)\cos(2\alpha) \right]^{1/2} \end{cases} \tag{6.5}$$

Some elementary curvatures for given primitives are listed in the following table.

body	$R_{x,1}$	$R_{x,2}$
elliptical punch	$+\infty$	$+\infty$
cylinder	$+\infty$	R_{cyl}
sphere	R_{sp}	R_{sp}

It is also important to notice that this formula can address both concave and convex surfaces. The following notation is used through this work:

1. if the surface is **convex** $R_{x,j}^{(k)} > 0$;

2. if the surface is **concave** $R_{x,j}^{(k)} < 0$.

6.3.2 Pressure distribution

Assuming the pressure distribution is of the form (see [27], Chapt. 2.4),

$$p(x, y) = p_0 \left(1 - \frac{x^2}{a^2} - \frac{y^2}{b^2} \right)^{n - 1/2}$$

and setting $n = 1$, the integral equation over the ellipse

$$\mathcal{A} = \left\{ (x, y) : \frac{x^2}{a^2} + \frac{y^2}{b^2} < 1 \right\}$$

generates the surface displacement

$$u_z(x,y) = \frac{p_0 b}{(ae)^2 E^*} \left((ae)^2 K(e) - (K(e) - E(e))x^2 - \left(\frac{E(e)}{1-e^2} - K(e) \right) y^2 \right)$$

where $K(e)$ is the complete elliptic integral of the first kind and $E(e)$ is the **complete elliptic integral of the second kind**

$$E(e) = \int_0^{\pi/2} \sqrt{1 - e^2 \cos^2 \theta}\, d\theta$$

and $e = \sqrt{1 - (b/a)^2}$ is the contact area eccentricity. Given the equation on the region of contact (assuming the mutual frame in which $C = 0$),

$$u_z(x,y) = h - g_0(x,y) = h - Ax^2 - By^2$$

$$h = \frac{p_0 b}{(ae)^2 E^*}(ae)^2 K(e) = \frac{p_0 b}{E^*}K(e)$$

$$A = \frac{p_0 b}{(ae)^2\, E^*}(K(e) - E(e)) \tag{6.6}$$

$$B = \frac{p_0 b}{(ae)^2\, E^*}\left(\frac{E(e)}{1-e^2} - K(e) \right)$$

where A, B are functions of the curvature radii of the body. The value p_0 can be obtained by the boundary equation.

$$P = 4\int_0^a \int_0^{b\sqrt{1-x^2/a^2}} p(x,y)dxdy$$

$$= 4\int_0^a \int_0^{b\sqrt{1-x^2/a^2}} p_0 \left(1 - \frac{x^2}{a^2} - \frac{y^2}{b^2} \right)^{1/2} dxdy$$

$$= \frac{2}{3}\pi\, p_0 ab,$$

$$p_0 = \frac{3}{2\pi}\frac{P}{ab} \tag{6.7}$$

6.3.3   Strategy for Hertzian contact calculations

Eccentricity of the contact area

The first step in the problem is to determine the eccentricity of the contact area e. From the proposed equations, it is possible to evaluate

$$\frac{1}{K(e) - E(e)}\left(\frac{E(e)}{1-e^2} - K(e) \right) = \chi(e) = \frac{B}{A} \to e \tag{6.8}$$

where

$$\frac{B}{A} = f(R_x^{(1)}, R_x^{(2)}, R_y^{(1)}, R_y^{(2)})$$

from which e can be determined. It is important to notice that the contours of g_0 (lines along which $g_0(x,y)$ is constant) are also elliptical, with eccentricity

$$e_g = \sqrt{1 - \frac{B}{A}} = \sqrt{1 - \chi(e)} \implies e_g = f(e), \quad e = f^{-1}(e_g)$$

However, the eccentricity of the contact area is generally larger than that of the composite profile. A good approximation of the eccentricity e, for low values of e_g $(0 < e_g < 0.4)$ is

$$e = \frac{2}{\sqrt{3}} e_g$$
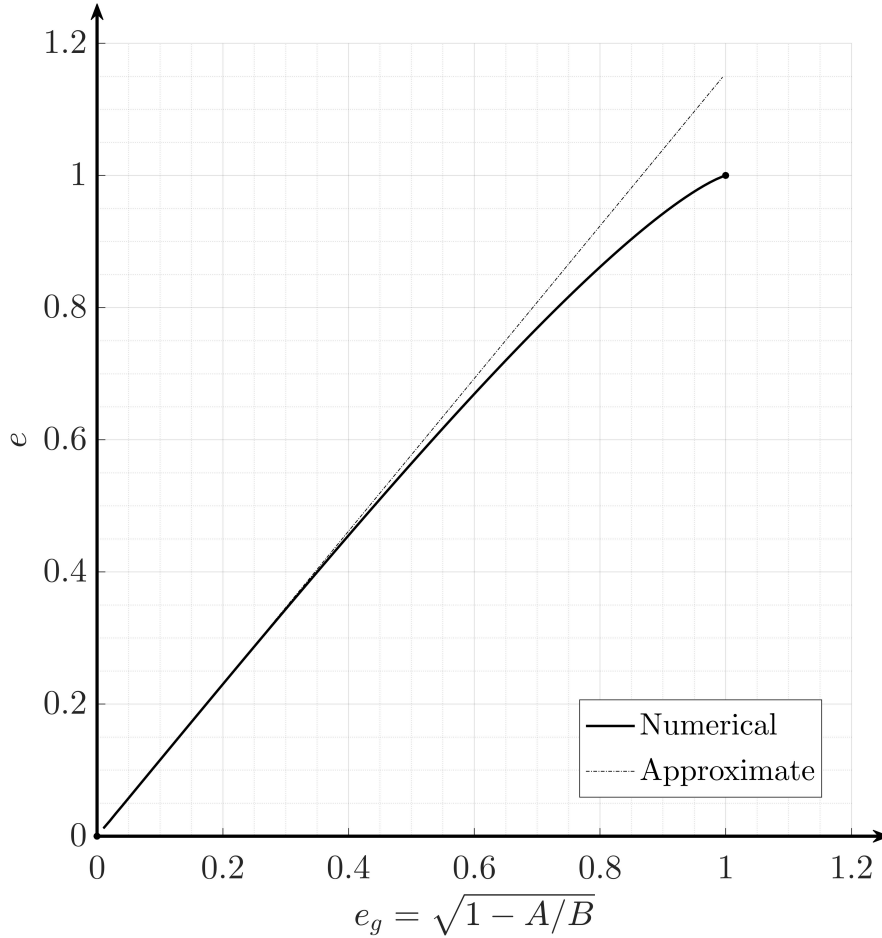
Figure 6.8: Eccentricity plot for a given contact eccentricity e_g.

Dimensions of the contact area

Equation 6.8 cannot be solved in closed form, but a numerical approximation will solve it for a specified numerical value of B/A. Once e is known, the major and minor axes a and b of the contact area can then be determined. Usually, either the total compressive force P or the rigid-body approach h will be prescribed. Alternatively, one may wish to determine the maximum allowable value of P or h if some critical value of the maximum contact pressure is not to be exceeded:

1. **Total force prescribed**: if P is specified, p_0 can be eliminated from B, given Equation 6.7, after which

$$\frac{B}{P} = \frac{\frac{p_0 b}{(ae)^2 E^*}\left(\frac{E(e)}{1-e^2} - K(e)\right)}{\frac{2}{3}\pi p_0 ab}$$

$$\implies a = \left(\frac{3}{2\pi}\frac{1}{E^*}\frac{1}{e^2}\left(\frac{E(e)}{1-e^2} - K(e)\right)\cdot\frac{1}{B}\cdot P\right)^{1/3}$$

after which $b = a\sqrt{1-e^2}$. Once a, b are known, the maximum contact pressure p_0 is obtained from Equation 6.7

$$p_0 = \frac{3}{2\pi}\frac{P}{ab}$$

and the relative rigid-body approach h of the bodies is then given by the above equation.

$$\frac{P}{h} = \frac{\frac{2\pi}{3}p_0 ab}{\frac{p_0 b}{E^*}K(e)} \implies$$

$$P = \left(\frac{2\pi}{3}E^*\right)\cdot\left(\frac{1}{K^3(e)\cdot e^2}\cdot\left(\frac{E(e)}{1-e^2} - K(e)\right)\cdot\frac{1}{B}\right)^{1/2}\cdot h^{3/2}$$

$$= \left(\frac{2\pi}{3}E^*\ell^{2-n}\right)\cdot\left(\frac{1}{K^3(e)\cdot e^2}\cdot\left(\frac{E(e)}{1-e^2} - K(e)\right)\cdot\frac{1}{B\ell}\right)^{2-n}\cdot h^n \quad (6.9)$$

$$= \kappa_{ref}\cdot h^n\cdot C_P$$

$$= P_{ref}\cdot C_P$$

where $n = 3/2$ and the coefficient C_P is the **contact force coefficent**, defined as

$$C_P = \frac{P}{P_{ref}} = \left(\frac{1}{K^3(e)\cdot e^2}\cdot\left(\frac{E(e)}{1-e^2} - K(e)\right)\cdot\frac{1}{B\ell}\right)^{2-n} \quad (6.10)$$

with the reference stiffness

$$\kappa_{ref} = \left(\frac{2\pi}{3}E^*\ell^{2-n}\right) \qquad [\kappa] = [F]/[L]^n \quad (6.11)$$

The same argument is brought for pressure. After defining a proper function for P,

$$p_0 = \frac{3}{2\pi}\frac{P}{ab}$$

$$p_0 = E^*\ell^{-1/2}\left((1-e^2)\frac{1}{K(e)e^2}\left(\frac{E(e)}{1-e^2} - K(e)\right)\cdot\frac{1}{B\ell}\right)^{-1/2}h^{1/2}$$

$$= E^*\ell^{n-2}\left((1-e^2)\frac{1}{K(e)e^2}\left(\frac{E(e)}{1-e^2} - K(e)\right)\cdot\frac{1}{B\ell}\right)^{n-2}h^{2-n} \quad (6.12)$$

$$= \tilde{\kappa}_{ref}\cdot h^{2-n}\cdot c_p$$

$$= p_{0,ref}\cdot c_p$$
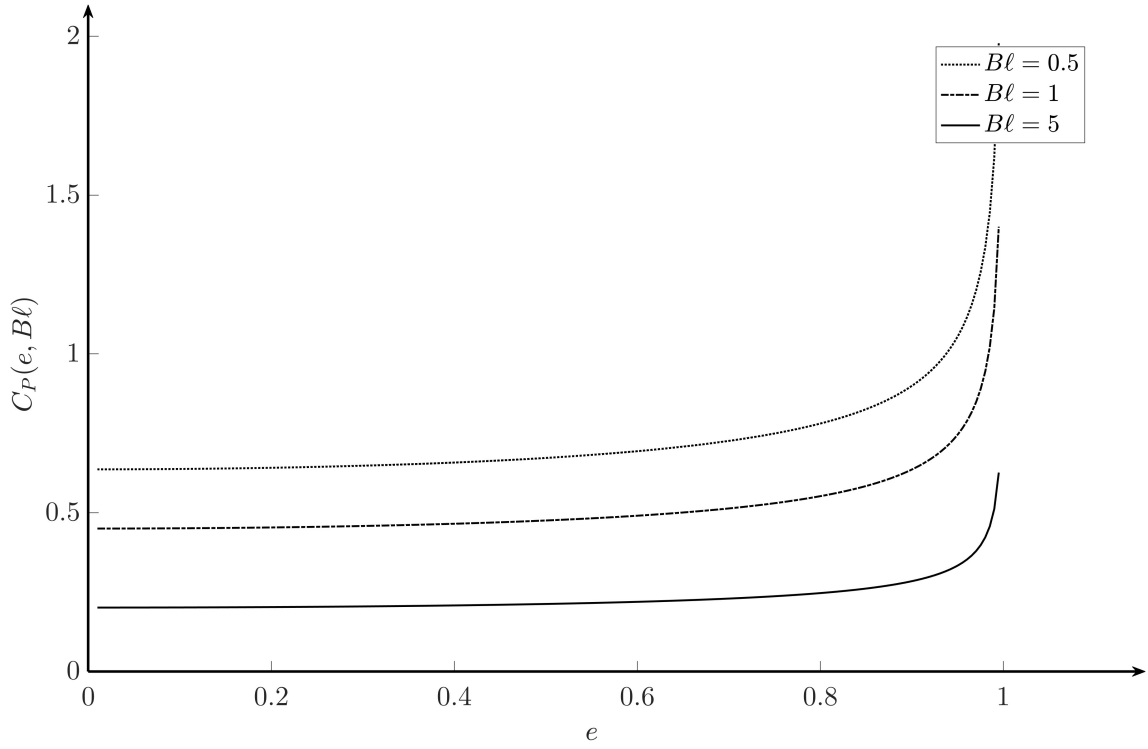
Figure 6.9: Contact force coefficient $C_P(e, B\ell)$ as a function of contact eccentricity for different values of $B\ell$.

with c_p the **contact pressure coefficient**

$$c_p = \frac{p_0}{p_{0,ref}} = \left((1 - e^2) \frac{1}{K(e)e^2} \left(\frac{E(e)}{1 - e^2} - K(e) \right) \cdot \frac{1}{B\ell} \right)^{n-2} \qquad (6.13)$$
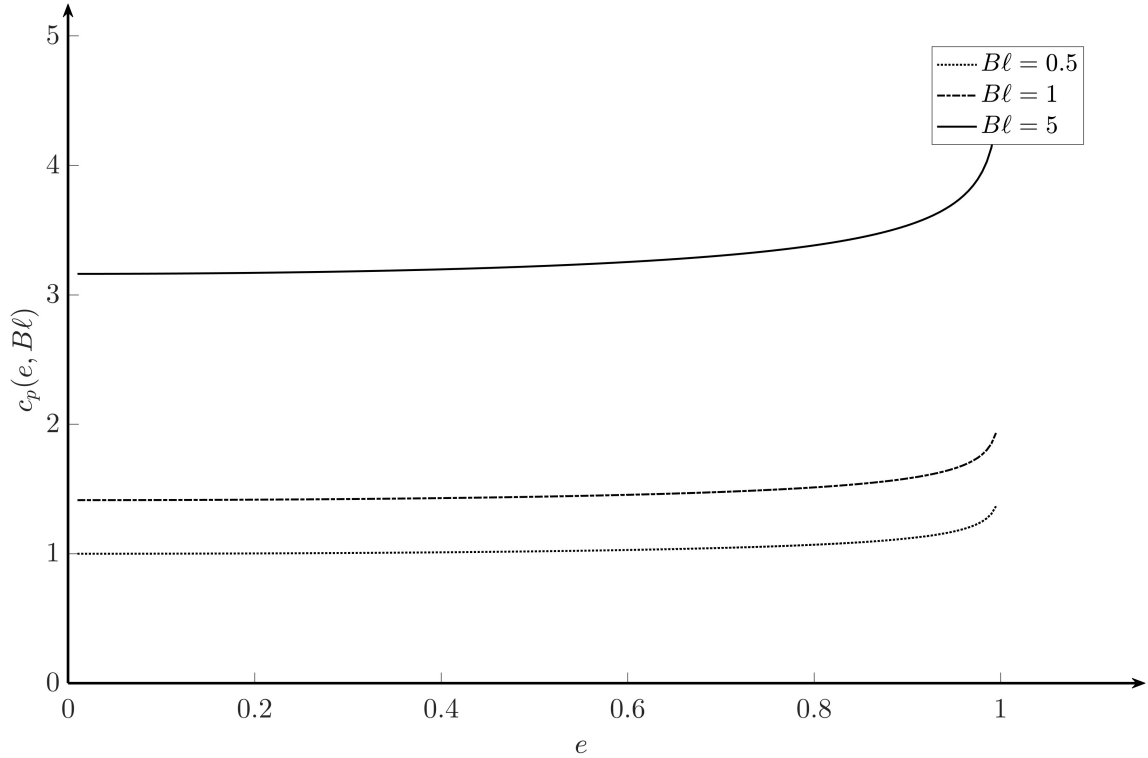
Figure 6.10: Contact force coefficient $c_p(e, B\ell)$ as a function of contact eccentricity for different values of $B\ell$.

$$\tilde{\kappa}_{ref} = E^* \ell^{n-2} \tag{6.14}$$

2. **Rigid body approach prescribed**: In this case, it is possible to eliminate p_0 between the equation of A, h to obtain

$$a = \sqrt{\frac{h}{Ae^2}\left(1 - \frac{E(e)}{K(e)}\right)}$$

after which $b = a\sqrt{1 - e^2}$ and $p_0 = h/(bK(e)) \cdot E^*$. Finally, the compressive force P is obtained by substituting these results into Equation 6.7. Notice that the dimensions a, b of the contact ellipse both increase with $h^{1/2}$. It follows that the maximum contact pressure

$$p_0 \sim h^{1/2}$$

and the total force

$$P \sim h^{3/2}$$

In other words, the Hertzian contact acts as a *stiffening spring*.

3. **maximum contact pressure prescribed**: In this case, one uses the definition of e to eliminate a from the definitions of A, B,

$$b = \frac{p_0(1 - e^2)}{a^2 A}(K(e) - E(e))$$

and therefore $a = b/\sqrt{1 - e^2}$. The total force P and the rigid-body approach h are then determined from Equation 6.7 and the equation for h respectively. In particular, by setting a certain limiting value over p_0 such as a robustness criterion [31]

$$\mathcal{F}_c \cdot k_p \cdot p_0 \leq \sigma_y \implies \mathcal{M}_c = \frac{\sigma_y/p_0}{k_p \mathcal{F}_c} - 1 \geq 0 \tag{6.15}$$

with:

(a) $\mathcal{F}_c$ the imposed safety factor;

(b) $\mathcal{M}_c$ the imposed safety margin;

(c) k_p is a pressure coefficient, which derives from the specific contacting geometry (whom values are found in [31], Chapter 6);

(d) σ_y is the yield strength of the material.

The **total admissible contact force load** can therefore be estimated as

$$
\begin{aligned}
P_{adm} &= \frac{2}{3}\pi \cdot \left(\frac{1}{k_p \mathcal{F}_c(\mathcal{M}_c + 1)}\frac{\sigma_y}{E^*}\right)^{n/(2-n)} E^*\ell^2 \left(\left(\frac{E(e)}{1-e^2} - K(e)\right)\frac{(1-e^2)^{3/4}}{e^2}\frac{1}{B\ell}\right)^{2(n-1)/(2-n)} \\
&= \frac{2}{3}\pi \cdot \left(\frac{1}{k_p \mathcal{F}_c(\mathcal{M}_c + 1)}\frac{\sigma_y}{E^*}\right)^{n/(2-n)} \cdot E^* \cdot \ell^2 \cdot C_g(e, B\ell, n) \\
&= \frac{2}{3}\pi \cdot \left(\frac{1}{k_p \mathcal{F}_c(\mathcal{M}_c + 1)}\right)^{n/(2-n)} \left(\frac{\sigma_y}{E^*}\right)^{n/(2-n)} \cdot E^* \cdot \ell^2 \cdot C_g(e, B\ell, n) \\
&= P_{adm,ref} \cdot C_g(e, B\ell, n)
\end{aligned}
$$

$$(6.16)$$

This equation contains four different aspects:

1. a safety coefficient (which contains $\mathcal{F}_c, \mathcal{M}_c$) from which safety regulations can be implemented;

2. material properties (which contains σ_y, E^*, n) that depend on the material properties of the material itself.

3. a characteristic length ℓ which is used to describe the geometrical fundamental aspects of the contact (i.e. the radius of a cylinder or a sphere).

4. C_g which is a dimensionless parameter that encompasses all the geometric aspects of the problem (geometry of the contacting bodies, the relative contact position, angle, etc.).

The fundamental aspect of this equation is the fact that this contact force is the maximum admissible (given a certain safety limit). Therefore, the lower the value of P_{adm} the more probable is the risk of irreversible deformation (or rupture). The following plot shows the geometric coefficent C_g as a function of e and $B\ell$.

$$
C_g = \frac{P_{adm}}{P_{adm,ref}} = \left(\left(\frac{E(e)}{1-e^2} - K(e)\right)\frac{(1-e^2)^{3/4}}{e^2}\frac{1}{B\ell}\right)^{2(n-1)/(2-n)} \tag{6.17}
$$
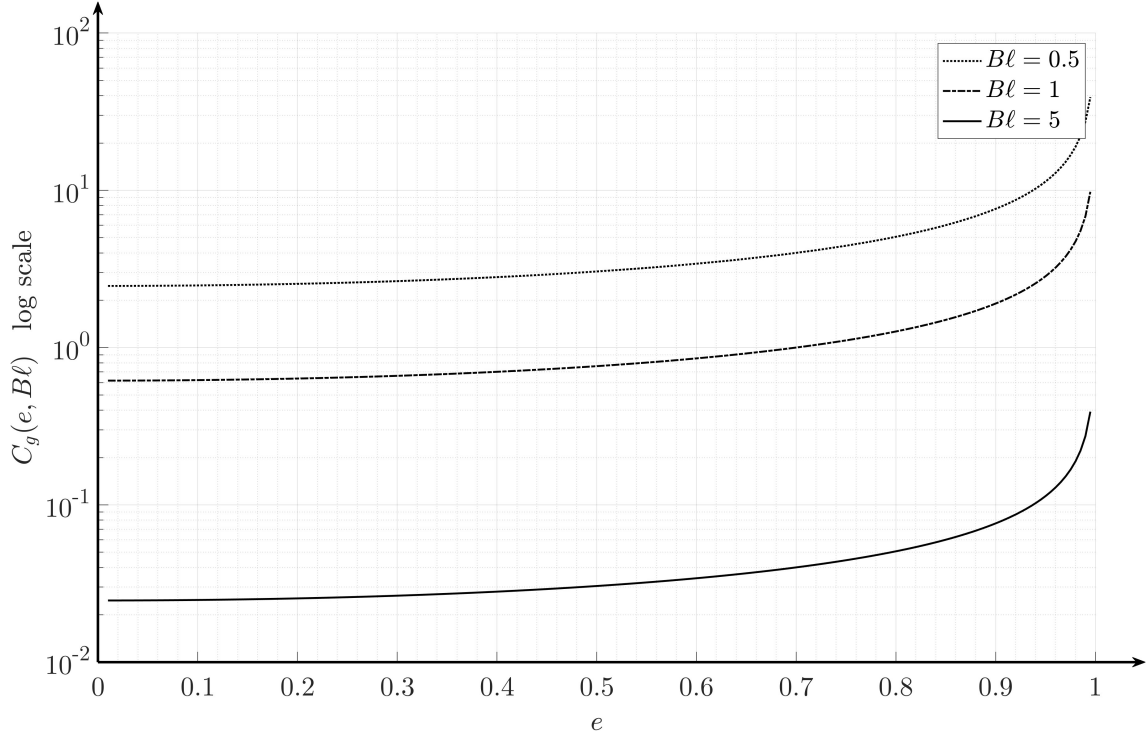
Figure 6.11: Contact geometry coefficient $C_g(e, B\ell)$.

These calculations are most easily performed numerically to compute $K(e)$, $E(e)$. The following graph shows the values for those integrals for different values of eccentricity.

where, the complete elliptic integral:

1. of the first kind is:

$$K(e) = \int_0^{\pi/2} \frac{1}{\sqrt{1 - e^2 \cos^2 \theta}}\, d\theta$$

2. of the second kind is:

$$E(e) = \int_0^{\pi/2} \sqrt{1 - e^2 \cos^2 \theta}\, d\theta$$

Figure 6.12: The complete elliptic integrals $K(e)$, $E(e)$ as functions of eccentricity e.
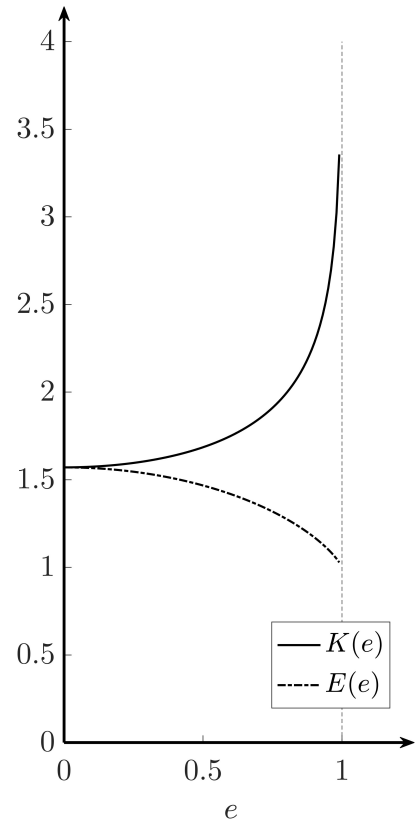
6.4 Tangential Loading

So far, the only problems in which no tangential tractions are transmitted across the contact interface have been considered. This will be the case if the contact is frictionless or if the contact interface is a plane of symmetry with regard to geometry, material properties and loading. In most other cases, normal contact tractions will tend to cause relative tangential displacement or slip at the interface, and in many cases, this will be opposed by *frictional tractions*.

6.4.1 Kinematics of tangential loading

Suppose that the two bodies can be approximated by half-spaces, and that the contact area is denoted by $\mathcal{A}$. A rigid-body tangential displacement on body (2) [the upper body] is imposed and labeled $\boldsymbol{U}(t)$, where t is time. In addition, will be some tangential elastic surface displacements in the two bodies identified as $u_x^{(k)}(x, y, t), u_y^{(k)}(x, y, t)$. It follows that the relative tangential motion between two contacting points at (x, y) [known as the *shift*] will be given by

$$\boldsymbol{h}(x, y, t) = \boldsymbol{U}(t) - \boldsymbol{u}(x, y, t) \tag{6.18}$$

in which

$$\begin{cases} u_x = u_x^{(1)} - u_x^{(2)} \\ u_y = u_y^{(1)} - u_y^{(2)} \end{cases}$$

Figure 6.13: Relative Tangential Loading.

With this sign convention, a positive shift is one where material points in the upper body move in the direction of the corresponding positive coordinate axis relative to points on the lower body.

One can also define the *slip velocity*

$$\boldsymbol{V}_s(x, y, t) = \dot{\boldsymbol{h}}(x, y, t) = \dot{\boldsymbol{U}}(t) - \dot{\boldsymbol{u}}(x, y, t) \tag{6.19}$$

which represents the relative velocity of a pair of material points in $\mathcal{A}$, one in each of the contacting bodies. The spatial derivatives of $\boldsymbol{h}$ are related to tangential surface strains. For example

$$\frac{\partial h_x}{\partial x} = \frac{\partial u_x^{(1)}}{\partial x} - \frac{\partial u_x^{(2)}}{\partial x} = \varepsilon_{xx}^{(1)} - \varepsilon_{xx}^{(2)}$$

since the rigid-body displacement is a function of time only.

6.4.2 Greens Functions for Tangential Forces and Displacements

In preparation for the formulation of contact problems involving tangential traction, one first need to generalize the results of the point force on a surface that includes tangential forces and displacements.

If a normal compressive force P and tangential force Q_x, Q_y origin on the surface of the elastic half-space, the resulting surface displacements are [27]:

$$\begin{cases} u_x = -\dfrac{(1-2\nu)(1-\nu)Px}{2\pi E r^2} + \dfrac{(1-\nu)^2 Q_x}{\pi E r} + \dfrac{\nu(1+\nu)x(xQ_x + yQ_y)}{\pi E r^3} \\[2mm] u_y = -\dfrac{(1-2\nu)(1-\nu)Py}{2\pi E r^2} + \dfrac{(1-\nu)^2 Q_y}{\pi E r} + \dfrac{\nu(1+\nu)y(xQ_x + yQ_y)}{\pi E r^3} \\[2mm] u_z = +\dfrac{(1-\nu)^2 P}{\pi E r} + \dfrac{(1-2\nu)(1+\nu)(xQ_x + yQ_y)}{2\pi E r^2} \end{cases}$$

Applying an equal and opposite force to the upper body (2), and using the same equations with appropriate sign changes, the relative displacements are [27]:

$$\begin{cases} u_x = u_x^{(1)} - u_x^{(2)} = -\dfrac{\beta Px}{2\pi E^* r^2} + \dfrac{Q_x}{\pi E^* r} + \dfrac{x(xQ_x + yQ_y)}{\pi \hat{E} r^3} \\[2mm] u_y = u_y^{(1)} - u_y^{(2)} = -\dfrac{\beta Py}{2\pi E^* r^2} + \dfrac{Q_y}{\pi E^* r} + \dfrac{y(xQ_x + yQ_y)}{\pi \hat{E} r^3} \\[2mm] u_z = u_z^{(1)} - u_z^{(2)} = +\dfrac{P}{\pi E^* r} + \dfrac{\beta(xQ_x + yQ_y)}{\pi E^* r^2} \end{cases}$$

where two new elastic moduli have been defined, respecively:

1. the **Dundur's bimaterial constant** β

$$\beta = E^* \left(\frac{(1-2\nu_1)(1+\nu_1)}{2E_1} - \frac{(1-2\nu_2)(1+\nu_2)}{2E_2} \right)$$

2. the second composite modulus $\hat{E}$

$$\frac{1}{\hat{E}} = \frac{\nu_1(1+\nu_1)}{E_1} + \frac{\nu_2(1+\nu_2)}{E_2}$$

If the contacting bodies can be approximated by half-spaces, the problem is considered *uncoupled* (i.e. tangential and normal loading are treated separately) if and only if Dundurs constant $\beta = 0$ (the most common case being that in which the two bodies are of similar materials).

6.4.3 Cattaneo's problem

Consider the case where the two bodies have quadratic surfaces (like in the context of Hertzian Contact) and are loaded by a purely normal force P_0. Since $\beta = 0$, no tangential tractions are developed during this process, and the normal tractions and the semi-axes a_0, b_0 of the elliptical contact area $\mathcal{A}_0$ are defined by the Hertzian equations. Suppose P_0 stays at a constant value whilst applying a tangential force Q_x that increases monotonically from zero to a value.
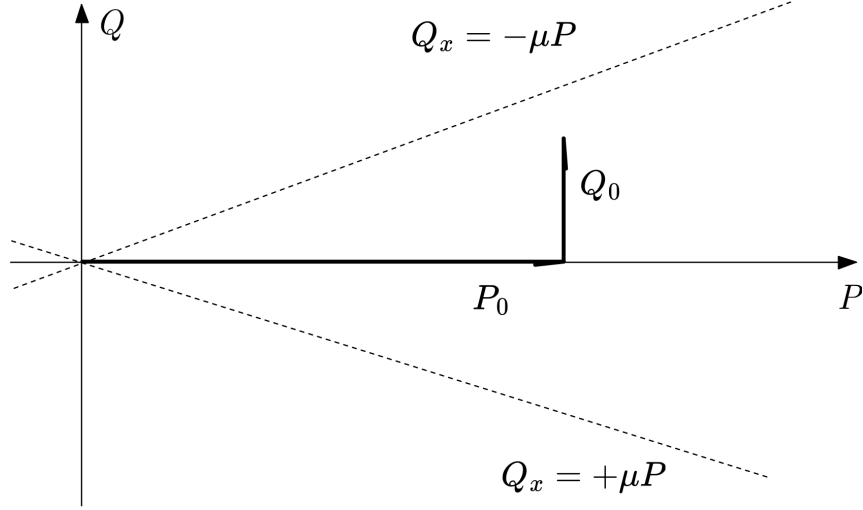
Figure 6.14: Loading scenario for Cattaneo and Mindlins problem.

This problem was first solved by Cattaneo (1938) and later by Mindlin (1949) who was most likely unaware of Cattaneos earlier publication. The contact area $\mathcal{A}_0$ is determined by the normal force and hence remains unchanged during the tangential loading phase. Cattaneo and Mindlin solved the tangential problem by first finding the tangential displacements due to the tangential traction distribution

$$q_x(x,y) = \mu \cdot p(x,y) = \frac{3\mu P_0}{2\pi a_0 b_0}\sqrt{1 - \left(\frac{x}{a_0}\right)^2 - \left(\frac{y}{b_0}\right)^2} = q_0\sqrt{1 - \left(\frac{x}{a_0}\right)^2 - \left(\frac{y}{b_0}\right)^2}$$
(6.20)

which corresponds to the case of *slip* in the $x-$direction over the entire elliptical contact area. To take into consideration also the *stick*, a new traction distribution is defined as follows

$$q_x(x,y) = \frac{3\mu P_0}{2\pi a_0 b_0}\sqrt{1 - \left(\frac{x}{a_0}\right)^2 - \left(\frac{y}{b_0}\right)^2} - \frac{3\mu P_1}{2\pi a_1 b_1}\sqrt{1 - \left(\frac{x}{a_1}\right)^2 - \left(\frac{y}{b_1}\right)^2} \quad (6.21)$$
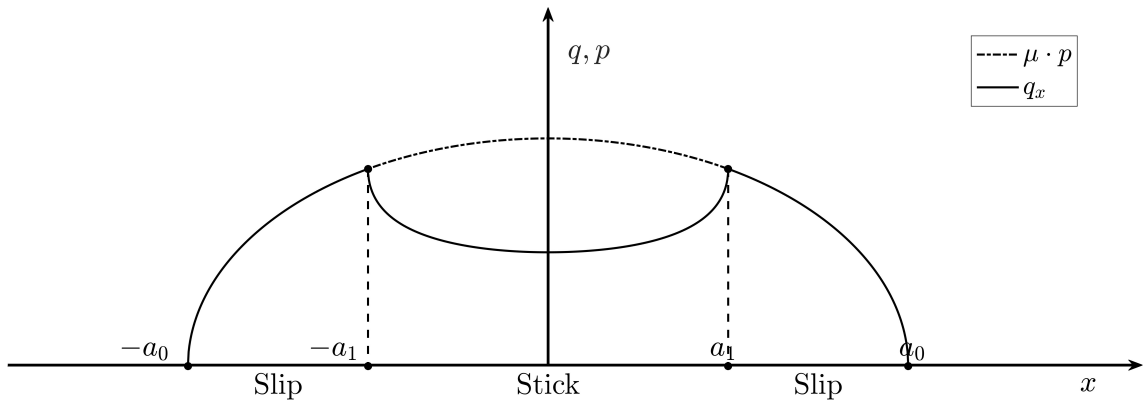
Figure 6.15: Tangential traction distribution along the major axis for Cattaneos problem

where a_1, b_1 are the semi-axes of the contact ellipse $\mathcal{A}_1$ corresponding to a different normal force $P_1 < P_0$, and the square roots are to be interpreted as zero in any region in which their respective arguments are negative. The variation of tangential traction along the major axis is illustrated the following figure.

The traction distribution in Equation 6.21 corresponds to a tangential force $Q_0 = \mu P_0 - \mu P_1$ and hence, if it's prescribed, one must choose

$$P_1 = P_0 - \frac{Q_0}{\mu}$$

Once P_1 is determined, the Hertz problem defines the dimensions of $\mathcal{A}_1$, which constitutes the stick region in the tangential loading problem. Notice that as Q_0 increases, P_1 decreases, so the stick region shrinks as expeceted, reaching zero when $Q_0 = \mu P_0$ (complete slip), after which gross slip would occur.

6.5 Terramechanics

The study of tangential contact problems spans a variety of different applications. For the purpose of this work, it is important to investigate also the contact of rigid (or elastic) bodies over *soft soil*. Examples of this problem can be found in the contact of the LPR tire with the lunar regolith. The current description follows from the Bekker Theory of contact [32] (an extract can be found on [29]).

6.5.1 Pressure-Sinkage relationship

Consider a homogeneous terrain subject to a normal force, applied via a rigid patch of width b. The reaction of this force would be a *pressure* which, when integrated over the contact area, is equal and opposite to the applied force. Its pressure-sinkage relationship (the result of the plate-sinkage test) may be characterized by the following empirical equation proposed by Bekker.

$$p = \sigma_{zz} = \kappa \cdot h^n = \left(\frac{k_c}{b} + k_\varphi \right) \cdot h^n \tag{6.22}$$

where:

1. $p = \sigma_{zz}$ is the applied pressure (equal to the tension on the surface of the medium from the equilibrium);

2. b is the width of the rectangular contact patch area,

3. h is the sinkage;

4. k_c, k_φ are pressure-sinkage related parameters;

5. n is the exponent of the sinkage.
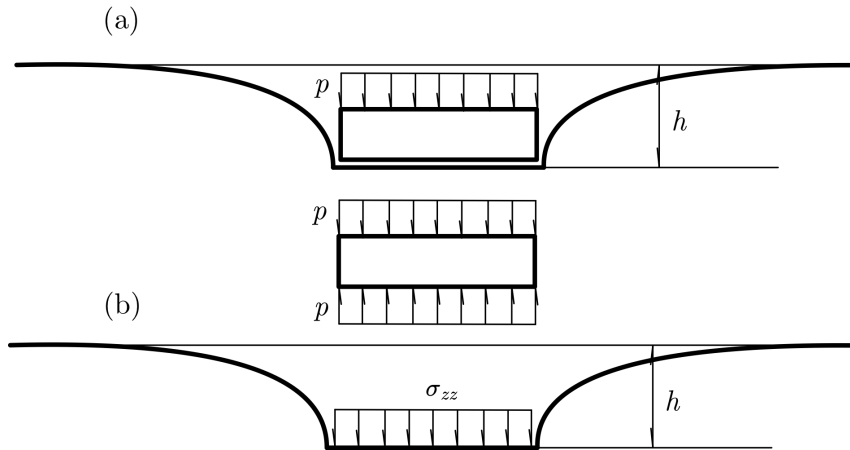
Figure 6.16: Plate-sinkage test used to determine the coefficients in the equation (a) and equivalent free body diagram (b).

This relation generalizes Hooke's Law such that $\boldsymbol{\sigma} = \boldsymbol{C} : \boldsymbol{\varepsilon}^n$. It is clear that the sinkage h takes the role of the deformations. In this context, the value of n determines whether the problem can be treated as linear or non-linear, extending the Hertzian theory contact problem not only by the forces applied but also to the type of stress-strain relationship.

6.5.2 Soil Failure

When a tangential force is exerted on a plane, it tends to "fail" on the microscopic level. This failure causes an irreversible transformation of the soil that, in the end, dissipates energy. This condition is what constitutes friction. There is a variety of criteria proposed for the failure of soils. One of the most widely used is the Mohr-Coulomb criterion which states that the maximum shear strength $\tau_{max,s}$ of the soil is

$$\tau_{max,s}(\sigma_{zz}) = c + \sigma_{zz} \cdot tan\varphi$$

where c is the apparent cohesion, σ is the normal stress and φ is the angle of internal shearing resistance of the material (also referred as internal angle of friction).
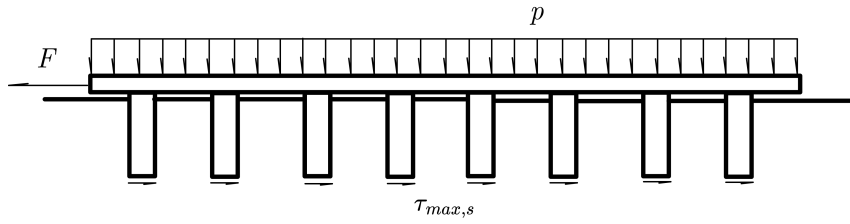
Figure 6.17: Shear test.

6.6 Tire-Road Interaction

One crucial example of the frictional problem presented in this work is the tire-road interaction. In the case of a moving wheel, the contact patch area can be determined as a function of sinkage h, the tires radius R_w, and elastic sinkage h_e using the following equations

$$\mathcal{A} = \{(\vartheta, y) : \vartheta_r \leq \vartheta \leq \vartheta_f \quad -b/2 \leq y \leq b/2\}$$

where ϑ_f and ϑ_r are the front and rear angles of the indentation and b is the tire's width.

$$\begin{cases} \vartheta_f(h) = \cos^{-1}\left(1 - \dfrac{h}{R_w}\right) \\ \vartheta_r(h_e) = \cos^{-1}\left(1 - \dfrac{h_e}{R_w}\right) \end{cases}$$

Due to the curvature of the tire, a curvilinear coordinate system is inserted (ξ, η, ζ) as shown in the following figure.
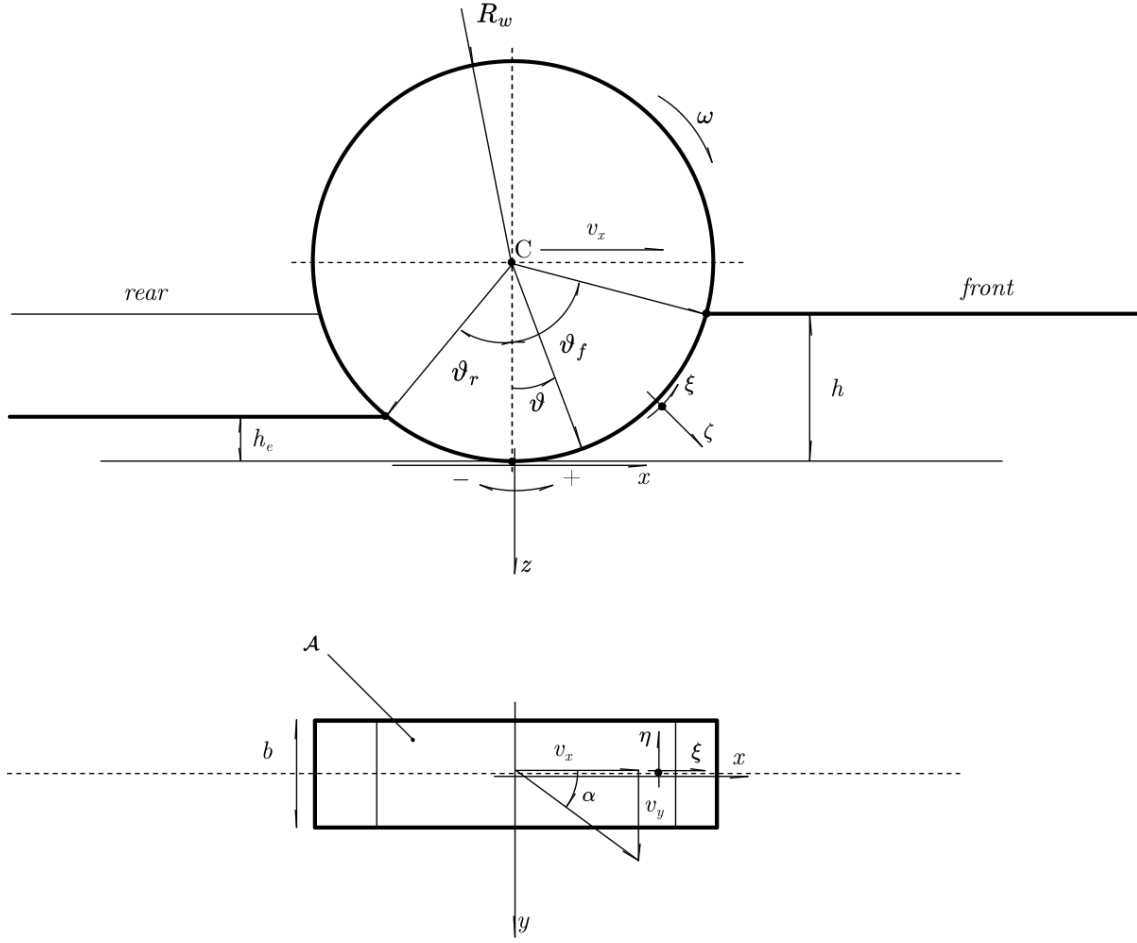
Figure 6.18: Tire-Road interaction geometry.

Using the pressure-sinkage relationship proposed by Bekker Equation 6.22, the tire normal stress distribution can be calculated as a function of wheel angle. Specifically,

$$
\sigma_{\zeta\zeta}(\vartheta) =
\begin{cases}
R_w^n \left(\dfrac{k_c}{b} + k_\varphi \right) (\cos\vartheta - \cos\vartheta_f)^n & \text{for } \vartheta_m \leq \vartheta \leq \vartheta_f \\[2ex]
R_w^n \left(\dfrac{k_c}{b} + k_\varphi \right) \left(\cos\left(\vartheta_f - \dfrac{\vartheta - \vartheta_r}{\vartheta_m - \vartheta_r}(\vartheta_f - \vartheta_m) \right) - \cos\vartheta_f \right)^n \\[1ex]
& \text{for } \vartheta_r \leq \vartheta \leq \vartheta_m
\end{cases}
\tag{6.23}
$$

where ϑ_m is the angle at which the normal stress is maximized and can be determined as

$$
\vartheta_m = (c_1 + c_2 \cdot \kappa) \cdot \vartheta_f
$$

In the above equation, c_1 and c_2 are parameters that depend on the wheel-soil interaction, κ is the longitudinal slip, and ϑ_f is tire entry angle.
Furthermore, Equation 6.24 can be modified in order to account for the contribution

of soil damping [29]. In that case, the normal stress distribution is given by

$$\sigma_{\zeta\zeta}(\vartheta) = \begin{cases} R_w^n \left(\dfrac{k_c}{b} + k_\varphi \right) (\cos\vartheta - \cos\vartheta_f)^n + \dfrac{c_s v_c}{\mathcal{A}} & \text{for } \vartheta_m \leq \vartheta \leq \vartheta_f \\[2em] R_w^n \left(\dfrac{k_c}{b} + k_\varphi \right) \left(\cos\left(\vartheta_f - \dfrac{\vartheta - \vartheta_r}{\vartheta_m - \vartheta_r}(\vartheta_f - \vartheta_m) \right) - \cos\vartheta_f \right)^n + \dfrac{c_s v_c}{\mathcal{A}} \\ & \text{for } \vartheta_r \leq \vartheta \leq \vartheta_m \end{cases}$$

(6.24)

where c_s is the soil damping, v_c is the soil compression rate/velocity and $\mathcal{A}$ is the contact area.

6.6.1   Influence of the coefficient of friction

As already mentioned, the maximum shear strength of the soil $\tau_{max,s}$ can be calculated using the Mohr-Coulomb failure criterion. In addition, the maximum shear strength between the tire and the soil $\tau_{max,t/s}$ can be approximated as a function of the pressure σ and the friction coefficient:

$$\tau_{max,t/s}(\sigma_{\zeta\zeta}) = \mu_s \sigma_{\zeta\zeta} \tag{6.25}$$

Consequently, the minimum shear strength (soiltire and internal soil) is used for the shear stress calculation in order to account for the friction between the tire and the soil.

$$\tau_{max}(\sigma_{\zeta\zeta}) = \max\{\mu_d \sigma_{\zeta\zeta}, c + \sigma_{\zeta\zeta} \cdot tan\varphi\}$$
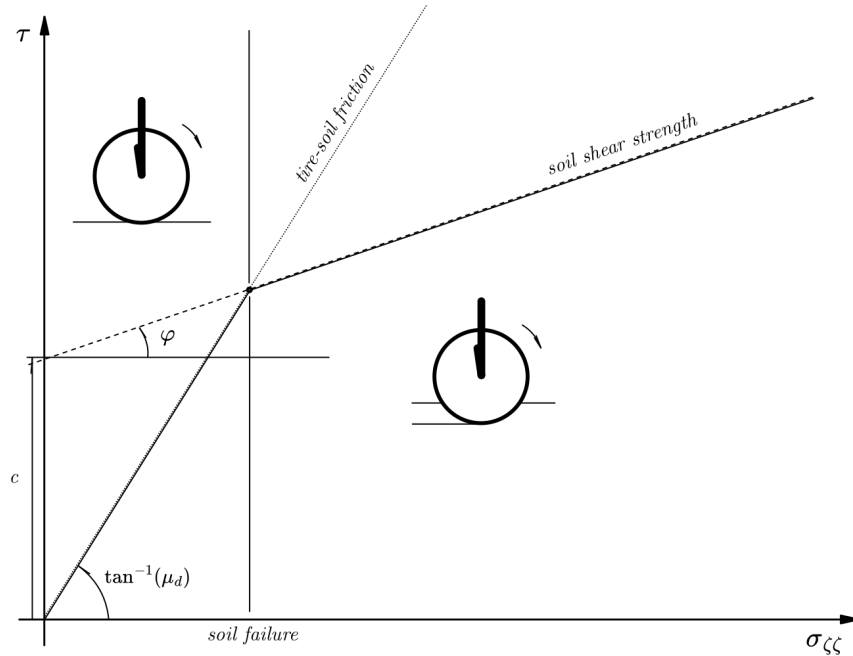
Figure 6.19: Maximum shear strength

6.6.2 Shear stress

The shear stresses are calculated using the following expressions

$$\begin{cases} \tau_{\xi\zeta}(\vartheta) = \tau_{max}\left(1 - e^{-\varepsilon_{\xi\zeta}(\vartheta)/k_\xi}\right) \\ \tau_{\eta\zeta}(\vartheta) = \tau_{max}\left(1 - e^{-\varepsilon_{\eta\zeta}(\vartheta)/k_\eta}\right) \end{cases}$$

Shear stress (frictional contact)
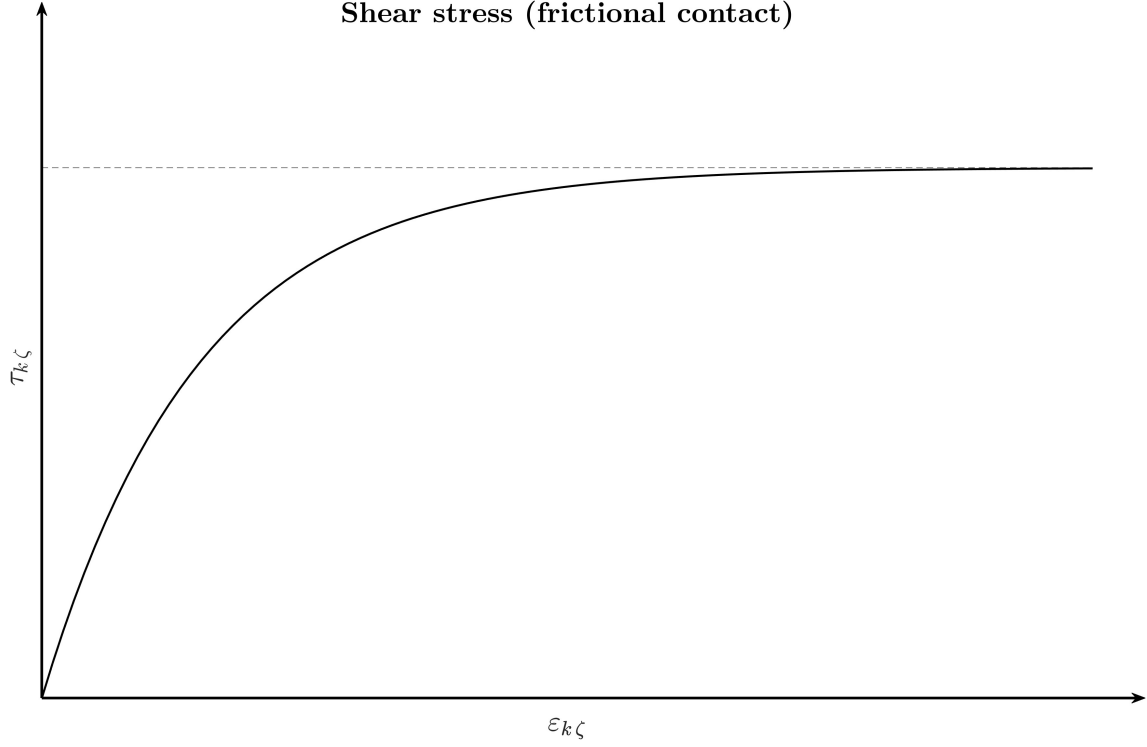
In the above equations, k_ξ and k_η represent the shear deformation modules and $\varepsilon_{\xi\zeta}, \varepsilon_{\eta\zeta}$ the relative soil deformations. For small deformations, those values can be interchanged with the corresponding k_x and k_y, which are provided by the following equations:

$$\begin{cases} k_x = k_{x,0}\alpha + k_{x,1} \\ k_y = k_{y,0}\alpha + k_{y,1} \end{cases}$$

with α as the lateral slip angle of the tire. Moreover, the soil deformations $\varepsilon_{\xi\zeta}, \varepsilon_{\eta\zeta}$ can be formulated as functions of the wheel angle ϑ [29].

$$\begin{cases} \varepsilon_{\xi\zeta}(\vartheta) = R_w(\vartheta_f - \vartheta(1 - \kappa)(\sin\vartheta_f - \sin\vartheta)) \\ \varepsilon_{\eta\zeta}(\vartheta) = R_w(1 - \kappa)(\vartheta_f - \vartheta)\tan\alpha \end{cases}$$

6.6.3 Bull-dozing Resistance

Bulldozing resistance is developed when a soil mass is displaced by the wheel. Regarding lateral forces, due to tires sinkage, a bulldozing force which acts on the side of the wheel must be added to the shear force exerted on the contact patch due to the tangential stresses τ_{ys}. In this tire model, the Hegedus resistance estimation

method [29] is used in order to calculate the bulldozing force. As depicted in Figure 6.20, a bulldozing resistance f_b is developed per unit width of a blade, as the blade moves toward the soil ($[f_b] = [F][L^{-1}]$), given by the equation:

$$f_b = \frac{\cot X_c + \tan(X_c + \varphi)}{1 - \tan \alpha' \tan(X_c + \varphi)} \left\{ h\,c + \frac{1}{2}\rho_s h^2 \left((\cot X_c - \tan \alpha') + \frac{(\cot X_c - \tan \alpha')^2}{\tan \alpha' + \cot \varphi} \right) \right\}$$

with ρ_s as the soil density and X_c as the **destructive angle** that can be appoximated as

$$X_c = \frac{\pi}{4} - \frac{\varphi}{2}$$
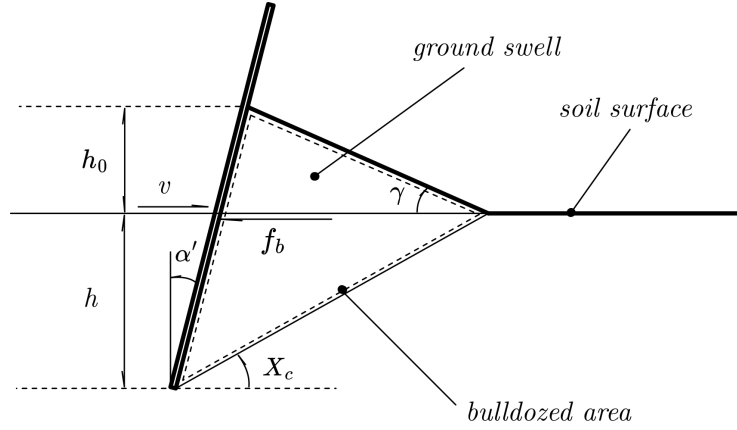
Figure 6.20: Bull-dozing resistance model (Hegedus method)

6.6.4   Tire Deformability

In order to account for tire deformability, a larger substitute circle is used to describe the contact patch between the tire and the soil, as depicted in Figure 6.21. In order to calculate the diameter of the substitute circle, an iterative procedure is followed until the soil vertical reaction force and the tire vertical force are balanced. The former is calculated from an integration of the normal and shear stresses in the contact patch area, while for the latter the vertical tire stiffness is used along with the tires deflection. More specifically,

$$F_{z,s} = bR_w^* \int_{\vartheta_r^*}^{\vartheta_f^*} (\tau_x(\vartheta^*) \sin \vartheta^* + \sigma(\vartheta^*) \cos \vartheta^*)d\vartheta^*$$

$$F_{z,t} = K_t f$$

$$\frac{R_w^*}{R_w} = \left(\sqrt{1 + \frac{f}{h}} + \sqrt{\frac{f}{h}} \right)^2$$

Those three equations need to be solved iteratively until a certain exit condition is imposed

$$|F_{z,t} - F_{z,s}| < t$$

for a given tolerance t of the tire's maximum vertical load F_z.
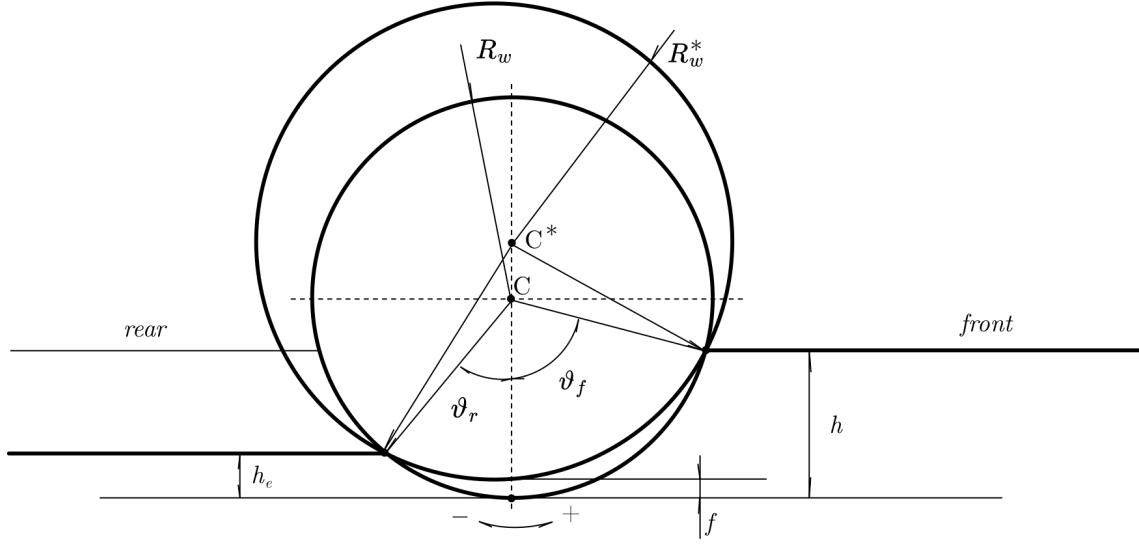
Figure 6.21: Substitute circle method for tire's deformability.

6.6.5 Multipass effect

For the multipass effect, the response of the soil to repetitive normal load needs to be established. Specifically, the mathematical description of the normal pressure distribution must be modified in cases of existing pre-compaction of the soil. In this case, the normal pressure distribution will be comprised initially from an elastic part $h_{el,0}$, which is equal to the elastic (unloading) sinkage created by a previous tire the pressure-sinkage relationship continues according to Equation 6.22. Finally, an unloading elastic part $h_{el,1}$ is encountered.

As already mentioned, one part of the induced soil deformation is elastic (elastic sinkage), and the remaining part (plastic sinkage) is irreversible. The elastic part is provided by the equation:

$$h_e = \frac{\sigma(\vartheta_m)}{E_s}$$

Where E_s is the soil elastic stiffness.

6.6.6 Tire Forces

To conclude, all the relevant actions acting on the tire are [29]:

1. Longitudinal force:

$$F_x = bR_w^* \int_{\vartheta_r^*}^{\vartheta_f^*} (\tau_x(\vartheta^*) \cos \vartheta^* - \sigma(\vartheta^*) \sin \vartheta^*) d\vartheta^*$$

2. Lateral force:

$$F_y = F_{y,shear} + F_{y,bull}$$

$$= bR_w^* \int_{\vartheta_r^*}^{\vartheta_f^*} (\tau_y(\vartheta^*)) d\vartheta^* + \int_{\vartheta_r^*}^{\vartheta_f^*} (f_b(R_w^* - h(\vartheta^*) \cos \vartheta^*) d\vartheta d\vartheta^* sin\alpha$$

3. Overturning moment:

$$M_x = (b(R_w^*))^2 \int_{\vartheta_r^*}^{\vartheta_f^*} \tau_y(\vartheta^*) \cos \vartheta^* d\vartheta^*$$

4. Rolling resistance moment:

$$M_y = (b(R_w^*))^2 \int_{\vartheta_r^*}^{\vartheta_f^*} \tau_x(\vartheta^*) \, d\vartheta^*$$

5. Self-aligning moment:

$$M_x = (b(R_w^*))^2 \int_{\vartheta_r^*}^{\vartheta_f^*} \tau_y(\vartheta^*) \sin \vartheta^* d\vartheta^*$$

If the tire is assumed rigid the asterisk values turn back into their rigid counterparts.

6.6.7   Typical Soil Parameter Values

As a conclusion for the chapter, typical values of terrain parameters listed in the above discussion are disclosed. If not otherwise stated, the principal source of such parameters is [29].

Terrain	Moisture	n	k_c	k_φ	c	φ
Dry sand (LLL)	0	1.1	0.99	1528.43	1.04	28
Sandy loam	15	0.7	5.27	1515.04	1.72	29
Sandy loam (LLL)	22	0.2	2.56	43.12	1.38	38
Sandy loam (Michigan, SB)	11	0.9	52.53	1127.97	4.83	20
Sandy loam (Hanamoto)	26	0.3	2.79	141.11	13.79	22
Clayey soil (Thailand)	38	0.5	13.19	692.15	4.14	13
Heavy clay	25	0.13	12.7	1555.95	68.95	34
Heavy clay (WES)	40	0.11	1.84	103.27	20.69	6
Lean clay	22	0.2	16.43	1724.69	68.95	20
Heavy clay (WES)	32	0.15	1.52	119.61	13.79	11
LETE sand (Wong)		0.79	102	5301	1.3	31.1
Upland sandy loam (Wong)	51	1.1	74.6	2080	3.3	33.76
Rubicon sandy loam (Wong)	43	0.66	6.9	752	3.7	29.8
North Gower clayey loam (Wong)	46	0.73	41.6	2471	6.1	26.6
Grenville loam (Wong)	24	1.01	0.06	5880	3.1	29.8
Snow (U.S.)		1.6	4.37	196.72	1.03	19.7
Snow (Sweden)		1.44	10.55	66.08	6	20.7
Units	%		kN/m^{n+1}	kN/m^{n+2}	kN/m^2	°

Table 6.1: Soil parameters data (via [29]).

Terrain	ρ
Sand	1650
Loamy sand	1600
Sandy loam	1550
Loam	1500
Sandy clay loam	1500
Silty clay loam	1500
Silty loam	1500
Clay loam	1450
Silty clay	1450
Sandy clay	1400
Clay	1350
Units	kg/m^3

Table 6.2: Soil bulk density data (via [29]).

Particular attention is dedicated to this regolith simulant [29], to get a comprehensive view of the parameters involved.

Parameter	Value	Units	Description
c	0.8	kPa	cohesion
φ	37.2	°	friction angle
X_c	26.4	°	soil distractive angle
k_c	1.37	kN/m^{n+1}	pressure-sinkage module
k_φ	8.14	kN/m^{n+2}	pressure-sinkage module
n	1		sinkage exponent
a_0	0.4		
a_1	0.15		
ρ	1600	kg/m^3	soil density
λ	$0.90 \div 1.10$		wheel sinkage ratio
$k_{\xi\zeta}$	$0.043\alpha + 0.036$	m	soil deformation module
$k_{\eta\zeta}$	$0.02\alpha + 0.013$	m	soil defornmtion module

Table 6.3: Parameter values for lunar regolith simulant (via [29]).

6.7   Numerical Contact Mechanics

Sometimes, it is important to have a simplified model, similar to that of the Hertzian contact theory, for soft-soil interaction. This is especially useful if the multibody solver, like ADAMS View, does not implement a soft-soil interaction. To be precise, multibody solvers like ADAMS View provide both rigid and soft soil models, but the latter may result in a more cost-ineffective calculation. In order to emulate the mechanical response of such terrains, while reducing the compulational time needed, a series of contact parameters are introduced which derive from the analysis of some reference texts.

Such parameters are employed in the formulation of contact forces via ADAMS *IMPACT* function for the normal component and Coulomb-like friction models for the tangential behavior. While this approach does not capture the full complexity of soil-tire interaction (e.g., shear displacement, rut formation, and stress-dependent sinkage), it provides a computationally efficient and sufficiently accurate framework for preliminary dynamic analysis and performance assessment of wheeled vehicles on soft terrains.

The normal contact force P is computed using the *IMPACT* function as follows:

$$P = \begin{cases} \kappa \cdot h^n + c \cdot \partial_t h, & h > 0 \\ 0 & h \leq 0 \end{cases}$$

where:

1. κ is the contact stiffness (N/m^n),

2. h is the penetration depth (m),

3. n is the force exponent,

4. c is the damping coefficient $(N/(m/s))$,

5. $\partial_t h$ is the relative normal velocity (m/s).

The frictional force Q is modeled via a velocity-dependent interpolation between static and dynamic friction coefficients:

$$\mu(v) = \mu_d + (\mu_s - \mu_d) \cdot e^{-\left(\frac{v}{v_{tr,s}}\right)^2}$$

$$Q = \mu(v) \cdot P$$

where:

- μ_s, μ_d are the static and dynamic friction coefficients respectively,

- v is the tangential relative velocity at the contact interface,

- $v_{tr,s}$ is the transition velocity for static friction.

Terrain	κ	n (-)	c	μ_s	μ_d	$v_{tr,s}$	$v_{tr,d}$	C_{rr}	Ref.
Dry Sand	50×10^7	1.8	250	0.7	0.6	0.03	0.15	0.1 - 0.3	[33]
Wet Sand	1.2×10^7	1.8	600	0.8	0.7	0.04	0.15	0.05 - 0.2	[34]
Fine Gravel	2×10^7	2	800	0.65	0.55	0.04	0.15	0.02 - 0.05	[32]
Gross Gravel	7×10^7	2	2000	0.6	0.5	0.06	0.2	0.01 - 0.03	[32]
Compact Clay	3×10^7	1.5	1200	0.9	0.8	0.03	0.15	0.05 - 0.1	[35]
Lime	0.8×10^7	1.7	600	0.75	0.65	0.03	0.15	0.05 - 0.1	[35]
Lunar Regolith Simulant (JSC-1A/NU-LHT)	5×10^7	1.9	1000	0.85	0.75	0.02	0.1	0.01 - 0.02	[36]
Units	N/m^n	–	$N/(m/s)$	–	–	m/s	m/s	–	

Table 6.4: Simplified Contact parameters for soft soil.

Chapter 7

The CLASP Docking Subsystem

Based on the considerations outlined so far, it is evident that the development of a novel docking system is necessary for terrestrial exploration missions, whether lunar or Martian. This work presents an alternative approach to the docking systems currently in use. The proposed docking architecture, hereafter referred to as **Circumferential Lunar Annular Mooring for Surface Pressurized operations docking subsystem - CLASP**, is introduced as a viable solution to address the identified limitations.

In the subsequent chapter, the fundamental characteristics of the CLASP system will be detailed. Additionally, key design parameters will be identified and analyzed to ensure compliance with the safety and operational requirements of the PROTEUS pressurized rover mission.

7.1   Subsystem requirements definition

Docking requirements can follow, as for all entirety of the rover, the guidelines presented by the ECSS. Specifically, they are all listed as "Performance" requirements, as the aim of this work is to provide a valuable understanding of the performance of a docking subsystem, often dispatched by other sources [25]. In the following description, the subsystem's requirements fall under 2 categories:

1. *Misalignment Requirements*, derived from the considerations proposed in chapter 5. Many missions provided those value at *initial contact*, a particular condition latter discussed. As such, driven from the observations proposed in Table 5.3, a set of "Misalignment Requirements" is proposed.

2. *Load Requirements*, driven from the considerations proposed in chapter 6. The main loads on the docking subsystem are contact and pressurization loads. As such, loads requirements regarding those actions are set for further investigation and sizing of the system.

---

[1]Vector sum of y and z misalignments.

ID	Name	Symbol	Value	Un.	Ref.	Description
R-PERF-B-05	Translational misalignment y	$y_d(t_1)$	± 0.1	m	[25]	At first contact, the Docking Subsystem shall be sized to sustain a relative translational misalignment along y of y_d
R-PERF-B-06	Translational misalignment z	$z_d(t_1)$	± 0.1	m	[25]	At first contact, the Docking Subsystem shall be sized to sustain a relative translational misalignment along z of z_d
R-PERF-B-07	Relative trans. velocity x	$\dot{x}_d(t_1)$	0.1	m/s	[25]	At first contact, the Docking Subsystem shall be sized to sustain a relative translational velocity along x of $\dot{x}_d$
R-PERF-B-08	Relative trans. velocity y	$\dot{y}_d(t_1)$	± 0.04	m/s	[25]	At first contact, the Docking Subsystem shall be sized to sustain a relative translational velocity along y of $\dot{y}_d$
R-PERF-B-09	Relative trans. velocity z	$\dot{z}_d(t_1)$	± 0.04	m/s	[25]	At first contact, the Docking Subsystem shall be sized to sustain a relative translational velocity along z of $\dot{z}_d$
R-PERF-B-10	Angular misalignment x (roll)	$\phi_d(t_1)$	± 5	$^\circ$	[25]	At first contact, the Docking Subsystem shall be sized to sustain a relative angular misalignment along x of ϕ_d
R-PERF-B-11	Angular misalignment y (pitch)	$\vartheta_d(t_1)$	± 5	$^\circ$	[25]	At first contact, the Docking Subsystem shall be sized to sustain a relative angular misalignment along y of ϑ_d
R-PERF-B-12	Angular misalignment z (yaw)	$\psi_d(t_1)$	± 5	$^\circ$	[25]	At first contact, the Docking Subsystem shall be sized to sustain a relative angular misalignment along z of ψ_d
R-PERF-B-13	Relative ang. velocity x (roll)	$\dot{\phi}_d(t_1)$	± 0.02	$^\circ/s$	[25]	At first contact, the Docking Subsystem shall be sized to sustain a relative angular velocity along x of $\dot{\phi}_d$
R-PERF-B-14	Relative ang. velocity y (pitch)	$\dot{\vartheta}_d(t_1)$	$\pm 0.2^*$	$^\circ/s$	[25]	At first contact, the Docking Subsystem shall be sized to sustain a relative angular velocity along y of $\dot{\vartheta}_d$
R-PERF-B-15	Relative ang. velocity z (yaw)	$\dot{\psi}_d(t_1)$	$\pm 0.2^*$	$^\circ/s$	[25]	At first contact, the Docking Subsystem shall be sized to sustain a relative angular velocity along z of $\dot{\psi}_d$

Table 7.1: CLASP Docking Subsystem Requirements (Misalignment Requirements).

ID	Name	Symbol	Value	Un.	Ref.	Description
R-PERF-C-16	Maximum Contact Force	P_{adm}	3 500	N	[25]	The docking ALN subsystem shall be able to sustain P_{adm} contacting force.
R-PERF-C-17	Press. Static Load	p_{press}	1	atm		The docking structure shall sustain pressurization load when fully mated, up to p_{press}
R-PERF-B-18	Final relative position error	$r_{d,final}$	$1-3$	mm		At the end of the mating operation, the docking subsystem is considered fully mated if the relative position is less than $r_{d,final}$
R-PERF-B-19	Shock absorber damping	$\max\{\zeta_{II}\}$	1			The shock absorber dimensionless damping should be at least crytical.
R-PERF-B-20	Shock absorber natural freq.	$\max\{\omega_{n,II}\}$	$\leq \Omega_c$	rad/s		The shock absorber natural frequency should be at least crytical.
R-PERF-B-21	Capture distance	$r_{d,c}$	0.1	m		The HCS should activated when the relative distance is less thane $r_{d,c}$.
R-PERF-B-22	Final capture force	$F_{h,f}$	100	N		The HCS shall remain pre-loaded once fully docked, with a final preload of $F_{h,f}$.

Table 7.2: CLASP Docking Subsystem Requirements (Load Requirements).

7.2 Architectural description

7.2.1 Principal Characteristics

In chapter 4, the subdivision of docking architecture can be made in terms of **compatibility**:

1. *Androgynous* systems;

2. *Non-Androgynous* systems (composed of a *male* and a *female* indenter).

Another classification is made in terms of **central arrangement**, in which docking subsystems can be referred as:

1. *central*, like the *probe and drogue* mechanism.

2. *peripheral*, like the APAS.

7.2.2 Trade study

A trade study is a procedure useful to find the most balanced solution amongst a set of possible candidates to solve a certain problem. Trade studies are necessary to avoid committing too early to a design that may not meet all the technical specifications of a project. In this regard, several criteria were defined to evaluate each of the five concepts above described based on a scoring system. Moreover, a weight was introduced to increase the relevance of some parameters. Finally, the

total score of each mechanism was computed leading to final concept selection. The same procedure is exposed also in [18], as the current and the cited work provide a suitable infrastructure for determining a suitable choice of the docking mechanisms. It is essential to emphasize that these docking systems are designed exclusively for spacecraft operating in orbit. This limitation arises from the fact that, to date, no pressurized spacecraft has been integrated into an environment such as that of a vehicle. Consequently, the trade-off analysis primarily considers this constraint.

Trade-off criteria

Among all the parameters that could have been considered, the main chosen ones were mass, mechatronic complexity, the ability to work with targets with different masses, energy consumption and reliability. In particular:

1. the total **mass** evaluates the total mass of the mechanism. Considering a specific cost of $\mathcal{C}/m = 3000$ \$/kg [18], a small mass may reduce the overall cost of the mission.

2. the **mechatronic complexity** takes into account the intricacy of the mechanism from the hardware point of view. For this purpose three different aspects were evaluated:

   (a) *Mechanical complexity*: this parameter considers the complexity of the mechanical elements that compose the structure of the mechanism.

   (b) *Sensors*: this aspect is related to the sensors dedicated to the control and monitoring of the docking mechanism. Both the type and the number of sensors contribute to defining this parameter.

   (c) *Actuators*: this item assesses the mechanism in terms of actuation. Here again, the evaluation related to this parameter is defined considering the type and number of actuators. A lower number of actuators leads to a better system.

3. the **energy consumption** takes into account the energy necessary to drive the sensors and actuators dedicated to the mechanism.

4. The number of subsystems that combined create the whole docking mechanism is the main parameter used to evaluate the expected **reliability**: a lower number of subsystems leads to a better score. To compute the number of subsystems the actuators, sensors, and transmission chains were considered.

7.2.3   Trade-off Results

Based on considerations from [18], it is possible to depict the current trade off analysis results. 5 candidates have been chosen for the study:

1. peripheral fixed, as the Gemini VIII docking subsystem;

2. probe and drogue, as the Soyuz docking subsystem;

3. IDSS-like subsystems, both with and active and passive counterpart; in this context it means that an IDSS-active docking subsystem performs alignment via an active actuator (like an active Steward-Gough platform); conversely, a IDSS-passive docking subsystem is a new candidate, which performs the same interaction but without the need of an active actuators, maximizing mechatronic complexity.

4. articulated arms, like the OECS docking subsystem.

Criteria	Peripheral Fixed	Probe & Drogue	IDSS-passive	IDSS-active	Articulated Arms	Weights
Mass	4	5	4	3	4	2
Mechatronic complexity	5	4	5	3	2	5
Energy consumption	5	4	5	2	3	2
Shock attenuation	1	1	3	5	3	4
Reliability	5	5	5	2	4	4
Total	67	62	**75**	53	52	

Table 7.3: Trade-off analysis results

Mass

Mass plays a critical role in launch and in-orbit maneuvering efficiency. Subsystems such as the *Probe & Drogue* and *Peripheral Fixed* scored highly (5 and 4, respectively), reflecting their relatively simple and lightweight mechanical design. In contrast, the *IDSS-active* system scored lower (3), due to the inclusion of motorized alignment mechanisms and additional sensors, which increase structural mass. The *Articulated Arms* solution, despite being modular, also incurs a higher mass due to its extended moving components.

Mechatronic Complexity

Complexity directly impacts development cost, failure probability, and ease of integration. The *Peripheral Fixed* and *IDSS-passive* architectures received the highest score (5), as they rely on passive mechanisms or minimal actuation, reducing points of failure. On the other hand, the *Articulated Arms* scored the lowest (2), due to the presence of multiple actuated joints, coordinated control algorithms, and sensors required for autonomous alignment. The *IDSS-active*, incorporating active capture and latching systems, also scored low (3), indicating higher integration and control challenges.

Energy consumption

Energy constraints are stringent in orbital applications. Passive systems like *IDSS-passive* and *Peripheral Fixed* scored highest (5), as they require minimal or no active power for docking alignment and capture. Conversely, *IDSS-active* scored only 2 due to continuous actuation needs during approach and mating, while *Articulated Arms*

(score: 3) also involve powered elements during operation, although to a slightly lesser extent.

Shock Attenuation

Shock attenuation is essential to protect onboard instruments and crew during docking impact. The *IDSS-active* system was rated highest (5) for incorporating active damping mechanisms capable of adapting to varying approach velocities. Passive systems such as *Peripheral Fixed* and *Probe & Drogue* scored poorly (1), lacking energy-absorbing elements beyond basic structural compliance. The *IDSS-passive* design offered moderate damping through integrated buffering materials, reflected in a score of 3.

Reliability

Reliability encapsulates failure rate under repetitive mating operations and design redundancy. *IDSS-passive*, *Peripheral Fixed*, and *Probe & Drogue* all scored highly (5), representing mature and flight-proven systems with limited mechanical complexity. *IDSS-active* received the lowest reliability score (2), due to its dependency on multiple actuation points, real-time sensing, and software-driven control, increasing susceptibility to fault propagation. *Articulated Arms*, while offering operational flexibility, also present moderate risk (score: 4) due to the number of failure-prone actuators and joints.

Conclusions

Overall, the scoring reflects a clear trade-off between subsystem sophistication and performance risk. Systems with lower complexity and passive designs tend to score higher in mass, energy efficiency, and reliability, while more complex active systems benefit in precision docking and shock attenuation but are penalized for their energy demands and reduced robustness. The IDSS-passive scored higher than the other candidates. Based on the considerations made in the trade off analysis, a *peripheral passive* docking subsystem is chosen.

As for the *compatibility*, non-androgynous docking designs, in which the two mating interfaces are functionally distinct (i.e., male and female), tend to be easier and more reliable to implement compared to androgynous systems. Their mechanical asymmetry simplifies alignment and latching, as only one interface requires active guidance or capture mechanisms, reducing system complexity and actuation redundancy. Additionally, non-androgynous systems often feature fewer moving parts and a more deterministic docking sequence, which enhances reliability and fault tolerance. In contrast, androgynous systems must accommodate mutual compatibility, leading to increased mechatronic and software complexity, bilateral actuation, and often a higher risk of mechanical or control failure during autonomous operations.

To conclude, given the trade study proposed, a **non-androgynous peripheral passive** is selected to be sized for the CLASP docking subsystem.

7.2.4 Docking subsystem subdivision

Modern docking systems are typically defined by the following key components:

1. **Alignment System** (**ALN**): This subsystem is responsible for correctly aligning and accommodating the chaser within the designated docking interface on the target spacecraft during the approach phase. It is therefore responsible for:

   (a) the minimization of misalignments between the chaser and the target, both in terms of linear and angular misalignments;
   (b) the minimization of relative velocity between the two modules.

2. **Soft Capture System** (**SCS**): This mechanism ensures the initial secure attachment of the chaser to the docking interface of the target, providing preliminary structural connection and alignment.

3. **Hard Capture System** (**HCS**): The primary function of this system is to establish a hermetic seal between the chaser and the target. This seal enables the pressurization of the docking interface, allowing for the controlled opening of hatches on both spacecraft and facilitating the transfer of crew and equipment between them.

For the ALN, a bell-shaped revolved structure in the form of a ***double torus*** (also referred as "baseball-glove") has been selected as the generating geometry based on the considerations outlined in the trade-off analysis. This choice was adopted for the simplicity of its design. The important aspect of innovation that this subsystem introduces is the fact that the whole system is completely passive with no active moving parts. Hence, no power is required for the movement and no electro-mechanical complexity is added to the whole docking subsystem. This solution therefore reduces the overall complexity of the system while enhancing its reliability. In order to attenuate the impact interaction, while maintaining the effectiveness of a passive system, a set of ***springs*** and ***dampers*** was assembled to assist the female part of the ALN subsystem.

For the SCS, the proposed solution introduces a significant distinction compared to previous docking systems designed for space applications. The presence of a solid terrain, and consequently the influence of a stronger gravitational field and friction between the wheels of the pressurized rover and the lunar surface, enables the possibility of utilizing wheel braking. In this context, the soft capture procedure can be enhanced by engaging the rovers ***wheel brakes***, thereby generating a braking torque to maintain the aligned position established by the ALN system.

And finally, for the HCS, the solution proposed by the IDSS has been adopted. This configuration consists of ***twelve pairs of passive and active hooks*** distributed between the chaser and the target. The implementation of this design ensures continuity with modern docking system developments, as it has demonstrated high reliability, particularly for missions requiring repeated docking operations over time.

Based on these preliminary choices, it is therefore possible to define the reference framework for the correct sizing of the CLASP docking system. Further chapters are dedicated to the investigation and the evaluation of the performance of such subsystem.
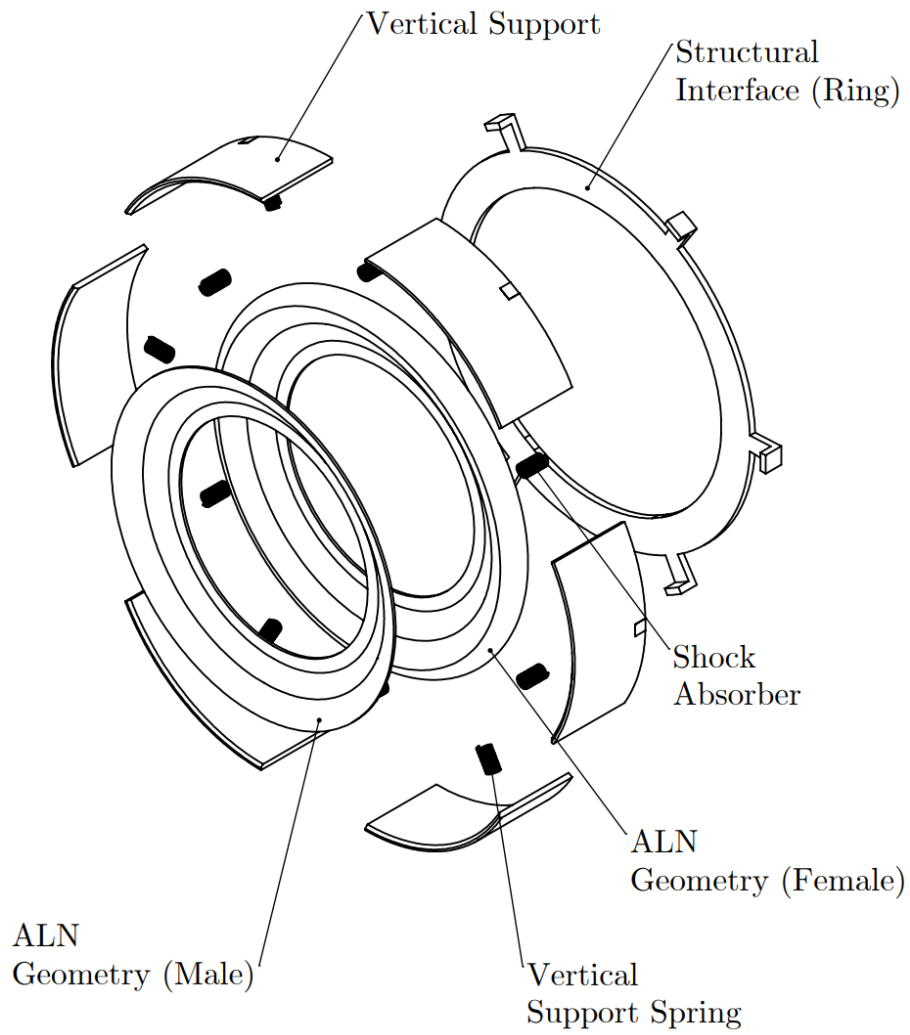
Figure 7.1: Exploded View of the Full docking subsystem (male and female).

Chapter 8

The Docking ALN Subsystem

The first set of components in the docking subsystem is the Alignment System (Docking) (ALN). To accurately size an ALN subsystem, a comprehensive review of the relevant literature is essential. The objective of this chapter is to conduct a detailed analysis of the appropriate geometric configuration and dynamic parameters governing the performance of the subsystem.

8.1 Performance evaluation

8.1.1 The performance model

In order to evaluate the performances properly, an exemplified model is introduced. Typical ALN subsystems are composed of an **alignment geometry** and a spring-damper mechanism (named **shock absorber**) to attenuate the impact interaction during docking, while reducing relative misalignment linear, angular and velocity errors. This motion can be ascribed as that of the following system (see Figure 8.1), subsequently referred as the *performance model*. Some ALN subsystem include both active and passive components. The proposed investigation uses only passive mechanism in order to achieve mating. The **performance model** is therefore composed of the following elements:
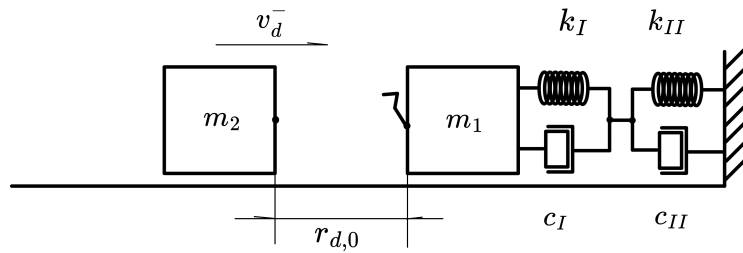
Figure 8.1: Performance model schematics.

1. mass m_1 and mass m_2 which emulate the mass of the alignment geometry (on the female side) and the total target and the ALN double torus structure (on the male side). In the reference $\mathcal{R}_0$, m_1 is at rest and m_2 is moving with velocity $v = v_d^-$ over a frictionless plane at a distance $r_{d,0}$ with respect to m_1. The value of this velocity is the longitudinal approach velocity listed in the Misalignment Requirements in chapter 7.

2. a stiffening, non-linear spring with coefficient k_I; this component mimics the contact of the alignment geometry, hence, given x_2 the position of mass m_2

$$F_I(t) = k_I x_I^n(t) = k_I h^n(t) = P(h) \tag{8.1}$$

where $k_I = \kappa_{ref} \cdot C_g$, contact parameters defined in chapter 6.

3. a linear spring-damper which resembles the homonym system mounted on the real structure. The whole intricacies of spring and dampers are modeled as k_{II} and c_{II}. The force is therefore

$$F_{II}(t) = k_{II} x_{II}(t) + c_{II} \dot{x}_{II}(t) \tag{8.2}$$

The aim of this model is to capture the essential components and parameters of the final model. Some hypotheses are therefore implicitly made:

1. geometries are neglected in this simple model and rotational motion of both m_1 and m_2 is not described. This is a limitation of the performance model that will further be addressed in the evaluation of the contact parameters.

2. Denoting Ω_c the contact characteristic frequency and $\omega_{n,II}$ the spring-damping natural frequency, and assuming $\omega_{n,II} \ll \Omega_c$, the motion of the two springs can be treated separately. In particular, the ratio between the two frequency is small

$$\frac{\omega_{n,II}}{\Omega_c} \ll 1 \tag{8.3}$$

This assumption is fair to assume given the scale of the displacements of those problems.

3. The two masses are *not* equivalent, i.e. $m_1 \ll m_2$; this is because in m_2 both ALN and the vehicle are considered, while in m_1 the target is considered still, and not moving with respect to $\mathcal{R}_0$.

4. After complete relaxation of the the shock absorber, the two bodies are kept together via a hook-mechanism, modeled with

$$F_{HCS} = k_{HCS} \cdot r_d$$

8.1.2   Docking sequence

The total maneuver is therefore described by the following time:

1. at $t = t_0$, the **Initial State** (**IS**). The mass m_2 is moving at a constant velocity $v_{d,ref} = v_d^-$ at a distance $r_{d,0}$ with respect to m_1;

2. at $t = t_1$ the (**ICC**) is achieved. Initial Contact is the time stamp in which the two alignment geometry initially touch. Misalignment requirements mentioned in chapter 7 refer to this condition.

3. at $t = t_2 = t_1 + \tau_I$ the first contact is considered completed. τ_I denotes the contact characteristic time, and it is related to the contact frequency by $\Omega_c = 2\pi/\tau_I$. The shock-absorber intervenes to dampen the system.

4. at $t = t_3 = t_2 + \tau_{II}$ the shock absorber reaches maximum abbreviation (and hence maximum spring force), and starts relaxing.

5. at $t = t_4$ the shock absorber is again fully extended.

6. at $t = t_5$ if the ALN female geometry has properly welcomed the male counterpart, the hooks are activated and the wheels are braked.

7. at $t = t_6$ the hooks are fully deployed, and the minimum distance is reached. The mating operation is considered completed and the pressurization can start.

8. at $t = t_7$ the pressurization has finished. The doors can be opened and the astronauts can transit.

The total time of the operation is therefore given by

$$t_{tot} = t_7 = t_{press} + t_{hooks} + 2\tau_{II} + \tau_I + \frac{r_{d,0}}{v_{d,ref}} \tag{8.4}$$

where:

1. t_{press} is the pressurization time.

2. t_{hooks} is the total time of activation of the hooks and the braking.

3. $r_{d,0}$ is the initial distance between the two bodies.

Given that the other times are relatively small compared to the approach time $d_{initial}/v_{ref}$, the total time is estimated as a fraction of this time

$$t_{tot} \cong (1 + k_{initial}) \frac{r_{d,0}}{v_{d,ref}}$$

with $k_{initial} = 0.5$.

8.1.3 Initial Contact Conditions

A particular attention is dedicated to Initial Contact Conditions. As stated before, those geometrical conditions are defined in the Misalignments Requirements in chapter 7. From this conditions $t = t_1$, imposing a certain motion (like ones depicted in chapter 5, Dynamics) it is possible to retroactively calculate the Initial State conditions of the mass m_2 at $t = t_0$. A notable example of this situation regards the decoupling approximation seen in chapter 5. If the following assumptions are made between t_0 and t_1:

1. the terrain is fairly planar;

2. the speed $v_{d,ref}$ is held constant in module;

3. the speed $v_{d,ref}$ is held constant in direction and so ϕ_d is held constant;
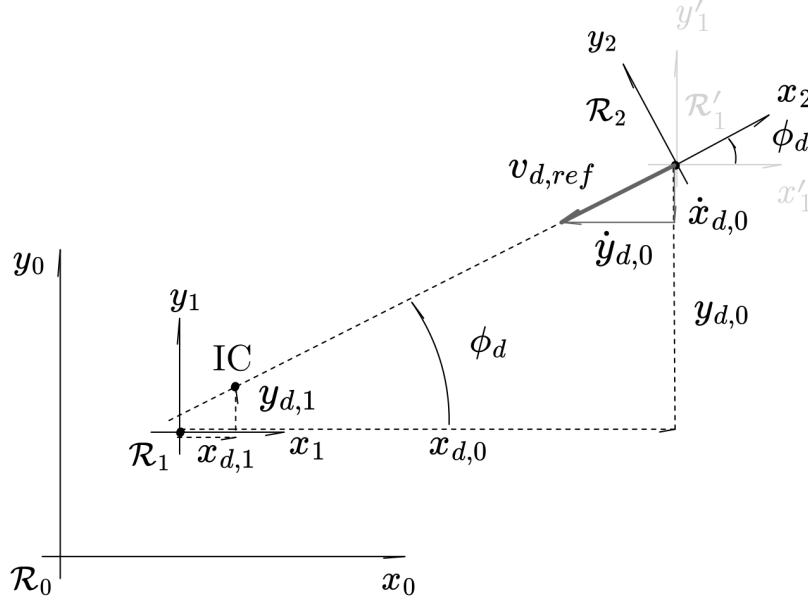
Figure 8.2: Initial Contact Conditions.

The ICC are defined by $(x_{d,1}, y_{d,1}, \phi_{d,1})$ set as requirement. The IS is therefore defined by:

$$\begin{cases} x_{d,0} - x_{d,1} = v_{d,ref} \cdot (t_1 - t_0) \cdot \cos \phi_{d,1} \\ x_{y,0} - x_{d,1} = v_{d,ref} \cdot (t_1 - t_0) \cdot \sin \phi_{d,1} \\ \phi_{d,0} = \phi_{d,1} \end{cases} \tag{8.5}$$

It is important to notice that on IC, the docking center are not coincident. From the image in fact, it is possible to describe a $r_{d,1} = \sqrt{x_{d,1}^2 + y_{d,1}^2} > 0$. This value can be discarded for time estimation, given that usually the approach distance $v_{d,ref} \cdot (t_1 - t_0)$ is usually large and therefore it is assumed that $\tilde{r}_{d,0} = v_{d,ref} \cdot (t_1 - t_0)$. For instance, in the previous example, the committed error is

$$\frac{r_{d,0} - \tilde{r}_{d,0}}{r_{d,0}} = 1 - \frac{1}{\sqrt{\left(\frac{x_{d,1}}{v_d \cdot (t_1 - t_0)} + 1\right)^2 + \left(\frac{y_{d,1}}{v_d \cdot (t_1 - t_0)} + 1\right)^2}} \tag{8.6}$$

8.1.4   Performance model dynamics

Contact modeling

Given the second assumption, the contact and the spring-damping motion can be decoupled. In this way, contact indentation $x_I = h$ and spring-damping displacement x_{II} are treated as two distinct problem. Moreover, given that the contact characteristic time is small compared to τ_{II}, it is assumed that x_I is an inertial reference frame. The motion of x_{II} is neglected during contact. Taking inspiration from [30], by denoting the *reduced mass* μ in the G reference frame of m_1 and m_2:

$$\frac{1}{\mu} = \frac{1}{m_1} + \frac{1}{m_2}$$
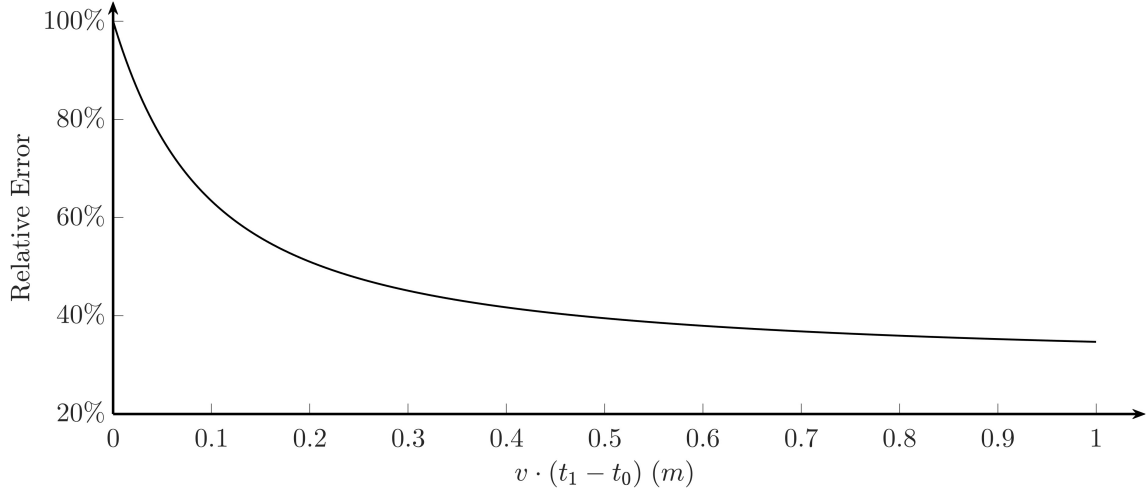
Figure 8.3: Relative error in initial position estimation. The values of ICC are listed in chapter 7.

The contact problem is described by the conservation of energy. Before contact, the total energy is kinetic, given the relative velocity v_{ref}

$$E = T = \frac{1}{2}\mu v_{ref}^2$$

and during the contact, this energy is balanced out by

$$E = T + U = \frac{1}{2}\mu \left(\frac{dx_I}{dt}\right)^2 + \frac{1}{2}Px_I$$

and given $P = F_I = k_I x_I \implies U = (1/2)k_I x_I^{n+1}$. The problem is therefore addressed by the following equation

$$\mu \left(\frac{dx_I}{dt}\right)^2 + k_I x_I^{n+1} = \mu v_{ref}^2 \tag{8.7}$$

The maximum indentation $\max\{x_I\} = \max\{h\} = h_{max}$ occurs when the final relative velocity is null, and therefore

$$h_{max} = \left(\frac{\mu v_{ref}^2}{k_I}\right)^{\frac{1}{n+1}} \tag{8.8}$$

Therefore, the maximum force is

$$P(h_{max}) = P_{max} = k_I h_{max}^n = (\kappa_{ref} \cdot C_P) \cdot h_{max}^n \tag{8.9}$$

To address the second hypothesis, the contact time is therefore evaluated as follows [30],

$$\tau_I = 2 \int_0^{h_{max}} \frac{1}{\sqrt{v_{ref}^2 - (k_I/\mu)h^{n+1}}} dh$$

$$= \frac{2}{v_{ref}} \int_0^{h_{max}} \frac{1}{\sqrt{1 - [(k_I/\mu v_{ref}^2)^{1/(n+1)} \cdot h]^{n+1}}} dh$$

$$= \frac{2}{v_{ref}} \int_0^{h_{max}} \frac{1}{\sqrt{1 - (h/h_{max})^{1/(n+1)}}} dh$$

$$= \frac{2 h_{max}}{v_{ref}} \int_0^1 \frac{1}{\sqrt{1 - s^{1/(n+1)}}} ds \qquad s = h/h_{max}$$

$$= \frac{2 h_{max}}{v_{ref}} \sqrt{\pi} \frac{\Gamma\left(1 + \frac{1}{n+1}\right)}{\Gamma\left(\frac{1}{2} + \frac{1}{n+1}\right)}$$

where $\Gamma(x)$ is Euler's Gamma function. For example, for $n = 3/2$ (as in the case of linear elastic materials considered in the Hertzian theory),

$$\tau_I = 2 \frac{h_{max}}{v_{ref}} \cdot \sqrt{\pi} \frac{\Gamma\left(1 + \frac{1}{n+1}\right)}{\Gamma\left(\frac{1}{2} + \frac{1}{n+1}\right)} \approx 2 \frac{h_{max}}{v_{ref}} \cdot 1.47 \tag{8.10}$$

Another remarkable observation is that, due to the third hypothesis

$$\mu = \frac{m_1 m_2}{m_1 + m_2} = \frac{m_1 m_2}{m_2(m_1/m_1 + 1)} \approx m_1$$

and therefore the reduced mass of the system is mostly attributed to m_1. It should be noted that if damping is inscribed, such that $P_{damp} = c_I \, dh/dt$, Equation 8.11 yields

$$\mu \left(\frac{dx_I}{dt}\right)^2 + k_I x_I^{n+1} - \mu v_{ref}^2 = -2 c_I \left(\frac{dx_I}{dt}\right) \cdot x_I \tag{8.11}$$

The maximum indentation depth h_{max} remains the same, but the contact time is different, although still proportional to τ_I. By inserting a small amount of damping in this system, the relative velocity is zero. The two masses are stuck together. But given that x_I is not an inertial frame, because it is mounted to the spring damper, the motion of the whole system is yet to be concluded in $\mathcal{R}_0$.

Spring-damper modeling

After contact $t = t_2$, the second phase of alignment is conducted. Assuming the two bodies remain in contact, the motion of the entire system is described by

$$M \ddot{x}_{II}(t) + c_{II} \dot{x}_{II}(t) + k_{II}[x_{II}(t) - \ell_{0,II}] = P(t)$$

with $M = m_1 + m_2$, whose solution is harmonic and well known in literature. Assuming the contact force is harmonic

$$P(t) = P_{max} \sin(\Omega_c(t - t_1)) \tag{8.12}$$

with $\Omega_c = 2\pi/\tau_I$. Although not harmonic (from the discussion in the previous section), it is safe to assume that the contact varies through time. This solution is
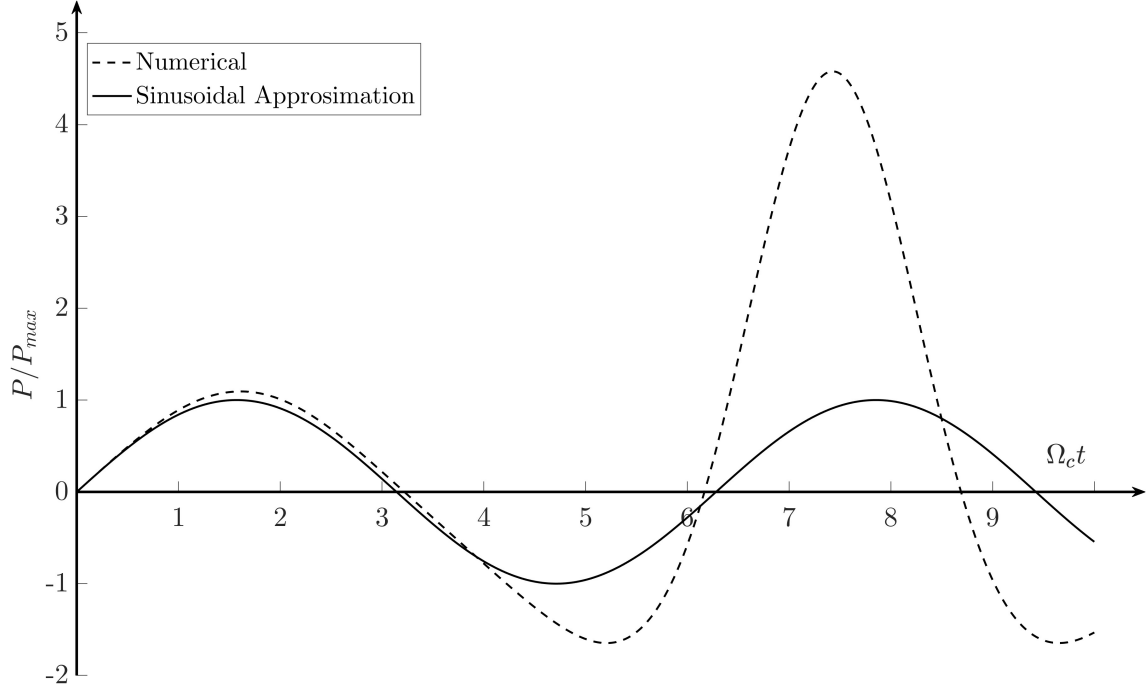
Figure 8.4: Sinusoidal approximation of contact force.

true in the first contact (i.e. after 1 period of contact τ_I). The following graph shows the relation between the numerical solution of Equation 8.11 with Equation 8.12.

After the contact, the velocity is

$$M v^+ = m_2 v^- = m_2 v_{ref}$$

$$\dot{x}_{II}(\tau_c) = v^+ = \frac{m_2}{M} v^- \cong v^- = v_{ref}$$

and setting $x_{II}(t_2) = \ell_{0,II}$, the complete problem is addressed by

$$\begin{cases} M \ddot{x}_{II}(t) + c_{II}\dot{x}_{II}(t) + k_{II}[x_{II}(t) - \ell_{0,II}] = P_{max} \sin(n\Omega_c(t - t_1)) \\ x_{II}(t_2) \cong x_{II}(t_1) = \ell_{0,II} \\ \dot{x}_{II}(t_2) \cong \dot{x}_{II}(t_1) = v_{ref} \end{cases} \tag{8.13}$$

whose solution is

$$x_{II}(t) = \frac{v_{ref}}{\omega_d} e^{-\zeta\omega_n(t-t_2)} \sin(\omega_d(t - t_2))$$

with the characteristic parameters of the problem

$$\begin{cases} \omega_{n,II}^2 = k_{II}/M \\ 2\zeta \cdot \omega_{n,II} = c_{II}/M \\ \omega_{d,II} = \omega_{n,II}\sqrt{1 - \zeta^2} \end{cases}$$

or, conversely, by choosing $M \cong m_2$ (which is the total mass of the LPR), Ω_c (which depends on contact properties from Equation 8.10) the dimensional properties of the problem can be calculated.

$$\begin{cases} k_{II} = \omega_{n,II}^2 M \\ c_{II} = 2\zeta\omega_{n,II} M \end{cases} \tag{8.14}$$

8.1.5   Model effectiveness

In order to evaluate the performance of the model, an **effectiveness parameter** is introduced to evaluate the performance of the model. This parameter functions as an objective of the optimization tool that is intended to be evaluated and needs to consider:

1. the practical achievement of the ALN manuever (minimizing the docking misalignment);

2. safety considerations, as some solutions that are extremely precise may be also extremely disruptive and lead to the damaging of the docking subsystem as well as the mating spacecraft.

The following effectiveness is therefore introduced as the **relative misalignment error**.

$$\text{þ} = \frac{r_d}{r_{d,1}} \quad \text{such that}$$
$$P < P_{adm} \tag{8.15}$$

in which:

1. r_d is the relative docking distance (between the two docking centers);

2. P is the contact force of the system;

3. $r_{d,1}$ is the reference relative docking distance at ICC as it is prescribed as requirement in chapter 7 as the vectorial sum of all misalignments at initial contact $r_{d,1} = r_d(t_1) = \sqrt{x_d^2(t_1) + y_d^2(t_1) + z_d^2(t_1)}$

4. P_{adm} is the reference contact force; this value is set as requirement in chapter 7.

To sum up, the performance problem consists of two inter-meshing masses m_1 and m_2 linked with two spring-damped mechanisms that mimic the two components of the ALN subsystem. The complete state of the system is therefore modeled by

$$m_1, m_2 \quad k_I, c_I \quad k_{II}, c_{II}$$

The mass estimate of the vehicle can be addressed in the first chapter, while the stiffness of the contact and the spring-damper characteristic need an in-depth investigation. The objective is to minimize the relative misalignment error. For the sake of completeness, it should be noted that þ (pronounced as Thorn, or þorn, as in the name of this author's work) is used as the symbol for relative misalignment error.

8.2 Geometry selection

8.2.1 Frustum

As for the alignment geometry, the current state of the art proposes **axial-symmetric structures** due to the nature of the problem. The simplest structure is that of a cone, or more specifically of the truncated cone, referred also as a **frustum**. ALN subsystems like the APAS and the Gemini VIII use or have used those types of geometry in order to achieve contact. As a first iteration, the same geometry is proposed.
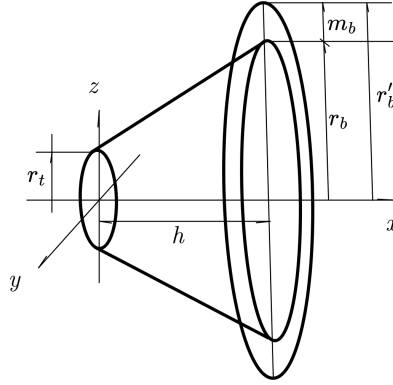
Figure 8.5: Frustum generative surface.

Given the rapid change in slope of the male frustum, an asymptotic discussion is addressed. It is possible to assume a small curvature radius on the male alignment system, revolving around the cone axis. The shape that this curvature radius creates is that of a **torus**. Assuming that the curvature radius is small the problem can be evaluated as that of a torus impacting over a planar surface, which is a good approximation of the surface of the female truncated cone. This contact problem is well discussed in [37] and [38]. A torus is a surface of revolution generated by revolving a circle in three-dimensional space one full revolution about an axis that is coplanar with the circle. It is described in space by the following equation (revolution about $x-$axis),

$$(\sqrt{y^2 + z^2} - r_t)^2 + x^2 = r_m^2$$
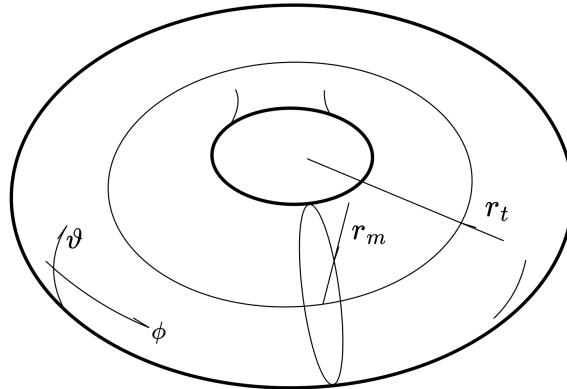
given r_m and r_t the meridional and the toroidal radii respectively. For simplicity, only the case of $r_m < r_t$ is discussed, as other solutions may lead to self-intersecting geometry. Given an implicit parametrization $(\phi, \vartheta) \equiv (u, v)$ along the

toroidal (around the revolution circle) and meridional (around the main circle) axis respectively, the two radii of curvature are [37] [39]:

$$R_u = \frac{r_m \cos \vartheta + r_t}{\cos \vartheta} = r_m + r_t \sec \vartheta \qquad R_v = r_m \qquad (8.16)$$

In both studies it is possible to evaluate that a large toroidal curvature (and hence a small toroidal curvature radius $R_v = r_m$) leads to an intensification of stresses on the torus. Moreover, it is safe to assume that small curvature radius will lead to a slippery contact between the two alignment geometries.

8.2.2   Single toroidal section

In order to attenuate internal stresses and provide a softer, continuous relative motion, a second iteration of the geometry is proposed, which consists of a **single toroidal section** on each geometry.
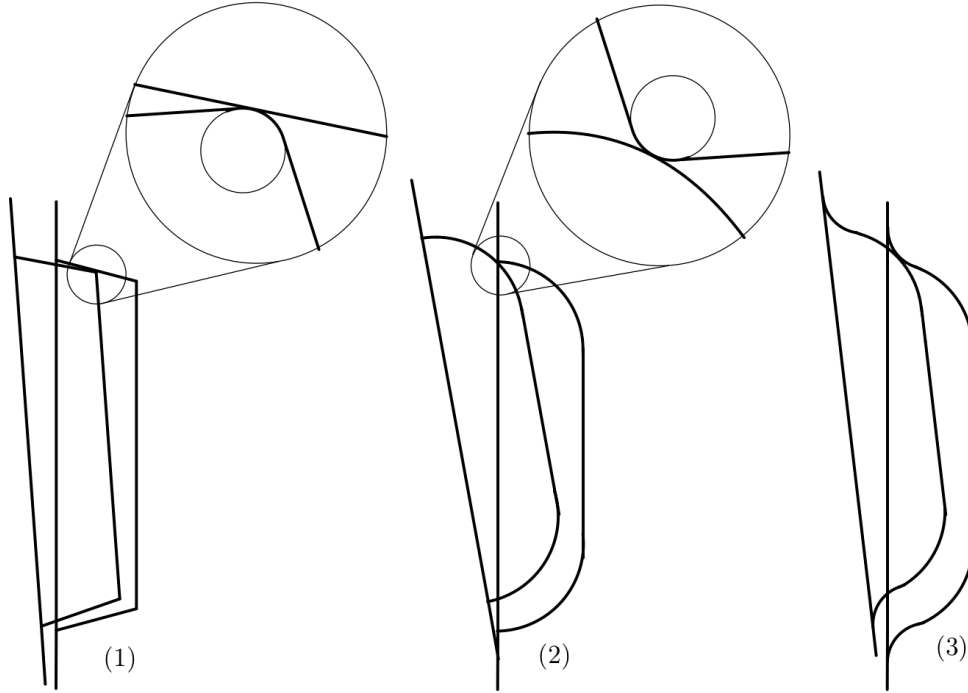
Figure 8.6: The three design iteration of the ALN geometry: the frustum (1), the single torus (2) and the double torus (3).

This solution solves some issues encountered with the former geometry, but addresses another problem. The same indentation argument and therefore the constitution of discontinuous friction comes at the tip of the female alignment geometry (see above figure). Therefore, the same argument is brought to the table and a third iteration of the alignment geometry is developed.

8.2.3 Double toroidal section

In this third iteration, a **double toroidal section** is developed as an alignment geometry. This solution attenuates stresses and friction in all the geometrical contact domain (i.e. in the two generating surfaces of the two alignment geometry). Each alignment geometry has a set of geometrical variables, listed as:

1. the inner torus toroidal radius r_t;

2. the inner torus meridional radius r_m;

3. the outer torus meridional radius r'_m;

4. the global radius of the structure (which is equal to the outer torus toroidal radius) r'_t;

5. the height of the structure h;

In order to evaluate the contact properties chapter 6 of the structure, some assumptions are proposed.
On both structures all the radii are respectively equal. That is

$$
\begin{cases}
r_m^{(1)} = r_m^{(2)} = r_m \\
r_t^{(1)} = r_t^{(2)} = r_t \\
r_m'^{(1)} = r_m'^{(2)} = r'_m \\
r_t'^{(1)} = r_t'^{(2)} = r'_t
\end{cases}
$$

Not all of these parameters are independent one with the others. In fact, the relationships between them are of geometric nature.

$$
\begin{cases}
h = r_m \\
r'_m - r'_m \sin \vartheta^* = r_m \sin \vartheta^* \\
r'_t = r_t + r_m \cos \vartheta^* + r'_m \cos \vartheta^*
\end{cases}
\tag{8.17}
$$

Given the set of 6 parameters (including ϑ^*) and 4 equations, only one parameter is left out as independent. In order to generalize the proposed results, the above equations are set dimensionless given the characteristic length $\ell = r'_t$:

$$
\rho'_m = r'_m/\ell \quad \rho'_t = r'_t/\ell = 1 \quad \rho_t = r_t/\ell \quad \rho_h = h/\ell
$$

and defining the **meridional ratio** between r_m and r'_m

$$
\varpi = \frac{r_m}{r'_m} = \frac{\rho_m}{\rho'_m}
$$

the problem is defined by

$$
\begin{cases}
\rho_h = \rho_m \\
\vartheta^* = \arcsin \left(\dfrac{\varpi}{1 + \varpi} \right) \\
\rho_t = 1 - \rho_m \cdot \sqrt{2\varpi + 1}
\end{cases}
\tag{8.18}
$$
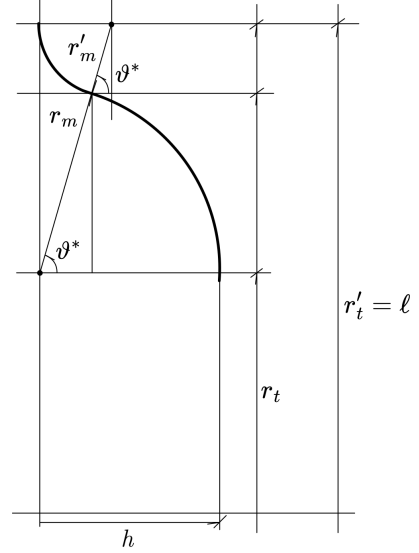
By the arguments proposed in chapter 6, the first step of analyzing a contact is to address the curvature radii of the two structures. The double torus offers 3 types of inter-meshing geometry:

1. inner-inner torus contact;

2. inner-outer torus contact;

3. outer-outer torus contact.

Given the symmetries in the figure, it is safe to assume that the most critical situation is the inner-outer torus contact. For this condition, the curvature radii of the two structures are given in the following table. For simplicity, it is assumed that the first body (1) is the outer torus, indenting with (2) as the inner torus.

Torus	R_u	R_v
(1)	$-(r'_m + r'_t \sec \vartheta^{(1)})$	r'_m
(2)	$r_m + r_t \sec \vartheta^{(2)}$	r_m

Table 8.1: Curvature radii of the two contacting torii.
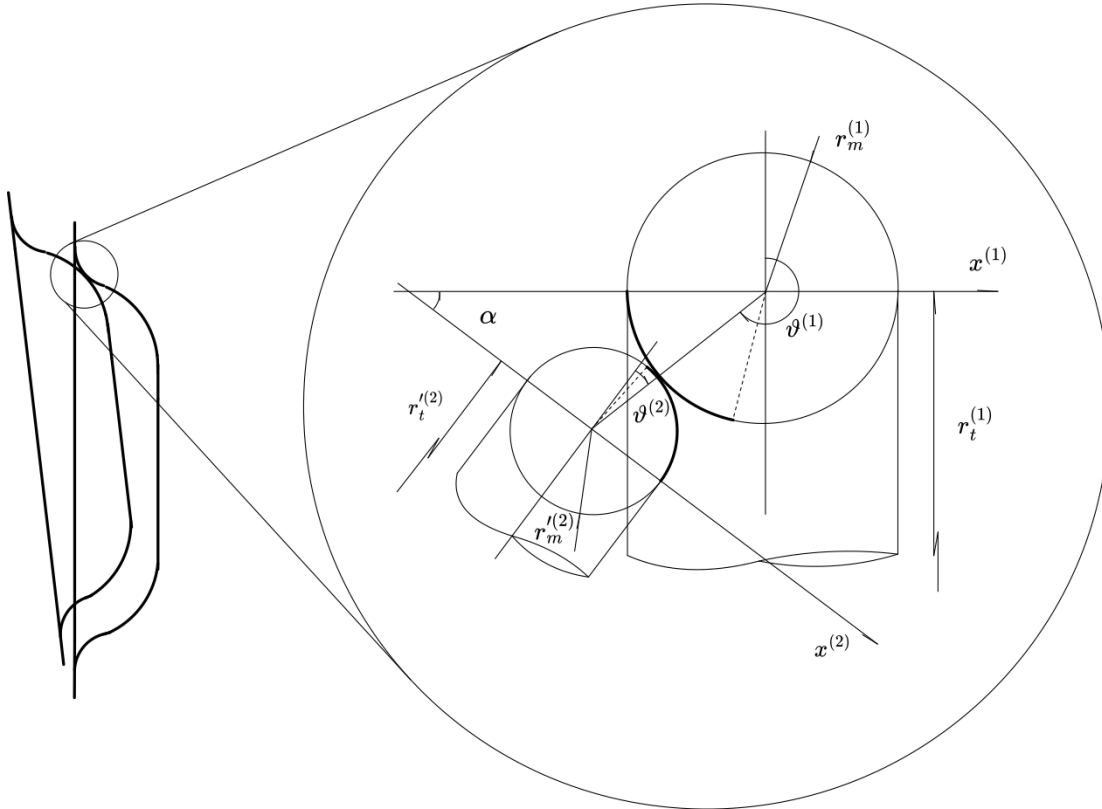
Figure 8.7: Inner-outer torus contact mechanics schematics.

with

$$\left(\frac{3}{2}\pi - \vartheta^{(1)}\right) + \left(\frac{\pi}{2} + \vartheta^{(2)}\right) + \alpha = \pi,$$

$$\vartheta^{(1)} - \vartheta^{(2)} = \pi + \alpha$$

$$\pi + \vartheta^* \le \vartheta^{(1)} \le \pi + \pi/2$$

$$\vartheta^* \le \vartheta^{(2)} \le \pi/2$$

The curvatures A, B are given from Equation 6.5. It is important to notice that e_g is not affected by a choice of a characteristic length

$$e_g = \sqrt{1 - \frac{A}{B}} = \sqrt{1 - \frac{A\ell}{B\ell}}$$

given $A\ell$ and $B\ell$ the dimensionless values of A and B. Therefore, **dimensionless curvature radii** are proposed, setting the characteristic length

$$\ell = r_t$$

and by setting $\vartheta^{(2)} = \vartheta \implies \vartheta^{(1)} = \vartheta + (\pi + \alpha)$, Table 8.2 proposes a correct evaluation for the dimensionless curvature radii.

Torus	$\boldsymbol{R_u/\ell}$	$\boldsymbol{R_v/\ell}$
(1)	$-(\varpi\rho_m + \sec(\vartheta + (\pi + \alpha)))$	$\rho'_m = \varpi\rho_m$
(2)	$\rho_m + \rho_t \sec\vartheta$	ρ_m

Table 8.2: Dimensionless curvature radii of the two contacting torii.

The computational process is therefore the following:

1. evaluate independent geometrical properties ϖ, ρ_m and choose a contacting condition α, ϑ.

2. evaluated dependent geometrical properties ρ_t, ϑ^*;

3. compute the curvature radii $R_k^{(j)}/\ell$;

4. compute the equivalent gap eccentricity e_g;

5. compute the contact area eccentricity e;

6. estimate the geometry coefficient C_g.

It should be noted that independent geometrical properties ϖ, ρ_m are design parameters and the objective of this sizing, while ϑ, α are determined by the contact conditions. Particularly, given Figure 8.8, the set of parameters is directly related to the stated misalignments $(x_{d,1}, y_{d,1}, \phi_{d,1})$, the following geometrical equations apply:

$$\begin{cases} x_d(t_1) = x_{d,1} = r_t \cdot \sin\alpha & + r_m(\sin(\vartheta + \alpha) - \sin\vartheta^*) + r'_m(\sin(\vartheta - \alpha) - \sin\vartheta^*) \\ y_d(t_1) = y_{d,1} = r_t \cdot (1 - \cos\alpha) & + r_m(\cos(\vartheta + \alpha) - \cos\vartheta^*) + r'_m(\cos(\vartheta - \alpha) - \cos\vartheta^*) \\ \phi_d(t_1) = \phi_{d,1} = \alpha \end{cases}$$

$$(8.19)$$
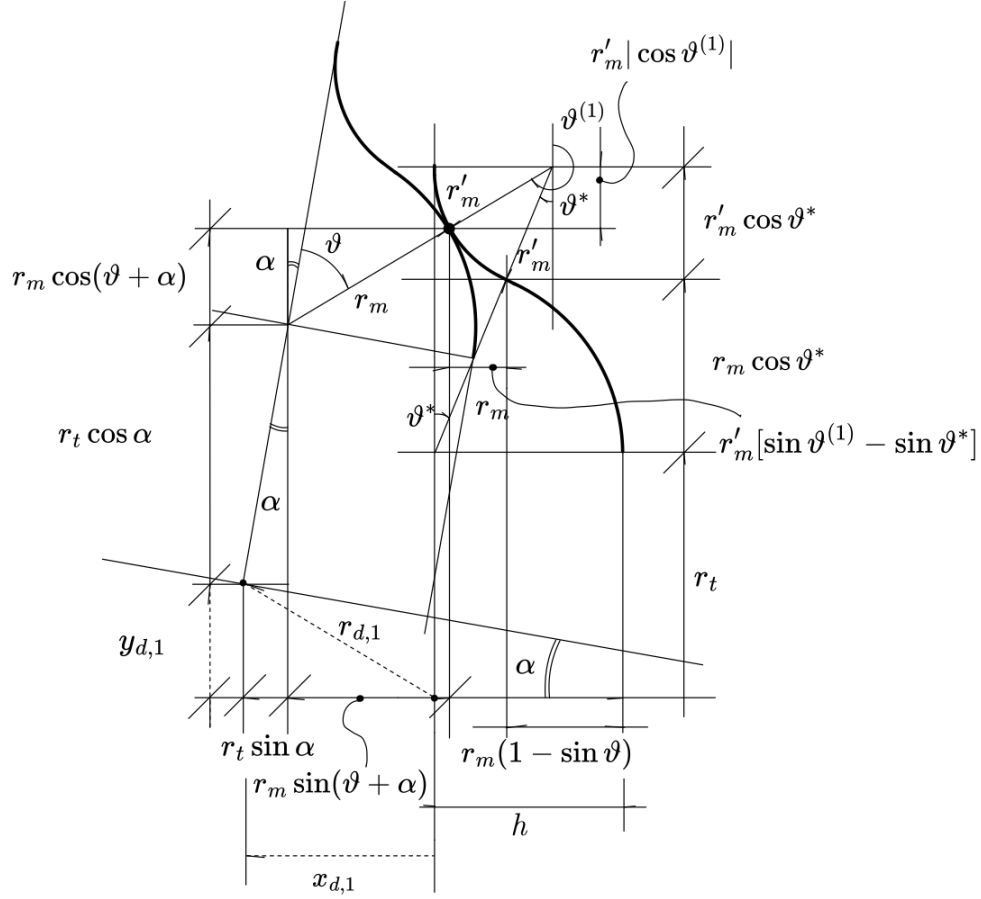
Figure 8.8: Geometrical relationship between misalignments parameters and boundary conditions in the contact problem.

Those equations, coupled with the torus parametrization yield a 1 : 1 correspondence to the aforementioned misalignments.

$$(x_{d,1}, y_{d,1}, \phi_{d,1}) \leftrightarrow (\alpha, \vartheta) + \text{torus parametrization}$$

Therefore, the objective for those two latter parameters is to choose a proper value that describes the geometrical effects of contact as an average for the whole system.

Dependence over initial conditions

The following plot shows the contact area eccentricity e as a function of ϑ for different values of ρ_m (α is set to zero and ϖ is set to one). The problem describes two axis-parallel tori indenting with the same meridional radius (the tori are not equal given $\rho'_t = r_t/r'_r \neq 1$). This problem is highly elliptical and more than often results in numerical discrepancy. Therefore ϑ is varied until a limiting angle $\vartheta^* \leq \vartheta \leq \vartheta_{lim} = \pi/2 \cdot (1 - \epsilon_\vartheta)$ (with $\epsilon_\vartheta = 0.05$). The fact that the problem becomes highly elliptical is attributed to the geometry of the problem itself. In the limiting case $\vartheta \to \pi/2$ and $\varpi \to 1$, the problem is adjacent to that of two indenting cylinders (bidimensional contact).
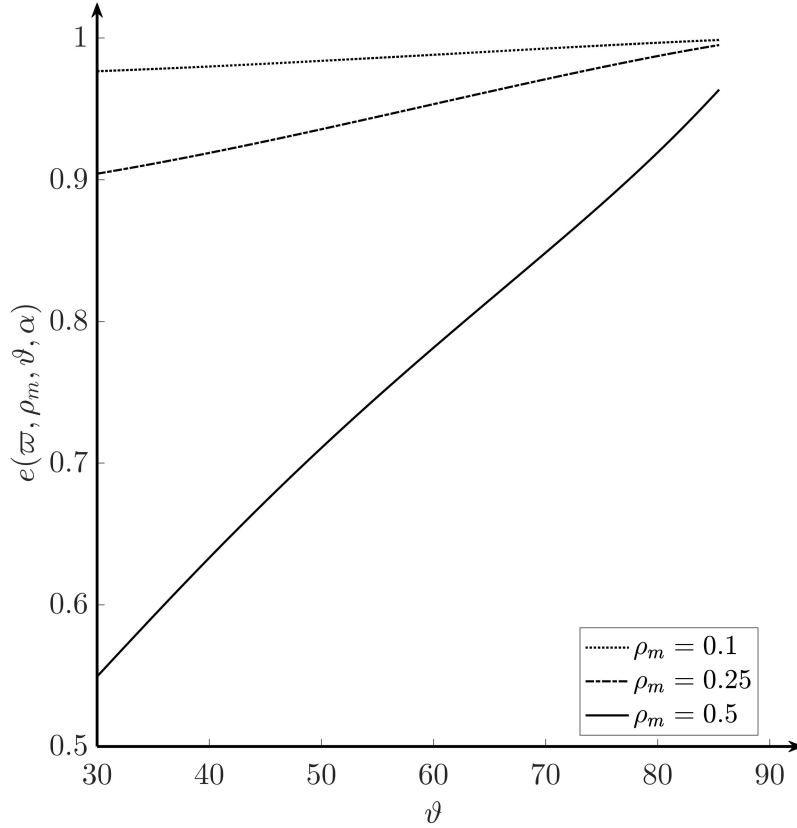
Figure 8.9: Eccentricity plot as a function of ϑ for different values of ρ_m ($\alpha = 0$, $\varpi = 1$).

Given discussion proposed in chapter 6, it is possible to parametrize the Geometry coefficient $C_g(e, B\ell, n)$. As the graph shows, an highly dependence over larger ϑ is expected (given the higher eccentricity), but less dependence from α is found. This result is also dependent by the fact that low inclinations are treated (given the requirements in chapter 7). In particular, the **minimum value** of C_g (and hence, the minimum admissible force P_{adm}) is found for $\vartheta = \vartheta^*$ and $\alpha = \alpha^* = 0$.

From those results it is possible to see that:

1. $\alpha = \alpha^* = 0$ is the most critical solution for relative misalignment;

2. $\vartheta = \vartheta^*$ is the most critical solution for relative position over the torus;

Moreover, given Figure 8.8 equations, it should be noticed that this condition corresponds to the aligned condition $(x_{d,1}, y_{d,1}, \phi_{d,1}) = (0, 0, 0)$.
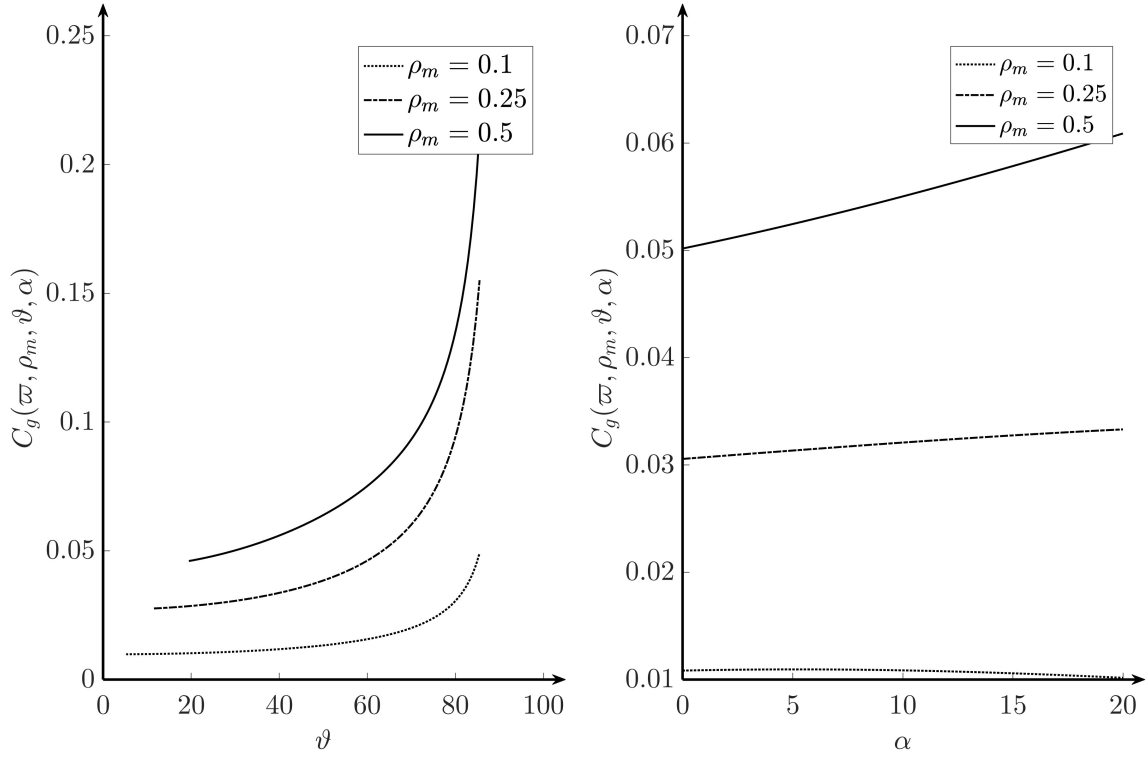
Figure 8.10: C_g plot as a function of ϑ and α for different values of ρ_m ($\varpi = 1$).

Dependence over design parameters

The following plot shows the contact dimensionless as a function of ϖ ($\alpha = \alpha^*$ and $\vartheta = \vartheta^*$) and ρ_m. From the first plot (left), it is possible to see that ϖ has a maximum dependent of ρ_m. This aspect is not peculiar given that:

1. for $r_m \ll r'_m$ the outer torus is more present;

2. for $r_m \gg r'_m$ the inner torus is more present.

Moreover, the graphs span on different limits, given the condition imposed on Equation 8.18, Equation 3:

$$\rho_t > 0 \implies 1 - \rho_m\sqrt{2\varpi + 1} > 0 \implies \varpi < \frac{1}{2}\left(\frac{1}{\rho_m^2} - 1\right)$$

It should also be noticed that this dependence is relevant for higher and higher values of ρ_m, hence for $\rho_m \ll 1$ a sampled value can be chosen. This choice is made for geometric reason, in order to facilitate the manufacturing process and not constrict builders to select the most precise value, if the result is not varying a lot. Particularly, a value of

$$\varpi = \varpi^* = 1$$

is selected in order to have the same meridional radius in the inner and outer torus. Those impositions refer to the sizing conditions, which are indicated with a "star" subscript (i.e. $C_g^*(\rho_m) = C_g^*(\rho_m, \varpi^*, \vartheta^*, \alpha^*)$) and are only dependent of ρ_m.
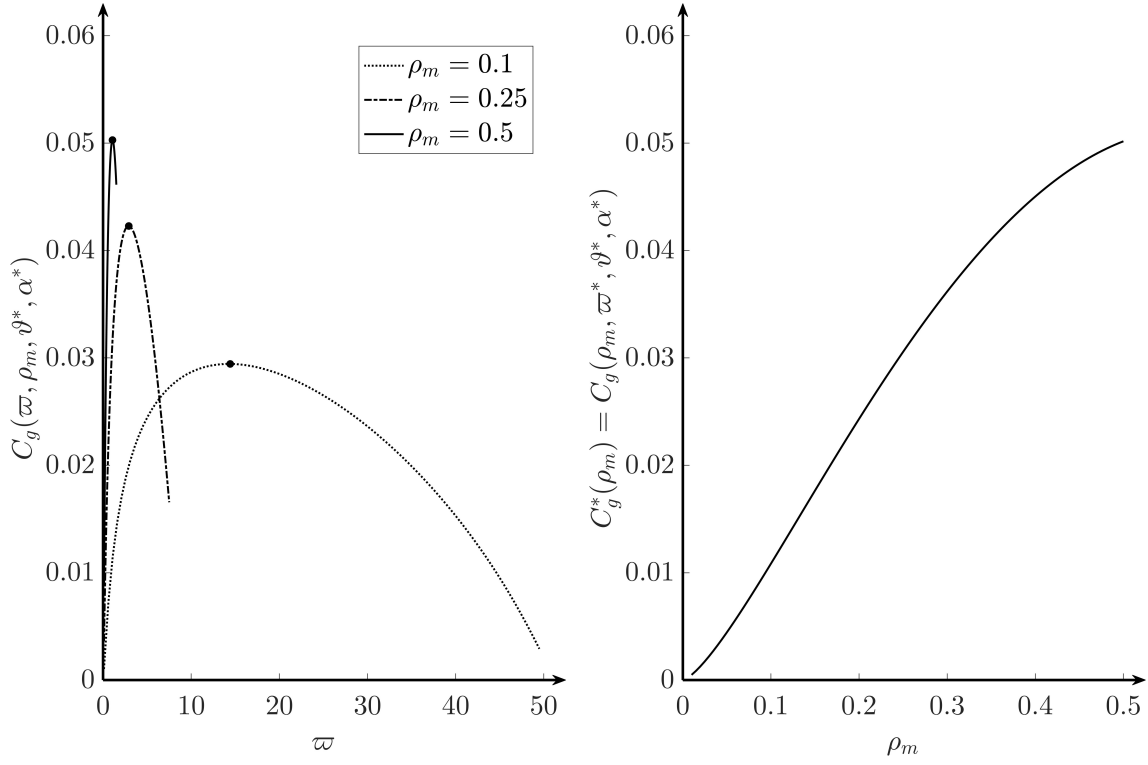
Figure 8.11: C_g plot as a function of ϖ (left) and C_g^* plot as a function of ρ_m (right).

From the following graph it is clear that higher values of ρ_m and hence higher values of r_m result in the augmentation of the geometry parameter C_g^* and therefore diminution of stresses (as proposed in [37]). Therefore, higher values of ρ_m are preferred. However, by enlarging ρ_m the overall mass of the system increases, given that it is proportional to the generating surface $\mathcal{S}_g$

$$
\begin{aligned}
m_1 \propto \mathcal{S}_g &= \vartheta^* r_m \cdot 2\pi r_t + \vartheta^* r_m' \cdot 2\pi r_t' \\
&= 2\pi \, \vartheta^* \cdot r_t'^2 \left(\frac{r_m}{r_t'} \frac{r_t}{r_t'} + \frac{r_m'}{r_t'} \right) \\
&= 2\pi \, \vartheta^* \cdot r_t'^2 \left(\rho_m \rho_t(\varpi, \rho_m) + \varpi \rho_m \right) \\
&\propto \rho_m
\end{aligned}
\tag{8.20}
$$

Therefore the mass grows as $m_1 \propto r_c$ (higher r_c leads to higher generating surface).
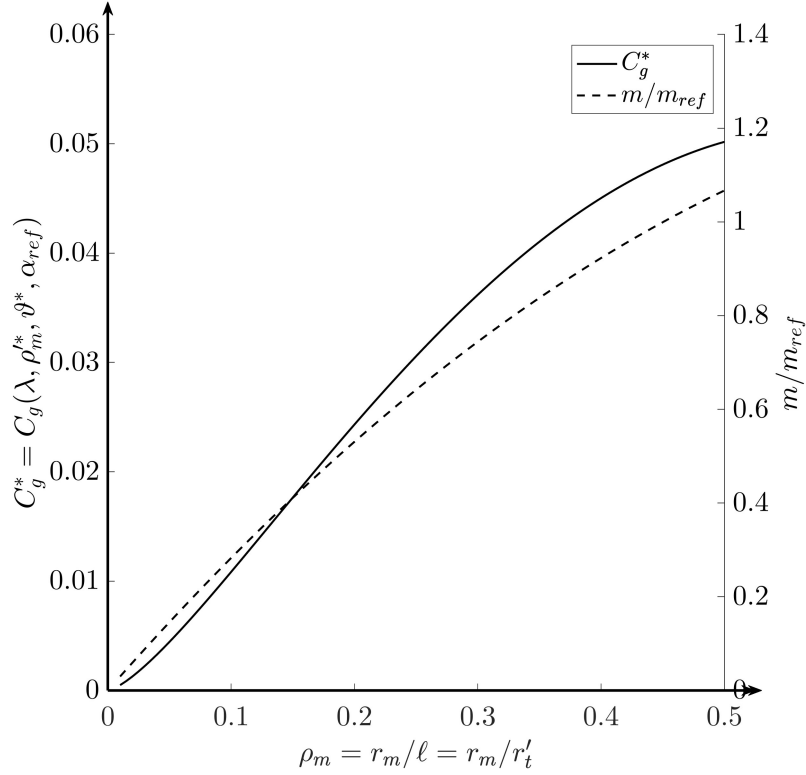
Figure 8.12: Mass and Admissible Contact force (dimensionless) prescribed as a function of $\rho_m = r_m/r'_t$. In this context with $m_{ref} = 2\pi\,\vartheta^* \cdot r'^2_t$.

8.2.4 Conclusion

In order to minimize the stresses, while reassuring a discrete mass, an intermediate value is chosen for the geometry. By choosing a limit on r'_t due to maximum interface size of the ALN system (i.e. the system is at least as big as the LPR) the following values are presented and will be chosen for the following analyses.

ρ_m	ℓ	r_m	ϑ^*	h	r_t	r'_m
0.15	1.35	0.2	30	0.2	1.0036	0.2
-	m	m	°	m	m	m

Table 8.3: Geometrical Properties of the selected configuration.

ρ_m	ℓ	C^*_g	m/m_{ref}
0.15	1.35	0.055	0.258
-	m	-	-

Table 8.4: Physical Dimensionless Properties of the selected configuration.

8.3 Pressurization sizing

Once the complete docking maneuver is completed, the pressurization process starts. In order to properly size the ALN subsystem, pressurization loads over a spherical shell have to be considered. Luckily, this problem was addressed by [40] (Chap. 8, Ex. 8.8). As a shell of revolution, a torus is subjected to the **hoop** and **meridional** stresses, named σ_u and σ_v respectively (following the same nomenclature proposed). Usually, for those problems, a proper "cut" is made in the surface to have at least one equilibrium equation. The second equation is the **meridional stress equation** which states:

$$\frac{\sigma_u}{R_u} + \frac{\sigma_v}{R_v} = \frac{p_{press}}{t} \qquad (8.21)$$

with:

1. σ_u and σ_v the hoop and meridional stress;

2. R_u and R_v the hoop and meridional curvature radii (which in this case correspond to Table 8.1);

3. p_{press} is the pressurization load (the pressure insisting over the surface);

4. t is the thickness of the shell.

Following [40], the difficulty in this problem lies in knowing which cut to make. A vertical cut through the centerline yields one equilibrium equation, but cuts the shell in two different places where σ_v cannot be expected to be the same. However, if the cut is made as in the figure, the stress σ_v at P is vertical and hence makes no contribution to the horizontal equilibrium equation, which can therefore be used to determine σ_v at Q.

The vertical pressure force acts on the annular area PQ whose outer radius is r_t and inner radius is

$$r = r_t + r_m \cos \vartheta$$

The area on which σ_v acts is $2\pi t r$, therefore

$$p_{press}(\pi r^2 - \pi r_t^2) - \sigma_v 2\pi r t \cdot \cos \vartheta = 0 \qquad (8.22)$$

$$\implies \sigma_v = p_{press} \cdot \frac{\rho_m}{2\tilde{t}} \cdot \left(1 + \frac{\rho_t}{\rho_m \cos \vartheta + \rho_t}\right)$$

with $\tilde{t} = t/\ell = t/r_t'$.
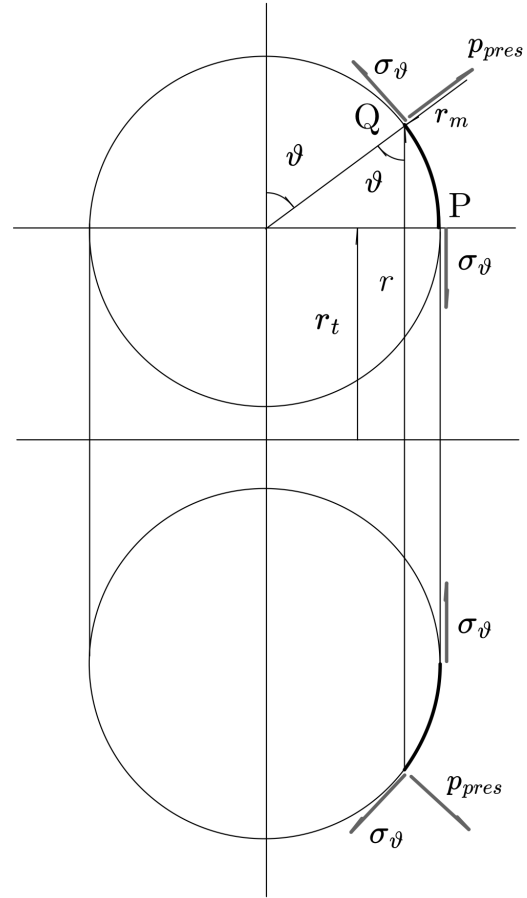
From Equation 8.21,

$$\sigma_u = R_u \left(\frac{p_{press}}{t} - \frac{\sigma_v}{R_v} \right) = p_{press} \cdot \frac{\rho_m}{2\tilde{t}}$$

It is interesting to note that σ_u is independent of ϑ and also of the radius r_t. In the limit $r_t \to +\infty$, the torus becomes a straight cylindrical tube of radius r_m and σ_u becomes the longitudinal stress σ_1 for the cylinder.

The above result shows that σ_u is exactly equal to this limiting value even for finite r_t. Therefore, no discontinuities of membrane stress are involved at a transition from a straight cylindrical tube to a circular bend, which is essentially a torus of less than $360°$. Therefore, the stresses in the problem are given by

$$\begin{cases} \sigma_u = p_{press} \cdot \dfrac{\ell}{2t} \cdot \rho_m = \sigma_{eq,ref} \cdot \tilde{\sigma}_u \\[2mm] \sigma_v = p_{press} \cdot \dfrac{\ell}{2t} \cdot \left(1 + \dfrac{\rho_t}{\rho_m \cos \vartheta + \rho_t} \right) = \sigma_{eq,ref} \cdot \tilde{\sigma}_v \end{cases}$$

An equivalent stress can be calculated, using, for example, the Von Mises Criterion.

$$\sigma_{eq} = \sqrt{\frac{(\sigma_u - \sigma_v)^2 + (\sigma_u - \sigma_w)^2 + (\sigma_v - \sigma_w)^2}{2}} \tag{8.23}$$

and given the planar-stress condition, the equation is simplified as

$$\sigma_{eq} = \sqrt{\sigma_u^2 + \sigma_v^2 - \sigma_u \sigma_v} = p_{pres} \cdot \frac{\ell}{2t} \sqrt{\tilde{\sigma}_u^2 + \tilde{\sigma}_v^2 - \tilde{\sigma}_u \tilde{\sigma}_v} = \sigma_{eq,ref} \cdot \tilde{\sigma}_{eq}(\varpi, \rho_m, \vartheta) \tag{8.24}$$

where the radicand term is only a function of $(\varpi, \rho_m, \vartheta)$.
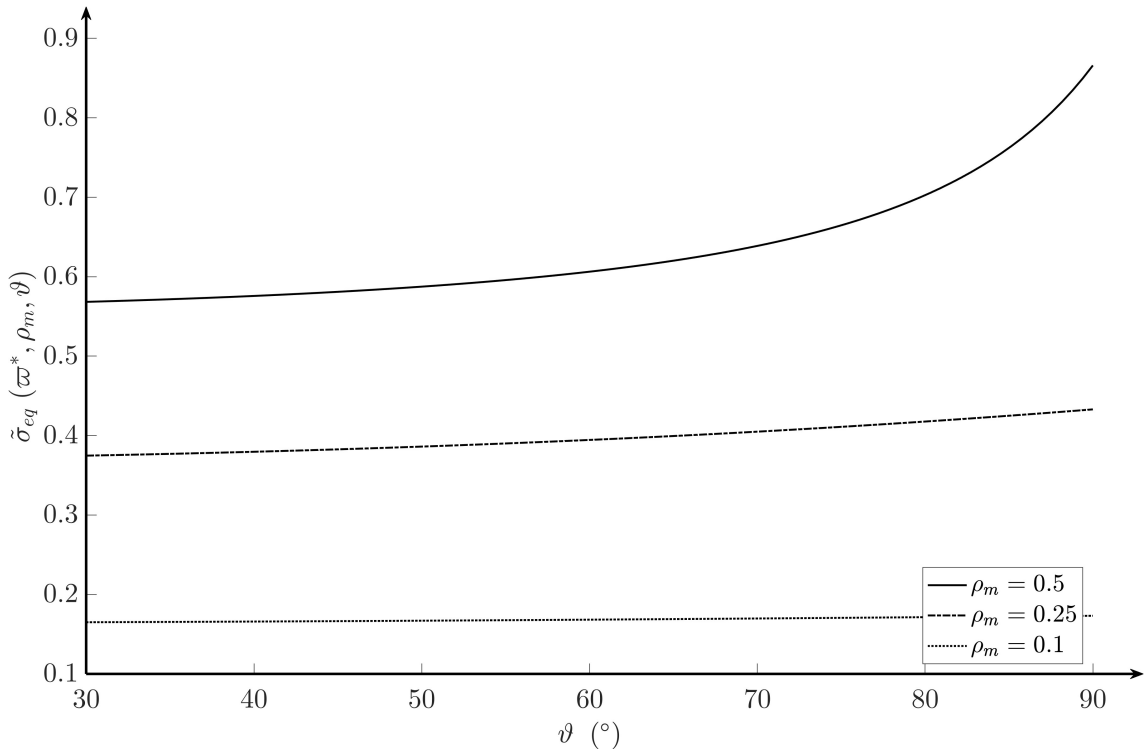
8.4 Material Selection

Once all dimensionless parameters have been parametrized, the dimensional parameters have to be considered. Particularly, in order to parametrize k_I and c_I, the structural parameters (such as material properties and thickness) have to be determined. The ALN structure is subjected to:

1. contact loads;

2. pressurization loads.

For each load, a robustness criterion is imposed.

$$\mathcal{F}_{imposed} \cdot \sigma_{eq} \leq \sigma_y \tag{8.25}$$

with:

1. $\mathcal{F}_{imposed}$ the imposed safety factor;

2. σ_{eq} the equivalent acting load;

3. σ_y the ultimate load of the material; in particular, given the linar and elastic field of discussion, this parameter corresponds to the yield strength of the material.

Particularly, defined the **margin of safety** as the difference between the ratio between the computed safety factor (currently acting on the element) and the imposed safety factor and the unity,

$$\mathcal{M} = \frac{\mathcal{F}}{\mathcal{F}_{imposed}} - 1 \geq 0 \qquad \mathcal{F} = \frac{\sigma_y}{\sigma_{eq}} \tag{8.26}$$

Each load is characterized by an equivalent stress, which depends on the material properties, the geometry and external condition. Table 8.5 examines the properties of each load. Table 8.6, on the other hand, presents a selection of materials commonly employed in space structures, along with their respective mechanical properties, to facilitate an informed material choice.
In particular:

1. a metallic material (such as Aluminum 2219) is selected as a candidate material, as it is currently employed on the IBDM petals;

2. the following three materials are currently used or being tested for elastomer sealant for the APAS [42]; the pecularity for those materials is the very low elastic modulus (estimated as the ratio of σ_y/ε_y in their small plasticity zone);

3. TPU is a more standard elastomer, broadly used in the industrial sector, which serves as a comparison for a non-space graded material, which may be used for the scaled prototype.

Parameter	Contact	Pressurization
Admissible stress/Load	$P_{adm} = \dfrac{2}{3}\pi \cdot \left(\dfrac{1}{k_p \mathcal{F}_c(\mathcal{M}_c+1)}\right)^{n/(2-n)}$ $\left(\dfrac{\sigma_y}{E^*}\right)^{n/(2-n)}$ $E^* \cdot \ell^2 \cdot C_g(e, B\ell, n)$	$\sigma_{eq} = \sigma_u G^*$ $= p_{press}\dfrac{\rho_m}{\tilde{t}}\dfrac{G^*}{2}$
Material parameters involved	E^*, σ_y	−
Geometrical involved parameters	$P_{adm} \propto \ell^2$	$\sigma_{eq} \propto 1/t$

Table 8.5: Contact and pressurization dependencies of materials.

Material	ρ	E	ν	σ_y	ε_y	c	n	Ref.
Aluminum 2219	2.84	73	0.33	345	0.47	100	1.5	[41]
S0383-70	1.28	0.03	0.33	8.0	265	100	1.5	[42]
S0899-50	1.18	0.0041	0.33	7.6	532	100	1.5	[42]
ELA-SA-401	1.13	0.00196	0.33	7.2	625	100	1.5	[42]
TPU	1.2	0.0012	0.45	25	250	100	1.5	[43]
	g/cm^3	GPa	−	MPa	%	$N/(m/s)$	−	

Table 8.6: Typical mechanical properties for materials.

ECSS standard categorize this as Pressurized Structure (PS). For this structure it is possible to define:

1. The **Maximum Expected Operating Pressure (MEOP)** is defined as the highest internal pressure that a pressurized structure or system is expected to experience throughout its operational lifetime, considering all nominal operating conditions and environmental influences. This includes effects such as temperature variations, transient pressure fluctuations, acceleration forces, and system regulation limits. In this context p_{press} is the MEOP.

2. The **Maximum Design Pressure (MDP)** represents the pressure level used for the structural design and verification of pressurized hardware. It is obtained by applying a safety margin to the MEOP, ensuring that the structure maintains integrity even under extreme conditions. The MDP accounts for uncertainties in operational environments, potential system malfunctions, and margin policies dictated by mission safety requirements.

3. The **Design Yield Load (DYL)** is the structural load threshold at which the material of a pressurized structure or docking system reaches its yield point, signifying the onset of permanent deformation. The DYL is determined by multiplying the maximum expected structural load by a safety factor, ensuring that the system can withstand mechanical and pressure-induced stresses without plastic deformation. In this context P_y is the DYL, defined as

$$P_y = P_{adm} \cdot (\mathcal{F}_{imposed,cont} \cdot (\mathcal{M}_{contact} + 1))^{n/(2-n)}$$
$$= \frac{2}{3}\pi \cdot \left(\frac{\sigma_y}{k_p E^*}\right)^{n/(2-n)} \cdot E^* \cdot \ell^2 \cdot C_g \tag{8.27}$$

The following additional parameters are imposed. A pressurization load of $p_{press} = 1\,atm$ is imposed, as commonly used on board of the ISS and it is used as a standard for lunar habitats [44], and a safety factor of $\mathcal{F}_{imposed} = 1.5$, as the norm for pressurized shells [45].

Parameter	Value	Units
$\mathcal{F}_{c,imposed}$	1.5	
$\mathcal{F}_{p,imposed}$	1.5	
p_{press}	1	atm
	101325	Pa
	0.101325	MPa

Table 8.7: Complementary input parameters for material selection analysis.

8.4.1 Contact parametric study results

The following plots show the yield stress (DYL) versus characteristic length and the maximum allowable pressure for different safety margin values. It can be seen that elastomers perform much better than aluminum, as they are less rigid and therefore more capable of absorbing shock.
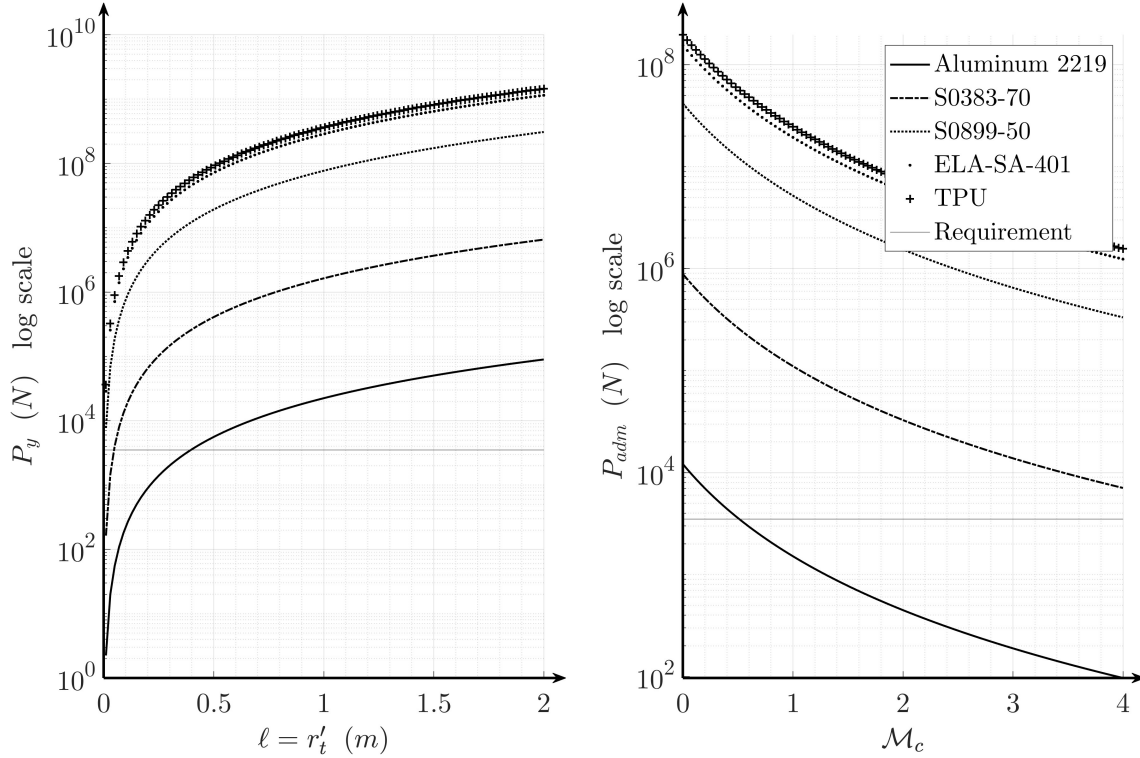
Figure 8.13: Trend study of the different materials subjected to the prescribed loads.

An additional margin of $\mathcal{M}_{c,selected} = 50\%$ is applied to the structure, for safety measures. From the analysis it is clear that the selected characteristic length ℓ respects safety margins. Moreover, materials respect the imposed margin. Particularly, TPU seems the best candidate. However, the material does not seem to be space graded, hence **ELA-SA-401** is selected as a candidate material.

Material	$P_{adm,computed}$	k_I	h_{max}
Al-2219	3580	1.4e+10	4e-05
S0383-70	262000	5900000	0.126
S0899-50	12300000	800000	6.22
ELA-SA-401	45900000	380000	24.4
TPU	58200000	2200000	8.95
Units	N	N/m^n	m

Table 8.8: Material analysis results for the selected thickness.

8.4.2 Pressurization parametric study result

The following graph instead shows the trend of the safety margin of pressurization compared to the thickness for the different materials. Again in this case a margin of $\mathcal{M}_{p,selected} = 50\%$ is selected.
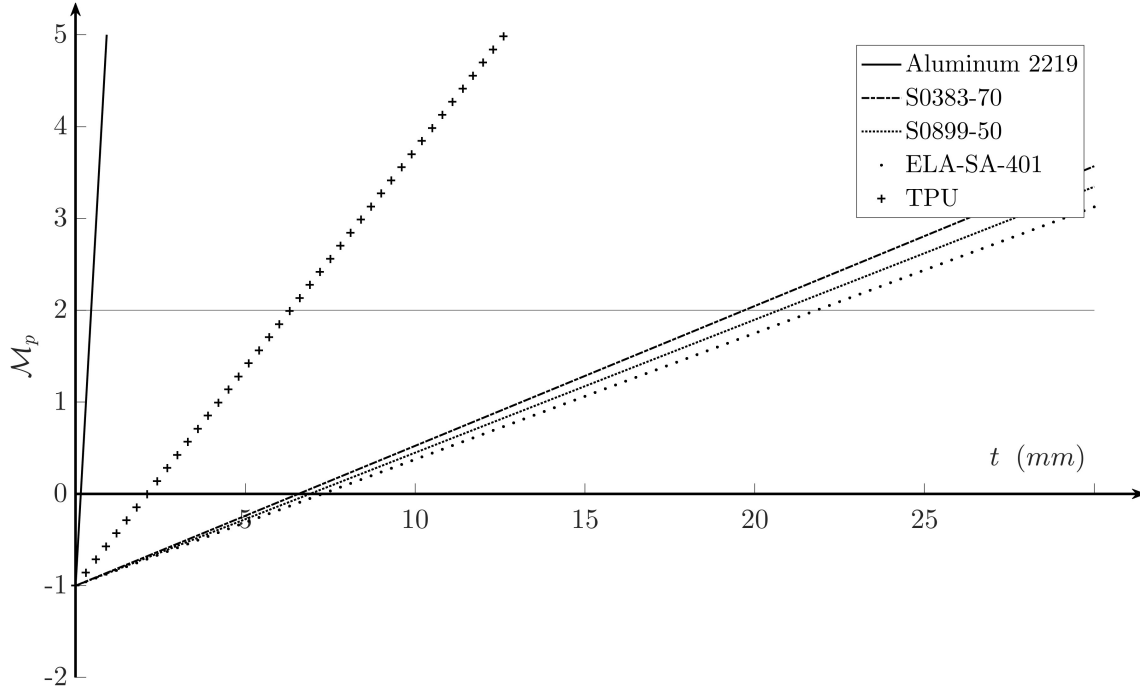
Figure 8.14: Pressurization safety margin for the selected materials.

Since aluminum is decidedly more robust, it has a much better performance (and hence, a lower mass). However, the same structure would be significantly heavier if made from aluminum because contact loads could be higher. Therefore metallic materials are discarded.

Material	Mass	Thickness
Al-2219	3.17	0.5
S0383-70	61.44	19.7
S0899-50	59.56	20.7
ELA-SA-401	60.08	21.8
TPU	18.48	6.3
Units	kg	mm

Table 8.9: Mass and thickness of the different materials for the selected safety margin.

8.5   Conclusions

The following is a collection of the results obtained through the chapter. Geometrical and mechanical properties have been modeled using mathematical models and need to be verified via a proper simulative tool. The expected indentation $h_{exp} = 0.01$ mm is estimated as a good value for numerical contact mechanics analysis.

ρ_m	ℓ	r_m	ϑ^*	h	r_t	r'_m
0.15	1.35	0.2	30	0.2	1.0036	0.2
-	m	m	°	m	m	m

Material	k_I	c_I	h_{exp}	Mass
ELA-SA-401	380000	100	1e-05	60.08
	N/m^n	$N/(m/s)$	mm	kg

Table 8.10: Conclusive properties table of the selected material and geometry.

8.6 Shock absorber preliminary sizing

The preliminary sizing strategy for a shock absorber intended for the docking system is formulated by analyzing the dynamic response of the system through a simplified gain function. The gain function $\mathcal{G}(\zeta, \omega_{n,II}/\Omega_c)$, representing the relationship between amplitude and input frequency ratio, is used to evaluate the damping behavior across a range of damping ratios ζ. In order to restrict the maximum amplitude while respecting Loads Requirements, low values of $\omega_{n,II}/\Omega_c$ and ζ have been used for preliminary sizing. This values will be used to get a scale of the parameters in action, in order to confine the boundaries for the subsequent optimization.
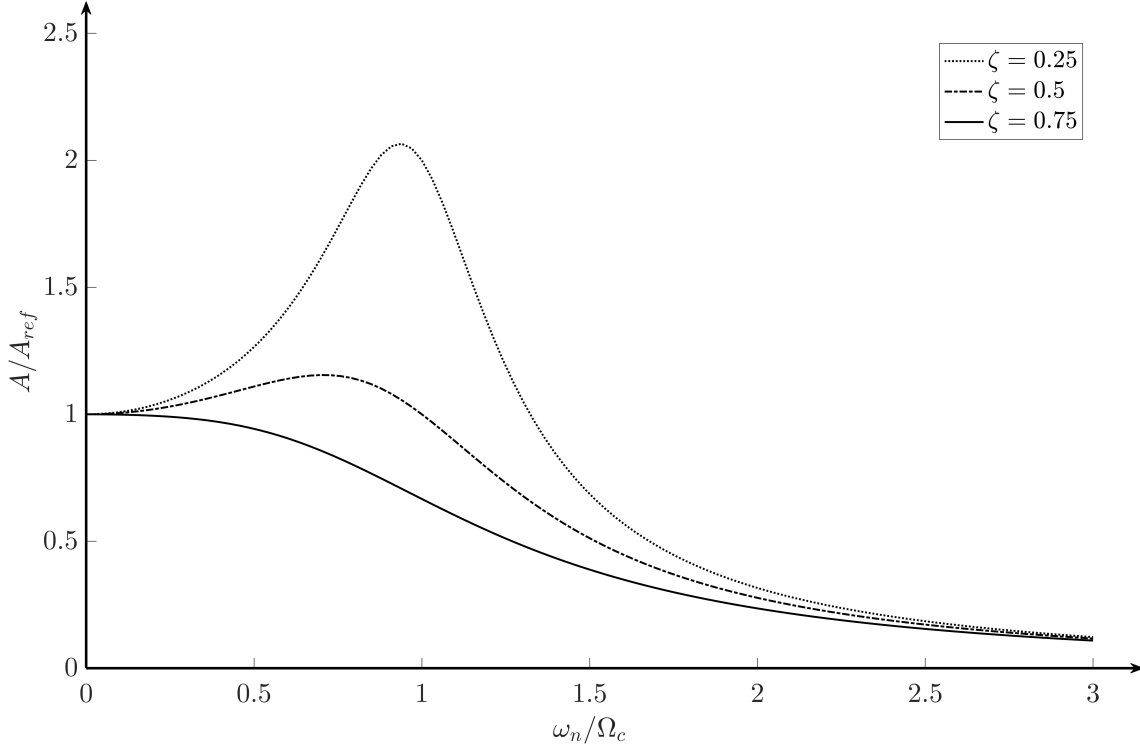
Figure 8.15: Gain function as function of the ratio $\omega_{n,II}/\Omega_c$ and ζ.

This function is plotted for various conditions to visualize system performance under oscillatory excitation, supporting the selection of suitable damping coefficients. The model considers a total vehicle mass $m_{tot} = m_2$, an estimated docking mass m_1, and a reference impact velocity $v_{d,ref}$. The reduced mass μ is computed to approximate the effective mass during docking. The non-linear stiffness law, characterized by a coefficient k_I and an exponent n, is used to estimate the maximum deformation h_{max} and the impulse response duration τ_I. For the proposed inputs, it is estimated that

$$\tau_I \cong 0.059 \ s$$

which is indicative of a elevated frequency. The following plot shows the shock absorber response of the performance model (1D simplified model), given the results in the previous sections.

The preliminary sizing strategy is therefore the following:

1. the set of parameters $\omega_{n,II}/\Omega_c$ and ζ is selected given the maximum loads requirements constraints in chapter 7.

2. Contact frequency is computed;

3. Shock-absorber parameters are evaluated given Equation 8.14,

$$\begin{cases} k_{II} = \omega_{n,II}^2 \, M \\ c_{II} = 2\zeta\omega_{n,II} \, M \end{cases}$$
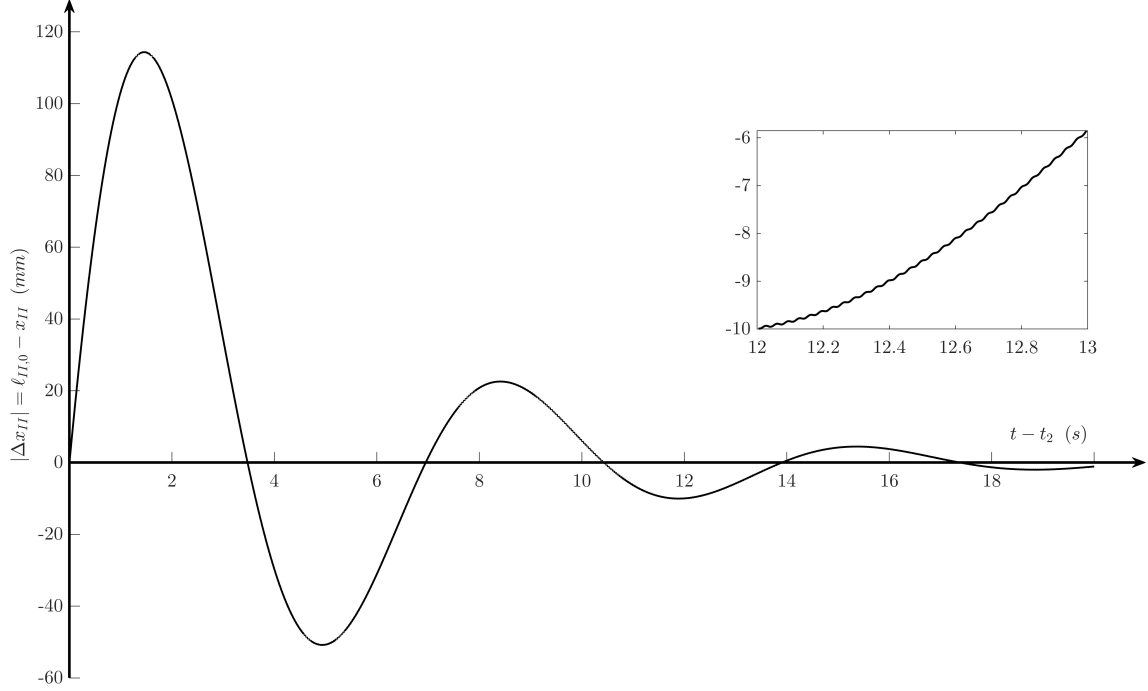
Figure 8.16: Shock absorber elongation $x_{II}(t)$ response for $\omega_{n,II}/\Omega_c = 0.005$ and $\zeta = 0.25$. It is possible to see that over time the response is gradually diminished and that contact frequency acts on the short period given its higher frequency (particular in the top right corner between 12 and 13 seconds after ICC.

Some notable observations of this results needs to be addressed. To start, the total stiffness and damping k_{II} and c_{II} refer to the total characteristic of the shock absorber. The intention of this work is to propose a valuable, passive, alternative to the IDSS-active counterpart. Therefore, in order to resemble the interaction, a set of $N_{spring} = 6$ springs and dampers are used in parallel. The single stiffness and damping of each shock absorber is

$$k_{II,single} = \frac{k_{II}}{N_{spring}} \qquad c_{II,single} = \frac{c_{II}}{N_{spring}}$$

The preliminary analysis showed that the following values can be suitable candidates for boundary setting of the subsequent optimization, in order not to have large elongations, corresponding to even larger initial lengths $\ell_{II,0}$ (hence heavier components):

$$\begin{cases} \omega_{n,II}/\Omega_c & = 0 \div 0.01 \\ \zeta & = 0 \div 0.25 \end{cases} \quad \text{corresponding to} \quad \begin{cases} k_{II,single} & = 0 \div 1000 \; N/m \\ c_{II,single} & = 0 \div 1000 \; N/(m/s) \end{cases}$$

$$(8.28)$$

Those boundaries are used in chapter 10.

Moreover, the presence of gravity adds an interesting problem to the bunch. Considering that usually, docking shock absorber system do not suffer from gravitational pull, shock absorbers do not tend to bend under this load. In order to prevent vertical bending, a set of 6 petals is designed in order to sustain the load of such system. Each petal is hooked to the rest of the structure via another spring (without
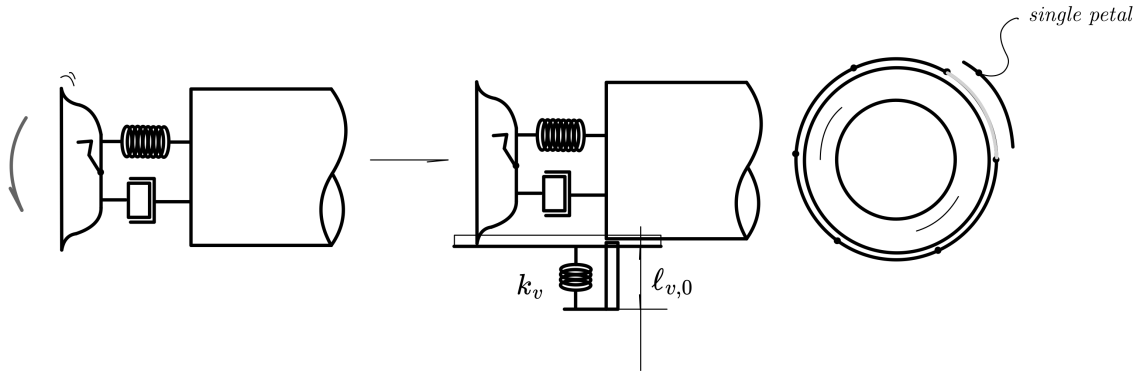
Figure 8.17: Vertical Bending and solution proposed. A set of petals is used to sustain ALN mass.

a damper). A preliminary sizing of such spring sees the conter-action of the ALN mass.

$$k_v \cdot z_v = m_1 g_{\mathbb{D}} \tag{8.29}$$
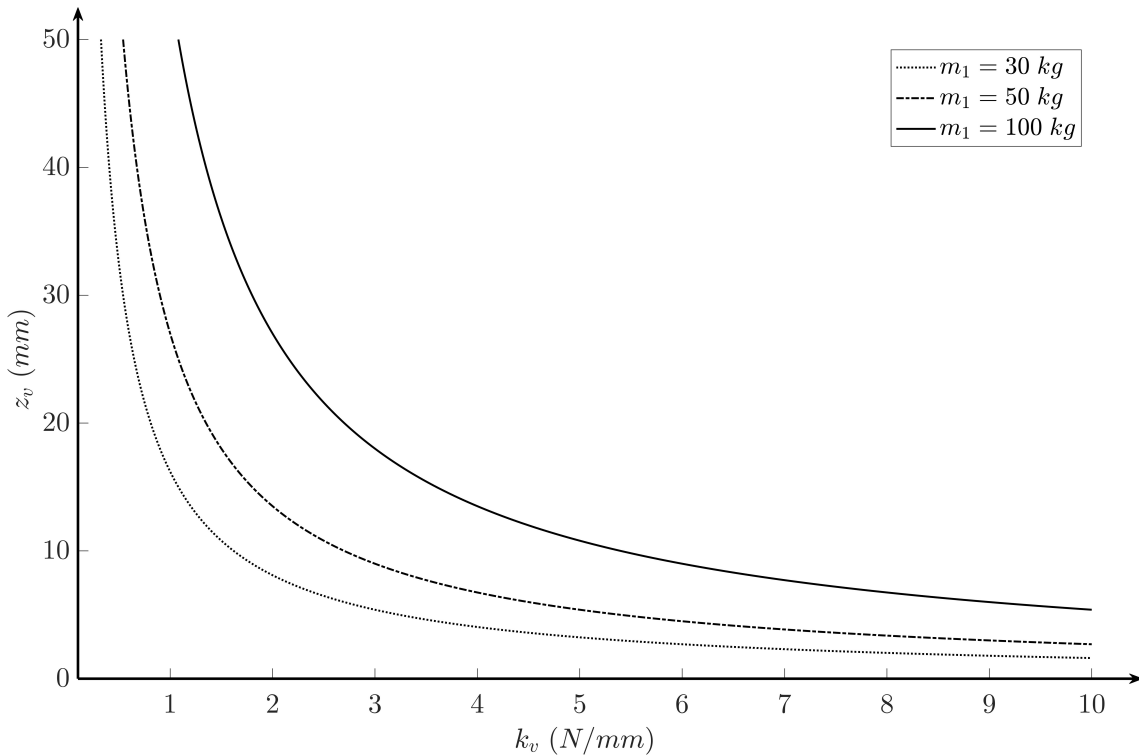
Figure 8.18: Preliminary study of the vertical elongation of the vertical support spring.

with:

1. k_v is the vertical spring stiffness;

2. z_v is the vertical displacement of the female ALN geometry;

3. m_1 is the ALN mass; this value was augmented by a factor of 2 in order to sustain additional masses and loads (such as the mass of the alignment geometry itself and the lateral contacting loads.

4. $g_{\mathbb{D}}$ is the Moon's acceleration.

As it is possible to see in Figure 8.18, stiffer springs produce smaller vertical elongations. Therefore, even here a boundary of

$$k_v = 1 \div 10 \ N/mm$$

is used for further optimization in chapter 10. Differently from the "horizontal" shock absorber, this value is not varied up to 0 N/mm as this will result in the collapse of the geometry. Some particular aspect regarding this vertical support are:

1. an **external fillet** is introduced in the female ALN geometry to better sustain friction with the support during approach and contact. This itself reduces the maximum height of the structure to the proposed r'_t in Table 8.10.
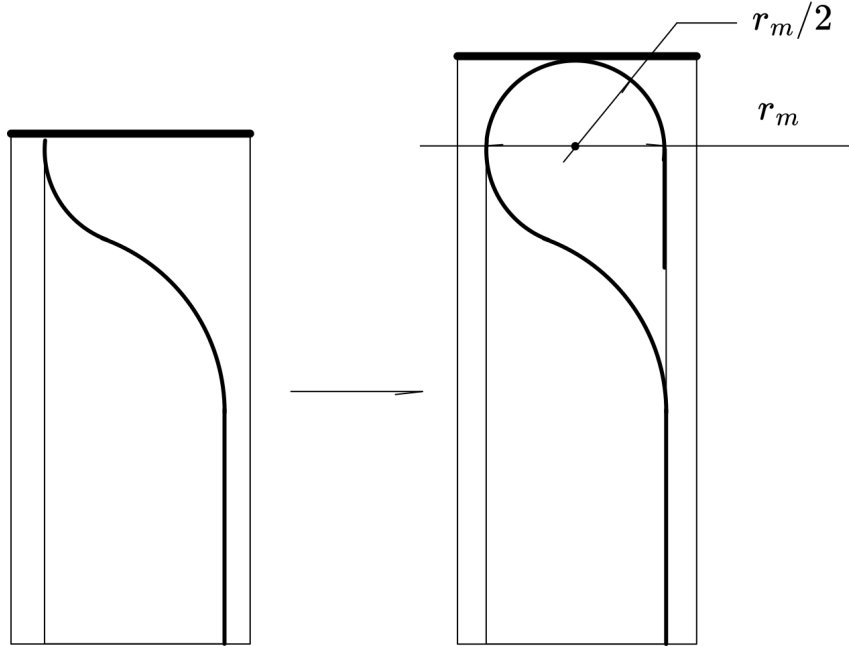
Figure 8.19: Particular of the external fillet in the female ALN structure.

2. this structure serves as an *external casing* which encapsulate the totality of the docking system, protecting it from asteroids and radiation. As such, a further investigation can be made regarding the used materials of such casing. For the purpose of this study, it is estimated that Aluminum 2219 is used given that not much importance is dedicated to external shielding in this particular context.

Given all those parameters in play, the evaluation through a $1D$ model is insufficient. Hence the proposed work suggest the implementation of a simulated model via ADAMS, proposed in chapter 10.

8.7   Spring Sizing

To conclude this chapter, a final statement is proposed for spring sizing.

In general [46], given the shear stress in a spring τ_{sp}, it is possible to calculate the minimum wire diameter d_{sp} that satisfies the safety condition

$$\tau_{sp} = K_{sp}\frac{8F_{sp} \cdot D_{sp}}{\pi d_{sp}^3} < \tau_{max}$$

with:

1. τ_{sp} is the applied shear stress on the spring;

2. τ_{max} is the maximum shear stress, which is dependent of the material;

Figure 8.20: Spring geometry.

3. $F_{sp} = k_{sp} \cdot x_{sp}$ is the linear spring force, equal to the product between the spring stiffness and the displacement.

4. d_{sp} is the desired wire diameter;

5. D_{sp} is the OD of the spring. This value is chosen given the **spring index**

$$C_{sp} = \frac{D_{sp}}{d_{sp}} = 8 \div 12$$

   as it is common practice.

6. K_{sp} is the Wahl correction coefficient, used to modify the shear stress calculation for helical springs, offering a more accurate analysis by taking into consideration the curvature and direct shear effects

$$K_{sp} = \frac{4C_{sp} - 1}{4C_{sp} - 4} + \frac{0.615}{C_{sp}}$$

Moreover, the number of active coils is given by

$$n_{sp} = \frac{Gd_{sp}^4}{8D_{sp}^3 k_{sp}}$$

with G the shear modulus of the material. Figure 8.21 shows a sizing strategy flow chart for a spring.

Figure 8.21: Spring sizing flow chart.

A MATLAB function is developed to perform preliminary design calculations for helical compression springs, integrating both mechanical constraints and material properties. The function accepts as input the maximum applied load F_{sp}, the expected deflection $\delta = x_{sp}$, the shear modulus G, the allowable shear stress $\tau_{\max}$, and a chosen spring index C_{sp}. The algorithm iteratively estimates the wire diameter d_{sp} required to satisfy the shear stress constraint by adjusting its value until the induced stress remains within the permissible limit.

The corresponding mean coil diameter D_{sp} is computed based on the spring index, and the Wahl correction factor is incorporated to account for curvature effects. Once the wire diameter is validated, the spring stiffness k is obtained via the linear load-deflection relationship, and the number of active coils n is derived from the classical stiffness equation. The results are rounded to values compatible with practical manufacturing tolerances.

```matlab
function [D, d, n, k] = spring_design(F, delta, C, G,
    tau_max)
  % INPUTS:
  % F        - Maximum load (N)
  % delta    - Expected Deflection (mm)
  % G        - Shear modulus of the material (MPa)
  % tau_max  - Allowable shear stress (MPa)



  % Estimate wire diameter based on shear stress
      formula
  % Solve: tau_max = K * (8FD / (pi*d^3)) for d
  % Need iterative approach or initial guess

  % Initial guess for wire diameter
  d = 1;   % mm
  converged = false;

  while ~converged
      D = C * d;
      K = ((4*C - 1)/(4*C - 4)) + (0.615/C);
      tau = K * (8*F*D) / (pi * d^3);

      if tau < tau_max
          converged = true;
      else
          d = d + 0.1;   % increase wire diameter until
              stress is ok
      end
  end

  % Final values
```

```matlab
31      k = F / delta;         % Stiffness
32
33      % Number of active coils
34      n = (G * d^4) / (8 * D^3 * k);
35
36      % Round to practical manufacturing values
37      d = round(d, 2);
38      D = round(D, 2);
39      n = ceil(n);  % usually rounded up
40      % k = round(k, 2);
41  end
```

Chapter 9

The Docking Capture System

After devoting particular attention to the alignment geometry and shock absorption characteristics of the innovative docking subsystem proposed in this work, possible capture systems are analyzed for once the alignment phase is completed during the docking maneuver.

9.1   Capture system architectures

The history of space docking subsystem in chapter 4 has brought this work to the attention of two particular HCS archetypes: *hooks and latches* or *magnets*. For manned docking maneuvers the quasi-totality of HCS are of the first kind. The only example brought in the previous chapter, in fact, the OECS, is not intended for a manned mission.

Hook-and-latch systems, such as those used in the APAS (Androgynous Peripheral Attach System) and Soyuz docking mechanisms, rely on robust mechanical actuators that engage once alignment is achieved, forming a secure and load-bearing interface. These systems offer high structural integrity and redundancy, making them well-suited for missions requiring frequent re-docking or long-duration connection. In contrast, magnet-based systemsexemplified by the OECS (Orbital Electrical Connection System)utilize high-strength electromagnets to draw the two spacecraft together and maintain contact. While generally simpler and potentially lighter, magnet-based systems often face limitations in terms of load capacity, environmental interference (e.g., magnetic fields in sensitive instruments), and the precision required for alignment.

To guide the selection of a hard capture system in a manned docking context, the following tradeoff aspects should be considered:

1. **Structural Load Capacity**: Evaluates the ability to withstand axial and shear forces during dynamic phases such as docking shocks and thermal expansion. Hook-and-latch systems typically perform better under high loads.

2. **Mass and Volume**: Accounts for the total weight and space envelope required. Magnet-based systems can offer lower mass but may lack the robustness of mechanical systems.

3. **Redundancy and Reliability**: Measures the systems ability to function despite partial failures. Mechanical systems generally incorporate multiple

latches or hooks, improving fault tolerance.

4. **Alignment Sensitivity**: Indicates how precisely the two docking ports must align. Magnetic systems require tighter tolerances for effective engagement, while mechanical systems can accommodate greater initial misalignment through guide mechanisms.

5. **Integration Complexity**: Considers the engineering effort for system integration and maintenance. Magnet-based systems are often simpler to integrate but may require careful magnetic shielding.

6. **Reusability and Maintenance**: Pertains to how easily the system can be reused or repaired between docking cycles. Mechanical systems may require more maintenance but are typically more durable.

7. **Environmental Compatibility**: Assesses performance in the presence of space environment factors such as microgravity, radiation, and electromagnetic interference (EMI). Magnetic systems must be carefully managed to avoid affecting sensitive onboard electronics.

Aspect	Hooks/ Latches	Magnets	Weight	Rationale for Weight
Structural Load Capacity	5	2	5	Essential for maintaining a secure, rigid connection under dynamic and pressurized loads.
Mass and Volume	3	5	3	Important for system efficiency but can be traded off for safety and performance.
Redundancy and Reliability	5	3	5	Critical for crew safetymust tolerate partial failure or misalignment.
Alignment Sensitivity	2	4	4	High tolerance reduces docking risk; essential when crew is onboard.
Integration Complexity	3	4	2	Simpler integration is beneficial but less crucial than reliability or load capacity.
Reusability and Maintenance	3	4	3	Long-term missions or reusable vehicles benefit from durable systems.
Environmental Compatibility	5	2	3	High for crewed modules; magnetic interference can be problematic near sensitive systems.
Total	**97**	82		

Table 9.1: HCS subsystem architecture tradeoff.

Given the proposed aspects of trade-off, the *hooks/latches* architecture is chosen as a suitable candidate for the CLASP docking subsystem. Nevertheless, given the

exploratory aspect of this work, an inspection into magnetic Hard Capture System (Docking) (HCS) is considered for completion.

9.2   Hooks and Latches sizing

The predominant mechanical nature of the first solution imposes a kinematic, dynamic and strucutral evaluation of the system. There are a variety of different latching models, both used for docking in space and for connecting two components on Earth. One of the simplest models is the **hooks and latches** mechanism which, has the name suggests, is composed of two distinct components: a *hook* which acts as the active part, and a *latch* which is the passive part. When the two docking subsystem are sufficiently near, imposing a rotating motion on the hooks guarantees contact and capture of the rectangular framed latch.
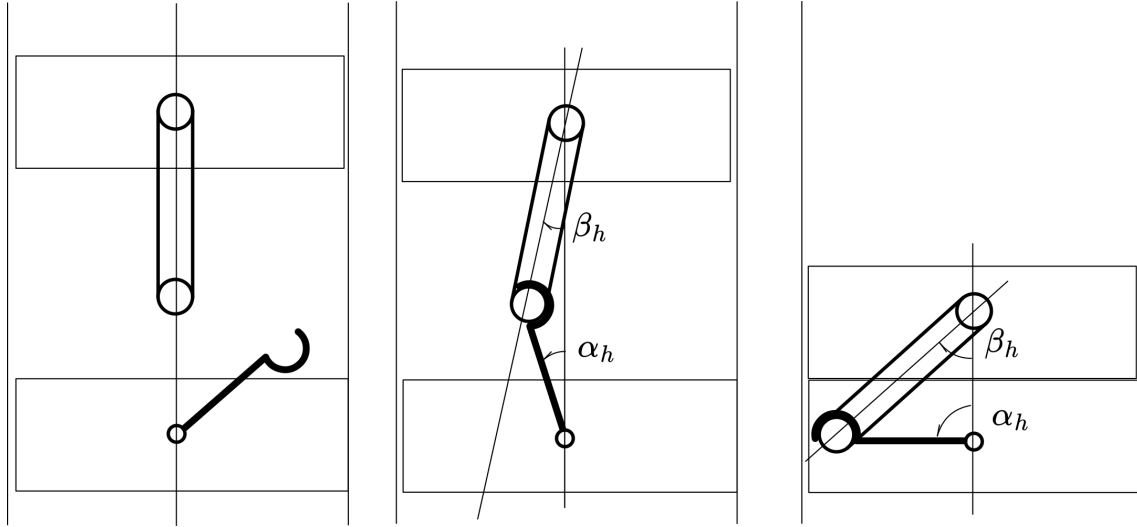
Figure 9.1: Hooks and Latches Mechanism.

9.2.1   Kinematical Analogy

This rotating motion is very similar to that of a *crank mechanism*. In general, a **crank mechanism** is a mechanical device that converts reciprocating (back-and-forth) motion into rotary (circular) motion, or vice versa.

Given the kinematical similarities, this model is used as a base for the kinematical and mechanical model of the system. The following figure shows the principal geometrical properties of the system:

$$F_i = M\ddot{x}_h$$

1. r_h is the hook's effective length, measured from the torque application point up to the center of the hook's upper circle.

In the crank analogy, this length is denoted as the **arm's length**.
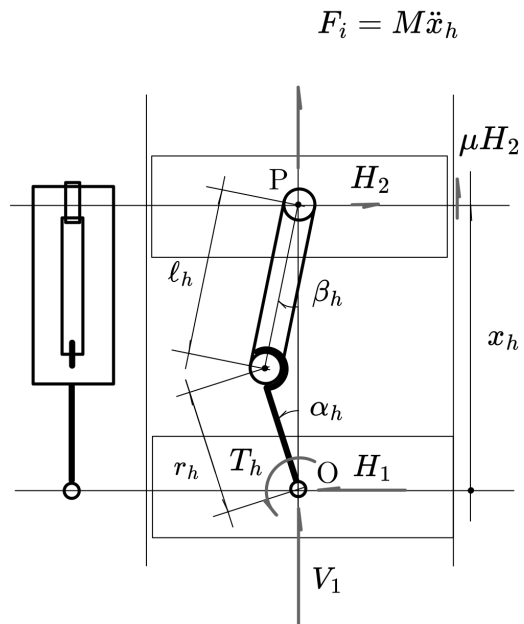
1. ℓ_h is the latch's effective length, measured from the center of the top beating up to the center of the bottom rod. In the same analogy, this is the **crank's length**.

2. $\alpha_h(t)$ and $\beta_h(t)$ denote the hook's and latch's angle with the reference line passing through the points O and P.

3. the relative distance between O and P is marked as $x_h(t)$.

As it is usual on such mechanisms [47], a crank "aspect ratio" is defined as follows:

$$\lambda_h = \frac{\ell_h}{r_h} \tag{9.1}$$

The subscript "h" refers to HCS. The relative distance is dipendent of the other parameters via

$$\begin{aligned} x_h(t) &= r_h \cos \alpha_h + \ell_h \cos \beta_h \\ &= r_h \left(\cos \alpha_h + \lambda_h \cos \beta_h \right) \end{aligned} \tag{9.2}$$

Given also that,

$$\ell_h \sin \beta_h = r_h \sin \alpha_h$$

$$\implies \sin \beta_h = \frac{1}{\lambda_h} \sin \alpha_h$$

$$\implies \cos \beta_h = \sqrt{1 - \sin^2 \beta_h} = \sqrt{1 - \frac{1}{\lambda_h^2} \sin^2 \alpha_h} = \frac{1}{\lambda_h} \sqrt{\lambda_h^2 - \sin^2 \alpha_h}$$

Therefore, assuming the angular speed $\dot{\alpha}_h = \omega_h$,

$$x_h(t) = r_h \left(\cos \alpha_h + \sqrt{\lambda_h^2 - \sin^2 \alpha_h} \right) = r_h \cdot \tilde{x}_h,$$

$$\dot{x}_h(t) = r_h \omega_h \left(-\sin \alpha_h + \frac{2 \sin \alpha_h \cos \alpha_h}{2\sqrt{\lambda_h^2 - \sin^2 \alpha_h}} \right) = r_h \omega_h \cdot \dot{\tilde{x}}_h, \text{ and} \tag{9.3}$$

$$\ddot{x}_h(t) = -r_h \omega_h^2 \left(\cos \alpha_h + \frac{\cos(2\alpha_h)}{\lambda_h} \right) - |\dot{x}_h(t)|\dot{\omega}_h = r_h \omega_h^2 \cdot \ddot{\tilde{x}}_h.$$

The final term in acceleration is dropped if the angular speed is assumed constant. In this case $\alpha_h(t) = \omega_d \cdot t$.

Usually, in the context of a crank mechanism design, those values are "mediated" given high speeds and continous motion. In the context of this design, it is assumed that the hook does not complete a full circle, but instead departs from a certain angle, $\alpha_{h,i} \geq 0$ and finishes at $\alpha_{h,f} = \pi/2$ as shown in the Figure 9.1. Therefore, the "large velocity" approximation is nevertheless discarded. The need for a non-null initial angle $\alpha_{h,i}$ is indicative of the fact that in this simple, one-dimensional model, the hook approaches a perfectly aligned geometry. In the real case, the initial misalignment is not just translational, but also angular and lateral. All this combined misalignments are taken into account.
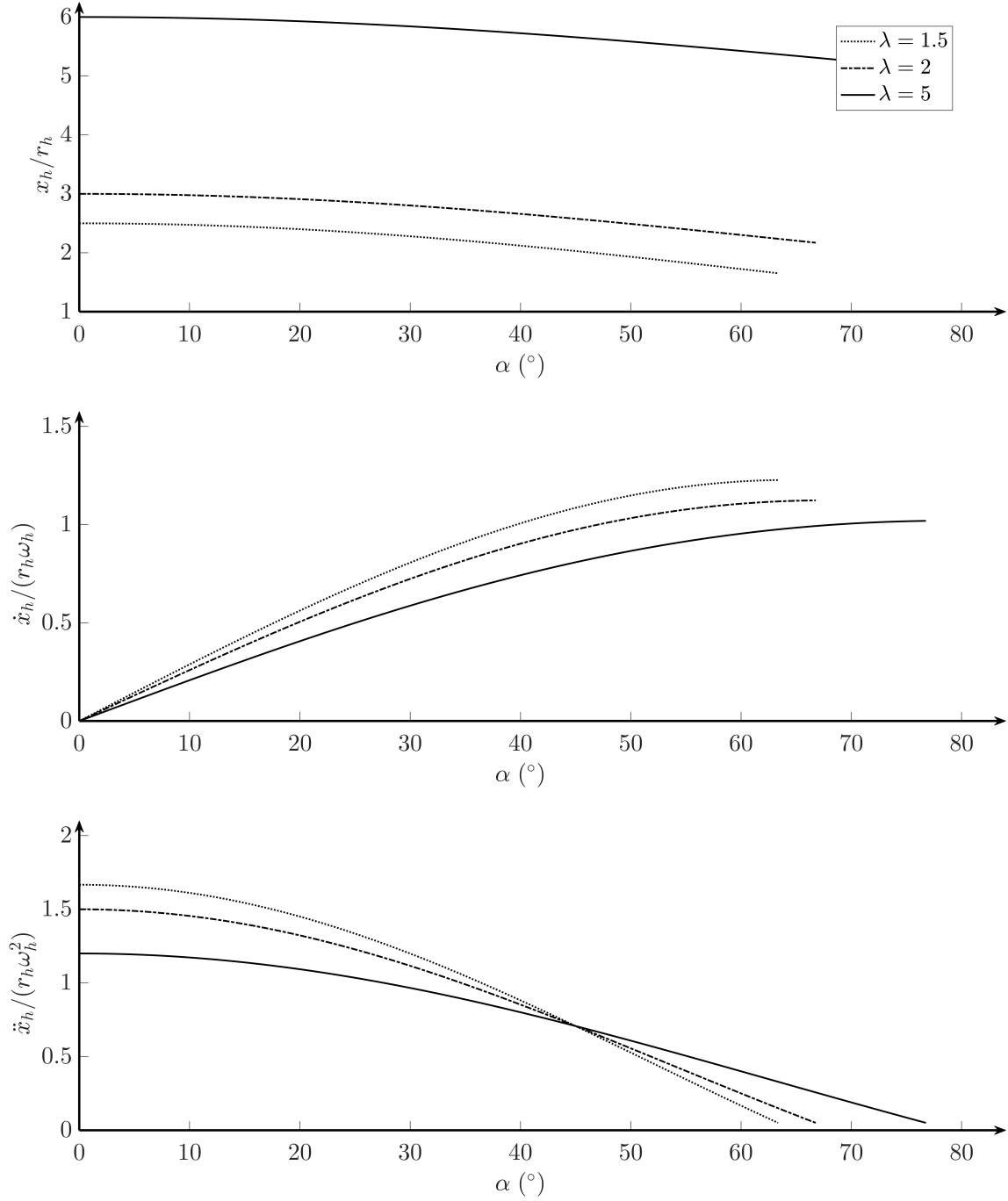
Figure 9.2: Trend study of the kinematics of the system, for different values of λ_h.

9.2.2 Dynamics

Given the free-body diagrams presented in the image, the subsequent set of equations is obtained. Again, it is noticed that this simple model derives from the same one-dimensional considerations of the performance model seen in chapter 8. Lateral accelerations and the shape of the alignment geometry are omitted in this section.

$$F_i = M\ddot{x}_h$$

Figure 9.3: Free body diagrams of the hook and the latch.

Hook   Latch

$$\begin{cases} \rightarrow : H_1 = E_h \cdot \sin\beta_h \\ \uparrow : V_1 = E_h \cdot \cos\beta_h \\ \circlearrowleft : T_h = E_h \cdot r_h \cdot \sin(\alpha_h + \beta_h) \end{cases} \qquad \begin{cases} \rightarrow : H_2 = E_h \cdot \sin\beta_h = H_1 \\ \uparrow : F_i + \mu H_2 = E_h \cdot \cos\beta_h = V_1 \\ \circlearrowleft : 0 \end{cases} \qquad (9.4)$$

where H_1, V_1 are the reaction force in O, H_2 is the guide reaction force, which is indicative of the reaction on the alignment geometry during hard capture, T_h is the motor torque request, E_h is the transmitted force between hook and latch, and F_i is the inertia of the mass m_{ref} to be moved. In this context, this latter interaction is the same as the **attractive force** that the HCS exibits.

$$F_i = F_h = -m_{ref}\ddot{x}_h(t) = -m_{ref}\omega_h^2 r_h \cdot \ddot{\tilde{x}}_h(t) \qquad (9.5)$$

The other important interaction is the **motor torque** which is indicative of the power request of the system. Indeed, the objective of the sizing requests:

1. a high attraction F_h, that ensures complete capture once the system is docked;

2. a low power consumption, and indeed a requested torque T_h.

Solving the system of equations yields

$$E_h = F_i \frac{1}{\cos\beta_h(1 - \mu\tan\beta_h)}$$

from which all the other forces can be estimated. Given that the set of angles is $0 \leq \alpha_h \leq \pi/2$, the first step is to identify the extrema points during the capture. One first approximation sees the constant angular velocity $\dot{\omega}_h = 0$.

$$\begin{cases} F_h = M\ddot{x}_h = m_{ref}\omega_h^2 r_h \left(\cos\alpha_h + \dfrac{\cos(2\alpha_h)}{\lambda_h} \right) \\ T_h = E_h \cdot r_h \cdot \sin(\alpha_h + \beta_h) \end{cases} \tag{9.6}$$

Given the requests, an **efficiency** of the latching mechanism can be estimated,

$$\eta_h = \frac{F_h \cdot \dot{x}_h}{T_h \cdot \omega_h} = \eta_h(\alpha_h, \lambda_h, \mu) \tag{9.7}$$

9.2.3 Sizing definition

Having clear the mechanical picture of the proposed problem, the following table summarizes the main geometrical properties that needs to be sized in order to fully define the system.

Property	Symbol	Strategy
Latch Length	ℓ_h (or λ_h)	Trend Study on λ_h
Hook Length	r_h	Initial capture condition req.
Cap Distance (offset)	d_{of}	Final capture condition
Final angle	$\alpha_{h,f}$	Final force (after mating) req.
Section diameter	D_h	Strucutural sizing
Latch ford	f_h	Geometrical considerations ($f_h \geq 2D_h$)
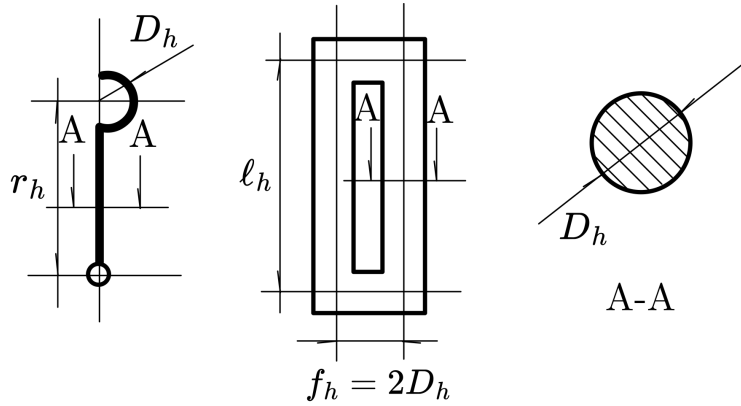
Figure 9.4: Sizing characteristics.

9.2.4 Trend study on λ_h

The following plots see the dependence of attractive force and torque during capture for different values of λ_h. The actions have been adimensionalized (respectively $\tilde{F}_h$ and $\tilde{T}_h$ denote the dimensionless fore and torque), so as to focus on those 2 parameters (time, or capture angle, and aspect ratio).

$$F_{h,ref} = m_{ref}\omega_h^2 r_h \qquad T_{h,ref} = T_{h,ref} = F_{h,ref} \cdot r_h = m_{ref}(\omega_h r_h)^2 \tag{9.8}$$
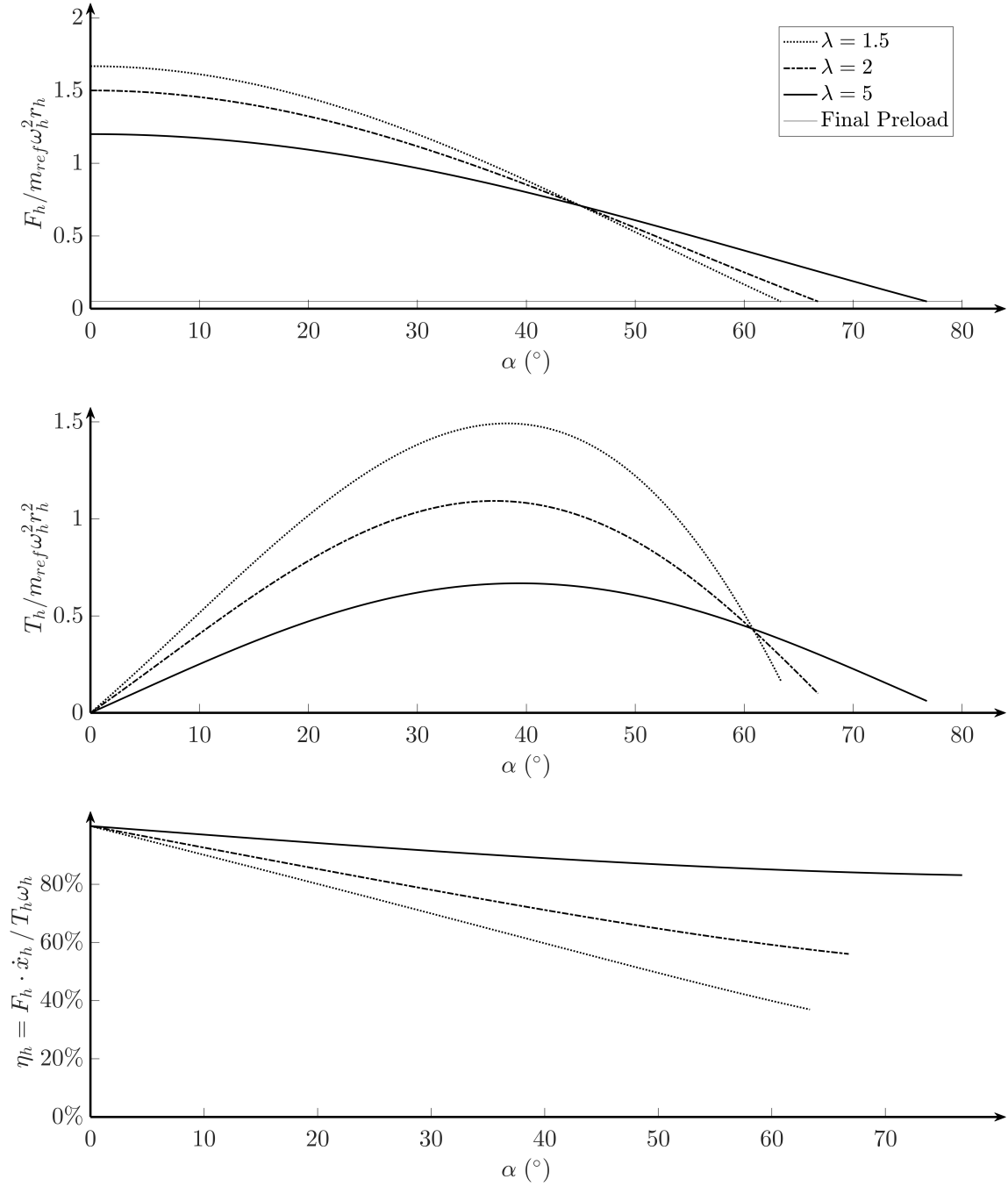
Figure 9.5: Trend study of the dynamics of the system for different types of λ_h.

From the following trends it is clear that the efficiency of the system grows with larger and larger λ_h, as it is common for those applications. It should be noted that a small dimensionless residual force was set as $\tilde{F}_{h,f} = 5\%$ in order not to arrive at null force at the end of the maneuver.

9.2.5   Initial and final conditions

By the geometrical considerations seen in Equation 9.3, it is possible to see that given a little offset d_{of} between the outer extent of the geometry and the OP segment (which provides further protection of the mechanisms and the motors):

$$x_h(t) = r_d(t) + d_{of} = r_h \cdot \left(\cos \alpha_h + \sqrt{\lambda_h^2 - \sin^2 \alpha_h} \right) = r_h \cdot \tilde{x}_h(\alpha_h, \lambda_h) \qquad (9.9)$$

Therefore, given the initial and final conditions in which $r_d(t_c) = r_d(\alpha_{h,c}) = r_{d,c}$ is set on the Loads Requirements in chapter 7 and $r_d(t_f) = r_d(\alpha_{h,f}) = 0$ the following set is of equations is proposed.

$$\begin{cases} r_{d,c} + d_{of} & = r_h \cdot \tilde{x}_h(\alpha_{h,c}, \lambda_h) \\ d_{of} & = r_h \cdot \tilde{x}_h(\alpha_{h,f}, \lambda_h) \end{cases} \implies \begin{cases} r_h & = r_{d,c}/(\tilde{x}_h(\alpha_{h,c}, \lambda_h) - \tilde{x}_h(\alpha_{h,f}, \lambda_h)) \\ d_{of} & = r_h \cdot \tilde{x}_h(\alpha_{h,f}, \lambda_h) \end{cases}$$

$$(9.10)$$
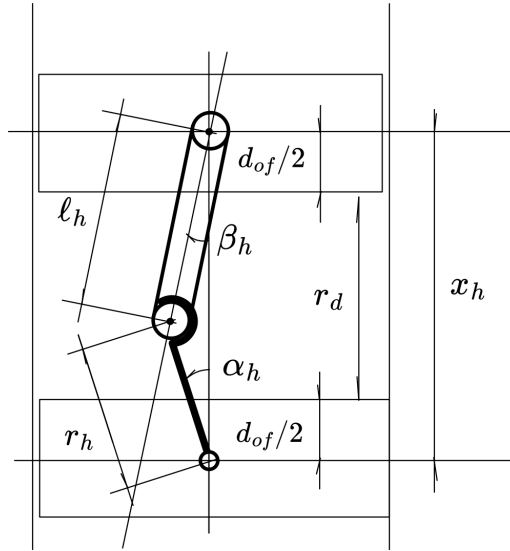
The following conditions impose larger and larger values of r_h and d_{of} given that the initial capture condition is fixed by the requirements. Therefore, to balance the high efficiencies (see the graph on the right) given by high values of λ_h and the compact form factor of the system, a candidate value of λ_h is selected. As it is possible to see (right graph), all the geometric properties listed in this section follows straight from this choice, given that

$$\ell_h = r_h \cdot \lambda_h$$
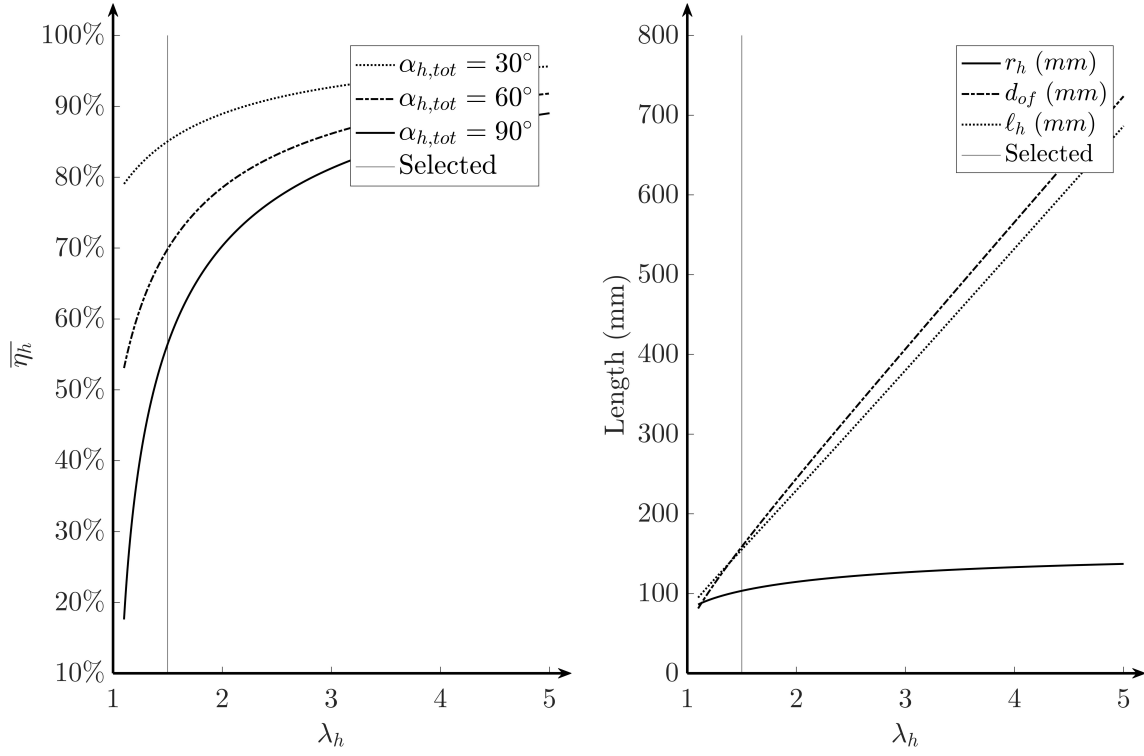
Figure 9.6: Final trend study on λ_h: effect of the aspect ratio on the mean value of the efficiency during different final angles (left) and on the dimensional values (right).

9.2.6 Structural sizing

Next on the list is the hooks' diameter D_h. As seen in chapter 8, the same discussion is proposed given

$$\mathcal{M}_h = \frac{\mathcal{F}_h}{\mathcal{F}_{h,imposed}} - 1 \geq 0 \qquad (9.11)$$
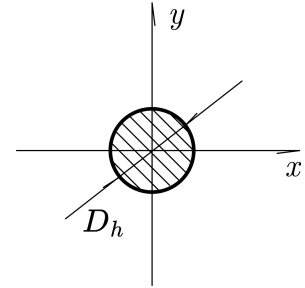
with:

1. $\mathcal{M}_h$ is the imposed safety margin;

2. $\mathcal{F}_h = \sigma_y / \max\{\sigma_{eq}\}$ is the minimum found safety factor on the structure;

3. $\mathcal{F}_{h,imposed} = 1.5$ is the imposed safety factor.

Given that the material is likely homogenous and isotropic (an alluminum/steel alloy can be fairly used), the Von Mises criterion is prescribed. Therefore, for each component (hook and latch), and for each segment of the component, the maximum equivalent stress is evalued, given

$$\sigma_{eq} = \sqrt{\sigma^2 + 3\tau^2}$$

Before starting, it should be noticed that a reference stress is addressed, as for all

the previous studies, as follows:

$$\sigma_{ref} = \frac{F_{h,ref}}{A_{ref}} = \frac{F_{h,ref}}{\pi(D_h/2)^2} \tag{9.12}$$

Moreover, the following table summarizes the principal properties of the cross-section of the components. Given the symmetry of the cross section, those values are referenced in the G-frame of the cross-section.

Name	Symbol	Value	Units
Cross Section Area	A_h	$\pi(D_h/2)^2$	m^2
Cross Section Static Moment (geometrical)	$S_{xx,h} = S_{yy,h}$	$\pi(D_h/2)^3/2 = A_h \cdot (D_h/2)/2$	m^3
Cross Section Inertia Moment (geometrical)	$I_{xx,h} = I_{yy,h}$	$\pi(D_h/2)^4/4 = A_h \cdot (D_h/2)^2/4$	m^4
Cross Section Polar Inertia Moment (geometrical)	$I_{p,h}$	$\pi(D_h/2)^4 = A_h \cdot (D_h/2)^2$	m^4

Table 9.2: Geometrical properties of the cross section of the components.

Latches

The latches are composed of a vertical rod long ℓ_h and an horizontal ford long f_h. This latter value is yet to be found, but it is safe to assume that at least it should be long enough to hold the hook when captured. Therefore,

$$f_h \geq 2D_h \tag{9.13}$$

The minimum value is chosen for sizing. As it will be shown, this does not affect importantly the results. The proposed table summarizes the principal stress acting on the latch.
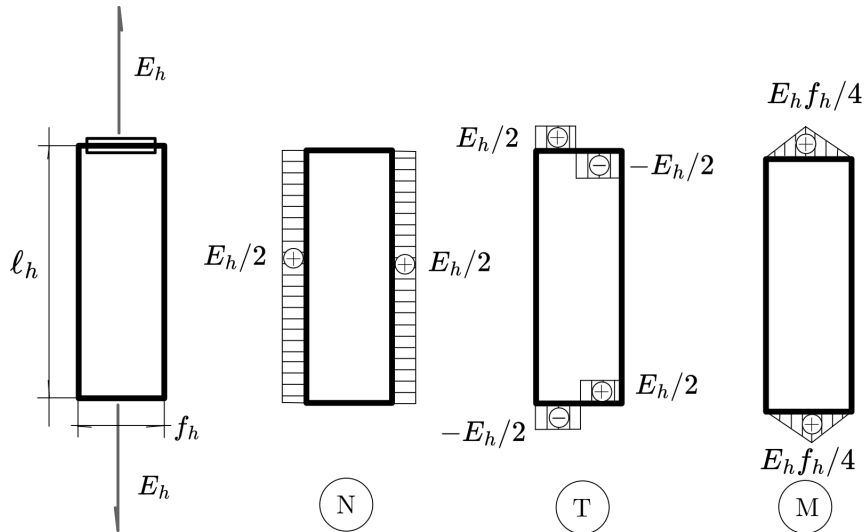
The proposed study suggests that the maximum load is in the horizontal section. This is aligned with the proposed analogy with the crank mechanism.

Stress	Horizontal	Vertical
σ	$$\begin{aligned}\sigma &= \frac{M_x}{I_{xx,h}} \cdot \frac{D_h}{2} \\ &= \frac{E_h f_h}{4 I_{xx,h}} \cdot \frac{D_h}{2} \\ &= \frac{F_{h,ref}}{A} \left(\tilde{E}_h \frac{A_h D_h f_h}{8 I_{xx,h}} \right) \\ &= \sigma_{ref} \left(4 \tilde{E}_h \right) \end{aligned}$$	$$\begin{aligned}\sigma &= \frac{E_h}{2A} \\ &= \sigma_{ref} \frac{\tilde{E}_h}{2}\end{aligned}$$
τ	$\tau = \dfrac{E_h}{2A} = \sigma_{ref} \dfrac{\tilde{E}_h}{2}$	0

Table 9.3: Latches Loads.

Hooks

Similarly, the same argument is brought to hooks. Here, it is possible to see that the maximum stress region is at the root of the hook, where all the stresses are transmitted to the subsequent component (the motor or the motor gear assembly).
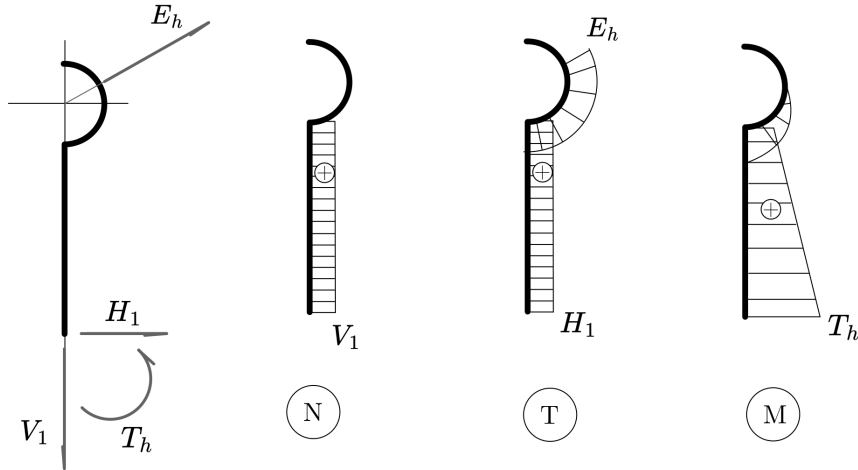
Stress	Root
σ	$$\begin{aligned}\sigma &= \frac{V_1}{A_h} + \frac{T_h}{I_{xx,h}} \frac{D_h}{2} \\ &= \frac{F_{h,ref}}{A_h} \left(\tilde{V}_1 + \tilde{T}_h \frac{A_h D_h r_h}{I_{xx,h}} \right) \\ &= \frac{F_{h,ref}}{A_h} \left(\tilde{V}_1 + \tilde{T}_h \frac{8}{D_h / r_h} \right) \\ &= \sigma_{ref} \left(\tilde{V}_1 + \tilde{T}_h \frac{8}{D_h / r_h} \right)\end{aligned}$$
τ	$\tau = \dfrac{H_1}{A} = \sigma_{ref} \tilde{H}_1$

Table 9.4: Hooks Loads.

Structural trends

The following plot shows the maximum dimensionless stress as a function of the capture angle α_h, for different values of D_h/r_h. The abrupt termination in the final zone is indicative of the different trends between the hooks and the latches. In this portion of the graph, the maximum load is in the latches. The bumps, instead, are mainly a function of the hooks loads trend with α_h. Therefore, the assumption that f_h is really not that important to structural sizing is validated. Given those trends,
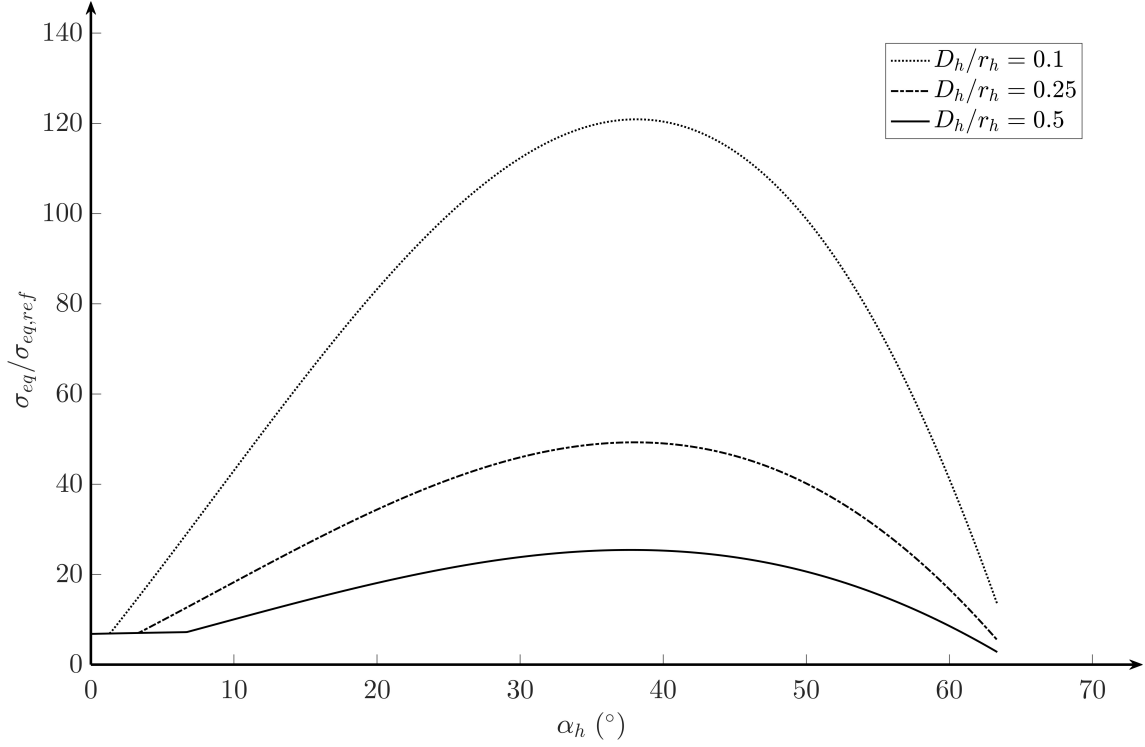
Figure 9.7: Dimensionless structural stress in the hooks and latches during capture.

it is possible to estimate the present safety factor and hence the safety margin. To compute dimensional value it is necessary to impose dimensional properties. Specifically, the reference force is evaluated considering:

$$F_{h,ref} = m_{ref}\omega_h^2 r_h$$

1. the reference mass is a function of the female alignment geometry, which will be pulled from the capture system during this moments. This value is augmented by a safety factor which stems from the considerations that the pulling force is also contrasting the resistive force of the springs and dampers on the shock absorber, in the back of the ALN geometry. Therefore:

$$m_{ref} = (1 + k_m) \cdot m_{aln}$$

with $k_m = 1.5$. The reference mass is therefore 2.5 times higher than the ALN mass.

2. the angular velocity is computed by setting a capture time Δt_c. Hence

$$\omega_h \cong \frac{\Delta\alpha_h}{\Delta t_c}$$

3. the hooks effective length r_h is given by the previous section.

Values regarding the angular velocity, and the RPM of the system are found in the following table.

Δt_c	$\alpha_{h,c}$	$\alpha_{h,f}$	ω_h	N_h
0.5000	0	63.3536	2.2115	21.1179
s	°	°	rad/s	RPM

Table 9.5: Angular velocity table.

The following plot shows the trend of the minimum safety margin (corresponding to the maximum equivalent stress, given by the previous trend) with respect to the cross-section diameter D_h. As it is possible to see, this trend is approximately parabolic given that

$$\sigma_{eq} \propto \frac{F_{h,ref}}{\pi(D_h/2)^2} \implies \mathcal{M}_h \propto \frac{1}{\sigma_{eq}} \propto D_h^2$$

Choosing a proper safety factor $\mathcal{M}_h = 100\%$ a value of the diameter is found. The following table, shows finally the geometric properties of the capture system.

$r_{d,c}$	λ_h	ℓ_h	r_h	d_{of}	Latch free length	Hook free length	D_h
100	1.5000	180	120	200	-80.0000	-20.0000	14
mm		mm	mm	mm	mm	mm	mm

Table 9.6: Geometrical properties of the selected configuration.

9.2.7   Force/Displacement Approximation

One of the important aspects of such sizing, apart from the geometry and sizing of the hooks, is the ability to express the capture force as a function of the relative displacement. Indeed, given the force F_h and the relative displacement $x_h = r_h + d_{of}$, which are both a function of the capture angle α_h, it is possible to compare the two properties in a graph.

As it is possible to see, this function is easily approximated by a linear trend.

$$F_{HCS}(r_d) = k_{HCS} \cdot (r_d - r_{d,0}) \tag{9.14}$$

Taking $F_{h,c}$ and $F_{h,f}$ as the extrema at the end and the beginning of the capture, it is possible to calculate

$$k_{HCS} = \frac{F_{h,c} - F_{h,f}}{x_{h,c} - x_{h,f}}$$

$$r_{d,0} = \left(x_{h,f} - \frac{F_{h,f}}{k_{HCS}} \right) - d_{of}$$

The proposed graph also shows the relative error committed. As it is possible to see, the approximation is quite superimposable to the real trend. In fact, it is assumed
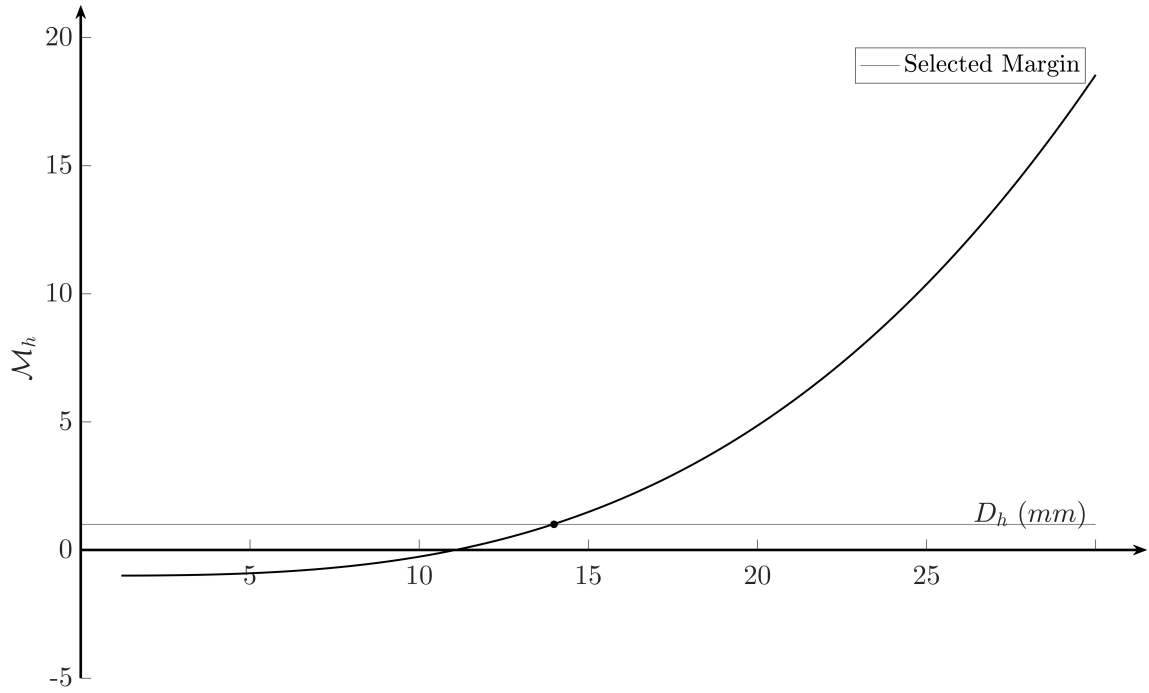
Figure 9.8: Margin of safety plot of the capture hooks with respect to the hook's cross section diameter.
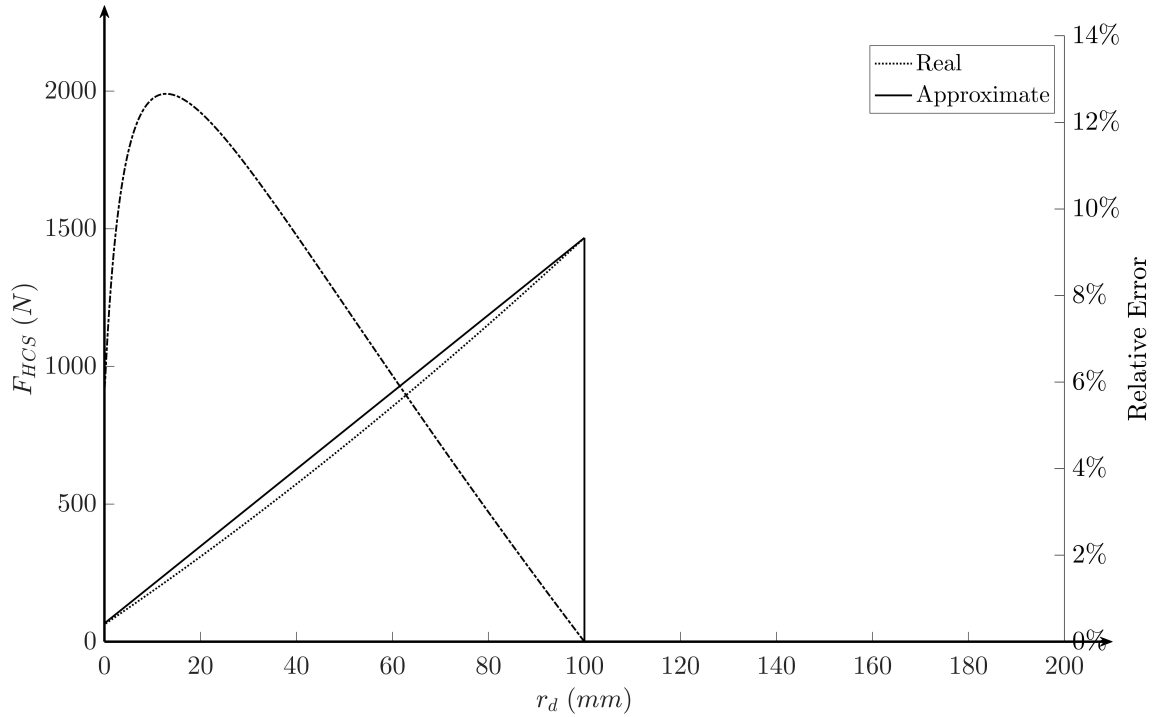
Figure 9.9: Force-distance plot of the mechanical HCS.

that in general capture system can be modelled via a power force of the relative distance and a capture coefficient which is a function of the geometrical, physical, mechanical and electrical properties of the capture solution.

$$F_{HCS} = k_{HCS}(r_d - r_{d,0})^q \tag{9.15}$$

for some exponent q. In the following example $q = 1$ and hence the problem is linear. The following table shows the corresponding results of the proposed variables. In particular, $F_{h,f} = F_{h,ref} \cdot \tilde{F}_{h,f} = 0.05 \cdot F_{h,ref}$, as it is set in the requirements.

$\boldsymbol{F_{h,c}}$	$\boldsymbol{F_{h,f}}$	$\boldsymbol{k_{HCS}}$	$\boldsymbol{r_{d,0}}$	Maximum relative error.
1500	44	14000	-4.8000	0.1300
N	N	N/m	mm	

Table 9.7: Force-related parameters for the selected configuration.

Those values serve as a ground foundation for the preliminary sizing in chapter 8 and for a subsequent optimization proposed in chapter 10. In particular, k_{HCS} will be used as an optimization variable.

9.2.8 Power Estimate

Finally, as a conclusive aspect of the sizing, a power estimation of the HCS is estimated. Given that the capture is the only active moment in the docking maneuver, this is indeed the total power request of the system. As proposed in the dynamical equations, given the requested force, and a set of N_{hooks}, the requested nominal torque on each of them is:

$$T_{h,nom} = \frac{T_h}{N_{hooks}}$$

Similarly, given that for emergency all the load is discharged on only one hook, the maximum torque request is:

$$T_{h,max} = N_{hooks} \cdot T_{h,nom} = T_h$$

The total power request for each of the motor, estimating a power loss in wirings and for motor friction of $\eta_{bus} = 50\%$ is

$$\mathcal{P}_{dock,s} = \frac{1}{\eta_{bus}} T_{h,nom} \omega_h$$

which corresponds to a total docking power request of $\mathcal{P}_{dock} = N_{hooks} \mathcal{P}_{dock,s}$. Finally, the current flowing in the motor, given the bus voltage requirement in chapter 2,

$$i_{dock} = \frac{\mathcal{P}_{dock,nom}}{V_{nominal}}$$

The results are presented in the following table.

$\boldsymbol{T_{h,nom}}$	$\boldsymbol{i_{dock}}$	$\boldsymbol{\mathcal{P}_{dock,nom}}$	$\boldsymbol{T_{h,max}}$	$\boldsymbol{\mathcal{P}_{dock}}$
4.38	0.69	19.36	26.27	116.18
$N\,m$	A	W	$N\,m$	W

Table 9.8: Docking power request table.

9.3   Magnets sizing

Magnetic force estimation is usually more difficult to estimate and measure given that there are usually no moving parts involved. This indeed is a bonus feature considering the lack of coverings (which is usually requested for hooks and latches) that serve as a protection for the environment, radiation and dust. Nevertheless, as for the mechanic counterpart, a simple model is derived to derive some relationships for the sizing. The simplest of the systems consists of an active magnet (an *electro-magnet*) and a passive magnet, made out of a mettallic plaque. Given that the ALN geometry is polymeric, as suggested in the material selection in chapter 8, EMI and parassite currents risks are lowered. The magnetic force of a single magnet can be derived from Maxwell's Equations:

$$\boldsymbol{F}_{m,2} = \nabla(\boldsymbol{m}_{d,2} \cdot \boldsymbol{B}_1) \tag{9.16}$$

with:

1. $\boldsymbol{F}_{m,2}$ is the force acting on the magnet 2.

2. $\boldsymbol{m}_{d,2}$ as the magnetic dipole moment of the magnet 2.

3. $\boldsymbol{B}$ is the magnetic field produced by the magnetic dipole 1.

It is assumed that:

1. Both magnets are approximated as magnetic dipoles;

2. The dipole moments are aligned; the alignment axis is denoted by x_h.

3. The active magnet is referred by 1 and passive magnet is referred by 2.

4. The separation between them is much larger than their size (far-field approximation).

Since both dipoles are aligned on the x_h-axis, the only force is

$$F_{mx,2} = \frac{d}{dx_h}(m_{d,2}B_1(x_h))$$

The magnetic dipole of the passive magnet is

$$m_{d,2} = M_2 \cdot \mathcal{V}$$

with $M_2 = B_r/\mu_0$ being the residual magnetization acting on the magnet, and $\mathcal{V}$ is the volume of the magnet. For simplicity, magnetic disks are used, so as given the diameter and the height of the magnet

$$\mathcal{V} = \pi \left(\frac{D_m}{2}\right)^2 h_m$$

Notably, $m_{d,2}$ is not a function of x_h. On the other hand, the magnetic field produced by dipole $m_{d,1}$ along the x_h-direction is:

$$B_1(x_h) = \frac{\mu_0}{4\pi} \frac{2m_{d,1}}{x_h^3}$$

with the magnetic dipole $m_{d,1}$:

1. being equal to $m_{d,2}$ if it is a permanent magnet;

2. being equal to $m_{d,2} = N_{coil} \cdot i \cdot A_m$ if it is an electromagnet turned on by a coil of N_{coil} turns and i current, with $A_m = \pi(D_m/2)^2$ being the face area of the magnet.
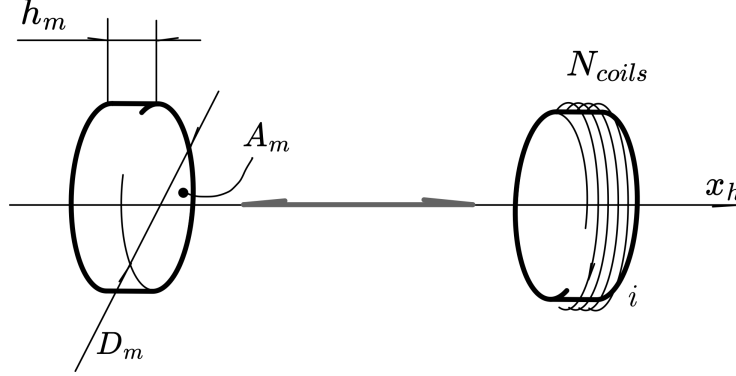
Therefore, by differentiating,

$$F_{m,2}(x_h) = -\frac{3\mu_0}{2\pi} \frac{m_{d,1}m_{d,2}}{x_h^4}$$

If, instead, the far-field approximation is dropped and the two magnets are in close contact (as it is the case for approaching magnets) the force becomes

$$F_{m,2}(x_h) \cong \frac{B_r^2 A_m}{2\mu_0}$$

Using this latter equation as a reference force, and adimensionalizing the force,

$$\tilde{F}_m = \frac{F_{m,2}}{F_{m,ref}} = \min\left\{3\left(\frac{N_{coil}iA_m}{B_r h_m^3/\mu_0}\right)\cdot\left(\frac{1}{x_h/h_m}\right)^4;1\right\}$$

$$= \min\left\{3\left(\frac{m_{d,2}}{m_{d,1}}\right)\cdot\frac{1}{\tilde{x}_h^4};1\right\}$$

$$= \min\left\{3\varkoppa\cdot\frac{1}{\tilde{x}_h^4};1\right\}$$

with $\varkoppa$ (read as "Qoppa") being a dimensionless parameter which can be interpreted as the ratio between the reference active magnetic dipole and the reference passive magnetic dipole.

$$\varkoppa = \frac{N_{coil}iA_m}{B_r h_m^3/\mu_0} \tag{9.17}$$

If both magnets are passive, then $\varkoppa$ resembles the form of an aspect ratio of the magnet.

$$\varkoppa = \frac{A_m}{h_m^2}$$

For instance, if the two magnets are considered permanent, with a residual magnetic field of $B_r = 0.75\ T$, the following parameter can be estimated so as to have a magnetic force in the near-field approximation equal to the $F_{h,c}$ proposed in the previous section. The selected values for the B_r are found in datasheets for **Neodymium Magnets**. It is also used to size the real prototyped version of the HCS proposed in chapter 11.
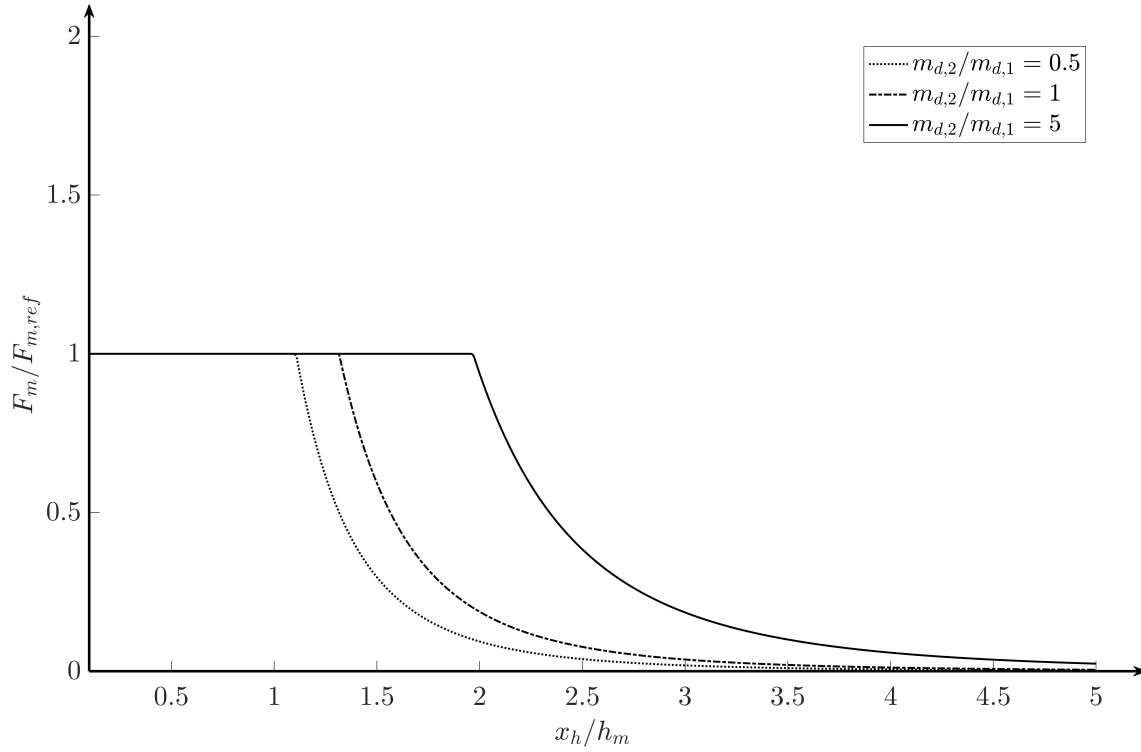
Figure 9.10: Dimensionless magnetic force with respect to dimensionless distance, for different values of $\Psi = m_{d,2}/m_{d,1}$.

$F_{m,ref} = F_{h,c}$	$N_{magnets}$	$\Psi = m_{d,2}/m_{d,1}$	B_r	D_m	h_m
1500	6	5	0.7500	60	33
N			T	mm	mm

Table 9.9: Example values for the magnetic HCS.

The following plot shows this trend along the dimensionless x_h direction, for diffrent values of Ψ.

9.3.1   Power estimate

As for its mechanical counterpart, the total power is concenctrated in the capture system. Here if one of the magnets is active, the power is

$$\mathcal{P}_{dock,s} = N_{coil} \cdot i \cdot V_{nominal}$$

If there are more magnets, the force, hence the power is multiplied by a factor of $N_{magnets}$. If instead, both magnets are permanent, the total power is completely null, hence the docking system is fully powerless. However, such solution is not feasable, given that a mechanical or some other system should be implemented to undock the two elements when the chaser departs from the target.

Chapter 10

Model Implementation

Once the theoretical aspects of the docking sizing have been defined, a real model is developed in order to test the assumptions. The aim of this chapter is to provide a schematic approach to the implementation of the model which follows a genetic optimization via MATLAB© to provide an efficient calculation of the dynamics implemented via a MSC ADAMS© file. The complete dynamics of the system passes through an iterative sizing in order to minimize the *relative misalignment error* objective presented in chapter 8, while maintaining proper contact constraints.

10.1   Implementation flow-chart

To get a correct view of the presented results the following flow-chart is developed. It consists of the following blocks:

1. design of a CAD in SolidWorks©, in order to have a clear definition of the sizes of the LPR;

2. SolidWorks© Motion Implementation: this plugin already installed in the software performs some preliminary motion analysis on the design. This step ensures that the dynamics is set and ready for the subsequent phases;

3. MSC ADAMS© export and parametrization: SolidWorks© Motion provides a direct export tool for the full dynamical setting into ADAMS. This ensures ease of result cross-checking among the two pieces of software. MSC ADAMS is used to perform a more in-depth analysis as it has gradually become a standard in the space sector for those types of problems. Moreover, a full **parametrization** of the problem can be implemented, in order to have a clear picture of the inputs and the outputs.

4. MATLAB© optimization of the objective function via the use of a genetic algorithm.

5. Results and sizing of the proper components.
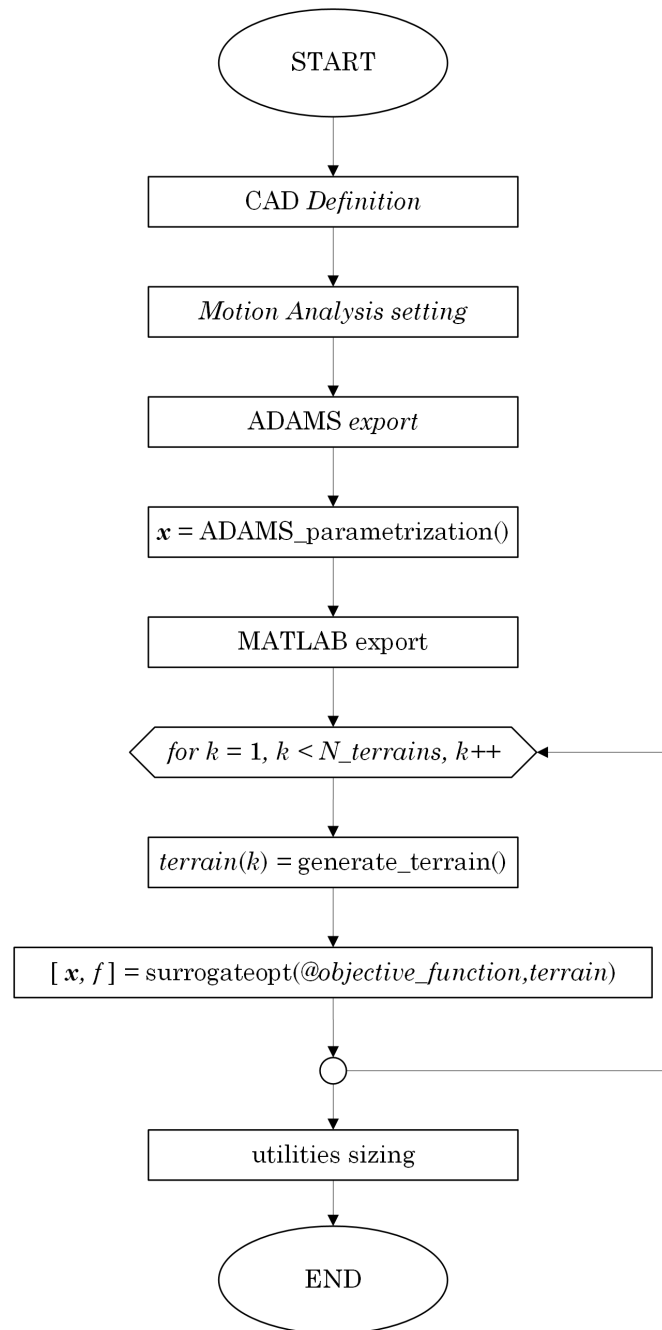
Figure 10.1: Implementation Flow-Chart

10.2 Implementation procedure

10.2.1 SolidWorks

The CAD Model consists of a Large Assembly (ASM_PROTEUS_LA) which contains the three main subcomponents in the simulation:

1. the PROTEUS Rover (ASM_PROTEUS);

2. the Habitat (ASM_Habitat) simulant, that stores the female docking assembly;

3. the lunar surface (LA_Terrain);

Each component follows the following nomenclature:

ASMNAME_COMPONENTNAME<PARTNUMBER>

Assemblies are listed via a "ASM" prefix (such as ASM_Habitat) and single components take the parent assembly name (for example, the structural pressurized structure of the PROTEUS Rover is called PR_Pressurized_Structure<1>). SolidWorks automatically assigns part numbers.
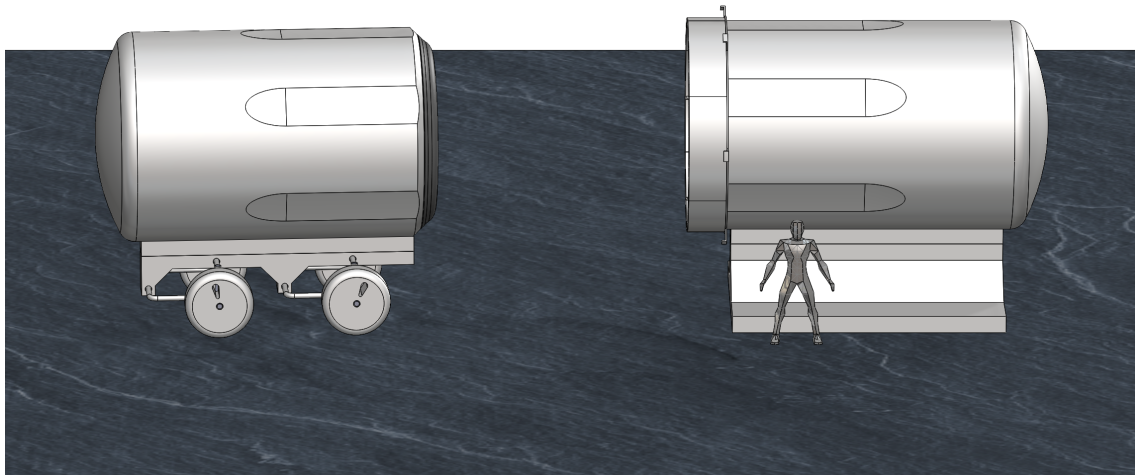
Figure 10.2: Visual Representation of the SolidWorks CAD model. A reference human is placed so as to have an idea of the dimensions of the Large Assembly.
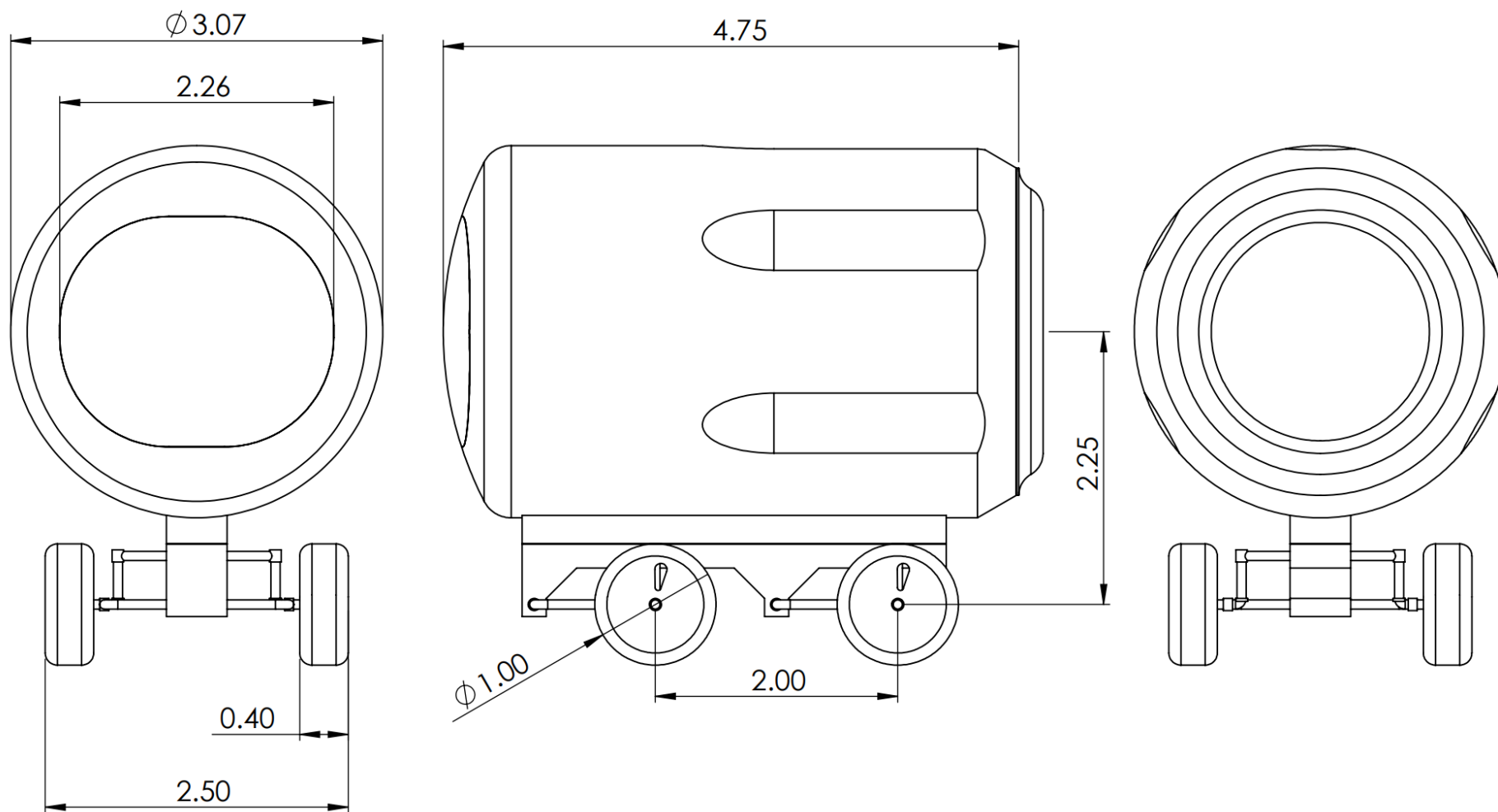
Figure 10.3: Technical Representation of the PROTEUS Rover.
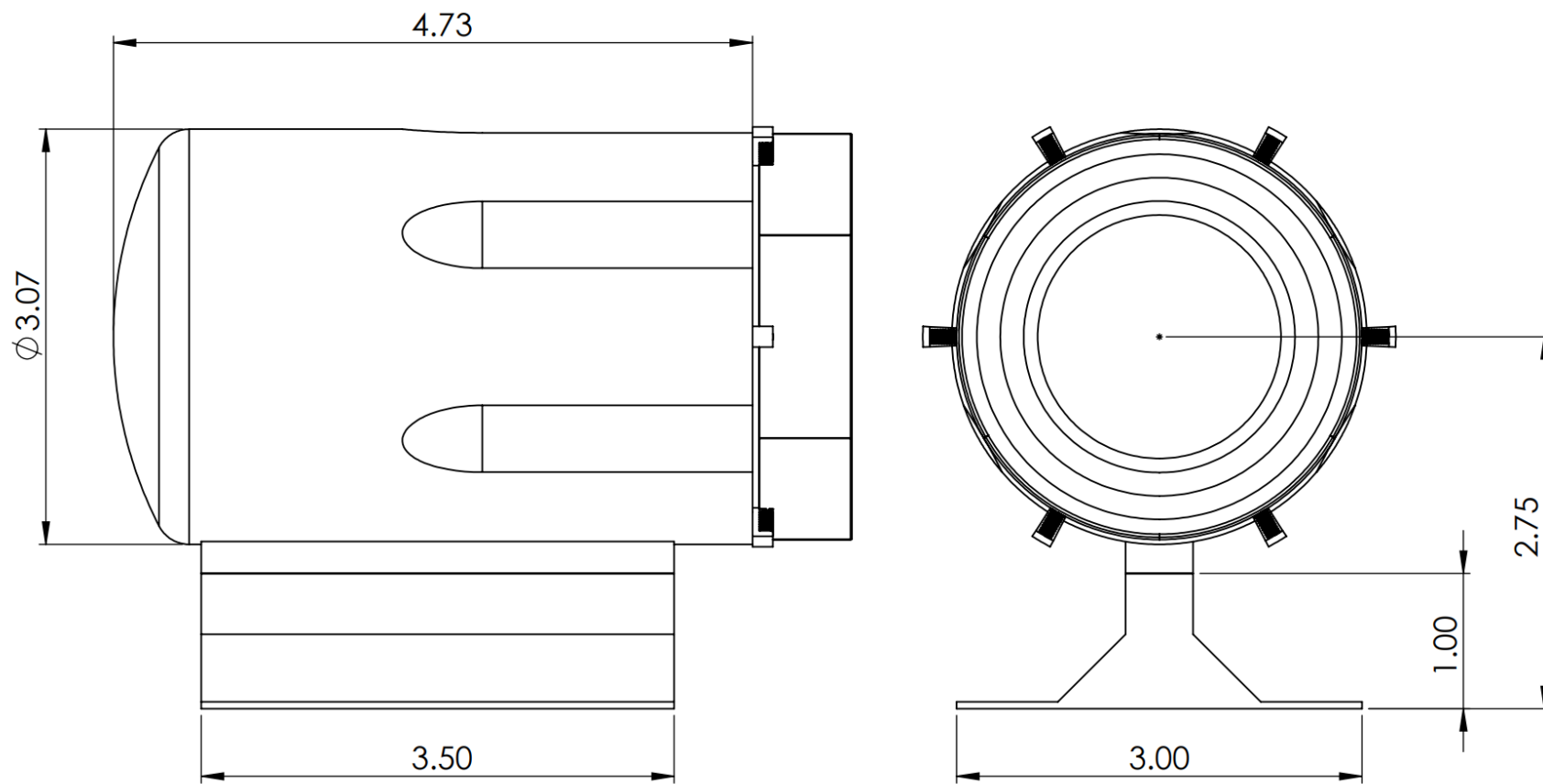
Figure 10.4: Technical Representation of the Habitat module with the female docking subsystem.
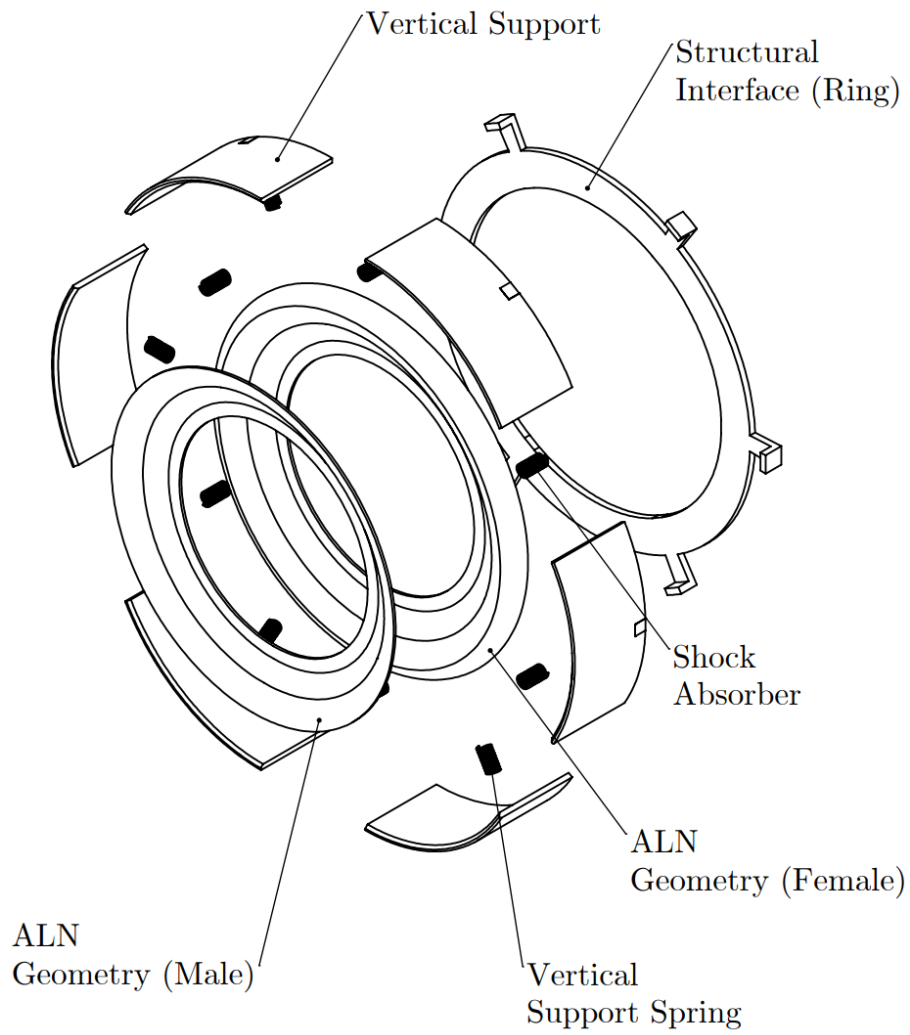
Figure 10.5: Exploded View of the Full docking subsystem (male and female).

Male Alignment Geometry   Female Alignment Geometry
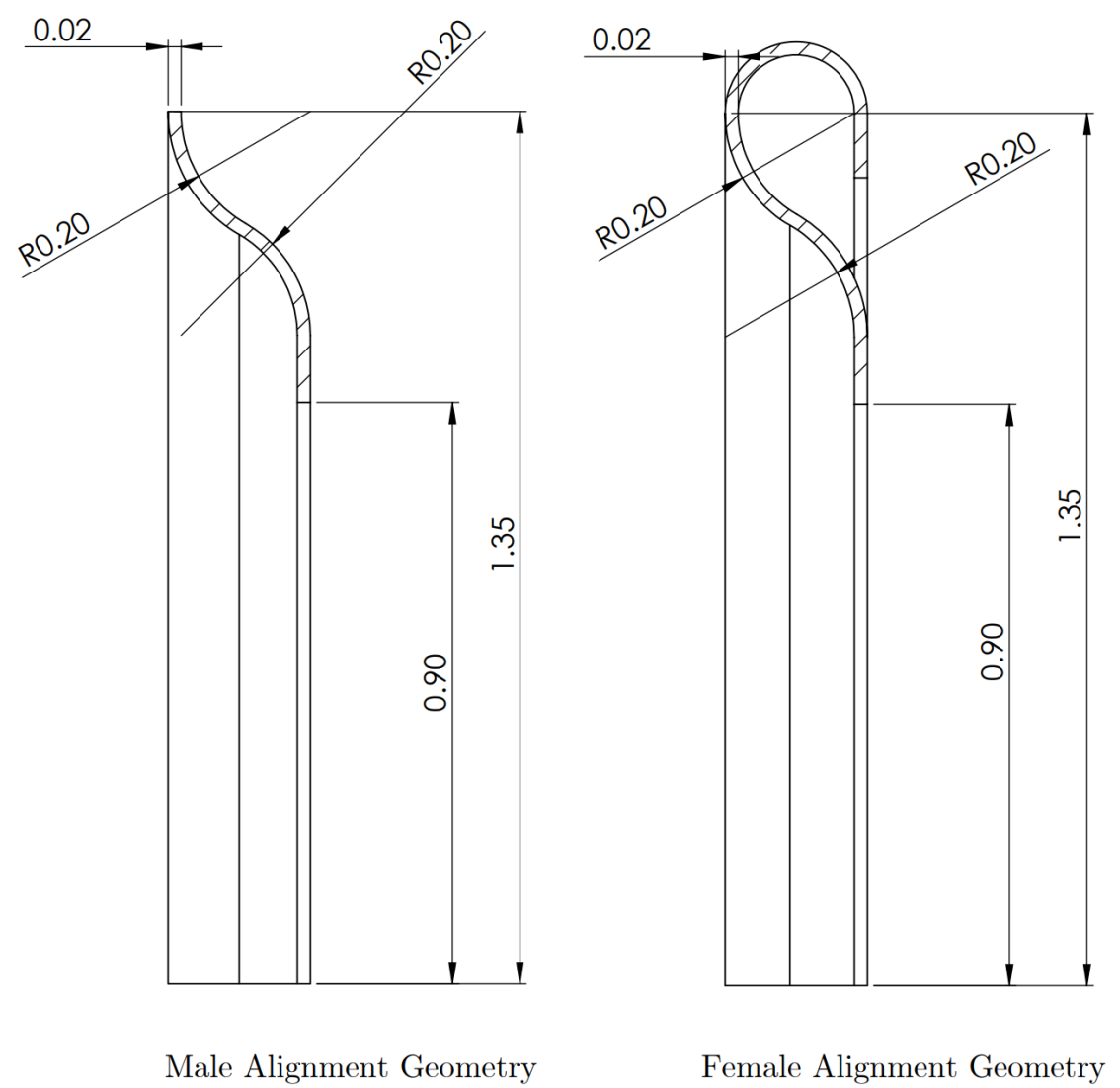
Figure 10.6: Female and Male Alignment Geometry representation.
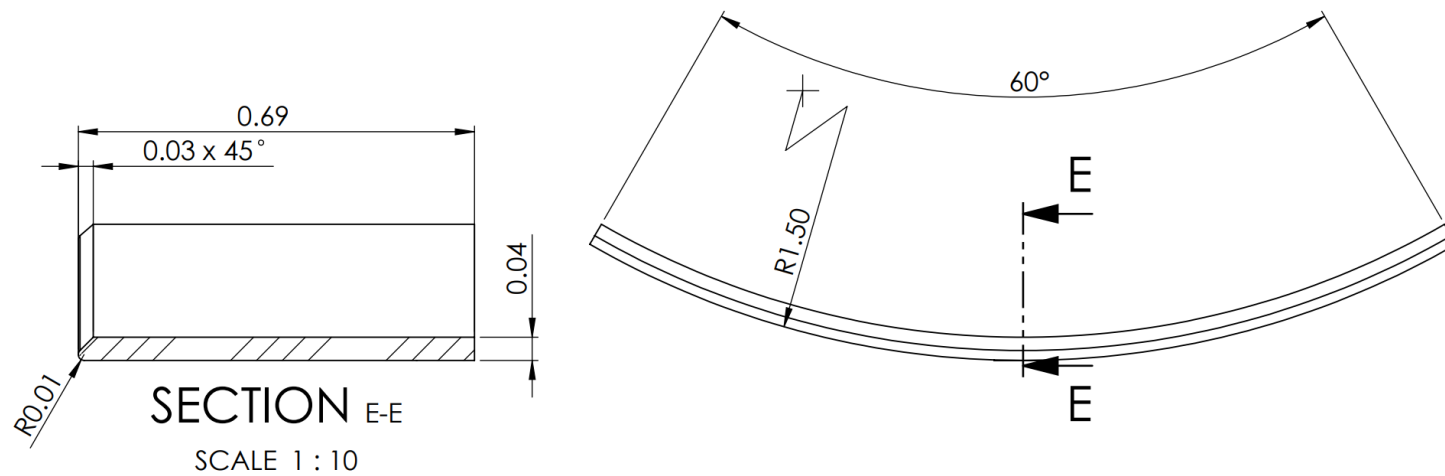
Figure 10.7: Technical Representation of the Vertical Support Geometry.

10.2.2 Motion Analysis

After properly defining all the geometrical aspects of the model and a correct mass for all the components, a SolidWorks Motion Analysis is performed. The following table shows a list of the interactions implemented in the Motion Analysis. Terrain contact properties have been estimated via Table 6.4, using the regolith simulant found in literature.
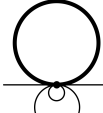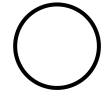
Interaction	Image	Expression	Input	Constant Parameter	Output
terrain contact		$CONTACT(\cdot, \cdot, \kappa_t, n_t, c_t, h_t)$		κ_t, n_t, c_t, h_t : from lunar regolith properties	
drive torque		T_d $\cdot STEP(v_d - v_{d,ref}, 0, 1, \epsilon, 0)$ $\cdot IF(r_d - r_{d,br}, 0, 0, 1)$		T_d : uninteresting $v_{d,ref}$: from reqs.	
braking torque		$-k_{br} \cdot \omega$ $\cdot IF(r_d - r_{d,br}, 1, 1, 0)$		k_{br} : uninteresting $r_{d,br} = r_{d,c}$: from reqs.	
ALN contact		$CONTACT(\cdot, \cdot, \kappa_I, n_I, c_I, h_I)$		κ_I, n_I, c_I, h_I : from material selection	P : for constraint evaluation
shock absorber		$k_{II}(x_{II} - \ell_{II,0}) + c_{II}\dot{x}_{II}$	$k_{II}, c_{II}, \ell_{II,0}$		
vertical support		$k_v \cdot z_v$	k_v		
HCS force		$k_{HCS} \cdot r_d$ $\cdot IF(r_d - r_{d,c}, 1, 1, 0)$	k_{HCS}		r_d : for objective evaluation

Table 10.1: Interaction Summary of the Motion Analysis Model.
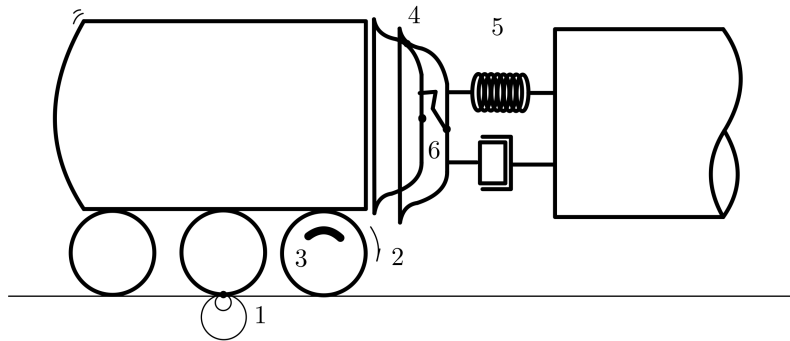
Figure 10.8: Interactions used in the Motion Analysis.

It should be noted that:

1. T_d is marked as "uninteresting" input, due to the fact that it is not aim of this work to investigate the mobility properties of the LPR. Drive torque is used to maintain and sustain the speed at constant $v_{d,ref}$ in order to emulate the proposed approach definition, seen in chapter 8. As such, a value of $T_d = 50 \ N \cdot m$ is chosen for the 2 back-wheels, given the proposed power estimates in the corresponding automotive counterparts, seen in the preliminary study in chapter 2.

2. the same argument is brought for braking. In the proposed simulation, the braking torque is $T_{br} = -k_{br} \cdot \omega_w$ with ω_w being the longitudinal wheel angular velocity. Given that no braking sizing is requested, a sample value of $k_{br} = 50 \ N \cdot m/(\text{rad}/s)$ is used, again stemming from automotive considerations.

3. It is chosen to synchronize braking and HCS activation by imposing an $IF(x : c_1, c_2, c_3)$ function. This ADAMS function returns c_1 when $x < 0$, c_2 when $x = 0$ and c_3 when $x > 0$ for a given input x. Following the definition in Table 10.1, this function "activates" both braking and HCS when $r_d - r_{d,ref} < 0 \implies r_d < r_{d,ref}$.

4. Similarly, the drive torque is "de-activated" when the same condition applies. In this way, given initial contact, the LPR starts braking and the latching system performs hard capture.

Table 10.2 follows the proposed description in detail.

Type	Property	Symbol	Value	Units	Based on
Terrain	Contact stiffness	κ_t	$5 \cdot 10^7$	N/m^n	[36]
Terrain	Contact exponent	n_t	1.9	–	[36]
Terrain	Contact damping	c_t	1000	$N/(m/s)$	[36]
Terrain	Contact depth	h_t	1.5	mm	[36]
Terrain	Static friction coefficient	$\mu_{s,t}$	0.85		[36]
Terrain	Dynamic friction coefficient	$\mu_{d,t}$	0.75		[36]
Terrain	Static friction trans. Velocity	$v_{tr,s,t}$	0.02	m/s	[36]
Terrain	Dynamic friction trans. Velocity	$v_{tr,d,t}$	0.1	m/s	[36]
Drive Torque	Max. Torque	T_d	50	$N\,m$	Automotive considerations
Brake Torque	Torque Coeff.	k_{br}	50	$N\,m/(rad/s)$	Automotive considerations
Brake Torque	Brake distance	$r_{d,c}$	0.1	m	Requirements

Table 10.2: Fixed parameter used in the multibody simulation.

The complete set of input parameters $\boldsymbol{x} = \{k_{HCS}, k_{II}, c_{II}, \ell_{II,0}, k_v\}$ forms the complete state vector of the model. The problem statement is therefore to find the optimal state vector corresponding to the minimum relative misalignment error $\not{p}$ such that the contact force is below the proposed "Loads Requirements" seen in chapter 7.

$$\not{p}_{min} = \min_{\boldsymbol{x}}\{\not{p}(\boldsymbol{x}) : P < P_{adm}\}$$

After correctly setting all the Motion Analysis interaction, the simulation is run in order to check the correct motion of the LA. By right-clicking in the model tree in the Motion Analysis and select *Export to ADAMS*, SolidWorks automatically export the Motion analysis as an .adm file.
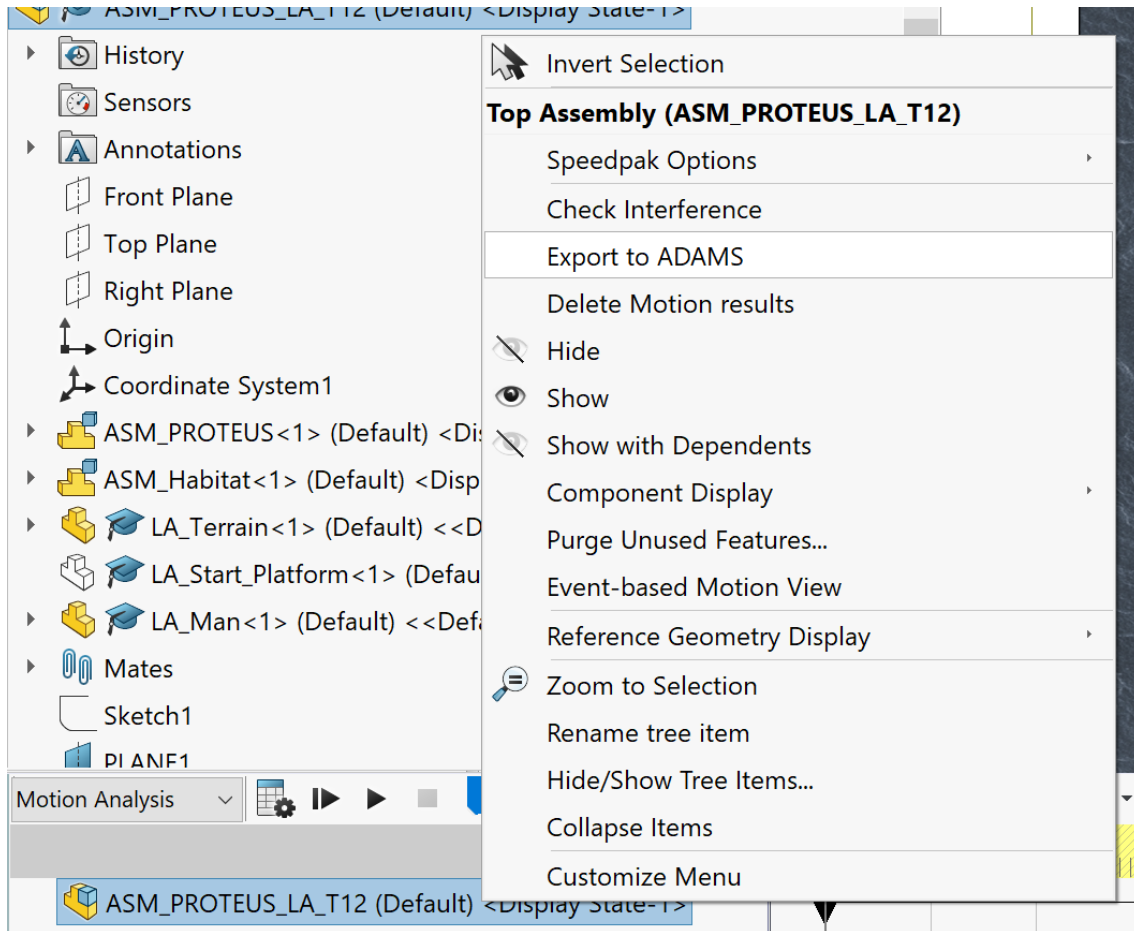
Figure 10.9: "Export to ADAMS" command from SolidWorks Motion Analysis. This command saves the Motion Analysis in an .adm file.

10.2.3 ADAMS Implementation

SolidWorks© Motion provides a direct export tool of the full dynamical setting into ADAMS as a .adm file. It should be noted, however, that the two programs may have some interface issues: specifically, SolidWorks refers to part numbers with a dash symbol, "-", while ADAMS usually prefers under-dashed names, "_". This may result in a mis-interpretation of the function in the ADAMS tree by MATLAB. For instance, due to this incompatibility, only "interactive" analysis can run and not "batch" analysis (see following section), which may result in unrelevant compilation time. In order to cope with this incomprehension, an ad-hoc script is implemented in order to rename the properties in the ADAMS tree. It should be noted that this prepatory script works on ".adm" files, as other ADAMS extensions may have different encoding of names and properties.

```
1  % OPT. PREPARATION : SOLIDWORKS to ADAMS post-processing.
     Some things are
```

```matlab
2   % removed from SOLIDWORKS and the file is ready to be
        Plant Exported
3   clear all
4   close all
5   clc
6
7   % ------------------------------
8   % DIRECTORY IDENTIFICATION
9   % ------------------------------
10
11  % ADAMS Working Directory (does not contain parent)
12  ADAMS_files_directory = "D:\Laurea-Magistrale\Tests\Test
        -10\ADAMS\Test_10_09";
13
14  % Output file from SolidWorks Motion Analysis
15  virgin_file_name = "ADM_LA_Virgin.adm";
16
17  % Un-dashed File
18  undashed_file_name = "ADM_LA_Undashed.adm";
19
20
21  % Input file for MATLAB GA
22  new_file_name = "ADM_LA.adm";
23
24
25  % ------------------------------
26  % REPLACE DASHES
27  % ------------------------------
28
29
30  % This Section replaces dashes in order to have a good
        compatibility
31  % bewtween SolidWorks, ADAMS and MATLAB.
32
33
34  % List of string values whose line usually contains "-"
35  not_allowed_values = ["adams_view_name"];
36
37
38  % Open old_file_name (read only)
39  fid = fopen(fullfile(ADAMS_files_directory,
        virgin_file_name), 'r');
40  if fid == -1
41      error('Unable to open virgin file.');
42  end
43
44  % Read content
45  fileContent = {};
```

```matlab
while ~feof(fid)
    line = fgetl(fid);
    fileContent{end+1} = line; %#ok<SAGROW>
end
fclose(fid);


% Line process
for i = 1:length(fileContent)
    containsNotAllowed = 0;
    line = fileContent{i};

    % Check if not_allowed_values is in line
    for k = 1:length(not_allowed_values)
        containsNotAllowed = contains(line, string(
            not_allowed_values(k)));
        if containsNotAllowed
            break;
        end
    end

    % Check if "-" is in line
    containsDash = contains(line, '-');


    % If both conditions are satisfied, substitute "-"
        with "_"
    if containsNotAllowed && containsDash
        fileContent{i} = strrep(line, '-', '_'); %#ok<
            SAGROW>
    end
end



% Write undashed_file_name
fid = fopen(fullfile(ADAMS_files_directory,
    undashed_file_name), 'w');
if fid == -1
    error('Unable to open undashed file.');
end

for i = 1:length(fileContent)
    fprintf(fid, '%s\n', fileContent{i});
end
fclose(fid);
```

10.2.4 MATLAB Implementation

The MATLAB Script is summarized in the following flowchart. A sample IO block is implemented in order to check the correct interaction between the various programs.

10.2.5 GA - Genetic Algorithms

A genetic algorithm (GA) is a metaheuristic inspired by the process of natural selection that belongs to the larger class of evolutionary algorithms (EA) [48]. Genetic algorithms are commonly used to generate high-quality solutions to optimization and search problems via biologically inspired operators such as selection, crossover, and mutation.

To correctly choose the optimization algorithm, a pros-and-cons table is performed in order to list the most suitable one.

```
START
  │
  ▼
Directory Identification
  │
  ▼
Terrain Variables Definition
  │
  ▼
ADAMS Comunication Set-up
  │
  ▼
Simulink Set-up
  │
  ▼
ADAMS-Simulink I/O Test
  │
  ▼
for k = 1, k < N_terrains, k++
  │
  ▼
terrain(k) = generate_terrain()
  │
  ▼
[ x, f ] = surrogateopt(@objective_function,terrain)
  │
  ▼
all_x(k) = x
  │
  ○
  │
  ▼
x_med = mediate(all_x,N_terrains)
  │
  ▼
Mediate_Solution = objective_function(x_med)
  │
  ▼
END
```

Algorithm	Pros	Cons
Genetic Algorithm (GA)	- Works well with discontinuous, stochastic, and noisy functions.	- Computationally expensive, requiring many function evaluations.
	- Does not require derivatives of the function.	- Slow convergence, especially when a high degree of precision is needed.
	- Can handle discrete, categorical, and complex search spaces.	- Parameter tuning (mutation rate, population size) can be tricky.
	- Global optimization capability, reducing the risk of getting stuck in local minima.	
Surrogate Optimization (surrogateopt)	- Designed for expensive-to-evaluate functions.	- Does not scale well to high-dimensional problems.
	- Fewer function evaluations needed compared to GA.	- Can get stuck in local minima if the surrogate model is inaccurate.
	- Can handle noisy and discontinuous functions.	- Limited support for discrete or categorical variables.
	- Automatically balances exploration and exploitation.	
Constrained Non-Linear (fmincon)	- Fast convergence for smooth functions.	- Requires continuous and differentiable functions (not ideal for non-numerical or noisy functions).
	- Works well when the function is differentiable and well-behaved.	- Easily gets trapped in local minima.
	- Can efficiently handle constraints.	- Not suitable for categorical or discontinuous search spaces.

Table 10.3: Comparison of the various types of optimization strategies implemented in the MATLAB Optimization Toolbox.

Surrogate optimization is chosen as a suitable candidate for optimization; therefore **surrogateopt** is prescribed for the analysis.

10.3   Planar terrain Results

Table 10.4 refers to the planar terrain results. Particularly, the following plots shows the distance r_d and the contact load P_{cont} before and after optimization. As it is possible to see, the system lowers its final relative distance as well as its contact force. Little interaction of the shock absorber is requested, compared with the vertical spring, indicating the strong interaction of gravity, differently from an on-orbit docking system.

No.	Seed	$r_{d,end}$	Relative Error	k_{HCS}	k_{sp}	c_{sp}	L_{sp}	k_v	Comp. Time
1	shuffle	0.55	0.24	26250.0	125.0	375.0	468.8	7750	00:12:08
Units		mm	%	N/m	N/m	N/(m/s)	mm	N/m	s

Table 10.4: Results for $z_{obst} = 0.00 \ m$.
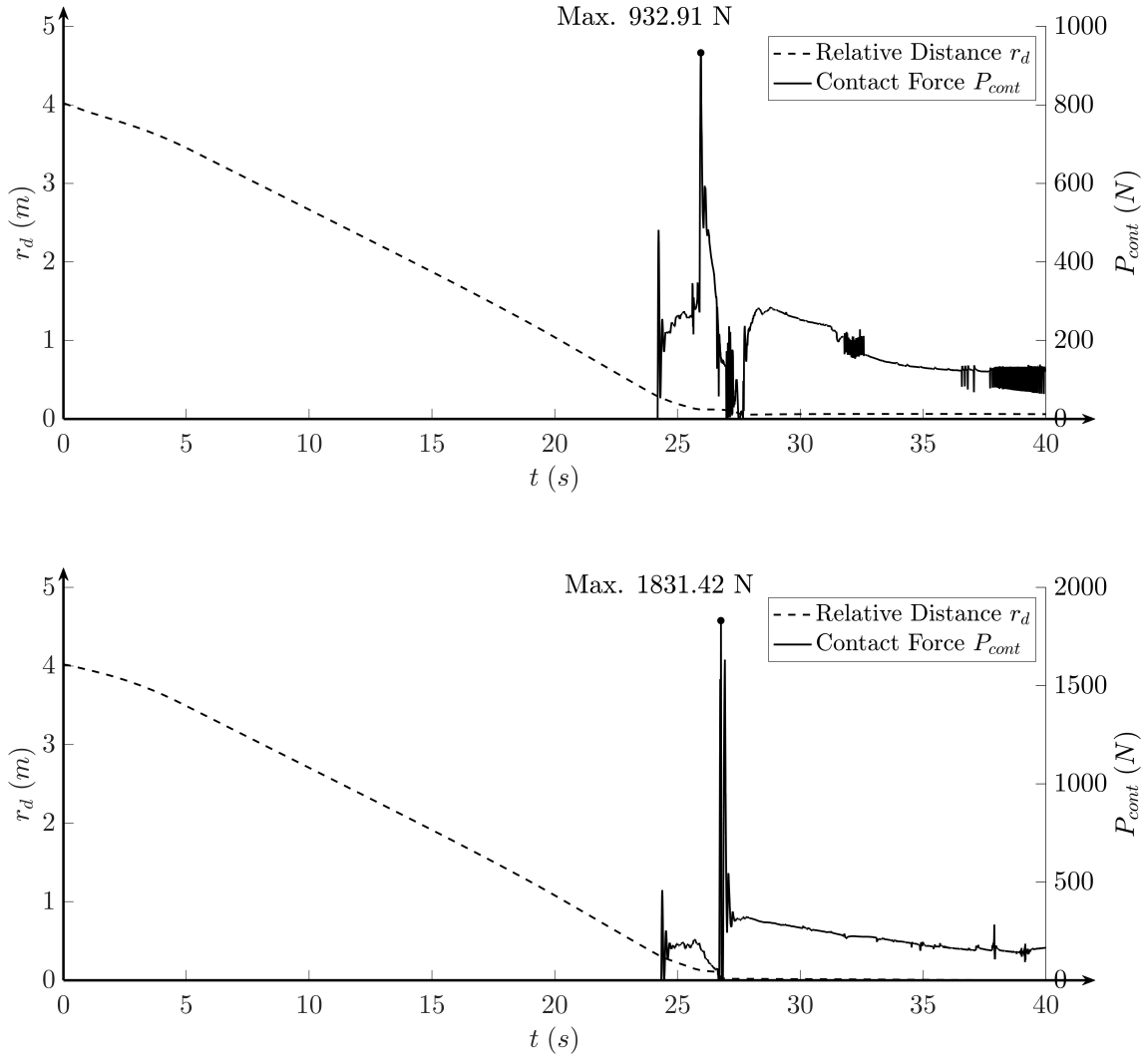
Figure 10.10: Relative docking distance r_d and contact force P_{cont} during docking *before* (top) and *after* (bottom) the optimization on planar terrain.

Name	Before	After	Units
Distance at simulation end $r_{d,end}$	60.42	0.55	mm
Final Relative Error $\flat$	27.021	0.24	%
Max. Contact Force $P_{cont,max}$	935	1831	N

Table 10.5: Results comparison between before and after the optimization.

10.4 Non-Planar Terrains

Procedural terrain generation is a widely adopted technique in computational graphics, geospatial simulations, and virtual environments. Among various noise functions utilized for terrain synthesis, Perlin Noise remains a preferred choice due to its smooth and continuous characteristics. This section presents an implementation of a **Perlin Noise**-based terrain generation algorithm in MATLAB, detailing its mathematical foundation, implementation strategy, and the impact of multi-octave noise synthesis on terrain realism.

10.4.1 Perlin Noise Generation

Perlin Noise, introduced by Ken Perlin in 1983, is a gradient noise function that produces pseudorandom patterns with spatial coherence. Unlike white noise, which is purely stochastic, Perlin Noise generates values that exhibit smooth transitions across space, making it particularly suitable for terrain modeling. The function achieves this by interpolating between a lattice of gradient vectors, ensuring that the resulting noise field exhibits continuity and controllable frequency characteristics.

A typical implementation of Perlin Noise for terrain generation involves:

1. Constructing a coordinate grid to define the terrain resolution.

2. Computing Perlin Noise values at each point in the grid.

3. Summing multiple layers (or octaves) of noise to introduce fine-grained details.

4. Normalizing the resultant heightmap to a predefined elevation range.

The MATLAB implementation presented in this chapter follows these steps to synthesize a procedurally generated landscape.

10.4.2 Perlin Noise Function Code

The following code presents a full implementation of the Perlin Noise Algorithm proposed in the work.

```matlab
% Perlin Noise Function
function z_perlin = perlin_noise(Nx,Ny,Lz,seed)

    % p : Polynomial degree of interpolation
    p = 0;

```

```matlab
 7     % Scale Definition
 8     octaves = 3;
 9     pixel_size = (1/2)^octaves;
10     scale = 1;
11     % grid_size = sqrt(Nx*Ny);
12
13     % Terrain Definition
14     z_perlin = zeros(Nx,Ny);
15
16     % Setting the seed : rng() controls the Random Number
           Generation
17     rng(seed)
18
19     while scale > pixel_size
20         % Random number matrix Nx X Ny (values between 0
               and 1)
21         random_terrain = rand(Nx,Ny);
22
23         % Smoothing of size [Nx * 2^p - (2^p-1)] X [Ny *
               2^p - (2^p-1)]
24         %                   = [2^p * (Nx-1) + 1] X [2^p * (
               Ny-1) + 1]
25         %           approx= (Nx X Ny) * 2^p
26         if (Ny > 1)
27             d = interp2(random_terrain,p,'spline');
28         else
29             d = interp1(random_terrain,p,'spline');
30             disp(d)
31         end
32
33         p = p + 1;
34
35         % Scaling inward : Selection of (Nx X Ny) points
36         if (Ny > 1)
37             d = d(1:Nx,1:Ny);
38         else
39             d = d(1:Nx);
40         end
41         scale = scale / 2;
42
43         % To give more weight to the smoothness
44         % weight propto 1 / scale
45         weight = 1 / scale;
46
47         z_perlin = z_perlin +  d * weight;
48     end
49
50     % Normalization & Scaling
```

```
51      min_z_normalized = -1;
52      max_z_normalized = 0;
53      z_perlin = Lz * ( min_z_normalized + (
           max_z_normalized-min_z_normalized) * (z_perlin ./
           max(z_perlin)) );
54
55  end
```

10.4.3   Discussion

The use of multi-octave Perlin Noise significantly enhances the realism of the generated terrain. By summing noise layers of different frequencies, the resulting elevation map exhibits both broad terrain undulations and fine-grained surface details. However, certain limitations exist:

- The interpolation-based noise approximation lacks the full control afforded by gradient-based Perlin Noise implementations.

- The generated terrain lacks geological realism (e.g., erosion effects), which could be addressed through additional post-processing techniques.

Future enhancements may involve implementing an improved noise function with gradient vectors, incorporating erosion simulation models, or integrating domain-specific constraints to better mimic real-world topography.

Terrain Wavelength : 2 m, Terrain Amplitude : 1 m
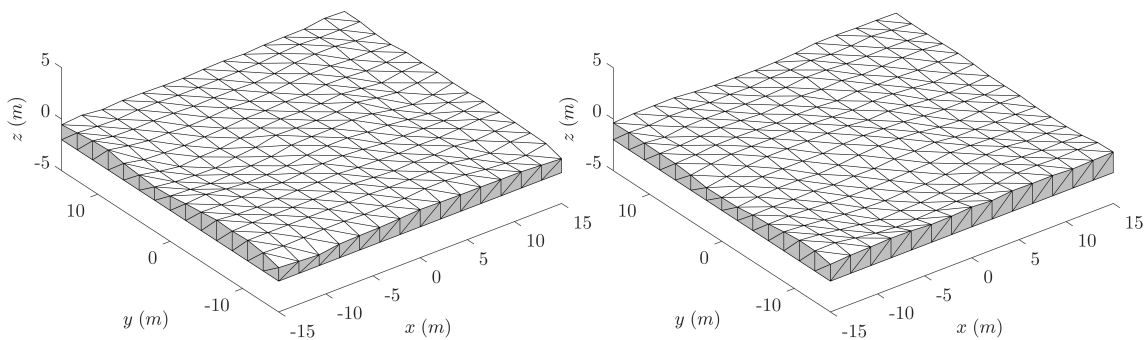
10.4.4   Suspension sizing

In the development of the LPR, the suspension system is sized by applying classical vibration theory as outlined in standard mechanical vibration textbooks [49]. The vehicles suspension is modeled as a single-degree-of-freedom (SDOF) system, where the suspended mass, stiffness, and damping define the dynamic response to terrain-induced excitations.
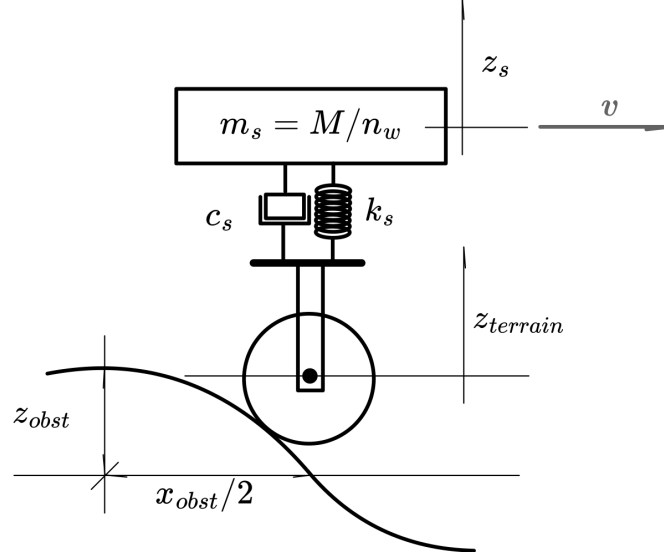
Figure 10.11: Single-degree-of-freedom (SDOF) system used for the suspension sizing.

The proposed SDOF system responds to the equilibrium equation:

$$m_s \ddot{z}_z + c_s(\dot{z}_s - \dot{z}_{terrain}) + k_s(z_s - z_{terrain}) = 0$$

where:

1. m_s is the mass acting on the wheels (equal to the total mass divided by the number of wheels);

2. c_s and k_s are the suspension damping and stiffness;

3. z_s is the vertical displacement of the suspension;

4. $z_{terrain}$ is the terrain roughness. Assuming that the terrain is fairly regular, and that it follows a sinusoidal pattern:

$$z_{terrain} = Z_{terrain,0} \cdot \sin(\Omega_{terrain} \cdot t)$$

with $Z_{terrain,0} = z_{obst}$ being the maximum terrain obstacle height, proposed in chapter 2 and

$$\Omega_{terrain} = 2\pi f_{terrain} = 2\pi \frac{v_{nom}}{x_{obst}}$$

with v_{nom} the nominal velocity and x_{obst} the terrain obstacle width, also specified in the requirements.

The transmittivity function is therefore obtained as [49]:

$$\frac{Z_{s,0}}{Z_{terrain,0}} = \frac{\sqrt{1 - \left(2\zeta_s \frac{\omega_{n,s}}{\Omega_{terrain}}\right)^2}}{\sqrt{\left(1 - \left(\frac{\omega_{n,s}}{\Omega_{terrain}}\right)^2\right)^2 + \left(2\zeta_s \frac{\omega_{n,s}}{\Omega_{terrain}}\right)^2}}$$

with $\omega_{n,s} = \sqrt{k_s/m_s}$ and $\zeta_s = c_s \omega_{n,s}/(2k_s)$. From automotive considerations, good values for those parameters were chosen and hence the system can be fully sized.

$\omega_{n,s}/\Omega_{terrain}$	ζ_s	x_{obst}	z_{obst}	$Z_{s,0}$	k_s	c_s
0.4	0.2	2	0.1	120	5400	33
-	-	m	m	mm	N/mm	N/(mm/s)

Table 10.6: Selected values for the suspension sizing.

Further investigations of the mobility system are proposed in [26].

10.5   Non-Planar terrain Results

As for the previous case, the following results show the results of the state vector for different non-planar terrains. Different values have been tested for z_{obst} which indeed result in a different slope angle for the obstacle, as well as its height.

No.	Seed	$r_{d,end}$	Relative Error	k_{HCS}	k_{sp}	c_{sp}	L_{sp}	k_v	Comp. Time
1	4596	1.70	0.7	26250.0	125.0	375.0	468.75	7750.00	00:13:00
2	7561	1.34	0.6	14382.2	227.9	789.4	386.72	5967.93	05:30:30
3	1686	1.02	0.4	26250.0	125.0	375.0	468.75	7750.00	02:26:56
4	5118	0.00	0.0	26250.0	125.0	375.0	468.75	7750.00	02:33:56
5	3125	1.57	0.7	15000.0	500.0	500.0	375.00	7000.00	00:05:23
6	6721	0.29	0.1	26250	125	375	468.75	7750.00	00:11:58
7	9138	0.24	0.1	26250.0	125.0	375.0	468.75	7750.00	00:11:01
8	5740	1.21	0.5	15000.0	500.0	500.0	375.00	7000.00	00:03:55
9	760	0.52	0.2	25244.4	198.4	447.1	440.13	4165.55	02:32:06
10	258	0.28	0.1	26250.0	125.0	375.0	468.75	7750.00	01:59:40
11	8018	1.97	0.9	12729.3	405.7	592.2	384.88	6034.02	06:53:41
12	9130	0.34	0.1	26250.0	125.0	375.0	468.75	7750.00	00:10:56
13	466	0.00	0.0	26250	125	375	468.75	7750.00	00:51:03
Mediated			0.4	22500	200	400	400	7100	
Units		mm	%	N/m	N/m	N/(m/s)	mm	N/m	s

Table 10.7: Results for $z_{obst} = 0.05\ m$.

No.	Seed	$r_{d,end}$	Relative Error	k_{HCS}	k_{sp}	c_{sp}	L_{sp}	k_v	Comp. Time
1	2830	0.31	0.1	26250.0	125.0	375.0	468.75	7750.00	00:10:43
2	3689	2.25	0.9	16017.0	246.3	898.6	398.77	8268.24	05:02:24
3	3109	0.45	0.2	15000.0	500.0	500.0	375.00	7000.00	00:04:04
4	8208	1.77	0.7	20312.1	190.2	1000.0	384.43	4000.00	02:21:54
5	4265	2.06	0.8	16875.0	187.5	312.5	421.88	4375.00	01:13:00
6	7118	2.39	1.0	29062.5	968.75	343.75	304.6875	4187.50	01:48:31
7	5872	0.00	0.0	26250.0	125.0	375.0	468.75	7750.00	02:58:10
8	4490	10.24	4.2	24605.4	457.4	688.8	395.57	5285.32	17:18:38
9	7112	0.80	0.3	26250.0	125.0	375.0	468.75	7750.00	00:13:27
10	3415	1.38	0.6	28125	562.5	687.5	453.125	5125.00	00:37:32
Mediated			0.9	22900	300	600	400	6100	
Units		mm	%	N/m	N/m	N/(m/s)	mm	N/m	s

Table 10.8: Results for $z_{obst} = 0.10\ m$.

No.	Seed	$r_{d,end}$	Relative Error	k_{HCS}	k_{sp}	c_{sp}	L_{sp}	k_v	Comp. Time
1	6814	4.57	1.7	29248.7	699.6	978.1	377.02	4693.93	22:42:23
2	7629	2.64	1.0	24555.8	574.8	972.7	305.94	4054.23	09:27:31
3	5463	320.43	119.0	21974.0	502.3	1000.0	499.87	4000.47	04:05:41
4	3282	333.20	123.7	12776.6	1000.0	1000.0	500.00	4056.15	05:26:26
5	258	0.28	0.1	26250.0	125.0	375.0	468.75	7750.00	01:59:40
6	6271	1.19	0.4	22522.2	970.1	638.1	343.8	4000.00	08:02:44
7	2570	260.92	96.9	12193.3	781.2	31.3	382.82	4562.43	02:31:53
8	4771	0.13	0.0	27032.6	987.2	450.7	290.47	4000.00	05:50:02
9	6127	10.07	3.7	19361.4	230.3	478.3	414.66	4000.00	15:07:05
Mediated			38.5	21800	700	700	400	4600	
Units		mm	%	N/m	N/m	N/(m/s)	mm	N/m	s

Table 10.9: Results for $z_{obst} = 0.15 \ m$.

No.	Seed	$r_{d,end}$	Relative Error	k_{HCS}	k_{sp}	c_{sp}	L_{sp}	k_v	Comp. Time
1	9769	309.53	103.2	25188.8	897.1	9.6	497.63	9993.34	04:42:11
2	6318	370.70	123.6	18861.4	961.5	997.3	500.00	4000.92	05:40:13
3	3109	0.45	0.2	15000.0	500.0	500.0	375.00	7000.00	00:04:04
4	8208	1.77	0.7	20312.1	190.2	1000.0	384.43	4000.00	02:21:54
5	4265	2.06	0.8	16875.0	187.5	312.5	421.88	4375.00	01:13:00
6	9769	309.53	103.2	25188.8	897.1	9.6	497.6	9993.34	04:42:11
7	6318	370.70	123.6	18861.4	961.5	997.3	500.00	4000.92	05:40:13
8	4720	213.36	71.1	14200.0	1000.0	588.6	500.00	4000.00	02:52:23
9	8208	1.77	0.7	20312.1	190.2	1000.0	384.43	4000.00	02:21:54
10	4265	2.06	0.8	16875	187.5	312.5	421.875	4375.00	01:13:00
Mediated			52.8	19200	600	600	400	5600	
Units		mm	%	N/m	N/m	N/(m/s)	mm	N/m	s

Table 10.10: Results for $z_{obst} = 0.20 \ m$.

As it is possible to see, higher and higher obstacle lead to:

1. a rising up in the shock absorber interaction which, however, turn out as an order of magnitude lower than the vertical spring.

2. a lowering of the vertical spring as well as the hard capture system.

z_{obst}	Seed	$r_{d,end}$	Relative Error	k_{HCS}	k_{sp}	c_{sp}	L_{sp}	k_v
0	0.02	26	0.1	0.4	500	7.8	497.63	9993.34
50	0.04	23	0.2	0.4	400	7.1	500.00	4000.92
100	0.09	23	0.3	0.6	400	6.1	375.00	7000.00
150	3.85	22	0.7	0.7	400	4.6	384.43	4000.00
200	5.28	19	0.6	0.6	400	5.6	421.88	4375.00
mm		N/mm	N/mm	N/(mm/s)	mm	N/mm	mm	N/m

Table 10.11: Averaged results for differente reference obstacle.
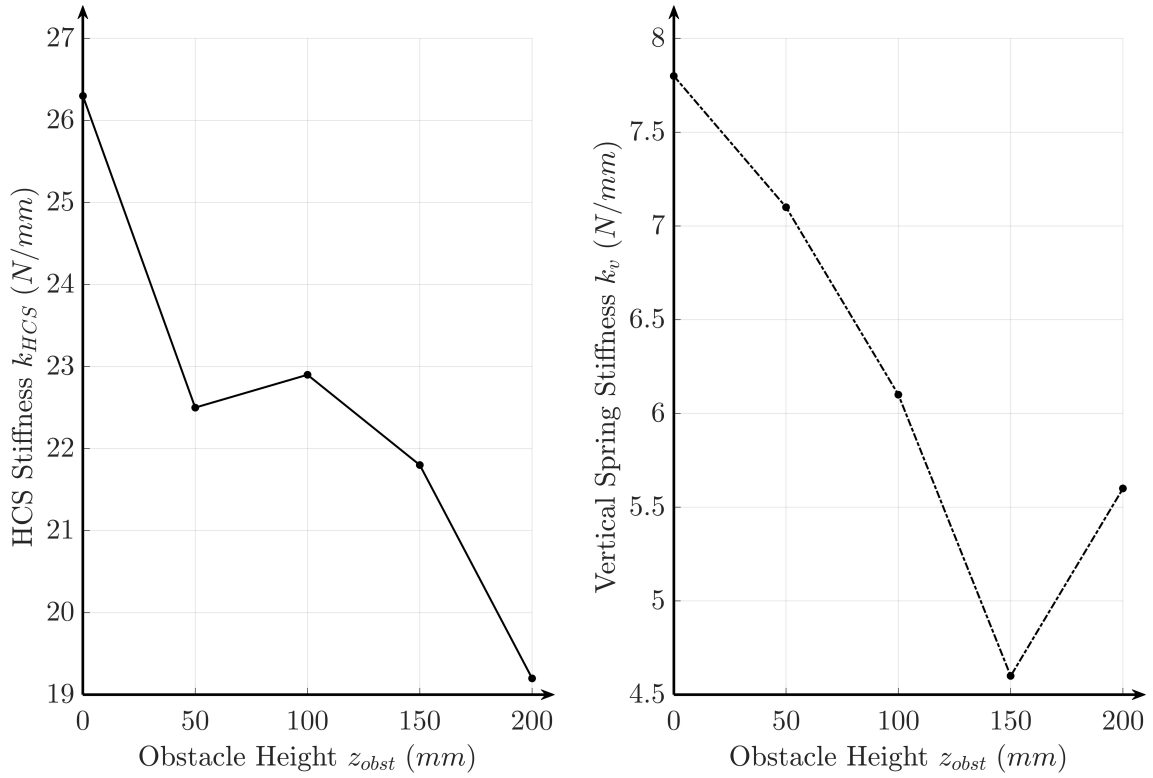
Figure 10.12: Sensitivity Analysis for the HCS and vertical spring.
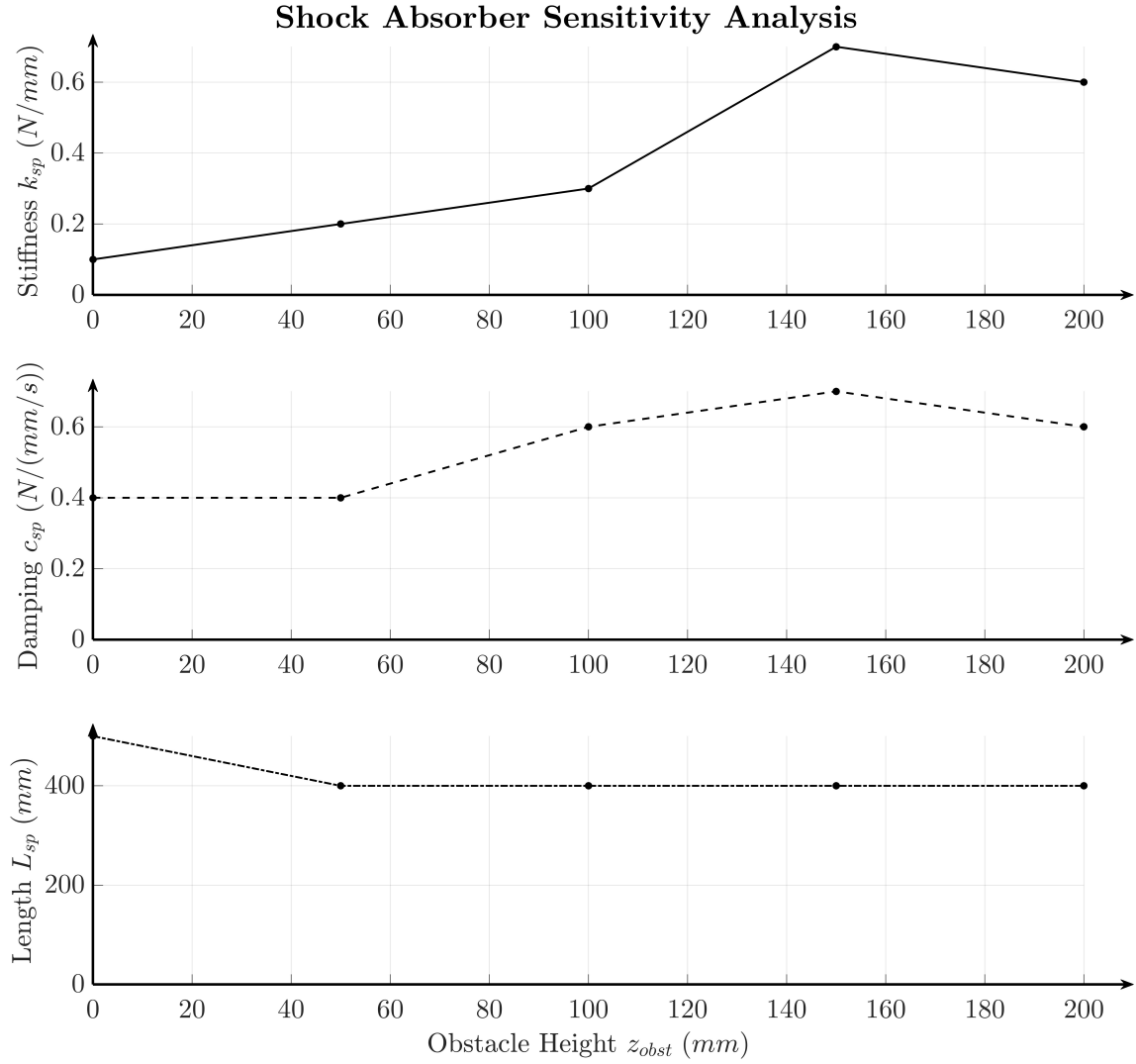
Figure 10.13: Sensitivity Analysis for the Shock absorber.

However, it is important to notice that higher and higher obstacles lead to higher final errors after optimization, not converging. This is because the system has been sized to sustain the proposed misalignment requirements and hence does not converge for coarser terrains. This explains the divergence in the trends for higher and higher z_{obst}. Moreover, the presence of those trends is perhaps indicative of the absence of a closed loop system for the mobility in the simulation. In this scenario, the system moves (or tries to move) at constant speed after initial acceleration. The presence of a solid, coarser terrain may impact on the overall error in velocity which is not corrected. Further studies will revolve around the definition of a GNC system for the LPR during docking maneuvers.

Part III

Docking Protoype

Chapter 11

Prototype Description

11.1   Introduction to the Prototype

To evaluate the performance and mechanical behavior of the docking system, a
1 : 10 scale prototype has been constructed. The primary objective of the prototype
is to simulate the mechanical engagement phase of a docking maneuver. The results
of this study aim to contribute to the growing body of research on autonomous
space systems, particularly in the context of scalable, lightweight, and high-precision
docking technologies.

11.1.1   Test Requirements

From the list of requirements presented in chapter 7, with particular attention to
"Misalignment Requirements", a list of Test Requirements is therefore proposed to
evaluate the performance of the innovative docking subsystem presented in scale.
The following table shows a comparison between the aforementioned requirements
(in the 1 : 1 scale model) and the 1 : 10 scale model.
   Those requirements refer to the Initial Contact Conditions (ICC), as for the real
model. To be more precise, Figure 11.1 shows the diffrence between two markers
$\mathcal{M}_1$ and $\mathcal{M}_2$ (represented by hollow white dots) placed on the chaser and the target
respectively to differenciate the ICC with the docked condition, represented by the
center of docking $\mathcal{R}_1$ and $\mathcal{R}_2$ (represented by full black dots). Particularly, the
prototype distinguishes 3 different moments for each tests:

1. INITIAL STATE (**IS**), t_0: initial condition of the system. The velocity of the
   chaser is null and it starts accelerating towards the target.

2. INITIAL CONTACT (**ICC**), t_1: time stamp in which the two alignment ge-
   ometry initially touch. The two markers $\mathcal{M}_1$ and $\mathcal{M}_2$ are coincident in this
   instant.

3. FINAL CONTACT (**FC**), t_f: time stamp in which the two alignment geometry
   finally touch. The two docking centers $\mathcal{R}_1$ and $\mathcal{R}_2$ are coincident and aligned
   in this instant.
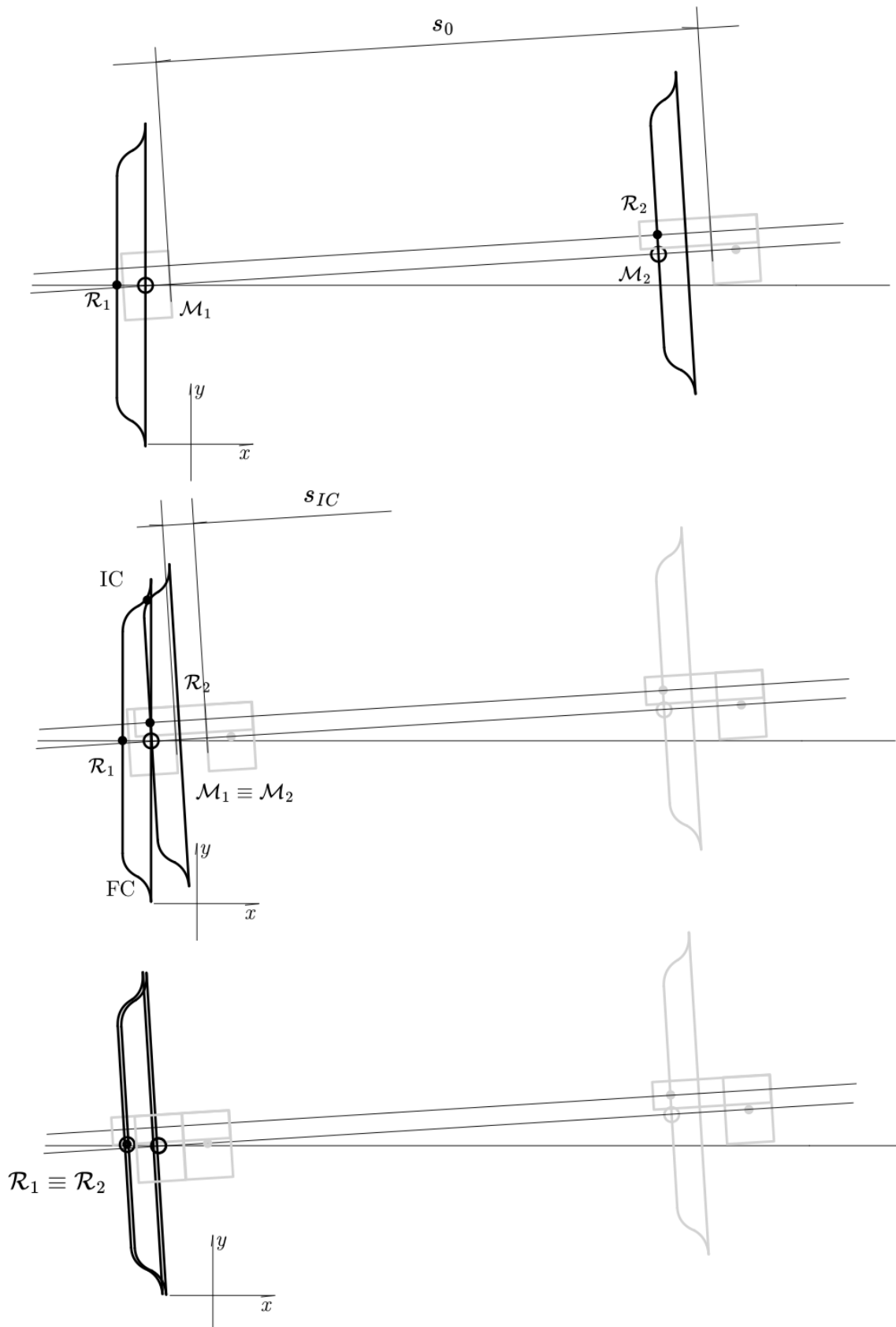
Figure 11.1: The three phases of the maneuver: initial state (IS), initial contact (ICC) and final contact (FC).

The proposed table shows the difference between the ICC of the 1 : 1 scale compared to the prototype counterpart. All geometric properties have been scaled.

ID	Name	Symbol	Value	Un.	Description
R-PERF-B-05	Translational misalignment y	$y_d(t_1)$	± 0.1	m	At first contact, the Docking Subsystem shall be sized to sustain a relative translational misalignment along y of y_d
R-PERF-B-07	Relative trans. velocity x	$\dot{x}_d(t_1)$	0.1	m/s	At first contact, the Docking Subsystem shall be sized to sustain a relative translational velocity along x of $\dot{x}_d$
R-PERF-B-10	Angular misalignment z (yaw)	$\psi_d(t_1)$	5	$^\circ$	At first contact, the Docking Subsystem shall be sized to sustain a relative angular misalignment along z of ψ_d

ID	Name	Symbol	Value	Un.	Description
R-TEST-A-01	Translational misalignment y	$y_d(t_1)$	10	mm	At first contact, the Docking Subsystem Prototype shall be sized to sustain a relative translational misalignment along y of y_d
R-TEST-A-02	Relative trans. velocity x	$\dot{x}_d(t_1)$	10	m/s	At first contact, the Docking Subsystem Prototype shall be sized to sustain a relative translational velocity along x of $\dot{x}_d$
R-TEST-A-3	Angular misalignment z	$\psi_d(t_1)$	5	$^\circ$	At first contact, the Docking Subsystem Prototype shall be sized to sustain a relative angular misalignment along z of ψ_d

Table 11.1: Comparison between real model Requirements and 1 : 10 prototype requirements.

11.1.2 Analysis Types

From this set of requirements, a list of tests for the prototype is selected in order to evaluate the various misalignments proposed, both taken individually and coupled. Each misalignment is evaluated at $1/2\times$, $1\times$ $2\times$ the value of the requirements, in order to build a cohesive trend of the study.

Each misalignment is imposed and maintained during the approach maneuver in order to emulate the movement of a vehicle without a proper GNC system, automated or manned. The choice, as for the analysis study during optimization, is made in order to evaluate the docking performances in the presence of a control error or if the GNC is not capable of coping such misalignment.

ID	Lateral misalignment ($y_{d,1}$)	Angular misalignment ($\psi_{d,1}$)	Test Purpose
TEST-00	0	0	Taring
TEST-01	0	2	Angular misalignment (1/2x) req. assessment
TEST-02	5	0	Lateral misalignment (1/2x) req. assessment
TEST-03	5	2	Combined misalignment (1/2x) req. assessment
TEST-04	0	5	Angular misalignment (1x) req. assessment
TEST-05	10	0	Lateral misalignment (1x) req. assessment
TEST-06	10	5	Combined misalignment (1x) req. assessment
TEST-07	0	10	Angular misalignment (2x) req. assessment
TEST-08	20	0	Lateral misalignment (2x) req. assessment
TEST-09	20	10	Combined misalignment (2x) req. assessment
Units	*mm*	°	

Table 11.2: Prototype Test List.

11.2 Prototype Design

11.2.1 Prototype Models and trade-off

From the selected test and requirements, two types of prototype models are investigated:

Vehicle Model   Railed Model
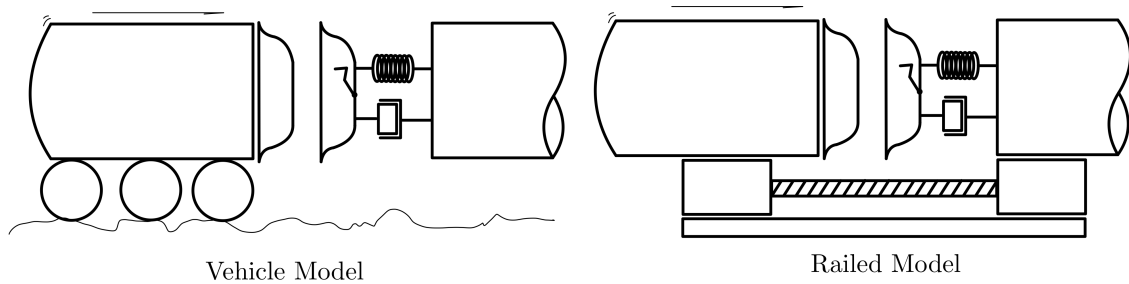
Figure 11.2: Prototype models disclosed in the tradeoff.

1. The first, called the vehicle model sees the mating maneuver between the chaser and the target obtained by a RC remoted vehicle that emulates the properties of a LPR. This prototype maintains the same structure of the 1:1 optimization counterpart, but lacks of control of the error estimation imposed at the beginning of the maneuver, which is vital for the performance evaluation.

2. The second, called the railed model, instead, relies on a linear guide to emulate the approach phase. This solution provides a more stable initial condition control, ensuring a better evaluation of the results.

A more detailed trade-off is proposed in Table 11.3. In particular:

1. The *Railed Model* significantly simplifies the mechanical assembly process due to its linear and constrained design. The *Vehicle Model*, by contrast, requires more complex mechanical integration to support untethered movement and power systems.

2. The *Vehicle Model* incurs higher costs arising from its need for embedded actuation, wireless communication, and battery systems. The *Railed Model*, leveraging passive guidance and reduced autonomy, provides a cost-effective solution.

3. Electrical integration in the *Railed Model* is simplified due to stationary components and ease of access. Conversely, the *Vehicle Model* demands a compact, mobile power and control infrastructure, complicating the electrical assembly.

4. The *Railed Model* supports superior initial condition control by physically constraining the chasers motion along a predefined path. This allows for accurate error estimation and repeatability of trials. The *Vehicle Model*, while mimicking realistic movement, lacks the necessary precision in initial alignment.

5. The *Vehicle Model* allows greater flexibility in defining initial conditions, offering the potential to emulate a broader range of approach scenarios. This freedom, however, comes at the cost of reduced repeatability and increased variability.

6. The *Railed Model* exhibits better structural robustness due to minimized dynamic stresses during motion. In contrast, the *Vehicle Model* is more susceptible to mechanical faults owing to the increased complexity and potential for impact-related wear.

7. The *Railed Model* ensures consistent and measurable impact conditions, which are critical for evaluating docking performance. The controlled trajectory improves reliability in capturing shock-related data, compared to the less predictable nature of the *Vehicle Model*.

8. The *Railed Model* eliminates terrain-induced variability through its fixed guide, ensuring surface consistency. The *Vehicle Model*, however, is subject to disturbances from surface irregularities, which introduces errors not related to the docking system itself.

Considering all aspects with assigned weights, the *Railed Model* obtained a total score of 19, outperforming the *Vehicle Model*, which scored 13. Based on this

Aspect	Vehicle Model	Railed Model	Weight
Mech. Assembly Easiness		X	3
Cost		X	4
Elec. Assemby Easiness		X	5
IC Control		X	4
IC Freedom	X		4
Mechanical Robustness		X	3
Shock Measure	X		5
Error by terrain roughness	X		4
TOTAL	13	**19**	

Table 11.3: Prototype Model Trade-off

structured analysis, the *Railed Model* is selected as the preferred configuration for the docking subsystem prototype.

11.2.2   Component Sizing

The following step in the prototype design is the correct sizing of each component needed to build the scaled model. In particular, for each misalignment described and for the approach phase the following components are selected:

1. A linear actuator, dubbed Linear Guide 1 for the correct control of the approach velocity;

2. A linear actuator, dubbed Linear Guide 2 for the insertion of the lateral misalignment;

3. A stepper motor for the insertion of the lateral misalignment.

Each error insertion is evaluated such that it respects the following Initial Contact Conditions during the approach phase.

Linear Guide 1

For the approach phase, the linear actuator is designed to have a proper stroke such that:

1. It enables a constant speed during the approach phase and the initial contact, as stated in the test requirements;

2. It reduces shocks and rapid deceleration phases, providing a ramp-up and ramp-down phases during the motion;

Those observations can be used to derive a proper ramp-up, constant speed and ramp-down time, based on the commonly reasonable values used for this class of actuators. For simplicity, and in order to distinguish the position of the chaser from that of the Linear Guide 1, $s(t), \dot{s}(t)$ and $\ddot{s}(t)$ are used to mark the respective position, velocity and acceleration of chaser on the linear guide. Each variable respects the particular aspects proposed above for each phase. In particular, the ramp-up and ramp down phases are set to be equal so that the actuator can resist to the same type of acceleration (given by $\ddot{s}_{I,III} = v_{nom}/\Delta t_{I,III}$). In the constant velocity phase, the $\dot{s}(t) = v_{nom}$ is held constant. The following table shows the selected time intervals for the three phases $\Delta t_I, \Delta t_{II}$, and Δt_{III} and corresponding accelerations.

Interval	Time interval, Δt_k	Acceleration, $\ddot{s}(t)$
Ramp-up	2	+5
Constant Speed	8	0
Ramp-down	2	-5
Units	s	mm/s^2

Table 11.4: Time interval and accelerations for the Linear Guide 1.

Given the following observations, a Linear Guide of a total stroke of $S_1 \geq 100\ mm$ is selected. The offset between initial and final contact is set as $10\ mm$, corresponding to the total deflection of the spring.
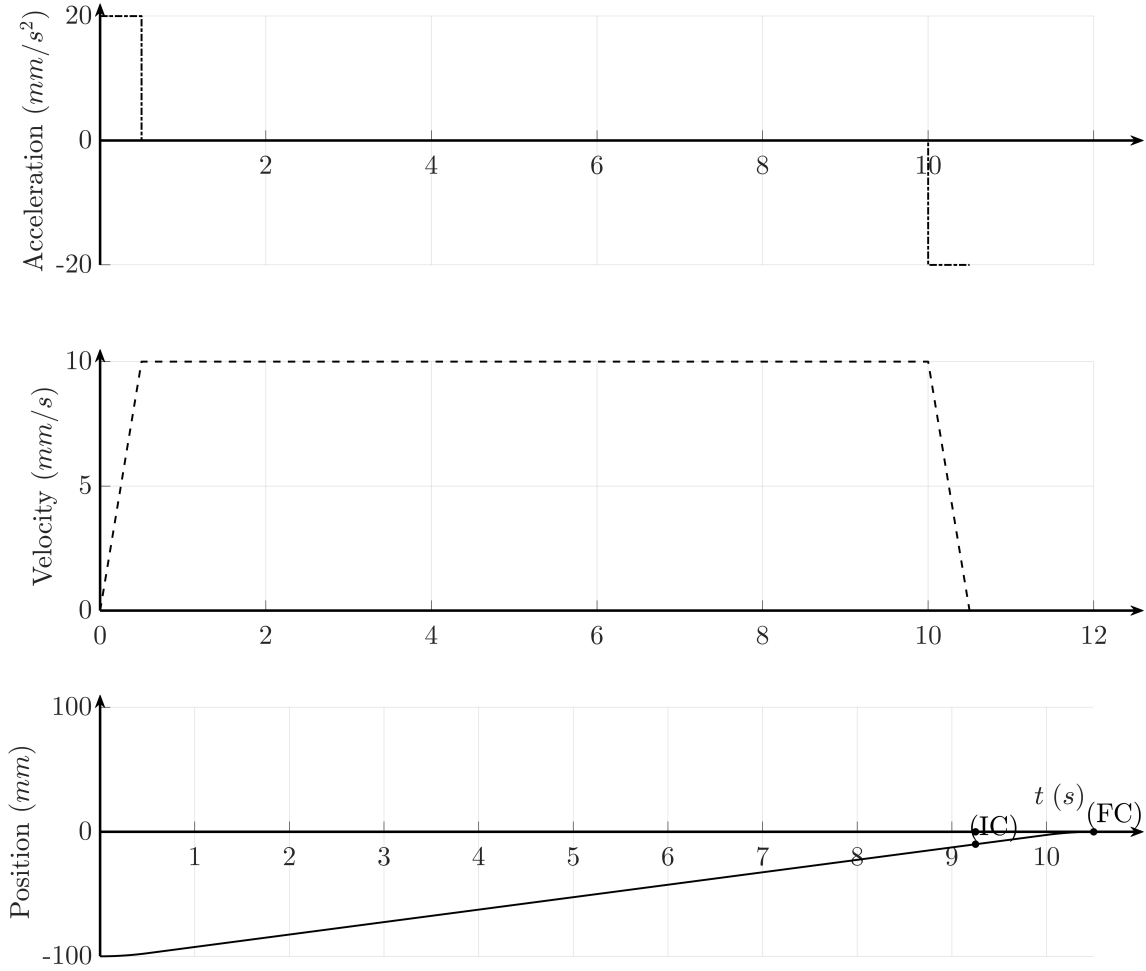
Figure 11.3: Linear Guide 1 Position, Velocity and Acceleration phases.

Linear Guide 2

For the lateral misalignment, the error insertion requirements is translated into the positioning on the linear actuation at a specific position on the guide. The produced misalignment is marked as Δ, in order to distinguish the error implemented during the test from the relative lateral position y_d which varies during both approach and contact in phases, as presented in the following picture.

Initial Contact (IC)   Inital State (IS)

$$\begin{cases} x_{d,1} = h \\ y_{d,1} = \Delta \\ \psi_{d,1} = 0 \end{cases} \qquad \begin{cases} x_{d,0} = s_0 + h \\ y_{d,0} = \Delta \\ \psi_{d,0} = 0 \end{cases}$$

The only requirement for the linear guide is that it is long enough as twice the maximum lateral misalignment (which corresponds to a total of $S_2 \geq 2 \cdot \Delta_{max} = 40\ mm$).
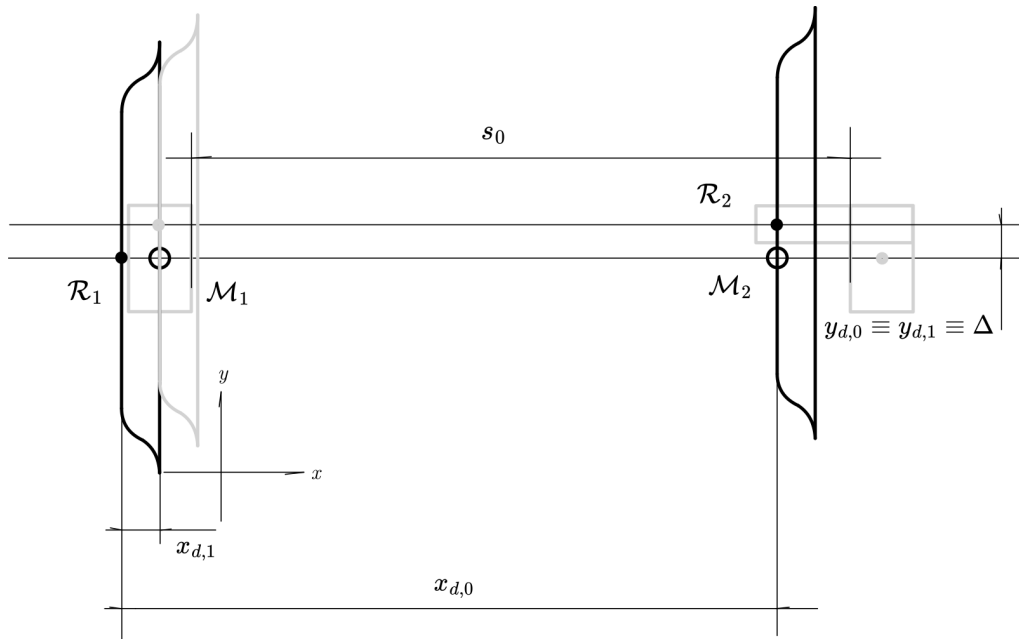
Figure 11.4: Lateral Misalignment Insertion Δ.

Stepper Motor

Finally, for the stepper motor, the error insertion requirements brings to the γ misalignment insertion. Again, the choice is driven so that it has no similarities with ψ_d, which varies during the mating operation.
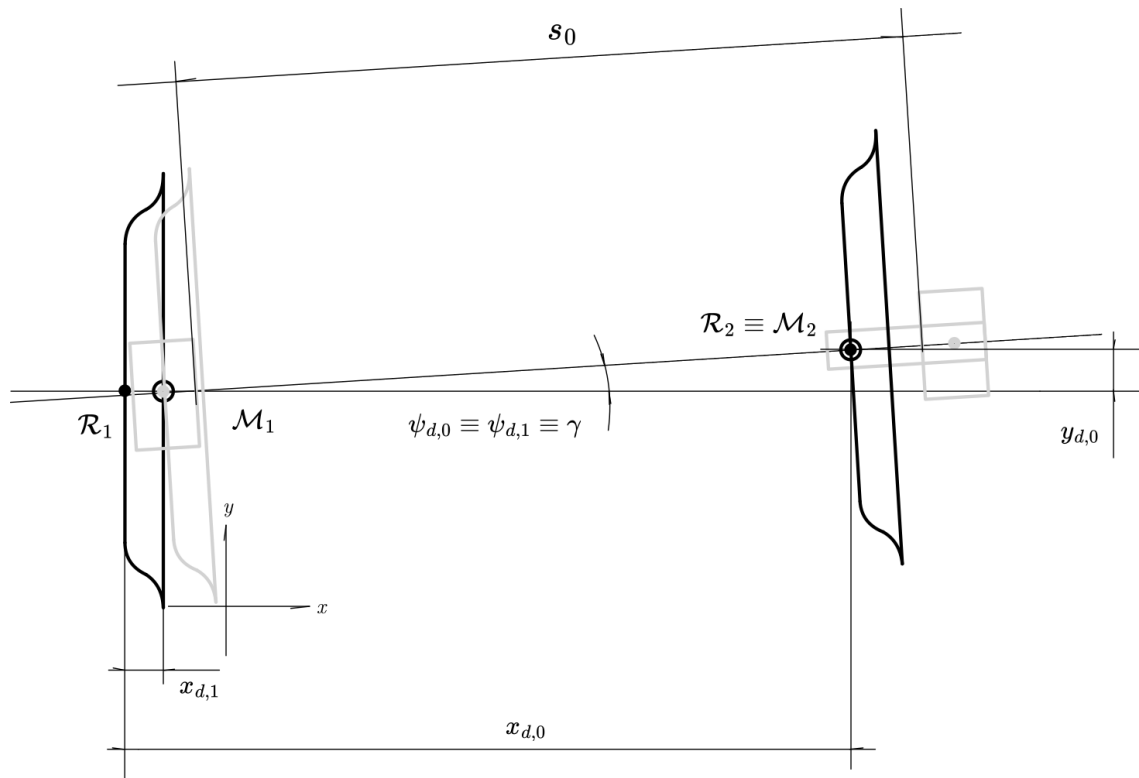
Figure 11.5: Angular Misalignment Insertion γ.

Initial Contact (IC)   Inital State (IS)

$$\begin{cases} x_{d,1} = h \\ y_{d,1} = 0 \\ \psi_{d,1} = \gamma \end{cases} \qquad \begin{cases} x_{d,0} = s_0 \cdot \cos\gamma + h \\ y_{d,0} = s_0 \cdot \sin\gamma \\ \psi_{d,0} = \gamma \end{cases}$$

Considering that it has to sustain both the chaser angular acceleration and the friction with the working table, the following formula is implemented.

$$T_{stepper} = \mathcal{F} \cdot (m_{chaser} \cdot S_1^2 \cdot \ddot{\gamma} + f \cdot m_{chaser} \cdot g \cdot S_1) \qquad (11.1)$$

in which:
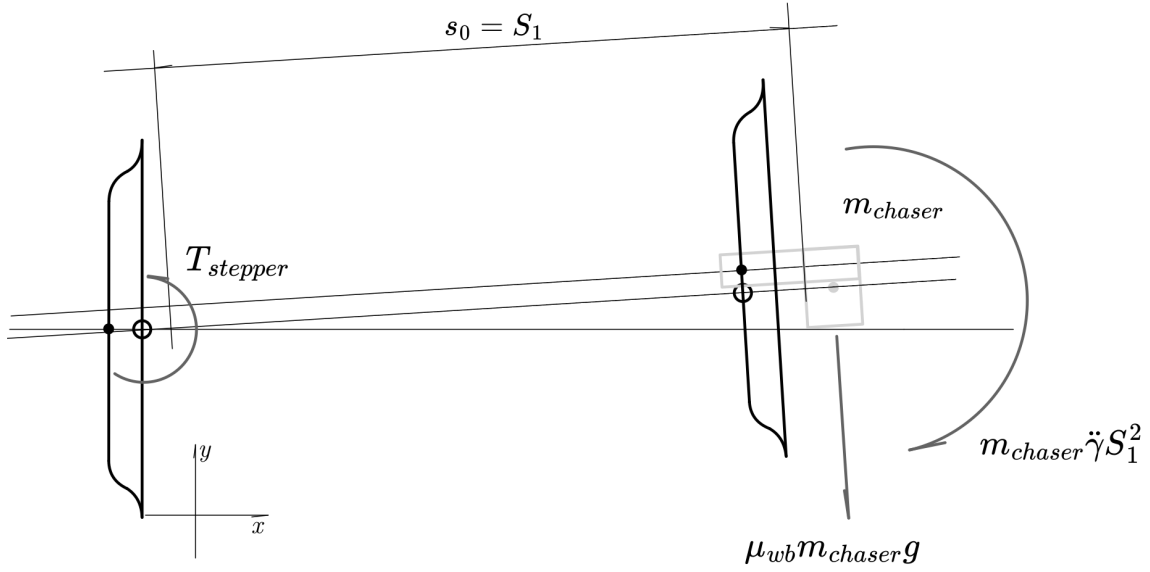
Figure 11.6: Stepper Motor Torque free body diagram.

1. $T_{stepper}$ is the stepper motor torque;

2. $\mathcal{F}$ is a safety factor $\mathcal{F} = 1.5$;

3. m_{chaser} is the total mass of the chaser, estimated as $1\ kg$ given the CAD Mass Evaluation;

4. S_1 is the Linear Guide 1 total stroke, assuming the center of mass of the chaser is coincident with this length at maximum (as safety measure);

5. $\ddot{\gamma} = 1/2 \cdot \gamma/\Delta t_{stepping}^2$ is the step acceleration. Stepper motors are selected due to their particular attention to **microstepping**, a practice in which it is possible to control the stepper angle with a good accuracy. In this way, normal "full step" angles performed by the stepper motor (which are normally set as $1.8° = 360°/200$ revolutions) can be drawn down to 256, giving a finer accuracy of the control. By setting this as the sizing parameter, and $\Delta t_{stepping}$ as $5\ ms$ of the stepping time, it is possible to estimate an angular acceleration of the motor.

6. f is the friction with the work table;

7. g is Earth's gravity acceleration.

For completion, the combined misalignments are represented in the following image.

Figure 11.7: Combined Misalignment Insertion.

Initial Contact (IC)   Inital State (IS)

$$\begin{cases} x_{d,1} = h - \Delta \sin \gamma \\ y_{d,1} = \Delta \cos \gamma \\ \psi_{d,1} = \gamma \end{cases} \qquad \begin{cases} x_{d,0} = s_0 \cdot \cos \gamma + (h - \Delta \sin \gamma) \\ y_{d,0} = s_0 \cdot \sin \gamma + \Delta \cos \gamma \\ \psi_{d,0} = \gamma \end{cases}$$

After evaluating the error insertion aspects of the problem, all the remaining aspects of the docking subsystem are therefore formulated.

1. Springs are sized using the same procedure discussed in chapter 8, Spring Sizing.

2. The alignment and the casing are additive manufactured. Given the considerations proposed in chapter 8, **TPU** is selected as a candidate material for the ALN geometry, both for its elasticity properties and for its versatility in production.

3. Particularly, the main frame and structure of the chaser and the target geometries (both of the ALN and the rest of the structure) are additive manufactured, in order to fast prototype and return rapid solutions.

4. To mimic the HCS, a set of Neodymium Magnets is used to test the capabilities of the system. Hooks are discarded given the lack of accuracy in the small scale. Moreover, permanent magnets are used instead of electromagnets, due to their simplicity in the application. The undocking maneuver is therefore achieved manually, by separating the magnets in the HCS. Using the same estimation proposed in chapter 9, the capture force was estimated as the $F_{mag} \propto \mathcal{F} \cdot m_{chaser} = 1.5 \ kg_f$.

Figure 11.8: Magnetic Force intensity of the total Neodymium magnets.

From the above observations, it is possible to derive a list of parameters used to choose the components for the model. The following table summarizes the component sizing results.

Component	Name	Value	Units
Linear Guide 1	S_1	100	mm
Linear Guide 1	v_{nom}	10	mm/s
Linear Guide 1	Δt_{tot}	12	s
Linear Guide 1	$\Delta t_{undocking}$	8	s
Linear Guide 1	Q_{max}	72.47	kg_f
Linear Guide 2	S_2	40	mm
Stepper Motor	$T_{stepper}$	17.17	$N\ cm$
Springs	$N_{springs}$	6	–
Springs	D_{sp}	13	mm
Springs	d_{sp}	1	mm
Springs	n_{sp}	10	–
Springs	k_{sp}	0.5	N/mm
Magnets	$N_{magnets}$	6	–
Magnets	$N_{magnets}$	6	–
Magnets	$F_{m,ref}$	105.4700	N
Magnets	φ	8.7300	–
Magnets	D_m	10	mm
Magnets	h_m	3	mm

Table 11.5: Prototype sizing results.

11.2.3   CAD Model

A CAD Model is designed to have a clear understanding of the geometries and bulk
size of the components. The following images and technical drawings depict the
main geometries of the model, addressing the details of each geometry.
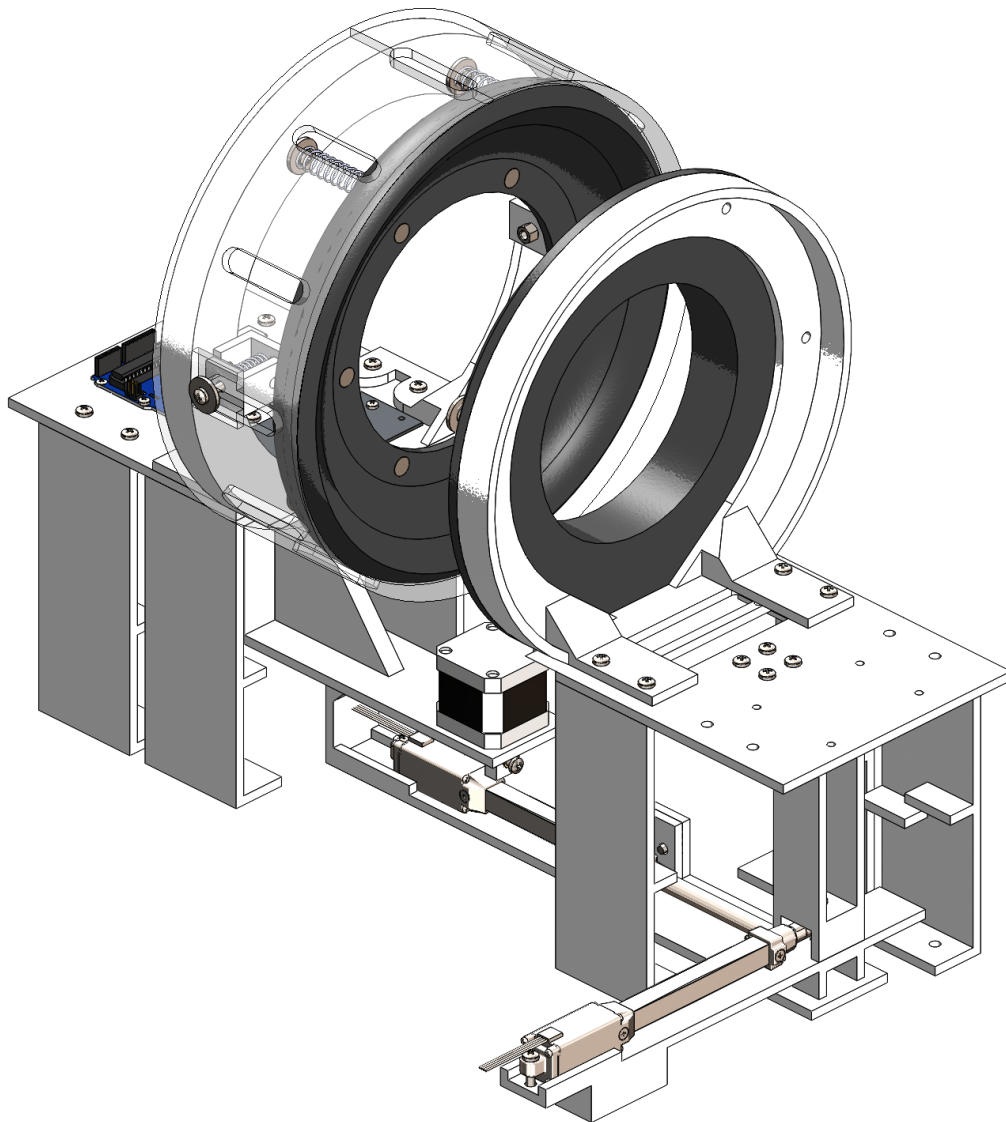
Figure 11.9: Isometric View of the CAD Model of the prototype.

6x ⌀ 10 x 3
Neodymium
Magnets

170.00

⌀ 240.00

380.00

150.00

Foot 1

Foot 3

Foot 2
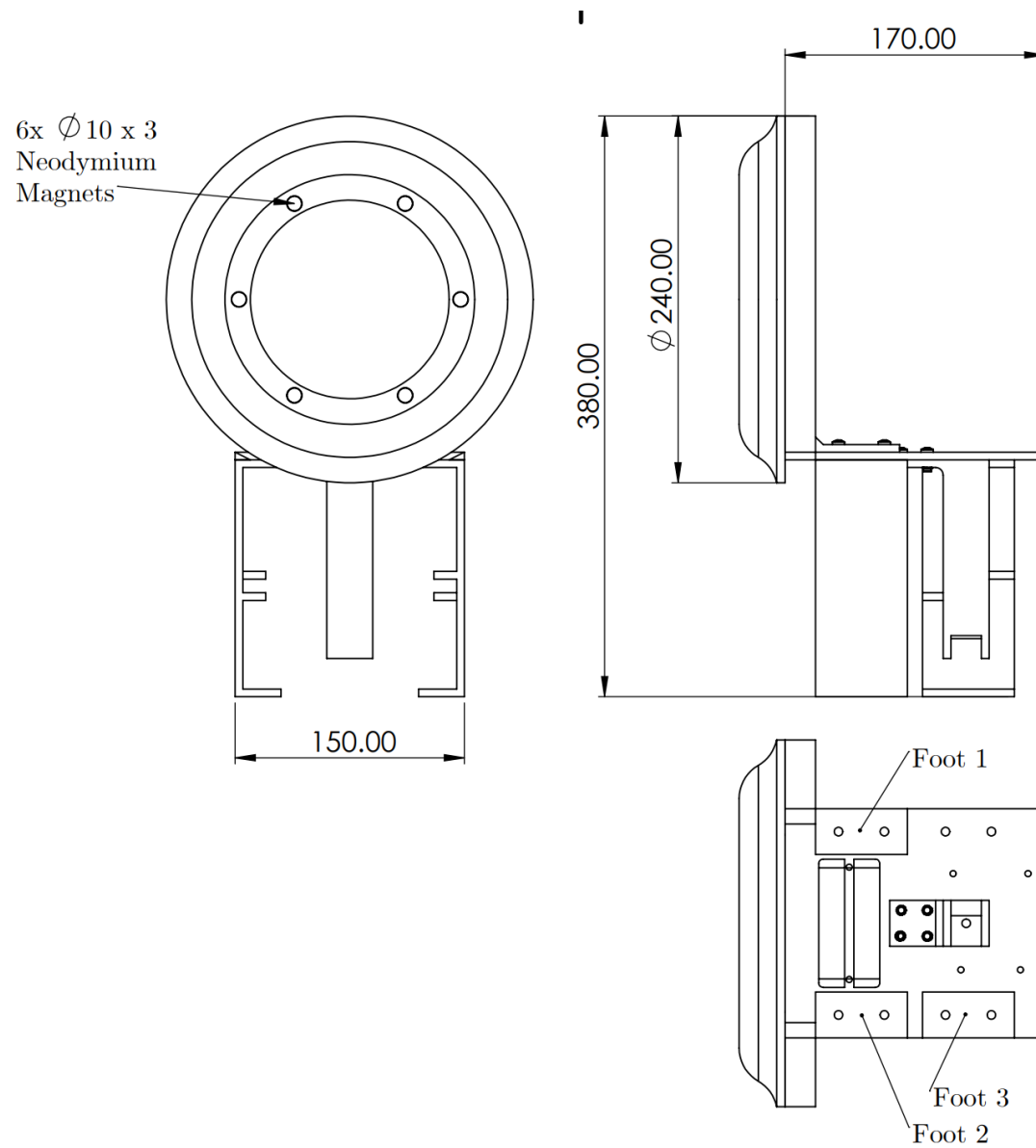
Figure 11.10: Technical Representation of the chaser of the prototype.
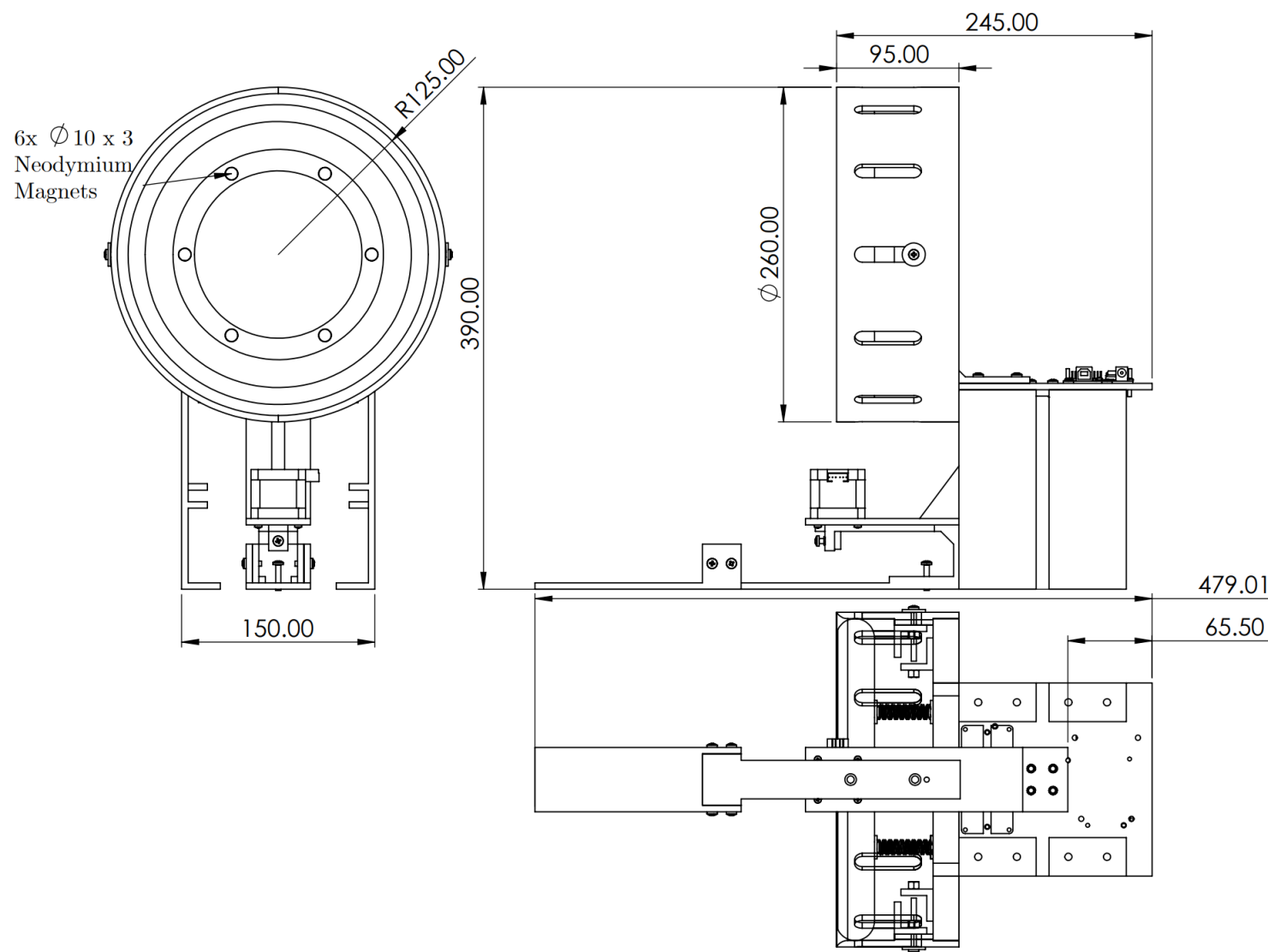
Figure 11.11: Technical Representation of the target of the prototype.

Male Alignment Geometry   Female Alignment Geometry
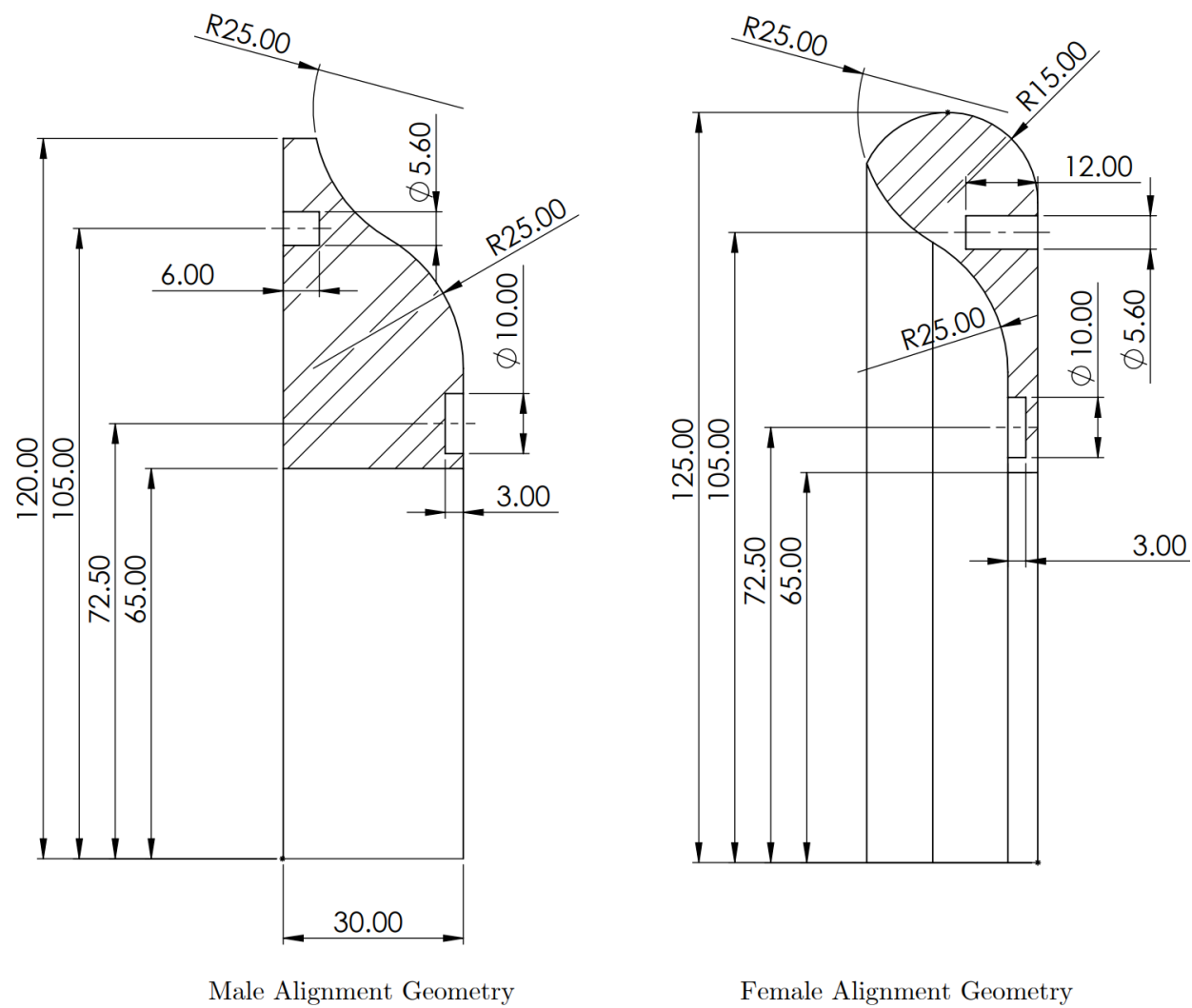
Figure 11.12: Female and Male Alignment Geometry representation of the prototype.
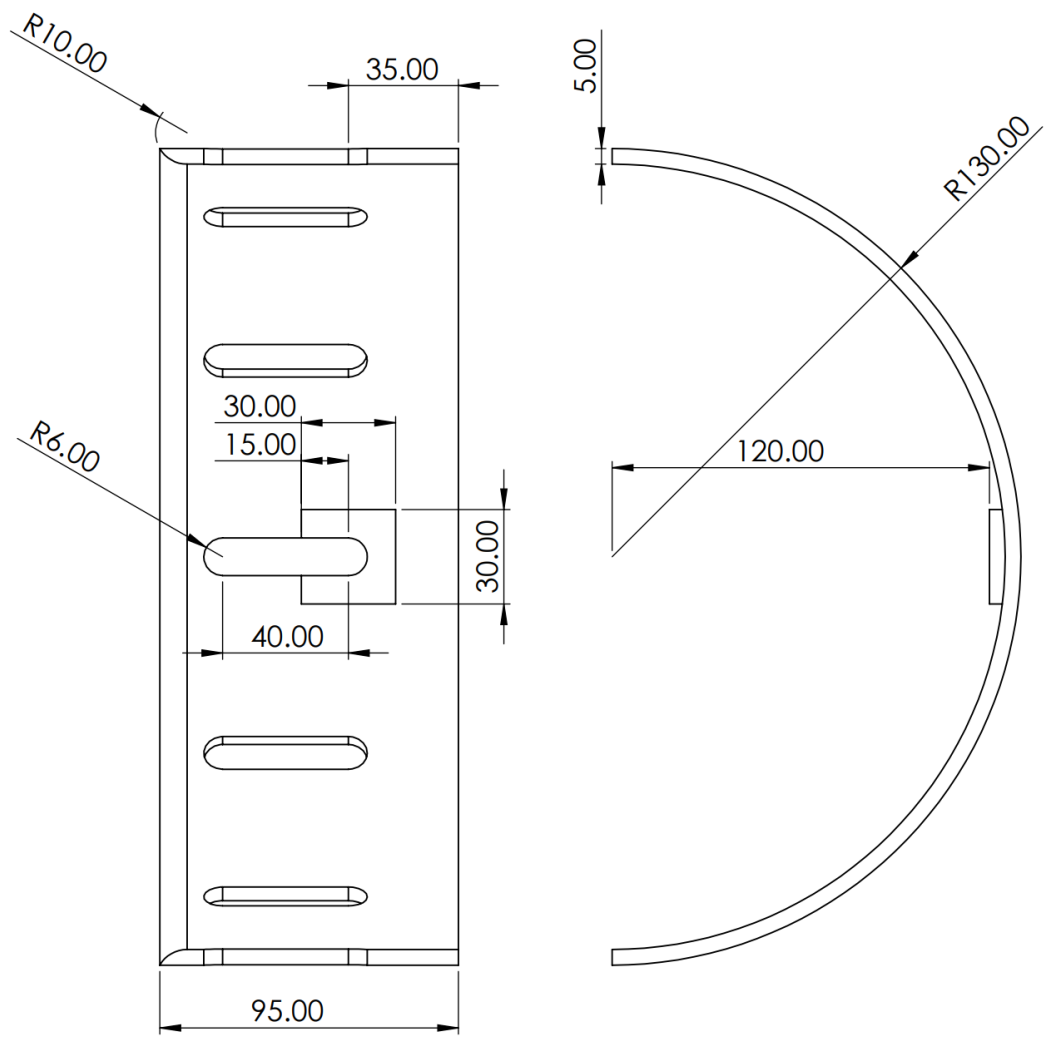
Figure 11.13: Technical Representation of the Vertical Support Geometry of the prototype.
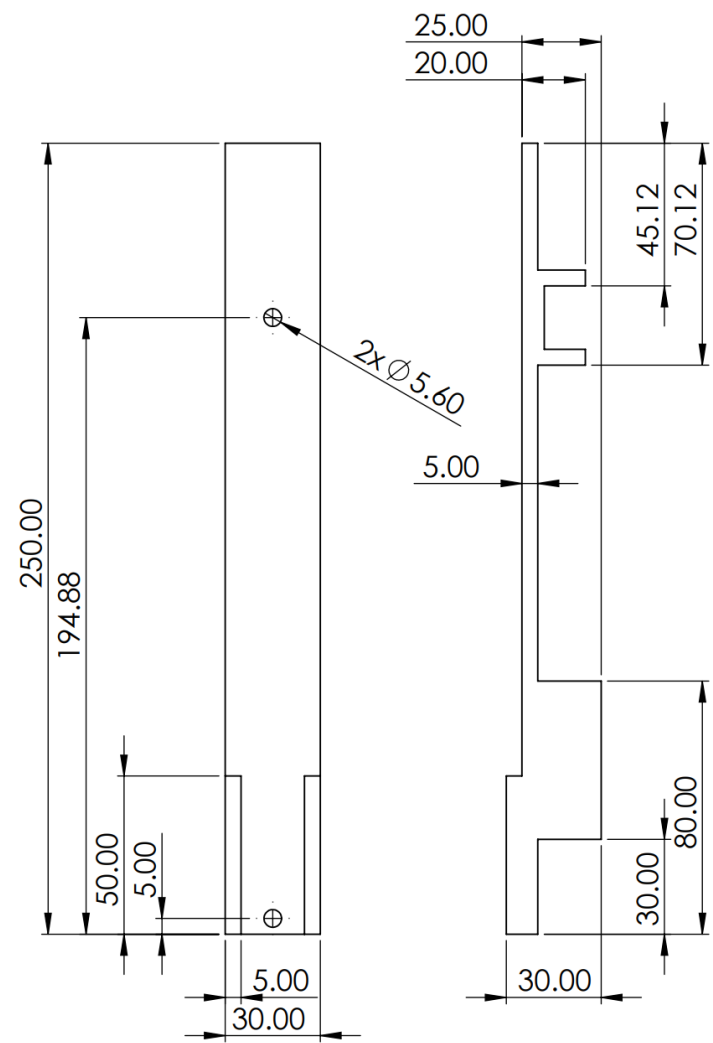
Figure 11.14: Technical Representation of the PR Interface component.
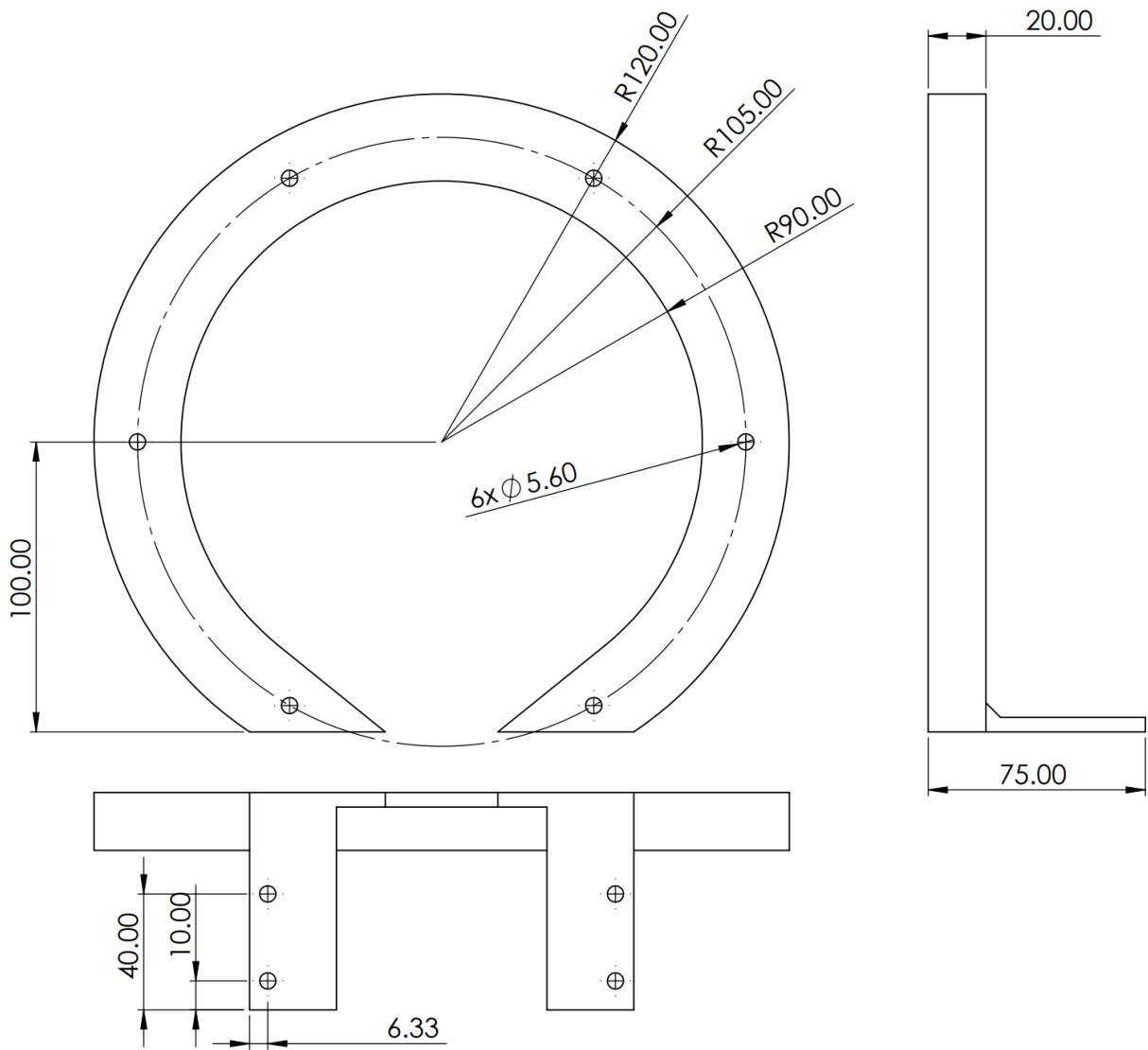
Figure 11.15: Technical Representation of the Chaser ALN Mount.
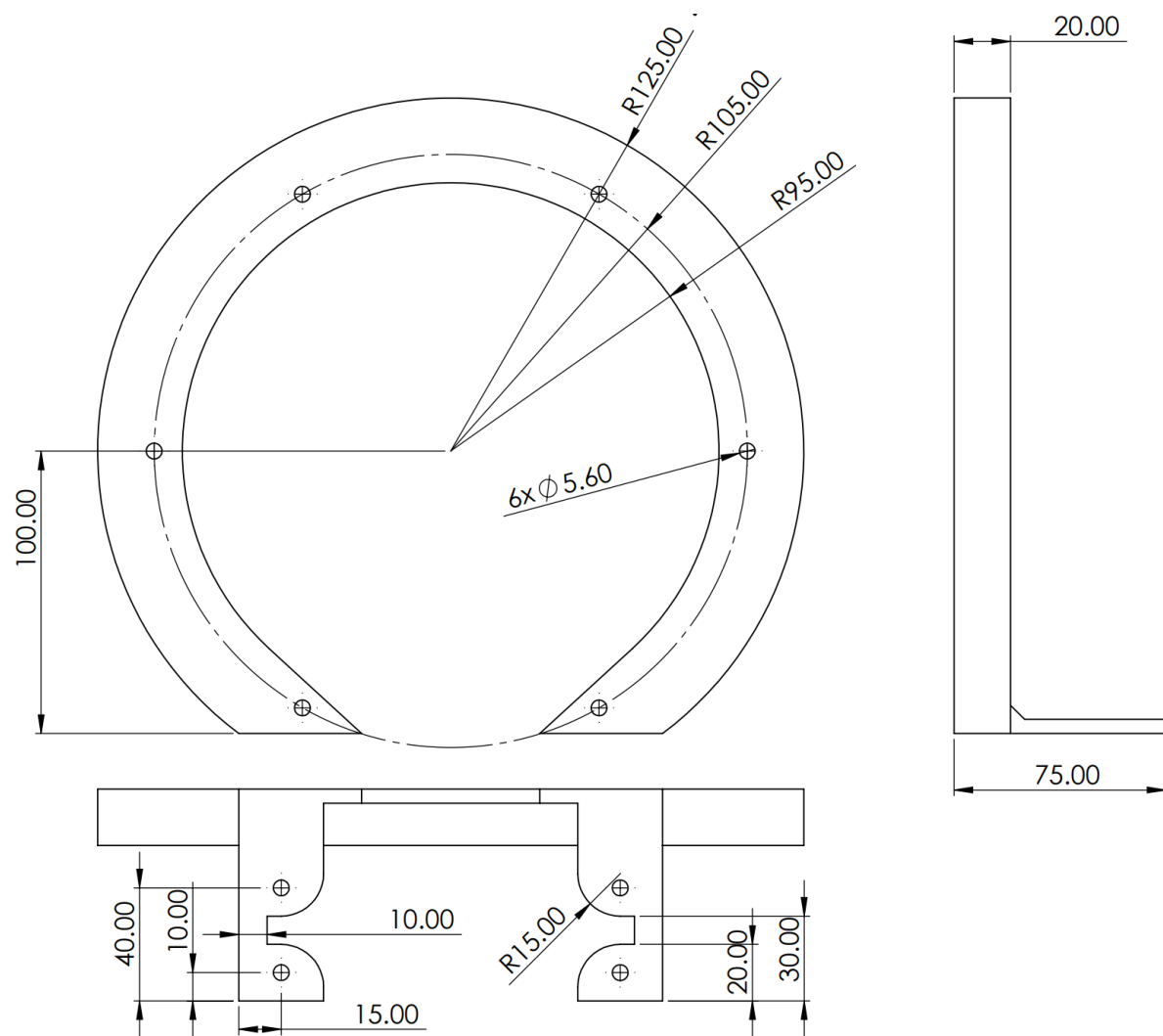
Figure 11.16: Technical Representation of the Target ALN Mount.
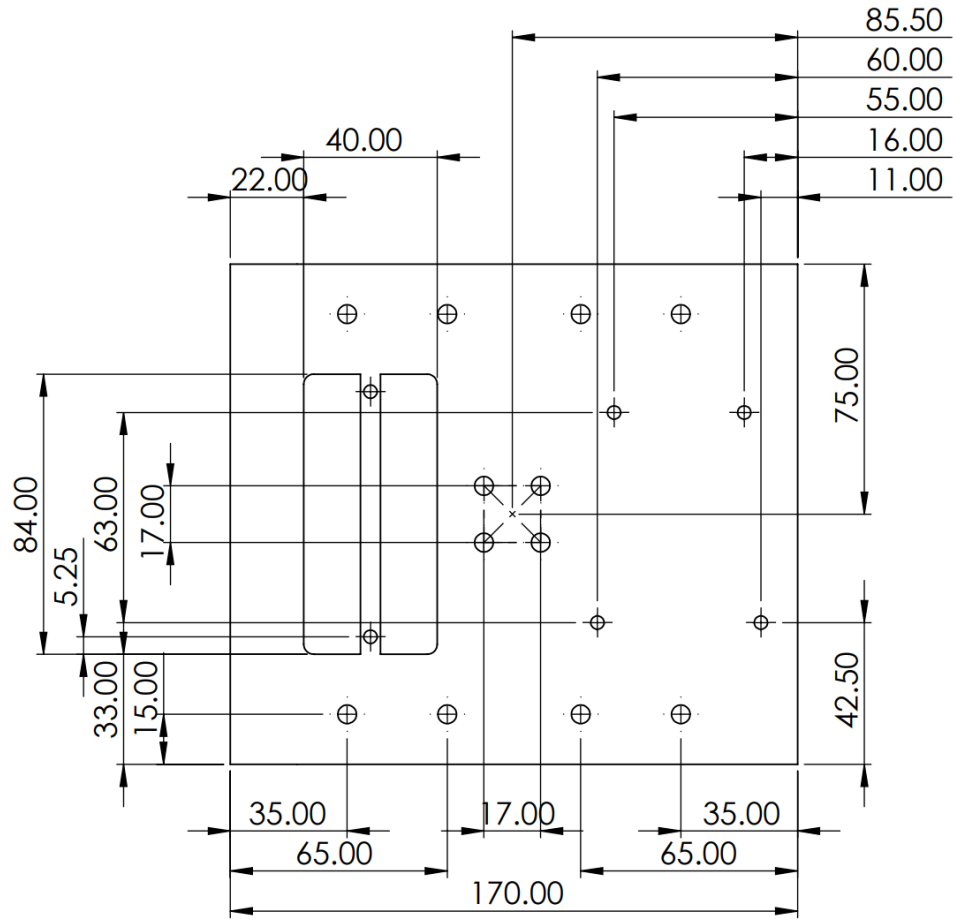
Figure 11.17: Technical Representation of the Plate.
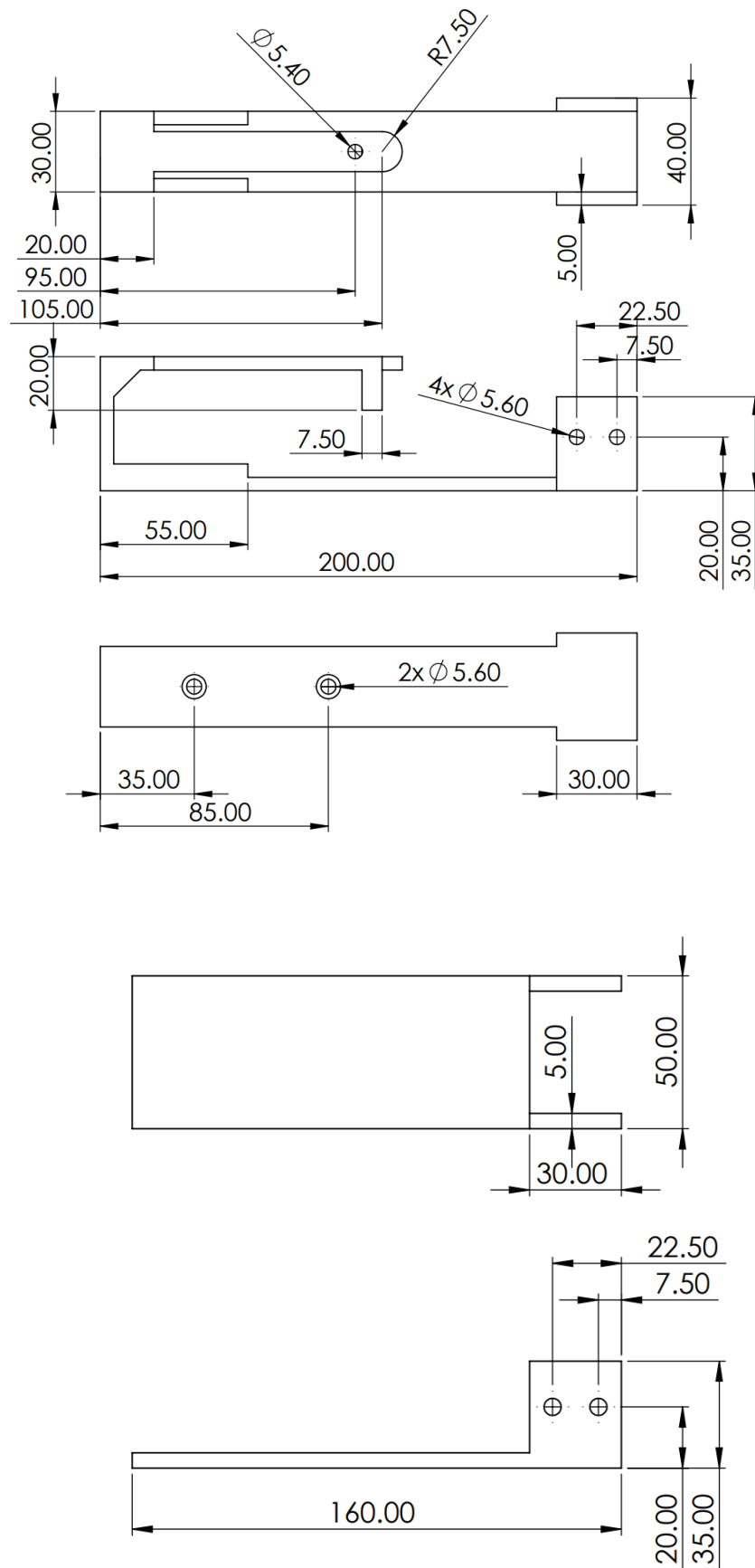
Figure 11.18: Technical Representation of the Linear Guide 1 Mount and Extender.
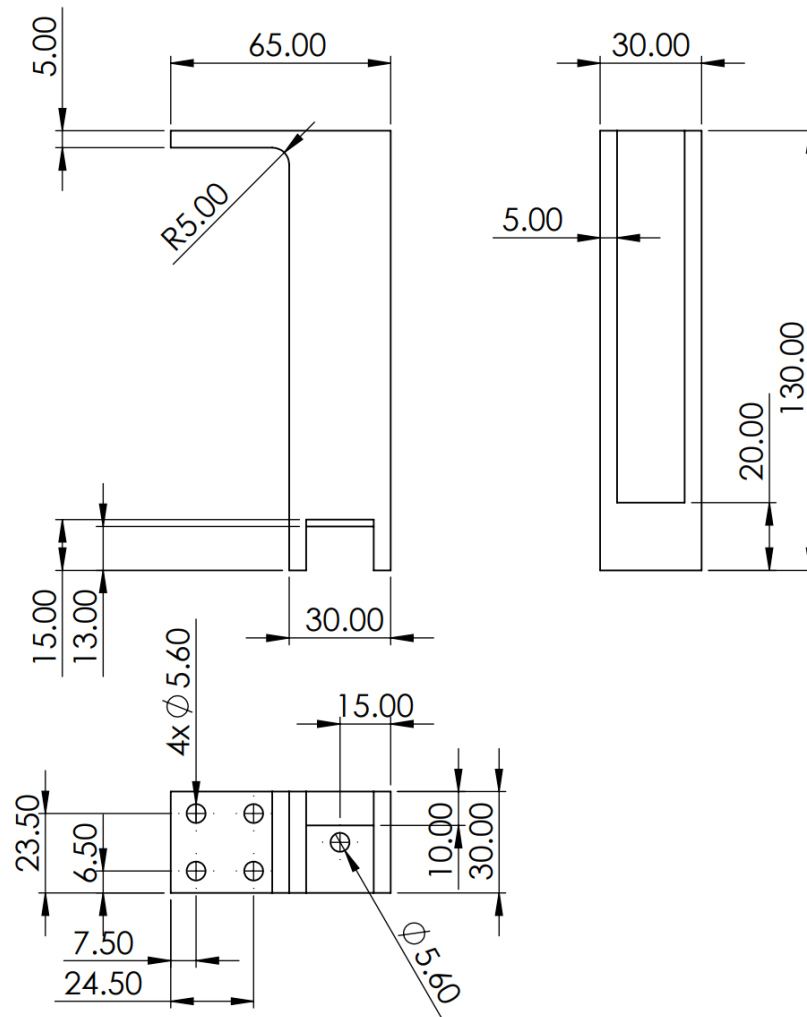
Figure 11.19: Technical Representation of the Linear Guide 2 Mount.
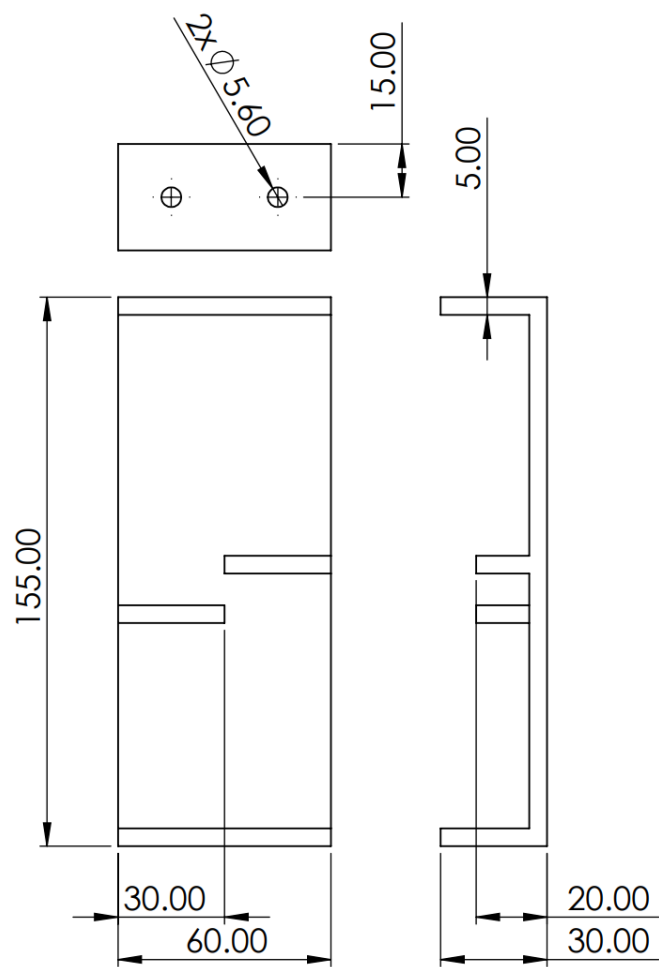
Figure 11.20: Technical Representation of the Prototype Foot.
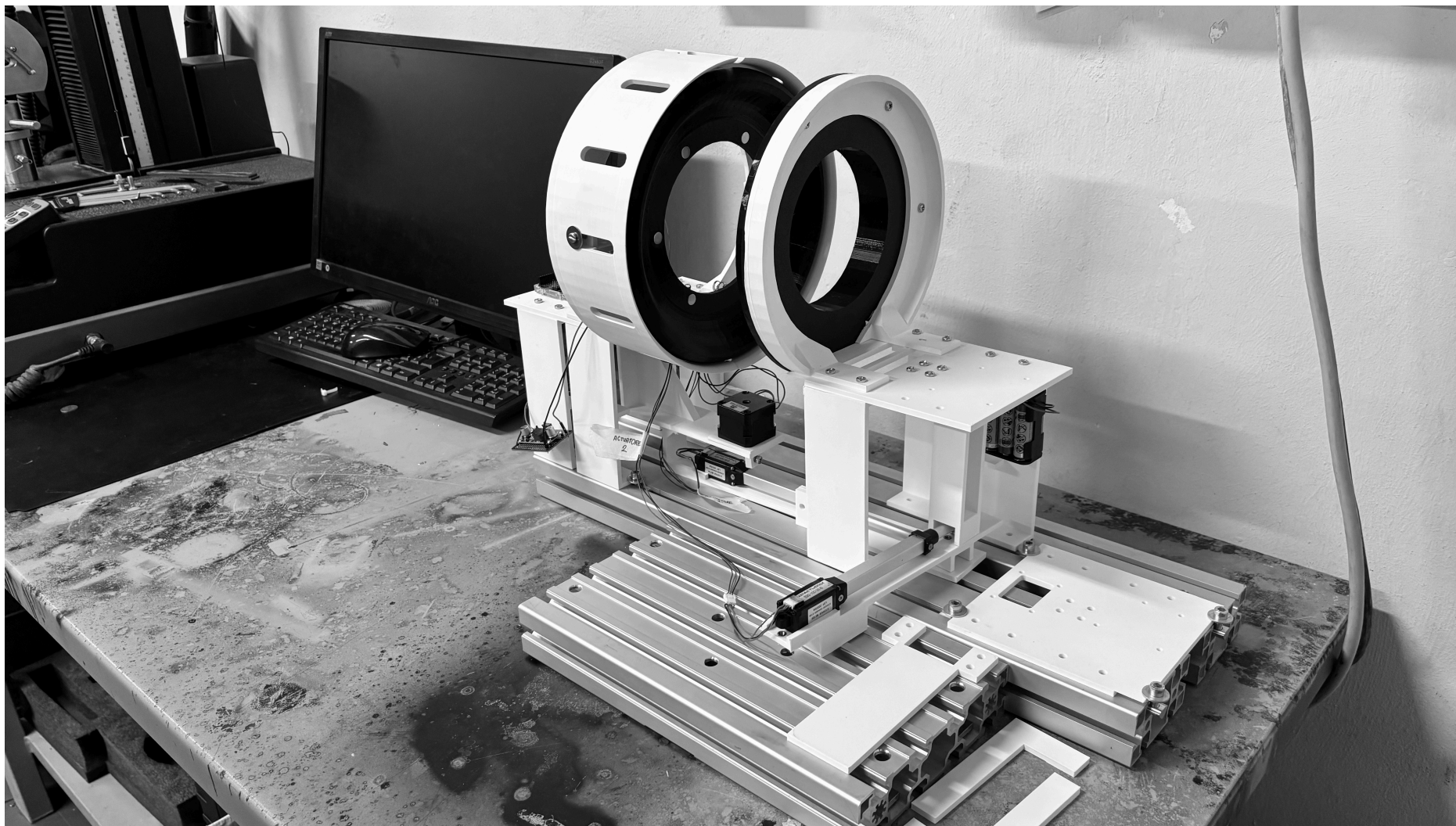
Figure 11.21: Docking Prototype Assembly.

The following table shows the bill of materials of all the parts listed in the above CAD model.

No.	Part Number	Qty.
1	ASM_Chaser	1
	DOCK_ALN_Male	1
	DOCK_Mount	1
	PR_Plate	1
	PR_Linear_Guide_2_Mount	1
	N45 Magnet	6
	ISO 7045 - M4 x 12 - Z - 12N	8
	M4 Insert	4
	HAB_Foot	3
2	PR_Interface	1
3	ISO 7045 - M4 x 16 - Z - 16N	2
4	ISO 7045 - M4 x 20 - Z - 20N	1
5	S20-100-38-B (Linear Actuator)	2
7	ASM_Target	1
	DOCK_ALN_Female	1
	DOCK_Mount	1
	DOCK_Vertical_Support_2	2
	DOCK_Vertical_Spring_L	4
	PR_Plate	1
	HAB_Stepper_Mount	1
	HAB_Guide_1_Mount	1
	HAB_Guide_1_Extender	1
	HAB_Foot	4
	DOCK_Spring	4
	DOCK_Spring	2
	M4 Insert	21
	M3 Insert	4
	ISO 7045 - M3 x 12 - Z - 12N	10
	Washer ISO 7094 - 5	10
	ISO 7045 - M4 x 20 - Z - 20N	5
	ISO 7045 - M4 x 12 - Z - 12N	21
	ISO 7045 - M4 x 40 - Z - 40N	2
	ISO - 4034 - M5 - N	4
	N45 Magnet	6
	Nema 17 Stepper Motor	1
	Arduino UNO	1
	PCB (81x53 mm)	1

Table 11.6: Bill of Materials for the prototype.

11.2.4   Electrical Model

To achieve the correct movement of each actuator in the system, a control board is chosen. Additionally, a power supply is set to withstand the energetic requirements of each item. Given that each actuator is driven by a stepper motor (each linear actuator is basically composed of a stepper motor and a thread mechanism), the motion algorithm is driven with the same specs.

The following script shows the control implemented in the prototype.

```
1  // ————————————————————————
2  // PIN DEFINITION
3  // ————————————————————————
4  const int STEP_PINs[] = {0,9,6,5}; // PWM PINS
5  const int DIR_PINs[]  = {0,8,7,4};
6
7
8  // Microstepping PINs
9  bool microstepping_enabled = false;
10
11 // const int msPIN_1 = 11;
12 // const int msPIN_2 = 12;
13 // const int msPIN_3 = 13;
14
15 const int EN_PINs[] = {0,11,12,13};
16
17 // ————————————————————————
18 // ERROR INTRODUCTION
19 // ————————————————————————
20 float deltas[] = {0,5,10,20}; // mm
21 float gammas[] = {0,2,5,10}; // deg
22
23 bool DEBUG_MODE = false;
24
25 // ————————————————————————
26 // MOTION PARAMETERS
27 // ————————————————————————
28 const float v_nom_mm_s      = 10.0; // mm / s        : Nominal
       velocity
29 const float screw_pitch_mm = 2.0;  // mm / rev      : Pitch
30 int steps_per_rev          = 200;  // steps / rev   (TBC)
31
32
33 // Timing for each phase
34 const float Dt_I   = 0.5;     // Ramp up time in seconds
35 const float Dt_II  = 11.0;    // Constant speed time in
       seconds
36 const float Dt_III = Dt_I; // Deceleration time in seconds
37
38 // Other time definition
```

```
39  int undocking_time = 10; // s
40  int wait_time       = 5; // s
41
42
43  // ————————————————————————————————
44  // SPECIFIC ACTUATOR PARAMETERS
45  // ————————————————————————————————
46  // Linear Guide 1
47
48  // Linear Guide 2
49  // Current Position (y_d)
50  float current_position_mm = 0.0; // mm
51
52  // Stepper Motor
53  // Current Angle (phi_d)
54  float current_angle_deg = 0.0; // deg
55
56
57
58  // ————————————————————————————————
59  // FUNCTIONS
60  // ————————————————————————————————
61  // stepMotor(STEP_PIN) : moves the stepper motor connected
        to the driver connected to the STEP PIN
62  void stepMotor(int motor)
63  {
64    digitalWrite(STEP_PINs[motor], HIGH);
65    delayMicroseconds(100);              // Minimum pulse width
66    digitalWrite(STEP_PINs[motor], LOW);
67    // Serial.println("!!! DEBUG : Moving stepper connected to
          PIN: " + String(STEP_PINs[motor]));
68  }
69
70
71  // ————————————————————————————————
72  // chaser_move(): Moves the chaser through the target
73  void chaser_move(bool forward = true, int motor = 1)
74  {
75    // Set direction
76    digitalWrite(DIR_PINs[motor], forward ? HIGH : LOW);
77
78    // Enable Motor
79    digitalWrite(EN_PINs[motor], LOW);
80
81    // Compute nominal steps per second
82    float steps_per_mm = steps_per_rev / screw_pitch_mm; //
          step / mm
83    float v_nom_steps_s = v_nom_mm_s * steps_per_mm;        //
```

```
           step / s
84
85    unsigned long start_time = millis();
86
87    unsigned long t_prev_step = micros();
88    float current_speed = 0.0;
89
90    while (true)
91    {
92      unsigned long t_now = millis();
93      float t = (t_now − start_time) / 1000.0; // seconds
94
95      // Determine phase and current speed
96      if (t < Dt_I)
97      {
98        current_speed = v_nom_steps_s * (t / Dt_I);   // Ramp–
              Up
99      }
100     else if (t < Dt_I + Dt_II)
101     {
102       current_speed = v_nom_steps_s;                    //
              Constant Speed
103     }
104     else if (t < Dt_I + Dt_II + Dt_III)
105     {
106       float t_dec = t − Dt_I − Dt_II;
107       current_speed = v_nom_steps_s * (1.0 − t_dec / Dt_III)
              ; // Ramp–Down
108     }
109     else
110     {
111       break; // End of movement
112     }
113
114     float step_interval_us = 1e6 / current_speed; //
              Microseconds between steps
115
116     if ((micros() − t_prev_step) >= step_interval_us)
117     {
118       stepMotor(motor);
119       t_prev_step = micros();
120     }
121   }
122
123
124   // Disable Motor
125   digitalWrite(EN_PINs[motor], HIGH);
126 }
```

```cpp
127
128  // ————————————————————————————————
129  // go_to_position(target_mm) : Moves a stepper connected to
         STEP_PIN up to target_mm millimeters from
         current_postion_mm
130  void go_to_position(float target_mm, int motor)
131  {
132    // Enable Motor
133    digitalWrite(EN_PINs[motor], LOW);
134
135    // Compute nominal steps per second
136    float steps_per_mm = steps_per_rev / screw_pitch_mm; //
           step / mm
137    float distance_mm = target_mm - current_position_mm; // mm
138
139    // Checks sign of the distance to travel
140    bool forward = distance_mm >= 0; // boolean
141    float total_distance_mm = abs(distance_mm);
142    unsigned long total_steps = total_distance_mm *
           steps_per_mm;
143
144    digitalWrite(DIR_PINs[motor], forward ? HIGH : LOW);
145
146    float v_nom_steps_s = v_nom_mm_s * steps_per_mm;
147    float step_interval_us = 1e6 / v_nom_steps_s;
148
149    unsigned long step_count = 0;
150    unsigned long t_prev = micros();
151
152    while (step_count < total_steps)
153    {
154      if ((micros() - t_prev) >= step_interval_us)
155      {
156        stepMotor(motor);
157        step_count++;
158        t_prev = micros();
159      }
160    }
161
162    current_position_mm = target_mm; // mm
163
164
165    // Disable Motor
166    digitalWrite(EN_PINs[motor], HIGH);
167  }
168
169  // ————————————————————————————————
170  // go_to_angle(target_deg) : Moves a stepper (motor) to
```

```
          target_mm millimeters from current_postion_mm
171  void go_to_angle(float target_deg, int motor)
172  {
173    // Enable Motor
174    digitalWrite(EN_PINs[motor], LOW);
175
176    float steps_per_degree = steps_per_rev / 360.0f; // step /
           deg
177    float angle_diff = target_deg − current_angle_deg; // deg
178    bool forward = angle_diff >= 0;
179    float total_angle = abs(angle_diff);
180    float total_steps = total_angle * steps_per_degree;
181    // Serial.println("!!! DEBUG : Total Steps go_to_angle: "
           + String(total_steps) + " steps.");
182
183    digitalWrite(DIR_PINs[motor], forward ? HIGH : LOW);
184
185    float v_nom_steps_s = v_nom_mm_s * (steps_per_rev /
           screw_pitch_mm); // convert to steps/s if desired
186    float step_interval_us = 1e6 / v_nom_steps_s;
187
188    unsigned long step_count = 0;
189    unsigned long t_prev = micros();
190
191    while (step_count < total_steps)
192    {
193      if ((micros() − t_prev) >= step_interval_us)
194      {
195        stepMotor(motor);
196        step_count++;
197        t_prev = micros();
198      }
199    }
200
201    current_angle_deg = target_deg;
202
203
204    // Disable Motor
205    digitalWrite(EN_PINs[motor], HIGH);
206
207  }
208
209  bool waitForUserResponse(String prompt, long timeout_ms)
210  {
211      // Ask the user a yes/no question and wait for input
             with timeout
212      Serial.println(prompt);
213      Serial.print("Enter 'y' or 'n' within ");
```

```
214       Serial.print(timeout_ms / 1000);
215       Serial.println(" seconds:");
216
217       unsigned long start_time = millis();
218       while (millis() - start_time < timeout_ms) {
219           if (Serial.available()) {
220           char response = Serial.read();
221           if (response == 'y' || response == 'Y') {
222               return true;
223           } else if (response == 'n' || response == 'N') {
224               return false;
225           }
226           }
227       }
228
229       // If timeout expires, assume "no"
230       Serial.println("No response received. Assuming motor is
              homed.");
231       return false;
232  }
233
234  void setup()
235  {
236
237       Serial.begin(9600);
238       Serial.println("——————————————————————————————————");
239
240
241       // ——————————————————————————————
242       // PIN ASSIGNMENT
243       // ——————————————————————————————
244       for (int stepper_index = 1; stepper_index < 4;
              stepper_index++)
245       {
246           pinMode(EN_PINs[stepper_index],  OUTPUT);
247           pinMode(DIR_PINs[stepper_index], OUTPUT);
248           pinMode(DIR_PINs[stepper_index], OUTPUT);
249
250
251           // Disable Motor
252           digitalWrite(EN_PINs[stepper_index],HIGH);
253       }
254
255       // ——————————————————————————————
256       // HOMING
257       // ——————————————————————————————
258       for (int stepper_index = 1; stepper_index <= 2;
              stepper_index++)
```

```
259        {
260            float position_mm = 0.0;         // mm : Initial
                   position
261            bool doHoming = true;
262
263            // Perform homing loop
264            while (doHoming)
265            {
266                // Ask for homing
267                Serial.println("——————————————————————————————");
268                doHoming = waitForUserResponse("Homing of motor
                       " + String(stepper_index)  + "? (y/n)",
                       20000);
269
270                if (doHoming)
271                {
272                    position_mm += 10.0; // mm
273                    go_to_position(position_mm, stepper_index);
274                }
275
276            }
277        }
278
279        // Homing Complete.
280
281        Serial.println("——————————————————————————————");
282        Serial.println("Homing procedure completed.");
283
284        current_position_mm = 0; // mm
285        current_angle_deg = 0.0; // deg
286
287
288
289        // pinMode(msPIN_1,OUTPUT);
290        // pinMode(msPIN_2,OUTPUT);
291        // pinMode(msPIN_3,OUTPUT);
292
293        // digitalWrite(msPIN_1,microstepping_enabled ? HIGH :
              LOW);
294        // digitalWrite(msPIN_2,microstepping_enabled ? HIGH :
              LOW);
295        // digitalWrite(msPIN_3,microstepping_enabled ? HIGH :
              LOW);
296
297
298        Serial.println("——————————————————————————————");
299        Serial.println("——————————————————————————————");
300
```

```
301     for (int delta_index = 0; delta_index <= 3; delta_index
            ++)
302     {
303         float delta_curr        = deltas[delta_index];
304         for (int gamma_index = 0; gamma_index <= 3;
                gamma_index ++)
305         {
306             float gamma_curr        = gammas[gamma_index];
307
308             go_to_position(delta_curr,2);
309             go_to_angle    (gamma_curr,3);
310
311             Serial.println("Current Delta : " + String(
                    delta_curr) + " mm. "  + "Current Gamma : " +
                    String(gamma_curr) + " deg");
312             Serial.println("————————————————————————————————————");
313             // Move forward
314             Serial.println("Moving Forward.");
315             chaser_move(true,1);
316
317             if  (!DEBUG_MODE)
318             {
319                 // Undocking
320                 Serial.println("Undocking Time.");
321                 delay(undocking_time * 1000); // Optional
                        pause
322
323
324                 // Move backward to return to starting
                        position
325                 Serial.println("Moving Backward.");
326                 chaser_move(false,1);
327                 go_to_position(0.0,2);
328                 go_to_angle    (0.0,3);
329             }
330
331             // Wait wait_time from one test and another
332             delay(wait_time * 1000);
333             Serial.println("————————————————————————————————————");
334         }
335     }
336
337
338         Serial.println("Test Complete.");
339         Serial.println("————————————————————————————————————");
340
341
342
```

```
343        for (int stepper_index = 0; stepper_index < 4;
               stepper_index++)
344        {
345            // Disable Motor
346            digitalWrite (EN_PINs[stepper_index],HIGH);
347        }
348    }
349
350
351    void loop()
352    {
353      // put your main code here, to run repeatedly:
354
355    }
```

The Arduino control system coordinates three stepper motors to execute the mechanical motions required by the ground docking subsystem prototype. Linear Guide 1 is actuated through a motor connected to pins 3 (STEP) and 4 (DIR), producing translational motion along a primary guide. The movement profile follows a trapezoidal velocity law, with distinct acceleration, constant velocity, and deceleration phases defined by user-set parameters. Linear Guide 2, controlled via pins 5 and 6, adjusts the system along a secondary axis by executing direct positioning commands based on a target displacement, calculated in steps from the screw pitch and stepper motor resolution. Rotational alignment is achieved through a third motor connected to pins 7 and 8, rotating the end effector to specific angles computed in terms of motor steps per degree. Microstepping is enabled via pins 11, 12, and 13 to improve resolution and minimize mechanical vibrations. The system initiates with a homing sequence, resetting all positions to a known zero reference. During testing, the prototype executes predefined sequences by alternating between discrete delta (linear displacement) and gamma (rotational angle) values. For each combination, the chaser carriage advances forward toward a target (simulating docking), pauses for a programmable duration, and subsequently retracts to its initial position, completing an engagement cycle. Movement commands are time-optimized by calculating nominal step intervals corresponding to a user-defined linear or angular velocity. Step pulses are generated manually with precise microsecond delays to maintain accurate synchronization across the motions.

11.3   Test Results

The presented table shows the results of the tests performed, for different error insertion cycles. As it is possible to see, the system responds perfectly to the imposed requirements, showing some difficulties for more stringent disalignments. A possible explanation for this behavior is to be attributed to the low power of the motor (of the linear actuator 1), or of the screws that act as linear guide and support the two vertical supports, sized according to the requirement and that may not be able to support an elongation equal to double the imposed misalignment. Nonetheless, the system responds correctly for most of the tests performed.

| Lateral mis. ($y_{d,1}$)	Angular mis. ($\psi_{d,1}$)	Test-001	Test-002	Test-003	Test-004	Test-005	Tot.
0	0	Positive	Positive	Positive	Positive	Positive	5
0	2	Positive	Positive	Positive	Positive	Positive	5
0	5	Positive	Positive	Positive	Positive	Positive	5
0	10	Positive	Positive	Positive	Positive	Positive	5
5	0	Positive	Failed	Positive	Positive	Positive	4
5	2	Positive	Positive	Positive	Positive	Positive	5
5	5	Positive	Positive	Failed	Positive	Positive	4
5	10	Positive	Positive	Positive	Positive	Positive	5
10	0	Positive	Positive	Positive	Positive	Positive	5
10	2	Positive	Positive	Positive	Positive	Positive	5
10	5	Positive	Positive	Positive	Positive	Positive	5
10	10	Positive	Positive	Failed	Positive	Positive	4
20	0	Positive	Positive	Positive	Positive	Positive	5
20	2	Positive	Negative	Positive	Positive	Positive	4
20	5	Negative	Failed	Failed	Positive	Positive	2
20	10	Negative	Negative	Failed	Positive	Positive	2
mm	**deg**						
Date		04/06/2025	04/06/2025	06/06/2025	06/06/2025	06/06/2025	
Start Time		16:30	17:10	16:00	16:51	17:06	
End Time		17:07	17:50	16:30	17:06	18:00	
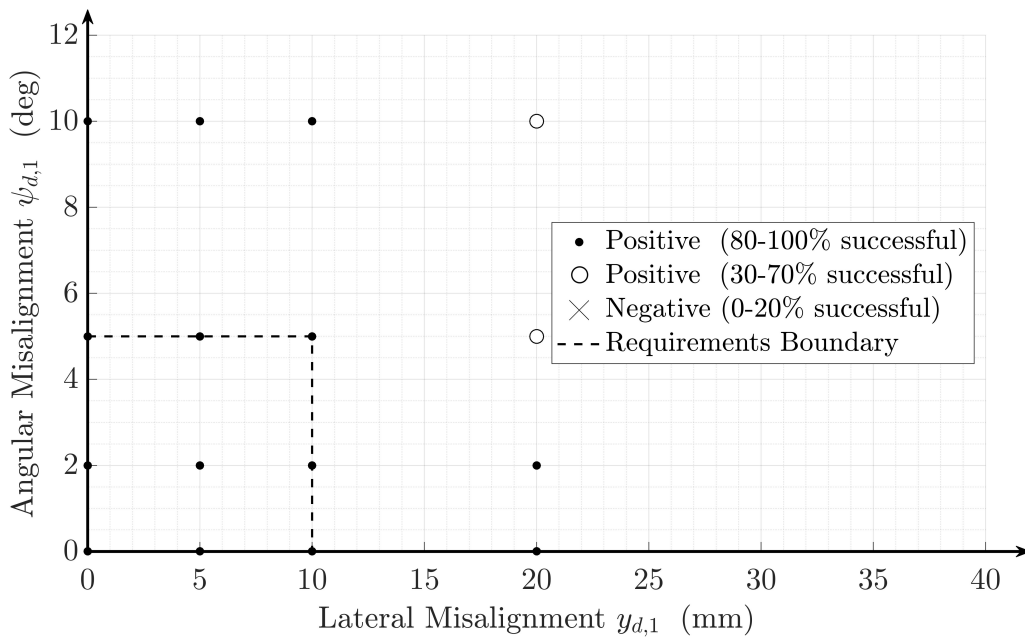
Figure 11.22: Prototype docking results table (top): Positive indicates a successful docking manuever, Negative a non-successful approach and Failed an error during the completion of the tests (i.e. one motor stalled). Prototype docking results map (bottom).

Figure 11.23: Docking test setting. Prototype (right) and PC with Arduino IDE and Serial monitor (left). The information about the test are shown on the monitor (i.e. disalinement insertion etc.)
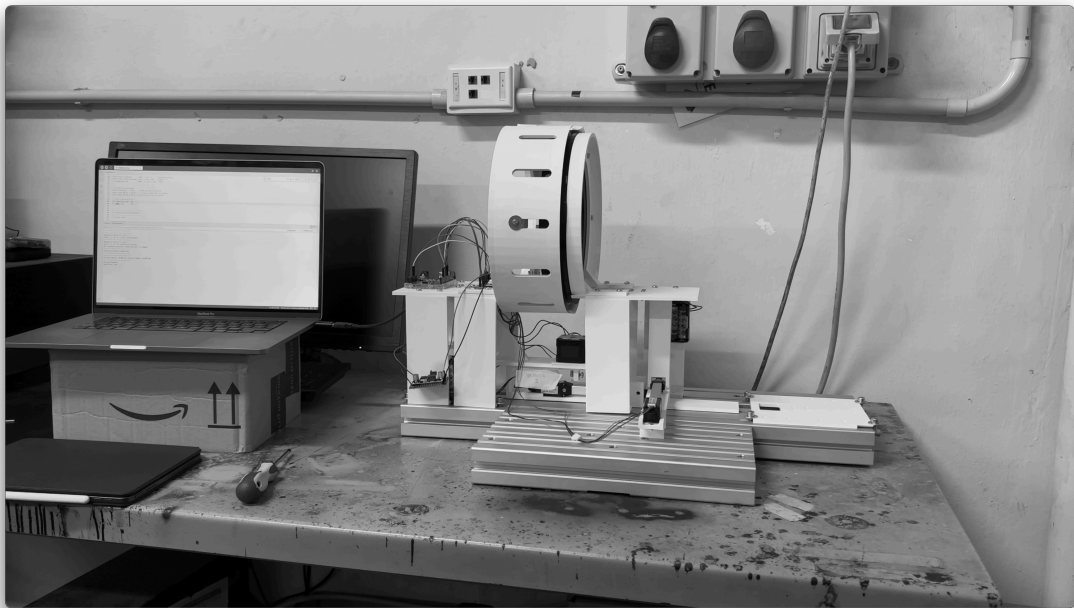

Figure 11.24: Docking test fully docked.

Chapter 12

Conclusions

This thesis has presented the comprehensive conceptualization, design, modeling, and preliminary implementation of a Pressurized Lunar Rover (PROTEUS), with a specific emphasis on the development and optimization of a novel docking subsystem suited for surface-based operations. Motivated by the renewed global interest in lunar exploration and the necessity for sustainable, long-term human presence on the Moon, the study established a clear set of mission-driven requirements for mobility, habitability, and safe docking.

The project initiated with a detailed examination of the lunar environment and mission profile, which informed the derivation of system-level requirements for the rover. These requirements formed the foundation for the subsystem-level design activities. Among all subsystems, the docking subsystem was identified as both mission-critical and technologically challenging, especially given the need to support repeated and autonomous mating operations in a gravitational and dusty terrain-conditions vastly different from traditional orbital docking environments.

To meet these unique constraints, a passive, mechanically robust docking system architecture inspired by the International Docking System Standard (IDSS) was proposed and subsequently modified to eliminate reliance on active alignment mechanisms. The innovative CLASP (Contact, Latch, Align, Shock Absorb, Pressurize) subsystem was developed to manage all phases of the docking sequence, integrating alignment geometry, shock absorption via spring-damper models, and structural capture mechanisms. A novel performance model was introduced to assess the interaction between docking partners, capturing the dynamics of contact through non-linear spring behavior and energy dissipation mechanisms.

The design was subjected to a rigorous trade-off analysis, which demonstrated that the passive IDSS-like architecture provided optimal performance in terms of mechatronic simplicity, energy efficiency, and reliability, outperforming conventional articulated or probe-drogue configurations. Geometric optimizations, particularly the selection of a double toroidal alignment section, further enhanced mating robustness and error tolerance. The systems behavior under misalignment conditions was modeled mathematically and validated via numerical simulations, leading to the preliminary sizing of critical components including springs, dampers, and support structures.

To evaluate the feasibility of the design, a scaled prototype was constructed and tested, allowing for experimental validation of theoretical assumptions. The physical model confirmed the subsystem's ability to tolerate significant translational

and angular misalignments, supporting its suitability for lunar applications. An implementation framework was developed using CAD modeling, SolidWorks motion analysis, MSC ADAMS dynamic simulation, and genetic optimization in MATLAB, culminating in an integrated design approach adaptable for further mission-specific refinements.

In conclusion, this work offers a holistic methodology for the development of a terrestrial docking system on lunar analogs, providing not only a proof-of-concept but also a scalable platform for future missions requiring secure and efficient vehicle-habitat mating on extraterrestrial surfaces. The design choices and modeling strategies demonstrated in PROTEUS lay a solid foundation for further advancement toward operational prototypes and contribute to the broader field of planetary surface systems engineering.
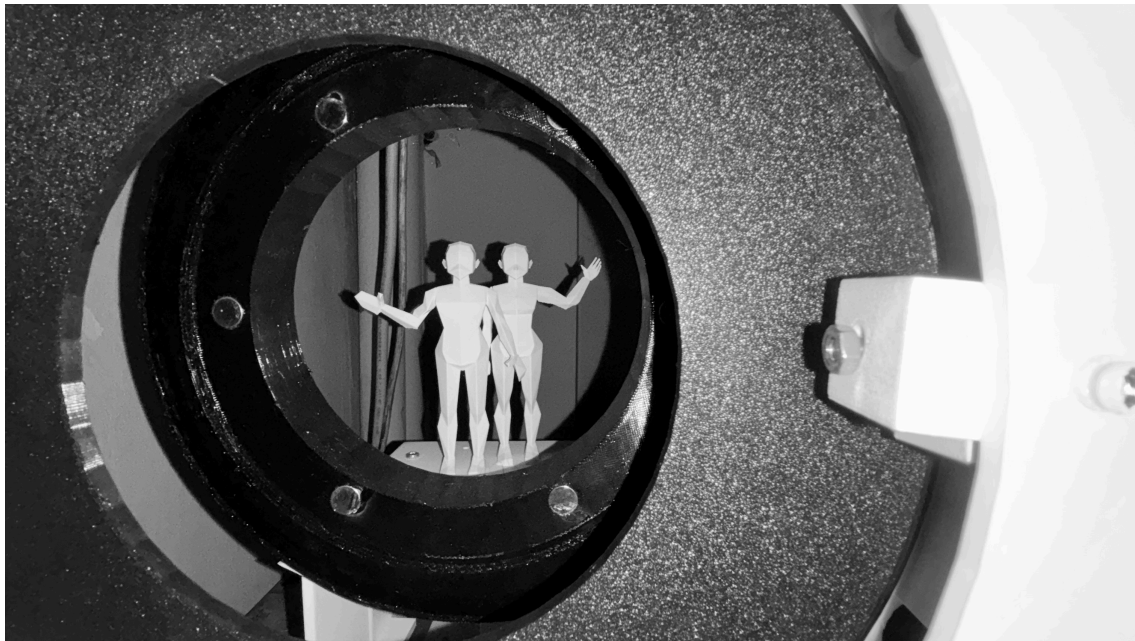

Figure 12.1: Two astronauts waving.

Acknowledgements

accanto durante i momenti di gioia e i momenti di paura ed ansia, ed è sempre riuscita a farmi tornare con il sorriso. Grazie per aver sempre accolto le mie follie e sregolatezze, i miei infiniti dubbi e i momenti passati insieme in riva ad un lago, non curanti della sessione.

A tutti voi, grazie.

Ascoltami ragazzo giapponese: gli aeroplani non sono né degli strumenti di guerra, né un mezzo di profitto commerciale. Gli aeroplani sono uno splendido sogno. Il progettista è colui che conferisce forma al sogno.

- Giovanni Battista Caproni, *Si alza il vento*, H. Miyazaki, 2011

Bibliography

[1] Y. Lin, "Return to the moon: New perspectives on lunar exploration," *Science Bulletin*, vol. 69, no. 13, pp. 2136–2148, 2024. Available: link.

[2] NASA, J. Zakrajsek, D. McKissock, J. Woytach, J. Zakrajsek, F. Oswald, K. McEntire, G. Hill, P. Abel, D. Eichenberg, and T. Goodnight, "Exploration rover concepts and development challenges," in *1st Space Exploration Conference: Continuing the Voyage of Discovery*, p. 2525, 2005. Available: link.

[3] D. Vaniman, R. Reedy, G. Heiken, G. Olhoeft, and W. Mendell, "The lunar environment," *Lunar Sourcebook*, vol. 1, pp. 27–60, 1991. Available: link.

[4] D. Acker, E. Gutierrez, J. P. Calatayud, P. Modi, A. Kugic, and S. Khan, "An Analysis of the Requirements for a Sustainable Lunar Transportation System to Enable Initial DIANA Infrastructure," in *Journal of Physics: Conference Series*, vol. 2526, p. 012115, IOP Publishing, 2023. Available: link.

[5] *ECSS-E-ST-10-06C*. Available: link.

[6] B. Imhof, S. Ransom, N. Frischauf, S. Häuplik-Meusburger, W. Hoheneder, S. Mohanty, K. Özdemir, and R. Waclavicek, "RAMA-Rover For Advanced Mission Applications," in *Proceedings of the 61th IAC (International Astronautical Congress)*, p. 10, IAF, 2010. Available: link.

[7] M. Bhardwaj, V. Bulsara, D. Kokan, S. Shariff, E. Svarverud, and R. Wirz, "Design of a pressurized lunar rover," tech. rep., NASA, 1992. Available: link.

[8] M. Clowdsley, "Protecting astronauts from space radiation on the lunar surface," in *Lunar Surface Innovation Consortium*, 2021. Available: link.

[9] J. Cluff, "Toyota lunar cruiser: Off-roading on the moon," *Gear Junkie*, 2022. Available: link.

[10] M. Thangavelu, "Usc artemis project: Maximum impact(maxim) moon mission tribute to apollo," *ReserchGate*, 10 2020. Available: link.

[11] SpaceX, *Falcon User's Guide*, 2021. Available: link.

[12] N. Grumann, "Cygnus spacecraft." Available: link.

[13] ESA, "Esa moonlight: Connectivity and navigation on the moon," *ESA Website*, 2025. Available: link.

[14] W. D. Carrier III, G. R. Olhoeft, and W. Mendell, "Physical properties of the lunar surface," *Lunar sourcebook, a user's guide to the moon*, pp. 475–594, 1991. Available: link.

[15] R. Agrawal and G. P. Pandey, "Solid polymer electrolytes: Materials designing and all-solid-state battery applications: An overview," *Journal of Physics D: Applied Physics*, vol. 41, p. 223001, 10 2008. Available: link.

[16] K. Creel, J. Frampton, D. Honaker, K. Mcclure, and M. Zeinali, "Pressurized lunar rover," tech. rep., NASA, 1992. Available: link.

[17] olympioi.com, "Proteus: The shape-shifting sea god of elusive wisdom," 2023. Available: link.

[18] T. Mohtar, *Design and modeling of a space docking mechanism for cooperative on-orbit servicing.* PhD thesis, Politecnico di Torino, 2018. Available: link.

[19] E. Ezell and L. Ezell, "The partnership: A nasa history of the apollo-soyuz test project. courier corporation," tech. rep., NASA, 1978. Available: link.

[20] NASA, "Space science data coordinated archive: Gemini 8," tech. rep., NASA, 2022. Available: link.

[21] NASA, "Space science data coordinated archive: Cosmos 186," tech. rep., NASA, 2022. Available: link.

[22] NASA, "Space science data coordinated archive: Apollo 9," tech. rep., NASA, 2022. Available: link.

[23] NASA, "Space science data coordinated archive: Astp - soyuz," tech. rep., NASA, 2022. Available: link.

[24] NASA, "Space science data coordinated archive: Sts 71," tech. rep., NASA, 2022. Available: link.

[25] NASA and S. R. Donahoe, "International Docking System Standard (IDSS) Interface Definition Document (IDD) Revision F," tech. rep., NASA, 2022. Available: link.

[26] L. Giacconi, "Lpr mobility system," Master's thesis, Politecnico di Torino, 2025. Available: link.

[27] J. Barber, *Contact Mechanics.* Springer, 2011.

[28] A. E. Green and Zerna, *Theoretical Elasticity.* Dover Publications, 1992. Available: link.

[29] ALTAIR, "Soft soil tire model," *Altair MotionView*, 2022. Available: link.

[30] L. Landau, E. Lifshits, A. Kosevich, E. Lifshitz, and L. Pitaevskii, *Theory of Elasticity: Volume 7.* Course of theoretical physics, Butterworth-Heinemann, 1986.

[31] K. Johnson, *Contact Mechanics.* Cambridge Press, 1985. Available: link.

[32] M. G. Bekker, "Introduction to terrain-vehicle systems," *University of Michigan Press*, 1969.

[33] J. Y. Wong, "Theory of ground vehicles," *Wiley*, 2008.

[34] S. Shoop, "Mechanics of tire-terrain interaction," *U.S. Army Cold Regions Research and Engineering Laboratory*, 2001.

[35] J. K. Mitchell and K. Soga, "Fundamentals of soil behavior," *Wiley*, 2005.

[36] H. H. Schmitt, W. D. Carrier, and J. K. Mitchell, "Lunar regolith properties and their influence on design," *NASA Technical Reports*, 2009.

[37] J. Kelley, K. Babaalihaghighi, N. Bader, C. Wege, F. Pape, and G. Poll, "Application of hertzian theory to torus on plane contacts," *Proceedings of the Institution of Mechanical Engineers, Part J: Journal of Engineering Tribology*, vol. 236, no. 11, pp. 2189–2208, 2022.

[38] J.-D. Wheeler, *Non-elliptical point contacts: The Torus-on-Plane conjunction.* PhD thesis, Université de Lyon, 2016.

[39] M. Irons, "The curvature and geodesics of the torus," *rdrop*, 2005. Available: link.

[40] J. Barber, *Intermediated Mechanics of Materials.* Springer, 2011.

[41] NASA, "Nasa technical report server," *NASA*, 2025. Available: link.

[42] M. Bastrzyk, "Material properties of three candidate elastomers for space seals applications," tech. rep., NASA, 2010. Available: link.

[43] BAMBULab, "3d printed comparison guide," *BAMBULab*, 2025. Available: link.

[44] NASA, D. W. Harris, P. D. Kessler, T. M. Nickens, A. J. Choate, B. L. Horvath, M. A. Simon, and C. Stromgren, "Moon to Mars (M2M) Habitation Considerations: A Snap Shot As of January 2022," tech. rep., NASA, 2022. Available: link.

[45] European Cooperation for Space Standardization (ECSS), *ECSS-E-ST-32-02C: Structural Design and Verification of Pressurized Hardware*, jul 2008. Available: link.

[46] AutoDesk, "Compression spring calculation formulas in metric units," *AutoDesk Website*, 2016. Available: link.

[47] H. Nigus, "Kinematics and load formulation of engine crank mechanism," *Mechanics, Materials Science & Engineering Journal*, 2015.

[48] A. Pétrowski and S. Ben-Hamida, *Evolutionary algorithms*, vol. 9. John Wiley & Sons, 2017.

[49] G. Jacazio and B. Piombo, *Esercizi Svolti di Meccanica applicata alle macchine.* Levrotto-Bella, 1997.